Democratic and Popular Republic of Algeria

Ministry of High Education and Scientific Research

THESIS

Presented at Faculty of Sciences
Department of Physics
To obtain the degree of

Doctor

Option: Condensed Matter Physics
By

KHADIDJA BOUDIAF

Title

Study of fundamentals physicals properties of the layered BaFAg*Ch* (*Ch*=S, Se and Te) by first principles methods

Discussed publicly at .. / .. / 2019 with the board of examiners:

Mr. M. BOUDISSA	Professor	Univ. F. ABBAS Setif 1	Chairman
Mr. A. BOUHEMADOU	Professor	Univ. F. ABBAS Setif 1	Supervisor
Mr. A. MOSBAH	M.C.A	Univ. F. ABBAS Setif 1	Examiner
Mr. T. CHIHI	M.C.A	Univ. F. ABBAS Setif 1	Examiner
Mr. R. KHENATA	Professor	Univ. M. STAMBOULI, Mascara	Examiner
Mr. S. MAHTOUT	Professor	Univ. A. MIRA, Bejaia	Examiner
Mr. N. GUECHI	M.C.A	Univ. F. ABBAS Setif 1	Invited

Acknowledgement

*First and last thanks to **Allah** who gives me the power to go forward in a way illuminated with His merciful guidance.*

I would like to express my thanks to Prof. Dr. A. Bouhemadou, Department of Physics, Laboratory for Developing New Materials and Their Characterization, for giving me the chance to be one of his students and for his generous advices, patience, valuable discussions which helped me greatly.

I would like to thank my thesis committee members

I am thankful to all members and colleagues, Laboratory for Developing New Materials and Their Characterization, Solid State Department for their support and appreciated help.

I am so grateful to all my teachers and professors throughout my academic career, from the elementary school to the University.

Finally, I would like to thank my family and friends for their continued support and encouragement over the years.

"Effective communicators make an effective team"

Dedication

To the memory of my dear mother.

K. BOUDIAF

Abstract

In the present work, the structural, elastic, electronic, optical, thermoelectric and thermodynamic properties of the layered BaFAg*Ch* (*Ch* = S, Se, Te) were investigated using the full potential linearized augmented plane wave (FP-LAPW) method in the framework of density functional theory (DFT). To evaluate the spin-orbit coupling (SOC) effect, both the scalar relativistic and full relativistic calculations were performed. The SOC effect is found to be not negligible in the title compounds. The calculated structural parameters are in good accordance with the existing experimental data. The monocrystalline and polycrystalline elastic modules of the title compounds were determined via the energy-strain method. The investigated compounds show a strong anisotropic behavior of the structural and elastic parameters. The calculated electronic band structures using the Tran-Blaha modified Becke-Johnson (TB-mBJ) potential reveal that the three considered systems are large direct band gap semiconductors. The assignments of the energy band electronic states and chemical bonding characters were accomplished with the help of the *l*-decomposed atomic densities of states diagrams. Frequency-dependent polarized optical functions, including dielectric function, absorption coefficient, refraction index, extinction coefficient, reflectivity and energy loss function, were computed for an energy range from 0 to 30 eV. The microscopic origin of the electronic states that are responsible of the optical spectra structures were determined. The optical spectra exhibit a considerable anisotropy. The FP-LAPW band structure and the semi-classical Boltzmann transport theory were used to study the charge-carrier concentration and temperature dependences of the thermoelectric parameters, including Seebeck coefficient, electrical conductivity, thermal conductivity and figure of merit. Our results show that the values of the thermoelectric parameters of the *p*-type compounds are larger than that of the *n*-type ones. The optimal *p*-type doping concentrations and temperatures that yield the maximum values of the figure of merit of the title compounds were calculated. These are important parameters to guide experimental works. The quasi-harmonic Debye model in combination with the FP-LAPW method was used to study the temperature and pressure dependences of the unit cell volume, bulk modulus, heat capacity, volume thermal expansion and Debye temperature.

Keywords: LaOAgS-type layered crystal; First-principles calculations; DFT; FP-LAPW; GGA; TB-mBJ; Spin-orbit coupling; Structural properties; Elastic modules; Electronic structure; Effective masse; optical functions; Thermoelectric parameters; Thermodynamic properties.

ملخص

لقد قمنا في هذا العمل البحثي بدراسة الخواص البنيوية، المرونة، الإلكترونية، الضوئية، الكهروحرارية و الثيرموديناميكية للمركبات BaFAgCh، حيث Ch = S, Se, Te ، باستعمال طريقة الأمواج المستوية المتزايد خطيا (FP-LAPW) في إطار نظرية دالية الكثافة (DFT). بغية تقييم تأثير ترابط العزم المغزلي بالعزم المداري (SOC)، تم إجراء الحسابات بطريقتين: حساب نسبي جزئي (دون إدخال ال SOC) وحساب نسبي مطلق (إدخال ال SOC). وجدنا أن تأثير ال SOC كان معتبرا في المركبات موضوع الدراسة. تتوافق القيم المحسوبة للمعاملات البنيوية توافقا جيدا مع القيم التجريبية المقابلة المتوفرة. تم تحديد ثوابت المرونة للمركبات المدروسة أحادية التبلور ومتعددة التبلور بالاعتماد على طريقة طاقة-تشوه. أبدت المركبات المدروسة وبشكل معتبر سلوكا متباين المناحي لكل من معاملات البنية البلورية وخواص المرونة. أظهرت البنية الإلكترونية باستخدام كمون TB-mBJ أن المركبات الثلاث المدروسة هي أشباه نواقل ذات فجوة طاقية مباشرة عريضة. تم تحديد الحالات الالكترونية المساهمة في شرائط الطاقة وتحديد طبيعة الروابط الكيميائية وذلك من خلال دراسة كثافة الحالات الالكترونية الجزئية. قمنا بدراسة تغيرات الدوال الضوئية: دالة العزل الكهربائي، معامل الامتصاص، معامل الإنكسار، معامل الخمود، الإنعكاسية ودالة ضياع الطاقة بدلالة تردد الموجة الضوئية في مجال الطاقة $0 \rightarrow 30$ eV. تم تعيين أصول الحالات الالكترونية المساهمة بفعالية في الذروات المشاهدة في طيف دالة العزل الكهربائي. وجدنا أن أطياف الدوال الضوئية متباينة المناحي. درسنا الخواص الكهروحرارية (معامل سيبيك S، الناقلية الكهربائية σ، الناقلية الحرارية κ و معامل الجدارة ZT) بدلالة درجة الحرارة و تركيز حاملات الشحنة الكهربائية باستعمال نظرية النقل لبولتزمان انطلاقا من حسابات البنية الإلكترونية بطريقة ال FP-LAPW . أظهرت النتائج المحصل عليها أن القيم العددية للمعاملات الكهروحرارية في حالة التطعيم من نوع p هي أكبر من تلك المقابلة في حالة التطعيم من نوع n. تم تحديد كلا من تراكيز الثقوب ودرجات الحرارة الأمثل الموافقة للقيم العظمى لمعامل الجدارة للمركبات الثلاث موضوع الدراسة؛ هاته النتائج مفيدة جدا في تسهيل وتوجيه العمل التجريبي. تم تقييم تأثير درجة الحرارة والضغط على حجم الخلية الأولية، معامل الانضغاطية، الحرارة النوعية، معامل التمدد الحراري ودرجة حرارة ديباي باستعمال طريقة نموذج ديباي الشبه توافقي انطلاقا من معطيات طاقة-حجم المتحصل عليها باستعمال طريقة ال FP-LAPW.

الكمات المفتاحية: بلورة من نوع LaOAgS؛ حسابات المبادئ الأولى؛ نظرية دالية الكثافة (DFT)؛ طريقة الأمواج المستوية المتزايد خطيا (FP-LAPW)؛ تقريب GGA؛ كمون TB-mBJ؛ ترابط عزم مغزلي-عزم مداري (SOC)؛ الخواص البنيوية؛ ثوابت المرونة؛ البنية الإلكترونية؛ الكتلة الفعّالة؛ الخواص الضوئية؛ المعاملات الكهروحرارية؛ الخواص الثيرموديناميكية.

Résumé

Dans le travail présent, nous avons étudié les propriétés structurales, élastiques, électroniques, optiques, thermoélectriques et thermodynamiques des composées BaFAg*Ch* (*Ch* = S, Se, Te) qui se cristallise dans une structure de type LaOAgS en utilisant la méthode des ondes planes augmentées linéarisé (FP-LAPW) dans le cadre de la théorie de la fonctionnelle de la densité (DFT). Pour évaluer l'effet du couplage spin-orbite (SOC), nous avons effectué les calculs à la fois sans et avec l'inclusion du couplage spin-orbite. Nous avons trouvé que l'effet du SOC est non négligeable dans les composés étudiés. Les paramètres structuraux calculés sont en bon accord avec les données expérimentales disponibles. Les constants élastiques des composés monocristallins et polycristallins sont déterminés en utilisant la méthode énergie-déformation. Les composés étudiés sont caractérisés par une forte anisotropie concernant les paramètres structuraux et les constants élastiques. Les structures de bandes d'énergie calculées via le potentiel TB-mBJ révèlent que les trois composés considérés sont des semi-conducteurs à large bande interdite. Les états électroniques formant les bandes d'énergie et la nature des liaisons chimiques sont déterminés à partir des diagrammes des densités d'états électroniques partielles. La dépendance des fonctions optiques (y compris la fonction diélectrique, coefficient d'absorption, indice de réfraction, coefficient d'extinction, la réflectivité et la fonction de perte d'énergie) en énergie des photons est étudiée dans un intervalle d'énergie de 0 à 30 eV. L'origine microscopique des états électroniques responsables des structures des spectres optiques est déterminée. Les spectres optiques présentent une forte anisotropie. Les dépendances des paramètres thermoélectriques (y compris le coefficient de Seebeck, conductivité électrique, conductivité thermique et figure de mérite) en température et en pression sont étudiées en utilisant la théorie semi-classique de transport de Boltzmann basée sur la structure de bande calculée via la méthode FP-LAPW. Les résultats obtenus montrent que les valeurs numériques des paramètres thermoélectriques des composés dopés *p* sont plus grandes que celles des composés dopés *n*. Les valeurs optimales de la concentration du dopant et de la température qui correspondent à la valeur maximale de la figure de mérite sont déterminées. C'est valeurs sont très importantes pour guider les travaux expérimentaux. Le modèle quasi-harmonique de Debye en association avec la méthode FP-LAPW, est utilisé pour étudier la dépendance en température et en pression du volume de la maille unitaire, module de compressibilité, capacité thermique, coefficient de dilatation thermique et la température de Debye.

Mots clés : Composés de type LaOAgS ; Calcul ab-initio ; DFT ; FP-LAPW) ; GGA ; TB-mBJ ; Couplage spin-orbite ; Paramètres structuraux ; Constantes élastiques ; Structure électroniques ; Masse effective ; Propriétés optiques ; Paramètres thermoélectriques ; Propriétés thermodynamique.

Contents

List of Figures

Chapter I

Chapter II

Chapter III

Chapter IV

List of Tables

Chapter IV

List of Symbols

ψ	Wave function of the quantum system.
$\widehat{H}$	The Hamiltonian operator.
DFT	Density Functional Theory.
ρ	Electronic density.
HK	Hohenberg and Kohn.
KS equations	Kohn-Sham equations.
XC	Exchange-Correlation.
HEG	Homogeneous electron gas.
LDA	Local Density Approximation.
GGA-PBEsol	Perdew-Burke-Ernzerhof functional for Solids.
GGA-PBE	generalized gradient approximations.
U	Hubbard parameter.
BR	Becke-Roussel exchange potential.
BJ	The exchange potential proposed by Becke and Johnson.
TB-mBJ	Tran-Blaha modified Becke-Johnson potential.
PP	Pseudo-potential method.
APW method	Augmented Plane wave Methods.
FP-LAPW method	The full-potential linearized augmented plane wave method.
MT spheres	The muffin-tin spheres.
E_l	The linearization energies.
U_l	The radial functions.
LAPW+LO	LAPW method amended by local orbitals (LO).
S.G	Space groupe.
BZ	Brillouin zone.
a.u	atomic unit.
EOS	Equation of state.
V	Volume.
P	Pressure.
B_0	The bulk modulus.
E	The internal energy.
BM	Birch Murnaghan.
E_{Coh}	The cohesive energies.

ΔH	Formation enthalpies.
C_{ij}	The elastic constants.
B	Bulk modulus.
G	Shear modulus.
B/G	Pugh's indicator.
ν	Poisson's coefficient.
θ_D	Debye temperature.
v_m	The average sound wave velocity.
v_s	Shear sound velocities.
v_l	Longitudinal sound velocities.
A^U	The universal anisotropy index.
T_m	The melting point.
E_g	Energy band gap.
VB	Valence Band.
CB	Conduction Band.
EF	Fermi energy level.
SR	The scalar-relativistic corrections.
SOC	The spin-orbit coupling correction.
m^*	The effective charge-carrier mass.
TDOS	Total Density Of States.
PDOS	Partial Density Of States.
$\mathcal{E}$	the dielectric function.
α	absorption coefficient.
n	The refractive index.
k	The extinction coefficient.
R	The optical reflectivity.
μ	Chemical potential.
CRTA	Constant relaxation time approximation.
RBA	Rigid band approximation.
τ	The relaxation time.
k_l	lattice thermal conductivities.
k_{min}	minimum lattice thermal conductivities.
S	Seebeck coefficient.

σ	Electrical conductivity.
κ_{el}	Electronic thermal conductivity.
PF	Power factor.
ZT	Figure of merit.
B_S	The adiabatic bulk modulus .
B_T	The isothermal bulk modulus .
α	The thermal expansion coefficient.
γ	Grüneisen parameter.
C_V	Constant volume heat capacity.
C_P	Constant pressure heat capacity.

Chapter I

GENERAL INTRODUCTION

General introduction

I.1. Preamble

Condensed matter physics and materials science play a primordial role in the technological revolution that we are living nowadays. Condensed matter physics investigates the physical properties of condensed matter through sophisticated and modern theories. Materials science deals with preparing and characterizing materials of whatever types. Researchers in condensed matter physics and materials science fields are continually searching for new materials that satisfy the increasing requirements of technological applications. Therefore, condensed matter physics and materials science are renewed, very extensive and very active fields for theoretical and experimental scientific research. In fact, before selecting and using a material for a specific technological application, it is primordial to ensure that its properties; structural, electronic, mechanical, optical, magnetic and so on, are adapted to the desired applications as first step. Therefore, detailed and accurate knowledge of the physical and chemical properties (structural, electronic, mechanical, magnetic, optical…etc.) of synthetized materials via experimental and theoretical methods is substantial and necessary to identify the possibilities of their usage in technological applications. The physical and chemical properties of materials are closely related to their electronic structures. Therefore, the main purpose of the solid-state matter physics and chemistry; a branch of the condensed matter physics and chemistry, is the determination of the electronic structures of solids. Determination of the electronic structures of materials is primordial to understand and explain the obtained experimental results on their properties and to predict their properties even if they are not yet experimentally determined. According to the quantum mechanics theory, the electronic structures of materials can be determined theoretically through the resolution of the corresponding Schrödinger equation. To resolve the Schrödinger equation for atoms, molecules and materials, theoretical chemists and physicists have developed two kind of theoretical methods, namely semi-empirical and *ab initio* (first-principles) methods. The so-called semi-empirical models often include many adjustable parameters where their

determinations require experimental input data. The so-called *ab initio* methods, which are more rigorous, more sophisticated and based on the fundamental quantum theory, require only atomic constants (i.e., the chemical nature of the constituting atoms of the material) as input parameters. Nowadays, the *ab initio* methods become a basic tool to study the structural, electronic, mechanical, optical…etc. properties of atoms, molecules and materials. They are also a tool of choice to explore specific properties and effects that are difficult or impossible to be determined experimentally and to predict new materials with specific properties; they sometimes replace costly experiments or even unattainable in the laboratory. The power of the *ab initio* calculations originates from the formalism of the density functional theory (DFT) [1, 2] and its two approximations for the exchange-correlation energy, namely the local density approximation (LDA) and the generalized gradient approximation (GGA). The basic formalism of DFT is based on the theorem of Hohenberg and Kohn (1964) [3], which is based on the idea that the total energy of a system is a functional of the density of electrons. Some different methods based on the DFT have been developed. The full potential linearized augmented plane wave (FP–LAPW) [4, 5] is one of the accurate methods that are developed in the framework of DFT. In the present work subject of the present thesis, the FP–LAPW approach based on the DFT was used to investigate the structural, elastic, electronic, optical, thermoelectric and thermodynamic properties of the BaFAg*Ch* (*Ch* = S, Se and Te) compounds.

I.2. Problematic, motivation and Key objectives

Recently, semiconductors with superlattice structure have attracted the interest of the condensed matter and material engineering communities due to their promising physical properties and practical applications. A superlattice is a periodic structure of layers of two or more materials. Typically, the thickness of one layer is several nanometres. The layered quaternary LaOAgS-like system, named also 1111 phases, which consist of a periodic stacking of two alternating layers [LaO] and [AgS], forming a natural superlattice. The layered crystallographic structure (see Fig.I.1) gives to this large family members (more than 200 compounds) two different bonding types; ionic and covalent, and might be the essential factor on the most interesting physical properties such as thermoelectricity [6], transparency [7], degenerate *p*-type electrical conductivity [8], ferromagnetic response [9], ionic conductivity [10] and medium-temperature

superconductivity [11,12]. Owing to their outstanding physical properties, the layered quaternary LaOAgS-like systems have various technological applications, such as *p*-type transparent semiconductors [13, 14], thermoelectrics [15] optoelectronic devices [16] and photovoltaics [17]. The whole set of the 1111-like systems can be classified into two main subgroups [12, 18]: (i) superconductors and (ii) transparent semiconductors. The first category comprises metallic-like phases, which attract the attention of researchers for their superconductivity and magnetic properties [11, 19]. The second one comprises the 1111-like systems exhibiting semiconducting behaviour, which possess some interesting optical and thermoelectric properties [7, 20-23]. The 1111-like materials show a high flexibility to a large variety of constituent elements. The 1111-like oxychalcogenides have attracted the main attention of the researchers; however, much less investigations have been performed on the 1111-like chalcogenide fluorides.

The history of the 1111-like semiconductor backs to 1994 when Zhu *et al.* [24] reported the synthesis of a new series of copper oxyselenides *R*CuSeO (*R* = La, Sm, Gd and Y) that are built of a fluorite type layer [*R*O] and an antifluorite type layer [CuSe] stacking alternatively along the *c* direction. They crystalize in a tetragonal crystalline structure

Starting from 2003, Yanagi *et al.* [25] reported the synthesis via solid-state reactions and the crystalline structure of two copper chalcogenide fluorides: BaCu*Q*F (*Q* = S, Se) materials, which are candidate transparent *p*-type conductors. They also characterized their bulk electrical and optical properties. Latter, based on the photoemission measurements and full-potential linearized augmented plane wave band-structure calculations, the origin of the high hole conduction in BaCu*Q*F (*Q* = S, Se) was investigated by Yanagi team [26]. The high hole mobility and stability in BaCu*Q*F relative to most oxides afford a significantly larger *p*-type conductivity.

Park *et al.* [27] found that the *M*Cu[Q_{1-x} Q'_x]F (*M* = Ba, Sr; *Q* and *Q*' = S, Se, Te) materials exhibit band gaps that allow transmission of much of the visible spectrum. These compounds are transparent in thin-film form with a band gap of 2.7 to 3.1 eV. Additional tuning of band gap and electrical properties can be achieved by replacing Ba with Sr and by replacing S with Se and Te. Later, the compound BaCuTeF has been prepared by using high-temperature reaction methods [28]. The electronic structure of BaCuTeF was computed using the full potential linearized augmented plane-wave formalism with the

GGA-PBE. However, the energy gap is somewhat different from those obtained from the absorption spectrum. Moreover, Seebeck and electrical conductivity measurements reveal *p*-type degenerate semiconductor behaviour.

Recently, the quaternary barium silver fluoride chalcogenides BaFAg*Ch* (*Ch* = S and Se) have been synthesized by Charkin *et al.* [29] via solid-state reactions of powdered BaCh, BaF_2 and Ag_2Ch. They crystallize in the tetragonal LaOAgS-type structure, symmetry group P4/nmm (No.129), Z = 2; which means that we have 8 atoms per unit cell. They are constituted of an alternating quasi-two-dimensional blocks [BaF] and [Ag*Ch*] stacked along the *c* crystallographic axis in the sequence… [BaF]/[Ag*Ch*]/[BaF]/[Ag*Ch*]…, in another word, they are a natural superlattice structure (See Fig. I.1). On the theoretical side, Bannikov *et al.* [30] calculated the electronic structures and optical spectra of BaAgSF and BaAgSeF employing the full-potential linearized augmented plane wave (FP-LAPW) method with the generalized gradient approximation (GGA).

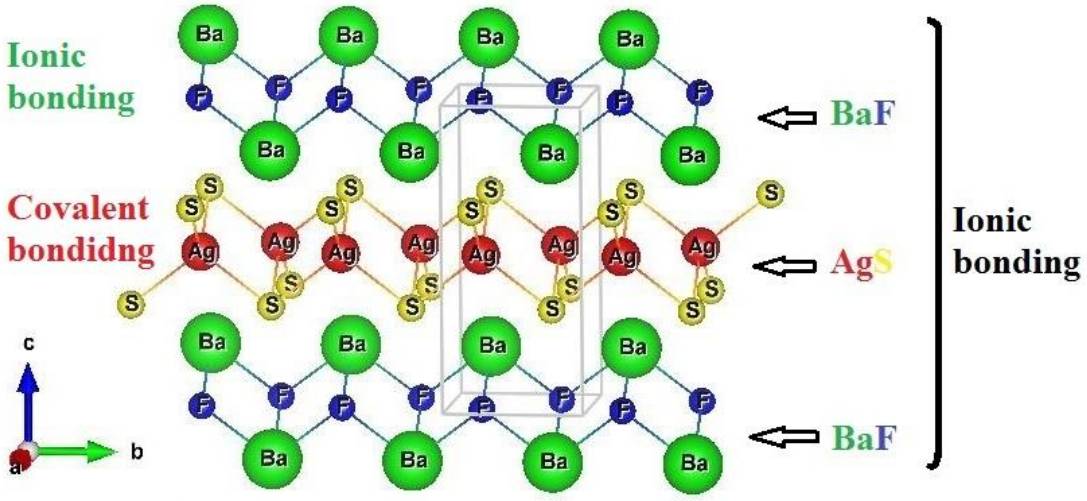

Figure I.1: The layered structure of the BaFAgS compound.

According to the previous studies, only the structural, electronic and optical properties of the BaFAg*Ch* (*Ch* = S and Se) compounds were theoretically studied using the FP-LAPW with the GGA-PBE functional to model the exchange-correlation potential. However, the common GGA and LDA are well known to yield unsatisfactory band gap values compared to the corresponding measured ones for semiconductors and insulators. This is because the standard GGA/LDA cannot describe accurately the excited electronic states. Some functionals beyond the GGA/LDA, such the GGA/LDA+U, hybrid functionals…etc., are developed in order to improve the treatment of the exchange–correlation potential and consequently better describing the electronic structures of semiconductors and insulators. Among the functionals that yield an improved band gap compared to the standard functionals with a reasonable calculating time, we find the Tran–Blaha modified Becke–Johnson (TB-mBJ) potential [31, 32]. The TB-mBJ functional yields accurate fundamental band gap values for large families of semiconductors and isolators [33, 34]. Additionally, the reported studies [29, 30] did not include the spin-orbit coupling effect [35], which is not negligible in the case of the BaFAg*Ch* (*Ch* = S, Se and Te) systems, similarly to BaCu*Ch*F [36]. Therefore, the first objective of the present work is the calculation of the electronic and optical properties, including band structure, charge-carrier effective masses, density of states, density of charge distribution and optical spectra, of the title compounds using the FP-LAPW method with the modified Beck-Johnson potential including the spin-orbit coupling effects. The BaFAg*Ch* crystals have natural superlattice characteristics, which would result in very favourable electronic properties for thermoelectrics [6, 36]. Therefore, the second objective of this study is the prediction of the thermoelectric properties of the BaFAg*Ch* compounds as functions of charge-carrier concentration and temperature using the semi-classical Boltzmann theory [37] in combination with the band structure obtained via the FP-LAPW method. For technological applications in the optoelectronic field, the semiconductor materials are generally grown as thin films on substrates. However, the lattice mismatch and difference in thermal expansion coefficients between the epitaxial layer and substrate can produce large stresses in the grown layer [38]. Hence, it is of extreme importance to estimate the elastic moduli that describe the response of materials to external stresses. To our best knowledge, there is no available data in the literature on the elastic constants (C_{ij}s) of the studied BaFAg*Ch* crystals. Therefore, it becomes necessary and important to calculate the C_{ij}s of the BaFAg*Ch* compounds in order to disclose their elastic properties. Prediction of the elastic moduli and related properties of the BaFAg*Ch* series constitutes the third

objective of the present work. Previews study does not give any information about the temperature and pressure effects on the macroscopic physical parameters. Variation of macroscopic properties of the mater under temperature and pressure is very necessary and important to evaluate its efficiency in harsh conditions and extreme environment. Hence, determination of the evolution of some macroscopic physical parameters with temperature and pressure constitutes the fourth objective of the present work.

In the present thesis, we have performed the following works:

- Accurate determination of the crystalline parameters, including the lattice parameters and atomic positions, of the title compounds using the FP-LAPW method with three different functionals to model the exchange correlation energy; the LDA [3-39], GGA-PBE [40] and GGA-PBEsol [41] as implemented in the Wien2K code [42]. The chemical and mechanical stability of the studied compounds were also checked by calculating the formation enthalpy and cohesion energy.
- Investigation of the electronic (including electronic band structure, effective mass, total and partial density of states and electronic charge density) and optical (including the dielectric function and the essential derived parameters such us the optical absorption coefficient, index of refraction, coefficient of extinction, reflectivity and electron energy-loss function) properties of the studied compounds. This study was performed using the FP-LAPW with both the GGA08 and TB-mBJ [43] methods to model the exchange-correlation potential.
- Prediction of the elastic properties of the studied compounds and related properties using total energy-strain method as implemented in the Wien2K series of packages.
- Evaluation of the spin-orbit coupling effect on the examined properties of the title compounds.
- Study of the thermoelectric properties, including Seebeck coefficient, electric conductivity, thermal conductivity, power factor and figure of merit, using the FP-LAPW method combined with the Boltzmann's semi-classical theory [37] as implemented in the BoltzTraP code [44].
- Investigation of the evolution with pressure and temperature of some macroscopic physical parameters, including unit cell volume, bulk modulus, thermal expansion coefficient, Grüneisen parameter, heat capacity, Debye temperature, internal

energy, free energy and entropy, using the FP-LAPW method combined with the quasi-harmonic Debye model as implemented in the Gibbs2 code [45, 46].

I.3. Thesis outline

This manuscript consists of four chapters, general conclusion and some indexes.

Chapter 1; General introduction, gives a literature survey about the considered compounds and the objectives of this thesis.

Chapter 2; Density Functional Theory (DFT), explains the basic fundaments and formalism of the Density Functional Theory.

Chapter 3; Full Potential-Linearized Augmented Plane Wave (FP-LAPW) method, gives the basic fundaments of the FP-LAPW method.

Chapter 4; Results and discussion, presents the obtained results for the structural, elastic, electronic, optical, thermoelectric and thermodynamic properties of the quaternary BaFAg*Ch* (*Ch* = S, Se and Te) compounds. These results are discussed and compared with the available results in the scientific literature.

The thesis is concluded by a general conclusion, which provides the main results obtained through this study, and some appendices about the Wien2K suite of programs, BoltzTraP code, Spin-Orbit coupling and Gibbs2 program.

We hope that the reported data in the resent thesis can provide theoretical support to the existing experimental and theoretical data and provide a basis for future experimental and theoretical studies in order to have insight about eventual technological applications of the title materials.

References

[1] R. G. Parr, and W. Yang, *Density functional theory of Atoms and molecules*, Oxford University Press, New York, (1989).

[2] R. M. Dreizler, E. K. U. Gross, *Density Functional Theory - An Approach to the Quantum Many-Body Problem* -, Springer-Verlag, Berlin, Germany, (1990).

[3] P. Hohenberg, and W. Kohn, *Inhomogeneous Electron Gas,* Phys. Rev. Vol. 136, No. 3B, (1964).

[4] D. J. Singh, L. Nordstrom, *planewaves, pseudopotentials and the LAPW method*,2nd Edition, Springer Science+Business Media, Inc., U.S.A, (2006).

[5] K. Schwarz, P. Blaha, and S.B. Trickey, *Electronic structure of solids with WIEN2k,* Mol. Phys., Vol. 108, No. 21–23, pp. 3147–3166, (2010).

[6] V.K. Gudelli, V. Kanchana, G. Vaitheeswaran, D.J. Singh, A. Svane, N.E. Christensen, and S.D. Mahanti, *Electronic structure, transport, and phonons of SrAgChF (Ch = S, Se, Te): Bulk superlattice thermoelectrics*. Phys. Rev. B, Vol. 92, No. 8, pp. 045206 (8), (2015).

[7] K. Ueda, H. Hiramatsu, M. Hirano, T. Kamiya, M. Hirano, and H. Hosono, *Wide-gap layered Oxychalcogenides semiconductors: Materials, electronic structures and optoelectronic properties.* Thin Solid Films, Vol. 496, No. 1, pp. 8-15, (2006).

[8] A. Zakutayev, R. Kykyneshi, G. Schneider, D.H. McIntyre, and J. Tate, *Electronic structure and excitonic absorption in BaCuChF (Ch=S, Se, and Te)*, Phys. Rev. B, Vol. 81, No. 15, pp. 155103(9), (2010).

[9] H. Yanagi, S. Ohno, T. Kamiya, H. Hiramatsu, M. Hirano and H. Hosono, *Magnetic and carrier transport properties of Mn-doped p-type semiconductor LaCuOSe: an investigation of the origin of ferromagnetism*. J. Appl. Phys., Vol. 100, No. 3), pp. 033717, (2006).

[10] M. Palazzi and S. Jaulmes, *Structure du conducteur ionique (LaO)AgS*, Acta Cryst Section B, Vol. 37, No. 7: pp. 1337-1339, (1981).

[11] Y. Kamihara, T. Watanabe, M. Hirano and H. Hosono, *Iron-Based Layered Superconductor La[$O_{1-x}F_x$]FeAs (x =0.05-0.12) with T_c = 26 K.* J. Am. Chem. Soc. Vol. 130, No. 11, pp. 3296-3297, (2008).

[12] V.V. Bannikov, I.R. Shein, and A.L. Ivanovskii, *Electronic, optical properties and chemical bonding in six novel 1111-like chalcogenide fluorides AMChF (A=Sr, Ba; M=Cu, Ag; and (Ch=S, Se, Te) from first principles calculations.* J. Solid State Chem. Vol. 196, pp. 601-606, (2012).

[13] R. Pöttgen and D. Johrendt, *Materials with ZrCuSiAs-type Structure.* Z. Naturforsch. B, Vol. 63, No. 10, pp. 1135–1148, (2008).

[14] J.F. Wager, D.A. Keszler, and R.E. Presley, *Transparent Electronics*, Springer, Berlin, (2008).

[15] M. Yasukawa, K. Ueda, and H. Hosono, *Thermoelectric properties of layered oxyselenides $La_{1-x}Sr_xCuOSe$ (x=0 to 0.2)*, J. Appl. Phys., Vol. 95, No. 7, pp. 3594(4), (2004).

[16] H. Hiramatsu, K. Ueda, H. Ohta, T. Kamiya, and M. Hirano, *Excitonic blue luminescence from p-LaCuOSe/n-InGaZn5O8 light-emitting diode at room temperature,* Appl. Phys. Lett., Vol. 87, No. 21, pp. 211107(3), (2005).

[17] J.A. Spies, R. Schafer, J.F. Wager, P. Hersh, H.A.S. Platt, D.A. Keszler, G. Schneider, R. Kykyneshi, J. Tate, X. Liu, A.D. Compaan, and W.N. Shafarman, *Pin double-heterojunction thin-film solar cell p-layer assessment*, Sol. Energy Mater. Sol. Cells, Vol. 93, No. 8, pp.1296-1308 (2009).

[18] D.O. Charkin, A.V. Urmanov, I.V. Plokhikh, A.D. Korshunov, A.N. Kuznetsov, and S.M. Kazakov, *Synthesis and crystal structures of novel LaOAgS-type alkaline earth – Zinc, manganese, and cadmium fluoride pnictides*. J. Alloys Compd., Vol. 585, pp. 644-649, (2014).

[19] D.C. Johnston, *The puzzle of high temperature superconductivity in layered iron pnictides and chalcogenides*, Adv. Phys. Vol. 59, No. 6, pp. 803, (2010).

[20] K. Ueda, H. Hiramatsu, H. Ohta, M. Hirano, T. Kamiya, and H. Hosono, *Single-atomic-layered quantum wells built in wide-gap semiconductors LnCuOCh, Ln=lanthanide, Ch=chalcogen*. Phys. Rev. B Vol. 69, No. 15, pp. 55305(4), (2004).

[21] H. Kamioka, H. Hiramatsu, M. Hirano, K. Ueda, T. Kamiya, and H. Hosono, *Excitonic properties related to valence band levels split by spin–orbit interaction in layered oxychalcogenide LaCuOCh(Ch=S,Se)*, J. Lumin. Vol. 112, No. 1-4. pp. 66-70, (2005).

[22] V.V. Bannikov, I.R. Shein, and A.L. Ivanovskii, *Design of novel magnetic materials based on ZrCuSiAs-like semiconducting pnictide-oxides from first-principles calculations*, Solid State Commun., Vol. 150, No. 41-42, pp. 2069- 2071, (2010).

[23] V.V. Bannikov, I.R. Shein, and A.L. Ivanovskii, Structural, *electronic properties and inter-atomic bonding in layered chalcogenide oxides LaMChO (where M = Cu, Ag, and Ch = S, Se) from FLAPW-GGA calculations*, Solid State Sci. Vol. 14, No. 1, pp. 89-93, (2012).

[24] W. J. Zhu, Y. Z. Huang, C. Dong et al. *Synthesis and crystal structure of new rare-earth copper oxyselenides: RCuSeO (R= La, Sm, Gd and Y).* Mater. Res. Bull, Vol. 29, No. 2, p. 143-147, (1994).

[25] H. Yanagi, and J. Tate, *p-type conductivity in wide-band-gap BaCuQF (Q=S, Se)*, Appl. Phys. Lett., Vol. 82, No. 17, pp. 2814(3), (2003).

[26] H. Yanagi, J. Tate, S. Park, C.-H. Park, D. A. Keszler, M. Hirano, and H. Hosono, *Valence band structure of BaCuSF and BaCuSeF*, J. Appl. Phys., Vol. 100, No. 8, pp. 083705(5), (2006).

[27] C. H. Park, D. A. Keszler , H. Yanagi, J. Tate, *Gap modulation in MCu[Q_{1-x} Q'_x]F (M=Ba, Sr; Q, Q'=S, Se, Te) and related materials*, Thin Solid Films, Vol. 445, pp. 288-293, (2003).

[28] C. H. Park, R. Kykyneshib, A. Yokochic, J. Tateb, D. A. Keszlera, *Structure and physical properties of BaCuTeF*, J. Solid State Chem., Vol. 180, No. 5, pp. 1672–1677, (2007).

[29] D. O. Charkin, A. V. Urmanov, S. M. Kazakov, *Preparation and crystal structures of novel LaOAgS-type copper and silver fluoride chalcogenides*, J. Alloys Compd., Vol. 516, pp. 134-138, (2012).

[30] V.V. Bannikov, I. R. Shein and A. L. Ivanovskii, *Electronic, optical properties and chemical bonding in six novel 1111-like chalcogenide fluorides AMChF (A=Sr, Ba; M=Cu, Ag; and Ch=S, Se,Te)from first principles calculations*, J. Solid State Chem., Vol. 196, pp. 601-606, (2012).

[31] A. D. Becke and E. R. Johnson, *A simple effective potential for exchange,* J. Chem. Phys., Vol. 124, No. 22, pp. 221101(4), (2006).

[32] F. Tran and P. Blaha, *Accurate Band Gaps of Semiconductors and Insulators with a Semilocal Exchange-Correlation Potential*, Phys. Rev. Lett., Vol. 102, No. 22, pp. 226401(4), (2009).

[33] F. Tran, P. Blaha, and K. Schwarz, *Band gap calculations with Becke-Johnson exchange potential*, J. Phys.: Condens. Matter, Vol. 19, No 19, pp. 196208(8), (2007).

[34] D. Koller, F. Tran, and P. Blaha, *Improving the modified Becke-Johnson exchange potential*, Phys. Rev. B, Vol. 85, No.15, pp. 155109(8), (2012).

[35] J. A. Reyes-Retana and F. Cervantes-Sodi, *Spin-orbital effects in metal dichalcogenide Semiconducting monolayers*, Sci. Rep., Vol. 6, No. 24093, pp. 1-10, (2016).

[36] D. Zou, H. Zheng, J. Li, *Predicted thermoelectric properties of natural superlattice structural compounds BaCuChF (Ch= S, Se and Te) by first-principles calculations*, J. Alloys Compd., Vol. 686, No. pp. 571-576, (2016).

[37] P.S. Kireev, *Semiconductor Physics*, Vysshaya Shkola, Moscow, (1975).

[38] A. Bouhemadou, D. Allali, S. Bin-Omran, E.M.A. Al Safi, R. Khenata, and Y. Al-Douri, *Elastic and thermodynamic properties of the SiB_2O_4 (B=Mg, Zn and Cd) cubic spinels: An ab initio FP-LAPW study*, Mater. Sci. Semicond. Process., Vol. 38, pp.192- 202, (2015).

[39] M. Gell-Mann, K. A. Bruegkner, *Correlation Energy of an Electron Gas at High Density*, Phys. Rev., Vol. 106, No. 2, pp. 364-368, (1957).

[40] J. P. Perdew, K. Burke, and M. Ernzerhof, *Generalized gradient approximation made simple*, Phys. Rev. Lett., Vol. 77, No. 18, pp. 3865(4), (1996).

[41] J. P. Perdew, A. Ruzsinszky, G. I. Csonka, O. A. Vydrov, G. E. Scuseria, L. A. Constantin, X. Zhou, K. Burke, *Restoring the Density-Gradient Expansion for Exchange in Solids and Surfaces*, Phys. Rev. Lett., Vol. 100, No. 13, pp. 136406(4), (2008).

[42] K, Schwarz, P. Blaha, G. K. H. Madsen, *Electronic structure calculations of solids using the WIEN2k package for material sciences*, Comput. Phys. Commun., Vol. 147, No 1-2, pp. 71-76, (2002).

[43] A. D. Becke and E. R. Johnson, *A simple effective potential for exchange,* J. Chem. Phys., Vol. 124, No. 22, pp. 221101(4), (2006).

[44] G.K.H. Madsen, D.J. Singh, BoltzTraP. *A code for calculating band-structure dependent quantities*, Comput. Phys. Commun., Vol. 175, No. 1, pp. 67-71, (2006).

[45] A. Otero-de-la-Roza, V. Luaña, *Gibbs2: A new version of the quasi-harmonic model code. I. Robust treatment of the static data*, Comput. Phys. Commun., Vol. 182, No. 8, pp. 1708-1720, (2011).

[46] A. Otero-de-la-Roza, D. Abbasi-Pérez, V. Luaña, Gibbs2: *A new version of the quasi-harmonic model code. II. Models for solid-state thermodynamics, features and implementation*, Comput. Phys. Commun., Vol. 182, No. 10, pp. 2232-2248, (2011).

Chapter II

Density Functional Theory (DFT)

Chapter II

II.1. Introduction

A solid is a collection of heavy, positively charged particles (nuclei) and lighter, negatively charged particles (electrons). If we have N identical nuclei, we are dealing with a problem of $3N(1+Z)$ electromagnetically interacting particles. This is a many-body problem, and because the particles are so light, quantum mechanics is needed. Quantum mechanics governs the electronic structure that is responsible for material properties, such as relative stability, chemical bonding, relaxation of atoms, phase transitions, electrical, mechanical, optical or magnetic properties…etc. Schrödinger's wave function seemed extremely promising as it contains all of the information available about a system. The form of the Schrödinger equation depends on the physical situation. However, the most general form is the time-dependent Schrödinger equation, which gives a description of a system evolving with time (t) [1]:

$$i\hbar \frac{d\psi(\vec{r}_i; t)}{dt} = \hat{H}\psi(\vec{r}_i; t) \qquad \text{(II. 1)}$$

where:

i: is the imaginary unit;

$\hbar$: is the reduced Planck constant or Dirac's constant ($\hbar = h/2\pi$; h: is the Planck's constant);

ψ: is the wave function of the quantum system;

$\hat{H}$: is the Hamiltonian operator, which characterizes the total energy of any given wave function and takes different forms depending on the situation.

The wavefunction can be written as $\psi(\vec{r}_i, t) = \psi(r_i)e^{-iEt}$, and it also satisfies the time-independent Schrödinger equation [2]:

$$\hat{H}|\psi\rangle = E|\psi\rangle \qquad \text{(II. 2)}$$

Calculation of the energy "*E*" of a crystal consisting of a very large number of interacting particles (electrons and atomic nuclei) is difficult. So necessarily, we go through a certain number of simplifying hypothesis. First, neglecting the effects of temperature, and limit the interactions between particles to the most important terms that constitute the Colombian interactions (neglecting the magnetic interactions spin-spin and spin orbits). So, the exact many-particle Hamiltonian for this system consists of the nuclei kinetic T_N, the electronic kinetic T_e part and the interaction part between the nuclei $V_{N\text{-}N}$ and electrons $V_{e\text{-}e}$ with nuclei-electrons interaction $V_{N\text{-}e}$:

$$H_{Tot} = T_N + T_e + V_{N-N} + V_{e-e} + V_{N-e} \qquad \text{(II. 3)}$$

For a solid system with *N* nuclei cores and *n* electrons, the Hamiltonian is written:

$$H_{tot} = -\frac{\hbar}{2}\sum_{I=1}^{N}\frac{\nabla^2_{\vec{R}_i}}{M} - \frac{\hbar}{2}\sum_{i=1}^{n}\frac{\nabla^2_{\vec{r}_i}}{m_e} + \frac{1}{8\pi\epsilon_0}\sum_{I=1,J\neq I}^{N}\frac{e^2 Z_I Z_J}{\left|\vec{R}_I - \vec{R}_J\right|} + \frac{1}{8\pi\epsilon_0}\sum_{i=1,j\neq i}^{n}\frac{e^2}{\left|\vec{r}_i - \vec{r}_j\right|}$$
$$- \frac{1}{4\pi\epsilon_0}\sum_{i=1}^{n}\sum_{I=1}^{N}\frac{e^2 Z_I}{\left|\vec{R}_I - \vec{r}_i\right|} \qquad \text{(II. 4)}$$

m_e: is the mass of the electron;

$\left|\vec{r}_i - \vec{r}_j\right|$: is the distance between the electron *i* and the electron *j*;

M: is the mass of nucleus;

$\left|\vec{R}_I - \vec{R}_J\right|$: is the distance between the nucleus *I* and the nucleus *J*.

Z_I, Z_J : are the atomic numbers of the nuclei *I* and *J*, respectively.

This Hamiltonian is subjected to the time-independent Schrödinger equation:

$$H_{tot}\,\psi(\vec{r}_i,\vec{R}_I) = E\psi(\vec{r}_i,\vec{R}_I) \qquad \text{(II. 5)}$$

where ψ is the normalized eigenfunction of the Hamiltonian operator $\hat{H}_{Tot}$. In (Eq. II.4), the last three terms have complex structure. It is out of question to solve this problem exactly. In order to find acceptable approximate eigenstates, we will need to make approximations at 3 different levels.

- The 1st level: Born Oppenheimer approximation.
- The 2nd level: Density-Functional Theory.
- The 3rd level: Solving the Kohen-Sham equation.

II.2. Born-Oppenheimer approximation

In 1927, physicists Max Born and Julius Robert Oppenheimer [3] published an approximation method to simplify the resolution of Schrödinger equation. Born-Oppenheimer approximation is based on the fact that nuclei are several thousand times heavier than electrons. The proton, itself, is approximately 2000 times more massive than an electron. In a dynamical sense, the electrons can be regarded as particles that follow the nuclear motion adiabatically, meaning that they are "dragged" along with the nuclei without requiring a finite relaxation time. Another consequence of the mass difference between electrons and nuclei is that the nuclear components of the wave function are spatially more localized than the electronic component of the wave function. In the classical limit, the nuclear are fully localized about single points representing classical point particles [3, 4]. Assuming this hypothesis, we particularly simplify the Schrödinger equation, since the kinetic energy of the nuclei becomes zero, the interaction energy of the nuclei becomes constant, but which can be rendered null by a suitable choice of the origin. Taking into account that $T_N = 0$ and $V_{N-N} = 0$, we can define an electronic wave function which depends on the coordinates of the nuclei only parametrically, and the Schrödinger equation is written as:

$$H_e\psi_e = (\,T_e + V_{e-e} + V_{N-e})\psi_e = E\,\psi_e \qquad \text{(II. 6)}$$

The total electron wave function depends on the coordinates of all the electrons making up the system and cannot be decomposed into single particle contributions because the electrons interact strongly with each other and their displacements are thus correlated. The difficulty always lies in

V_{e-e}; the term describing the set of electrons in mutual interaction, which unlike T_e and V_{N-e} couples the coordinates of all interacting electrons, which makes analytical resolution of the Schrödinger equation impossible, even numerically, except in very simple cases like that of the hydrogen atom. In order to circumvent this difficulty, we are led to make a series of approximations; we go to the second level of approximation [5].

II.3. Density Functional Theory

The quantum many body problem obtained after the first level approximation (Born-Oppenheimer) is much simpler than the original one, but still far too difficult to solve. Several methods exist to reduce (Eq. II.6) to an approximate but tractable form. A historically very important one is the Hartree-Fock method (HF). It performs very well for atoms and molecules, and is therefore used a lot in quantum chemistry. For solids it is less accurate, however. A more modern and probably also more powerful method: Density Functional Theory (DFT) was developed to resolve the many body problem. Although its history goes back to the early thirties of the 20th century, DFT has been formally established in 1964 by two theorems due to Hohenberg and Kohn [6] .

The fundamental concept of the density functional is that the energy of an electronic system can be expressed as a function of its density. It is in fact an old idea dating mainly from the works of Thomas [7] and Fermi [8]. The use of electronic density as a fundamental variable to describe the properties of the system has existed since the earliest approaches to the electronic structure of matter, but it has obtained proof only by the demonstration of the two so-called Hohenberg and Kohn theorems.

The wave function ϕ of an *N*-electron system includes *3N* variables, while the density, ρ no matter how large the system is, has only three variables *x*, *y*, and *z*. Moving from $E[\phi]$ to $E[\rho]$ significantly reduces the computational effort needed to understand electronic properties of atoms, molecules, and solids.

II.3.1. Hohenberg-Kohn theorems

The theorem upon which DFT is based is that of Hohenberg and Kohn. It states that the total energy, *E*, of a non-spin-polarized system of interacting electrons in an external potential (for our purposes the Coulomb potential due to the nuclei in a solid) is given exactly as a functional of the ground state electronic density ρ [9]:

$$E = E[\rho] \qquad \text{(II. 7)}$$

The theory can be extended to nonzero temperatures by considering a statistical electron density defined by Fermi–Dirac occupation numbers [10]. The theory is also easily extended to the spin-indexed density [11].

The traditional formulation of the two theorems of Hohenberg and Kohn [6] is as follows:

1st theorem: There is a one-to-one correspondence between the ground-state density $\rho(\vec{r})$ of a many-electron system (atom, molecule, solid) and the external potential, V_{ext}. An immediate consequence is that the ground-state expectation value of any observable $\hat{O}$ is a unique functional of the exact ground-state electron density:

$$\langle\psi|\,\hat{O}\,|\psi\rangle = \hat{O}[\rho] \qquad \text{(II. 8)}$$

2nd theorem: For $\hat{O}$ being the hamiltonian $\hat{H}$, the ground-state total energy functional $H[\rho] \equiv E_{V_{ext}}[\rho]$ is of the form:

$$E_{V_{ext}}[\rho] = \langle\psi|\hat{T} + \hat{V}|\psi\rangle + \langle\psi|\hat{V}_{ext}|\psi\rangle = F_{HK}[\rho] + \int \rho(\vec{r})V_{ext}(\vec{r})d\vec{r} \qquad \text{(II. 9)}$$

where the Hohenberg-Kohn density functional $F_{HK}[\rho]$ is universal for any many-electron system. $E_{V_{ext}}[\rho]$ reaches its minimal value (equal to the ground-state total energy) for the groundstate density corresponding to V_{ext}.

For these theorems, three keywords are remarkable: inevitability (one-to-one correspondence $\rho \leftrightarrow V_{ext}$), universality and variational access (minimal value).

It is obvious that a given many-electron system has a unique external potential, which by the Hamiltonian and the Schrödinger equation yields a unique ground-state many particles wave function. From this wave function, the corresponding electron density is easily found. An external potential hence leads in a well-defined way to a unique ground-state density corresponding to it. The density contains as much information as the wave function does (i.e., everything you could possibly know about an atom, molecule or solid). All observable quantities can be retrieved therefore in a unique way from the density only, i.e., they can be written as functionals of the density.

Eq. II.9 is easily written by using the density operator, and supposing the ground-state density is known, the contribution to the total energy from the external potential can be exactly calculated. An explicit expression for the Hohenberg-Kohn functional F_{HK} is not known. But anyway, because F_{HK} does not contain information on the nuclei and their position, it is a universal functional for any many-electron system. This means that in principle an expression for $F_{HK}[\rho]$ exists which can be used for every atom, molecule or solid which can be imagined.

The second theorem makes it possible to use the variational principle of Rayleigh-Ritz in order to find the ground-state density. Out of the infinite number of possible densities, the one which minimizes $E_{V_{ext}}[\rho]$ is the ground-state density corresponding to the external potential $V_{ext}(\rho)$. Of course, this can be done only if (an approximation to) $F_{HK}[\rho]$ is known. But having found ρ, all knowledge about the system is within reach. It is useful to stress the meaning of the energy functional $E_{V_{ext}}[\rho]$ once more. When it is evaluated for the density ρ corresponding to the particular V_{ext} for this solid, it gives the ground state energy. When it is evaluated for any other density however, the resulting number has no physical meaning [9].

DFT theory is based on Hohenberg–Kohn theorems, which show that the external potential function $V_{ext}(\vec{r})$ of an *N*-electron system is determined by its ground-state electron density ρ.

II.3.2. The Kohn-Sham equations

The equations of Kohn and Sham, published in 1965 [12], turn DFT into a practical tool. They are a practical procedure to obtain the ground state density. The Hohenberg-Kohn functional $E_{V_{ext}}[\rho]$ can be expressed as follows :

$$E_{V_{ext}}[\rho] = T_0[\rho] + V_H[\rho] + V_{xc}[\rho] + V_{ext}[\rho] \qquad (\text{II.}10)$$

Here, T_0 is the functional for the kinetic energy of a non-interacting electron gas, V_H stands for the Hartree contribution and V_{xc} for the exchange-correlation contribution and V_{ext} for the external potential. One can interpret the above expression as the energy functional of a non-interacting classical electron gas, subject to two external potentials: one due to the nuclei, and one due to exchange and correlation effects. The corresponding Hamiltonian – called the Kohn-Sham Hamiltonian – is:

$$\hat{H}_{KS} = \hat{T}_0 + \hat{V}_H + \hat{V}_{xc} + \hat{V}_{ext} \qquad (II.11)$$

The theorem of Kohn and Sham, published in 1965, that turns DFT into a practical tool [12], is formulated as follows: The exact ground-state density $\rho(\vec{r})$ of an *N*-electron system is:

$$\rho(\vec{r}) = \sum_{i=1}^{N} \phi_i(\vec{r}) * \phi_i(\vec{r}) \qquad (II.12)$$

where the single-particle wave functions $\phi_i(\vec{r})$ are the N lowest-energy solutions of the Kohn-Sham equation:

$$\hat{H}\phi_i(\vec{r}) = \varepsilon_i \phi_i(\vec{r}) \qquad (II.13)$$

To find the ground-state density, we don't need to use the second Hohenberg-Kohn theorem any more, but we can rely on solving familiar Schrodinger-like no interacting single-particle equations (Kohn-Sham equations). The alternative of using the regular Schrodinger equation, would have led to a far more difficult system of coupled differential equations, because of the electron-electron interaction. Be aware that the single-particle wave functions $\phi_i(\vec{r})$ are not the wave functions of electrons! They describe mathematical quasi-particles, without a direct physical meaning. Only the overall density of these quasi-particles is guaranteed to be equal to the true electron density. Also the single-particle energies ε_i are not single-electron energies. Both the Hartree operator V_H and the exchange-correlation operator V_{xc} depend on the density $\rho(\vec{r})$, which in turn depends on the $\phi_i(\vec{r})$, which are being searched. This means we are dealing with a self-consistency problem: the solutions ($\phi_i(\vec{r})$) determine the original equation (V_H and V_{xc} in H_{KS}), and the equation cannot be written down and solved before its solution is known. An iterative procedure is needed to escape from this paradox (See Fig. II.1). Some starting density ρ_0 is guessed, and a Hamiltonian H_{KS1} is constructed with it. The eigenvalue problem is solved, and results in a set of ϕ_1 from which a density ρ_1 can be derived. Most probably ρ_0 will differ from ρ_1. Now ρ_1 is used to construct H_{KS2}, which will yield a ρ_2…etc. The procedure can be set up in such a way that this series will converge to a density ρf which generates a H_{KSf} which yields as solution again ρ_f, this final density is then consistent with the Hamiltonian.

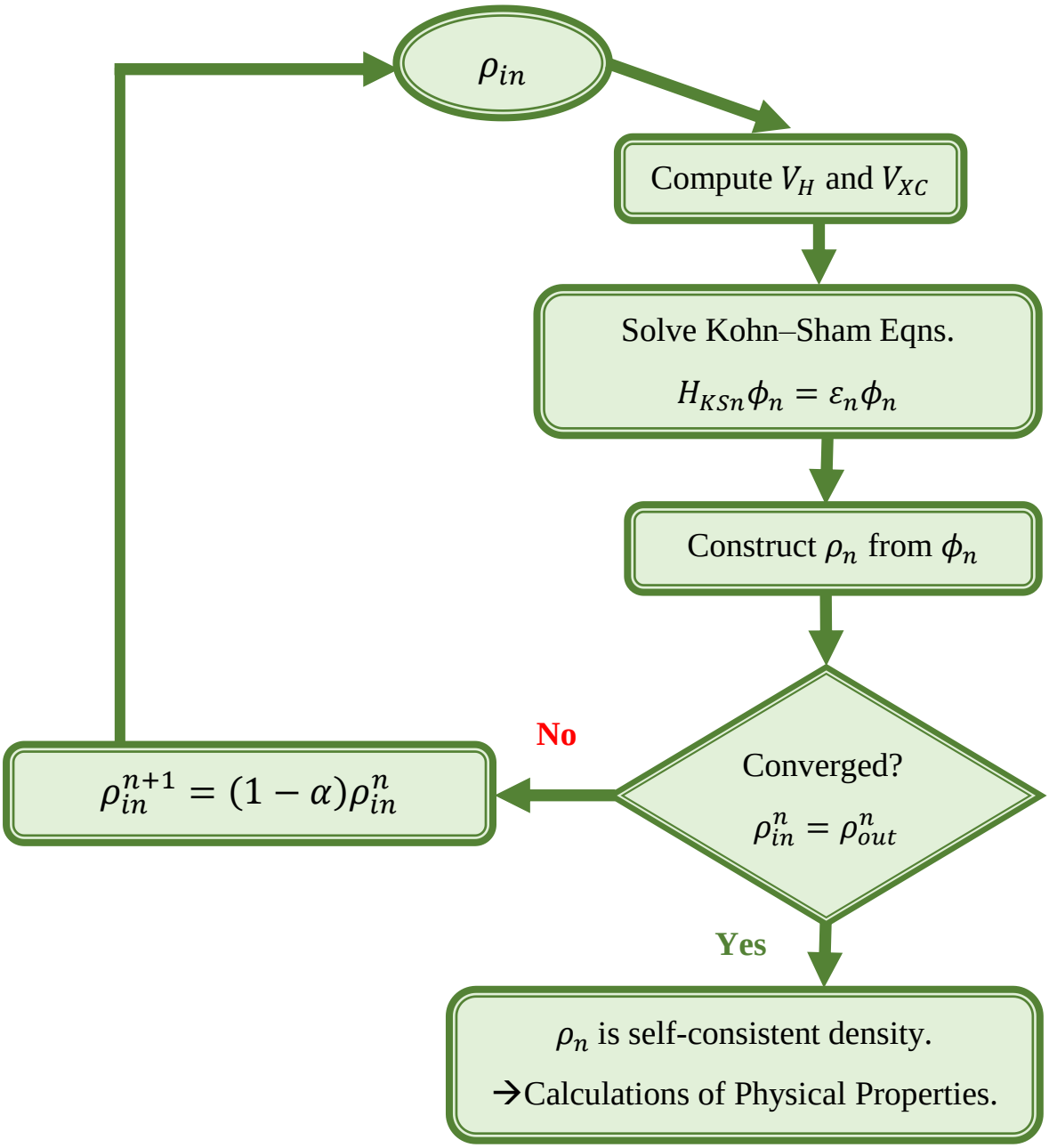

Figure II.1: Schematic representation of the organization chart of KS equations resolution within self-consistent way based on an initial guess and convergence criteria [9, 13].

II.4. Solving the Kohn–Sham equations

The resolution of the Schrödinger equation in the context of the Kohn-Sham approach is reduced to solving equations of the following form:

$$\left(\hat{T}_0 + V_{ext} + V_H + \hat{V}_{XC}\right)\psi_i = \varepsilon_i \psi_i \qquad \text{(II. 14)}$$

Various ab-initio methods for calculating the electronic structure are based on DFT and can be classified according to the representations used for the density, potential and Kohn-Sham orbitals of. 'Solving' in most methods means that we want to find the coefficients c_{ij} needed to express ψ_i in a given basis set ϕ_j:

$$\psi_i = \sum_j c_{ij}\, \phi_j \qquad \text{(II. 15)}$$

Since, given a choice of basis, these coefficients are the only variables in the problem (note that the density depends only on the KS orbitals), and since the total energy in DFT is variational, solution of the self-consistent KS equations amounts to determining the c_{ij} for the occupied orbitals that minimize the total energy.

It is very common to separate the determination of the c_{ij} and the determination of the self-consistent charge density in density functional calculations. The solutions for the density and the c_{ij} are done hierarchically in this case, as shown schematically in (Fig. II.1). In this scheme, it is necessary to repeatedly determine the c_{ij} that solve the single particle equations for fixed charge density. This may be done using standard matrix techniques. Specifically, given the basis, the Kohn-Sham Hamiltonian and overlap matrices, *H* and *S* are constructed and the matrix eigenvalue equation [14],

$$(H - \phi\varepsilon_i S)c_i = 0 \qquad \text{(II. 16)}$$

II.5. Exchange-Correlation potential

The term exchange-correlation has its origins in the electron-electron interaction, and its knowledge is necessary for the study of the electronic system. It should be noted, however, that $V_{XC}[\rho]$ is only known approximately [13].

The physical idea behind the notion of an exchange and correlation is that due to Pauli's exclusion principle electrons of parallel spin cannot come arbitrarily close to each other in space, and that the repulsive interaction leads to a further reduction of the pair density for small distances of the particles in the pair.

Numerous approximations to the exchange-correlation energy $E_{XC}[\rho_\uparrow, \rho_\downarrow]$ as a functional of the spin-densities $\rho_\uparrow$ and $\rho_\downarrow$ ($\rho = \rho_\uparrow + \rho_\downarrow$) have been developed and tested. One possible criterion for the discussion of approximations to $E_{XC}[\rho_\uparrow, \rho_\downarrow]$ is whether the functional is fitted to experimental data or if it is constructed to satisfy physical constraints. Most existing functionals combine these two approaches, i.e., while they are subject to physical constraints, parameters are added to better fit the experimental data. In the search for higher accuracy, we have recently observed the appearance of functionals with an increasing number of fitted parameters. Often physical constraints on the functional are abandoned in favour of higher accuracy on the selected experimental data set. Increasingly, parameters are recommended which are constructed to absorb technical problems in the solution of the Kohn–Sham equations [15].

In order to discriminate between approximations to the exchange-correlation energy $E_{XC}[\rho_\uparrow, \rho_\downarrow]$, we employ the criterion of whether the functional is fitted to a certain experimental data set or if it is constructed to satisfy physical constraints.

II.5.1. Local Density Approximation (LDA)

Local-density approximations (LDA) are a class of approximations to the exchange–correlation (*XC*) energy functional in density functional theory (DFT) that depend solely upon the value of the electronic density at each point in space (and not, for example, derivatives of the density or the Kohn–Sham orbitals). Many approaches can yield local approximations to the *XC* energy. However, overwhelmingly successful local

approximations are those that have been derived from the homogeneous electron gas (*HEG*) model [16].

In the local density approximation witch originally introduced by Kohn and Sham, one uses the exchange-correlation energy per electron E_{XC} of a homogeneous electron gas of the electron density ρ. In case of the inhomogeneous electron gas, for each $\vec{r}$ and $\rho(\vec{r})$ the local exchange-correlation energy is approximated by the corresponding value of $E_{XC}(\rho(\vec{r}))$ of the homogeneous electron gas [17].

$$E_{XC}^{LDA}[\rho] = \int \rho(\vec{r}) E_{XC}^{unif}\big(\rho(\vec{r})\big) d^3\vec{r} \qquad \text{(II. 17)}$$

Where $E_{XC}^{unif}\big(\rho(\vec{r})\big)$ is the exchange-correlation energy per particle of a uniform electron gas (jellium). It can be decomposed into exchange and correlation terms linearly:

$$E_{XC}^{unif} = E_X^{unif} + E_C^{unif} \qquad \text{(II. 18)}$$

The exchange contribution is derived as:

$$E_X^{unif} = -\frac{3}{2\pi}\left(\frac{9\pi}{4}\right)^{\frac{1}{3}}\frac{1}{r_s} \approx -\frac{0.916}{r_s} \qquad \text{(II. 19)}$$

where $\left(\frac{4\pi\rho}{3}\right)^{-\frac{1}{3}}$ is the Wigner-Seitz radius (radius sphere that contains one electron). Unlike the exchange term which takes on a simple analytic form for the *HEG*. Only limiting expressions for the correlation density are known exactly, leading to numerous different approximations for E_C^{unif}.

$$E_C^{unif} = \left(\frac{2}{\pi^2}\right)(1 - ln2)\ln(r_s) + C + \text{terms that vanish as } r_s \to 0 \qquad \text{(II. 20)}$$

where in each case the constant C was calculated approximately.

The LDA has been very successful for describing ground-state properties such as total energies and structural properties.

II.5.2. Generalized Gradient Approximation (GGA)

The simplest approximation is the local-density approximation (LDA), which is based on the *XC* energy of the homogeneous electron gas and only requires the density at each point in space. A slightly more elaborate approach consists in using both the density and its gradient at each point in space in the so-called generalized gradient approximation (GGA).

The GGA proposed here retains correct features of LDA, and combines them with the most energetically important features of gradient-corrected nonlocality.

The GGA (so-called PBE relative to Perdew, Burke and Ernzherhof) form for the exchange energy is simply [18-20] ,

$$E_{XC}^{GGA}[\rho_\uparrow, \rho_\downarrow] = \int f(\rho_\uparrow, \rho_\downarrow, \nabla\rho_\uparrow, \nabla\rho_\downarrow)\, d^3\vec{r} \qquad \text{(II. 21)}$$

The GGA exchange energy will be constructed as:

$$E_X^{GGA} = \int d^3\vec{r} E_X^{unif}(\rho(\vec{r}))F_X(s(\vec{r})) \qquad \text{(II. 22)}$$

Where E_X^{unif} is the exchange energy density of a uniform electron gas $E_X^{unif} = -3e^2K_F/4\pi$, $s = |\nabla\rho|/(2K_F\rho)$ [with $K_F = (3\pi^2\rho)^{1/3}$] is the dimensionless density gradient, and $F_X(s)$ is the enhancement factor for the given GGA. Any GGA that recovers the uniform gas limit has

$$F_X = 1 + \mu s^2 + \cdots (s \to 0) \qquad \text{(II. 23)}$$

where $\mu = 2\mu_{GE}$, and the gradient expansion, $\mu_{GE} = 10/81 \approx 0.1235$.

The GGA for correlation in the form,

$$E_C^{GGA}[\rho_\uparrow, \rho_\downarrow] = \int d^3r\rho[\, E_C^{unif}(r_s, \zeta) + H(r_s, \zeta, t)] \qquad \text{(II. 24)}$$

where r_s is the local Seitz radius $\left(\rho = {}^3/_4\,\pi r_s^3 = {}^{K_F^3}/_{3\pi^2}\right)$, $\zeta = (\rho_\uparrow - \rho_\downarrow)/\rho$ is the relative spin polarisation, and $t = \left|\nabla_\rho\right|/2\phi k_s\rho$ is the appropriate reduced density gradient

for correlation. Here $\phi(\zeta) = \left[(1+\zeta)^{2/3} + (1-\zeta)^{2/3}\right]/2$ is a spin-scaling factor, and $k_s = \sqrt{4K_F/\pi a_0}$ is the Thomas-Fermi screening wave number ($a_0 = \hbar^2/me^2$).

Unlike the LDA, there is more than one GGA:

- PBE "Perdew-Burke-Ernzerhof " [18, 19].
- PBEsol "Perdew-Burke-Ernzerhof GGA reparametrized for solids" [20], The PBEsol functional retains the same analytical form as the PBE functional, but two parameters were modified in order to satisfy other conditions. The value of μ (the parameter in the exchange part which determines the behavior of the functional for $s \to 0$) was set to $\mu = \mu_{GE} = {}^{10}/_{81}$ in order to recover the second-order gradient expansion of the exchange energy, and a parameter in the correlation part was chosen to yield good surface exchange-correlation energy for the jellium model [21].
- WC "by Wu and Cohen" [22], where the gradient expansion for slowly varying densities to construct a GGA with a functional form corresponding to diffuse cut-off. The XC-GGA damps the gradient enhancement, which results in improved equilibrium volumes for densely packed solids, but poorer exchange energies of atoms compared to the PBE [23].
- AM05 functional "by Armiento and Mattsson" [24] show a large success for crystalline solids "exceptionally well for surfaces" [25, 26].The AM05 functional is the first functional constructed according to the subsystem functional scheme. It can be seen as a consistent improvement over LDA in the sense that it reproduces the exact *XC* energy for two types of model systems: The uniform electron gas and the jellium surfaces, describing two situations with fundamentally different physics.
- HTBS functional "by Haas, Tran, Blaha, and Schwarz" [27]; a functional achieves an outstanding performance for both, molecules and solids; it show an acceptable accuracy than for PBE. However, HTBS performs poorly for vibrational quantities [28].

Normally the five generalized-gradient approximation (GGA) functionals improve over some of the drawbacks of the LDA, although this is not always the case.

PBEsol becomes exact for solids under intense compression, where real solids and their surfaces become truly slowly varying, and exchange dominates over correlation.

II.5.3. Problems with LDA and GGA

One of the problems with the LDA is the absence of orbital dependence in the exchange-correlation potential. Since the potential does not distinguish between orbitals with different m-quantum numbers, for systems containing a partially filled d or f shell one obtains a corresponding partially-filled band with a metallic-type electronic structure unless the exchange and crystal field splitting create a gap between the up and down channel. Thus, the late transition metal oxides, which are insulators, are predicted to be metals by the (non-spin-polarized) LDA.

Depending on the system you will have to consider methods going beyond DFT:

- DFT+U
- TB-mBJ potential
- Hybrid functional

The Band Gap Problem; Excitations are not well-predicted by the standard LDA, GGA forms of DFT.

II.5.4. LDA+U

Electrons in the s and p orbitals responsible for the bonding can be described properly by using conventional LDA band calculations. However, the highly correlated transition metal d-electrons and exited states. Therefore, it is necessary to treat the highly correlated d-electrons separately from the bonding electrons. The treatment of strongly interacting and correlated particles is especially problematic in (semi)local DFT. To reproduce band structure closer to experiment a common remedy has been applied to the DFT+U scheme [29, 30].

If your system is based on d-d transitions, or highly correlated states, then you can used DFT+U or Onsite-hybrid.

The LDA+U approach, first introduced by Anisimov and co-workers [31, 32], has allowed to study a large variety of strongly correlated compounds. This approach Treat strong on-site Coulomb interaction of localized electrons, e.g., d and f electrons (incorrectly described by LDA or GGA) with an additional Hubbard-like term. Strength of on-site interactions usually described by U (on site Coulomb) and J (on site exchange), $U_{eff}^{DFT+U} = U - J$, which can be extracted from ab-initio calculation [33, 34], but usually

are obtained semi-empirically, e.g., fitting to experimental formation energies or band gaps.

In the LDA+U method, an orbital-dependent potential *U* acting only on localized d or f states is introduced on top of the LDA potential.

For Mott–Hubbard insulators or rare-earth metal compounds where the partially filled 3d or 4f bands are split by the Coulomb interaction, forming the upper and lower Hubbard band, the LDA+U works reasonably well. The band structure, however, is unsatisfactory. Another problem with the method arises for systems with partially-filled 3d shells which are metallic, like the transition metals. In this case, the LDA+U would produce unphysical results since it would split the partially-filled band [35].

II.5.5. TB-mBJ approach

Theoretical methods leading to more accurate excited states are LDA+U, and GW. LDA+U (which is as cheap as LDA) can only be applied to localized states (typically 3d and 4f electrons). Whereas, GW are expensive methods. Recently, Becke and Johnson [36] (BJ) proposed an exchange potential, which was designed to reproduce the exact exchange potential in atoms. The BJ potential, which does not contain any empirical parameter, reads

$$V_X^{BJ}(\vec{r}) = V_X^{BR}(\vec{r}) + \frac{1}{\pi}\sqrt{\frac{5}{12}}\sqrt{\frac{2t(\vec{r})}{\rho(\vec{r})}} \qquad \text{(II. 25)}$$

where $\rho = \sum_{i=1}^{N}|\psi_i|^2$ is the electron density,

$$t(\vec{r}) = \frac{1}{2}\sum_{i=1}^{N}\nabla\psi_i^*(\vec{r}).\nabla\psi_i(\vec{r}) \qquad \text{(II. 26)}$$

is the KS kinetic-energy density, and

$$V_X^{BR}(\vec{r}) = -\frac{1}{b(\vec{r})}\left(1 - e^{-x(\vec{r})} - \frac{1}{2}x(\vec{r})e^{-x(\vec{r})}\right) \qquad \text{(II. 27)}$$

is the Becke-Roussel (BR) [37] exchange potential, x is determined from a nonlinear equation involving $\rho, \nabla\rho, \nabla^2\rho,$ and t, and then b is calculated with $b = [x^3e^{-x}/(8\pi\rho)]^{1/3}$. Note that for reference points r very far from a finite system, (Eq. II.27) yields the asymptotic potential,

$$\lim_{|r|\to\infty} V_X^{BR}(\vec{r}) = -\frac{1}{r} \qquad \text{(II. 28)}$$

In various types of solids, the BJ potential leads to only moderately improved band gaps compared to standard LDA and GGA [38]. However, the improvement was moderate. Further improvement has been achieved by a the modified version given by Tran and Blaha (TB-mBJ) [39], where a new parameter are introduced to change the relative weights of the two terms in the BJ potential:

$$V_X^{TB-mBJ}(\vec{r}) = cV_X^{BR}(\vec{r}) + (3c-2)\frac{1}{\pi}\sqrt{\frac{5}{12}}\sqrt{\frac{2t(\vec{r})}{\rho(\vec{r})}} \qquad \text{(II. 29)}$$

c was chosen to depend linearly on the square root of the average of $|\nabla\rho|/\rho$, (note that for $c = 1$ the original BJ potential is recovered).

$$c = \alpha + \beta\left(\frac{1}{V_{cell}}\int_{cell}\frac{|\nabla\rho(r')|}{\rho(r')}d^3r'\right)^{1/2} \qquad \text{(II. 30)}$$

V_{cell} is the unit cell volume and α and β are two free parameters whose values are α = -0.012 and β =1.023 bohr$^{1/2}$ according to a fit to experimental results [39].

One remember that the TB-mBJ give just the exchange potential, Correlation effects are taken into account by adding a LDA or PBE correlation potential.

The semi-local TB-mBJ potential is able to yield highly accurate energy band gaps in most semiconductors and insulators. It works not only for the classical sp-type semiconductors, but also for strongly correlated transition-metal compounds such as NiO. Because the high accuracy and predictive power could be achieved by determining a parameter c, using a larger testing set of solids, Different and new parameterizations were introduced [40, 41].

If your band gap is based on charge transfer transitions, you cannot use DFT+U and onsite-hybrid. Thus, the less expensive approach will be TB-mBJ potential which will give the band gap but not the forces.

II.5.6. Hybrid functionals

Hybrid functionals witch introduced by Axel Becke in 1993 [42] are a class of approximations to the exchange–correlation energy functional in density functional theory (DFT) that incorporate a portion of exact exchange from Hartree–Fock theory with the rest of the exchange-correlation energy from other sources (ab initio or empirical). This

hybridization provides a simple scheme for improving the calculation of many molecular properties, such as atomization energies, bond lengths and vibration frequencies, which tend to be poorly described with simple *ab initio* functionals.

As we see later, in the condensed matter physics community, the most widely used exchange-correlation functionals have been the local density approximation (LDA) and semilocal generalized gradient approximation (GGA). The so-called hybrid functionals, defined by the sum of a local V_{XC} and of a term proportional to the Hartree-Fock exact-exchange operator. Within the generalized Kohn-Sham (GKS) formalism, the total nonlocal potential V_{GKS} is given by: [43, 44]

$$V_{XC}(\vec{r},\vec{r}') = V_H(\vec{r}) + V_{XC}(\vec{r},\vec{r}') + V_{ext} \qquad (\text{II.}31)$$

Where $V_{XC}(\vec{r},\vec{r}')$ is now fully nonlocal and can be expressed as:

$$V_{XC}(\vec{r},\vec{r}') = \beta V_X^{sr-ex}(\vec{r},\vec{r}';\omega) + \alpha V_X^{lr-ex}(\vec{r},\vec{r}';\omega) + (1-\beta)V_X^{sr}(\vec{r};\omega) + (1-\alpha)V_X^{lr}(\vec{r};\omega) + V_C(\vec{r}) \qquad (\text{II.}32)$$

where α and β are parameters that determine the amount of long-range (*lr*) and short-range (*sr*) exact exchange, respectively. The long-range nonlocal potential $V_X^{lr-ex}(\vec{r},\vec{r}';\omega)$ is defined as:

$$V_X^{lr-ex}(\vec{r},\vec{r}';\omega) = -\sum_{i=1}^{N_{occ}} \phi_i(\vec{r})\phi_i^*(\vec{r}')\frac{erf(\omega|\vec{r}-\vec{r}'|)}{|\vec{r}-\vec{r}'|} \qquad (\text{II.}33)$$

where ω is a parameter (separation length) and ϕ_i are single-particle, occupied electronic orbitals. The short-range potential $V_X^{sr-ex}(\vec{r},\vec{r}';\omega)$ is defined in a similar manner, with the complementary error function replacing the error function in (Eq. II.33):

$$V_X^{sr-ex}(\vec{r},\vec{r}';\omega) = -\sum_{i=1}^{N_{occ}} \phi_i(\vec{r})\phi_i^*(\vec{r}')\frac{erf\,c(\omega|\vec{r}-\vec{r}'|)}{|\vec{r}-\vec{r}'|} \qquad (\text{II.}34)$$

The Coulomb potential is partitioned as:

$$\frac{1}{\vec{r}-\vec{r}'} = \frac{erfc(\omega|\vec{r}-\vec{r}'|)}{|\vec{r}-\vec{r}'|} + \frac{erf(\omega|\vec{r}-\vec{r}'|)}{|\vec{r}-\vec{r}'|} \qquad (\text{II.}35)$$

When $\alpha = \beta$, a full-range hybrid functional is obtained and α determines the fraction of exact exchange entering the definition of the potential:

$$V_{XC}(\vec{r}-\vec{r}') = \alpha V_X^{ex}(\vec{r}-\vec{r}') + (1-\alpha)V_X(\vec{r}) + V_C(\vec{r}) \qquad \text{(II. 36)}$$

The parameter α are used us an adjustable parameter to reproduce the experimental band gap of solids. For non-metallic, condensed systems the screening of the long-range tail of the Coulomb interaction is proportional to the inverse of the static dielectric constant ε_∞^{-1} and it is thus intuitive to relate the parameter α in (Eq. II.36) to ε_∞^{-1}. One may also justify such a relation by using many-body perturbation theory. The self-consistent cycle used to determine the sc-hybrid functional is shown in (Fig. II.2). The self-consistency loop is started with an initial guess for α, which is bound to range from 0 to 1; α determines the amount of exact exchange $V_X^{ex}(\vec{r},\vec{r}')$ included in the exchange correlation potential expression of (Eq. II.36).

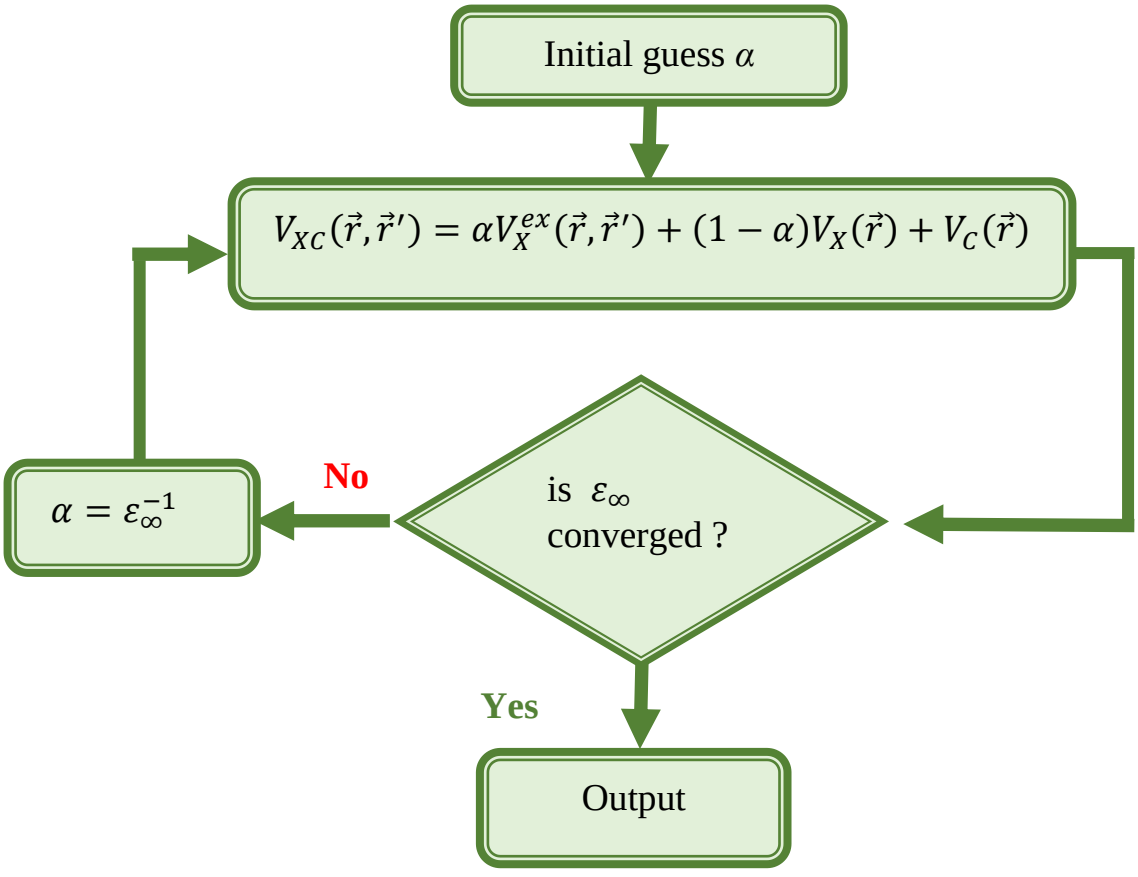

Figure II.2: Diagram of the self-consistent hybrid scheme [43].

References

[1] R. Shankar, *Principles of Quantum Mechanics*, 2nd edition, Kluwer Academic Plenum Publishers, New York, (1994).

[2] P. Urban, W. Thirring, *The Schrödinger Equation: Proceedings of the International Symposium "50 Years Schrödinger Equation" in Vienna*, 10th–12th June 1976, 1st edition, Springer-Verlag Wien, (1977).

[3] M. Born and J. R. Oppenheimer, *Zur Quantentheorie der Molekeln [On the Quantum Theory of Molecules]*," Ann. Phys, Vol. 389, No. 20, pp. 457–484, (1927).

[4] H, Akbas, and O. T. Turgut, *Born-Oppenheimer approximation for a singular system*, J. Math. Phys., Vol. 59, No. 1, pp. 012107 (2018).

[5] K. Haddadi, *Etude des propriétés structurales, élastiques et électroniques des composés antiperovskites de type XNCa3*, Doctorate thesis, Faculty of Science, University of Setif 1, Algeria, (2013).

[6] P. Hohenberg and W. Kohn, *Inhomogeneous electron gas*, Phys. Rev, Vol. 136, No. 3B, pp. B864, (1964).

[7] L. H. Thomas, *The calculation of atomic fields*, In Mathematical Proceedings of the Cambridge Philosophical Society, Cambridge University Press, Vol. 23, No. 05, pp. 542-548 (1927).

[8] E. Fermi, *Eine statistische Methode zur Bestimmung einiger Eigenschaften des Atoms und ihre Anwendung auf die Theorie des periodischen Systems der Elemente*. Z. Phys., Vol. 48, No. 1-2, pp. 73-79, (1928).

[9] D. J. Singh, Plane waves, *Pseudopotentials and the LAPW Method*, 2nd Ed, Naval Research Laboratory, Washington, USA, (2006).

[10] N. D. Mermin, *Thermal Properties of the Inhomogeneous Electron Gas*, Phys. Rev, Vol. 137, No. 5A, pp. A 1441-1443, (1965).

[11] U. von Barth and L Hedin, *A local exchange-correlation potential for the spin polarized case. I*, J. Phys. C: Solid State Phys., Vol. 5, No. 13, pp. 1629–1642, (1972).

[12] W. Kohn and L. J. Sham, *Self-consistent equations including exchange and correlation effects*, Phys. Rev, Vol. 140, No. 4A, pp. 1133-1138, (1965).

[13] S. Cottenier, *Density Functional Theory and the Family of (L)APW-methods: a step-bystep introduction*, ISBN 90-807215-1-4, (2004).

[14] G. Kresse, J. Furthmuller, *Efficient iterative schemes for ab initio total-energy calculations using a plane-wave basis set*, Phys. Rev. B, Vol. 54, No. 16, pp. 11169(18), (1996).

[15] M. Ernzerhof and G. E. Scuseria, *Assessment of the Perdew–Burke–Ernzerhof exchange-correlation functional*, J. Chem. Phys., Vol. 110, No. 11, pp. 5029-5036, (1999).

[16] M. Gell-Mann, K. A. Bruegkner, *Correlation Energy of an Electron Gas at High Density*, Phys. Rev., Vol. 106, No. 2, pp. 364-368, (1957).

[17] J. P. Perdew, *Physical Content of the Exact Kohn-Sham Orbital Energies: Band Gaps and Derivative Discontinuities*, Phys. Rev. Lett., Vol. 51, No. 20, p. 1884-1887, (1983).

[18] J. P. Perdew, J. A. Chevary, S. H. Vosko, K. A. Jackson, M. R. Pederson, D. J. Singh, C. Fiolhais, Atoms, molecules, solids, and surfaces: *Applications of the generalized gradient approximation for exchange and correlation*, Phys. Rev. B, Vol. 46, No. 11, pp. 6671-6687, (1992).

[19] J. P. Perdew, K. Burke, and M. Ernzerhof, *Generalized gradient approximation made simple*, Phys. Rev. Lett., Vol. 77, No. 18, pp. 3865(4), (1996).

[20] J. P. Perdew, A. Ruzsinszky, G. I. Csonka, O. A. Vydrov, G. E. Scuseria, L. A. Constantin, X. Zhou, K. Burke, *Restoring the Density-Gradient Expansion for Exchange in Solids and Surfaces*, Phys. Rev. Lett., Vol. 100, No. 13, pp. 136406(4), (2008).

[21] P. Haas, F. Tran, and P. Blaha, *Calculation of the lattice constant of solids with semilocal functionals*, Phys. Rev. B, Vol. 79, No. 8, pp. 085104(10), (2009).

[22] Z. Wu and R. E. Cohen, *More accurate generalized gradient approximation for solids*, Phys. Rev. B, Vol. 73, No.23, pp. 235116(6), (2006).

[23] G. K. H. Madsen, *Functional form of the generalized gradient approximation for exchange: The PBE functional*, Phys. Rev. B, Vol. 75, No. 19, pp. 195108(5), (2007).

[24] R. Armiento and A. E. Mattsson, *Functional designed to include surface effects in self-consistent density functional theory*. Phys. Rev. B, Vol. 72, No. 8, pp. 085108, (2005).

[25] A. E. Mattsson, R. Armiento, J. Paier, G. Kresse, J. M. Wills et al, *The AM05 density functional applied to solids*, J. Chem. Phys., Vol. 128, No. 8, pp. 084714(11), (2008).

[26] G. I. Csonka, J. P. Perdew, A. Ruzsinszky, P. H. T. Philipsen, S. Lebègue, J. Paier, O. A. Vydrov, and J. G. Ángyán, *Assessing the performance of recent density functionals for bulk solids*, Phys. Rev. B, Vol. 79, No. 15, pp. 155107(14), (2009).

[27] P. Haas, F. Tran, P. Blaha, and K. Schwarz, *Construction of an optimal GGA functional for molecules and solids*, Phys. Rev. B, Vol. 83, No. 20 pp. 205117(6), (2011).

[28] L. He, F. Liu, G. Hautier, M. J. T. Oliveira, M. A. L. Marques, F. D. Vila, J. J. Rehr, G. M. Rignanese, and A. Zhou1, *Accuracy of generalized gradient approximation functionals for density functional perturbation theory calculations*, Phys. Rev. B, Vol. 89, No. 6, pp. 064305(15), (2014).

[29] V. Ivády, R. Armiento, K. Szász, E. Janzén, A. Gali, and I. A. Abrikosov, *Theoretical unification of hybrid-DFT and DFT+U methods for the treatment of localized orbitals*, Phys. Rev. B, Vol. 90, No. 3, pp. 035146(13), (2014).

[30] A. I. Liechtenstein, V. I. Anisimov, J. Zaanen, *Density-Functional theory and strong interactions: Orbital ordering in Mott-Hubbard insulators*, Phys. Rev. B, Vol. 52, No. 8, pp. 5467(4), (1995).

[31] V. I. Anisimov, J. Zaanen, and O. K. Andersen, *Band theory and Mott insulators: Hubbard U instead of Stoner I*, Phys. Rev. B, Vol. 44, No. 3, pp. 943-954, (1991).

[32] V. I. Anisimov, F. Aryasetiawan, and A. I. Lichtenstein, *First-principles calculations of the electronic structure and spectra of strongly correlated systems: the LDA+ U method*, J. Phys.: Condens. Matter, Vol. 9, No 4, pp. 767–808, (1997).

[33] M. Cococcioni and S. de Gironcoli, *Linear response approach to the calculation of the effective interaction parameters in the LDA+U method*, Phys. Rev. B, Vol. 71, No. 3, pp. 035105(16), (2005).

[34] S. J. Youn, *Calculation of the Hubbard U parameters by the Solid Atom Method*, Journal of Magnetics, Vol. 10, No. 2, pp. 71-75, (2005).

[35] F. Aryasetiawany, and O. Gunnarssonz, *The GW method*, Rep. Prog. Phys., Vol. 61, No. 3, pp. 237–312, (1998).

[36] A. D. Becke and E. R. Johnson, *A simple effective potential for exchange*, J. Chem. Phys., Vol. 124, No. 22, pp. 221101(4), (2006).

[37] A. D. Becke, and M. R. Roussel, *Exchange holes in inhomogeneous systems: A coordinate-space model*, Phys. Rev. A, Vol. 39, No. 8, pp. 3761-3767, (1989).

[38] F. Tran, P. Blaha, and K. Schwarz, *Band gap calculations with Becke-Johnson exchange potential*, J. Phys.: Condens. Matter, Vol. 19, No 19, pp. 196208(8), (2007).

[39] F. Tran and P. Blaha, *Accurate Band Gaps of Semiconductors and Insulators with a Semilocal Exchange-Correlation Potential*, Phys. Rev. Lett., Vol. 102, No. 22, pp. 226401(4), (2009).

[40] D. Koller, F. Tran, and P. Blaha, *Merits and limits of the modified Becke-Johnson exchange potential*, Phys. Rev. B, Vol. 83, No. 19, pp. 195134(10), (2011).

[41] D. Koller, F. Tran, and P. Blaha, *Improving the modified Becke-Johnson exchange potential*, Phys. Rev. B, Vol. 85, No.15, pp. 155109(8), (2012).

[42] A. D. Becke, *A new mixing of Hartree–Fock and local density functional theories*, J. Chem. Phys., Vol. 98, No. 2, pp. 1372(6), (1993).

[43] J. H. Skone, M. Govoni, and Giulia Galli, *Self-consistent hybrid functional for condensed systems*, Phys. Rev. B, Vol. B 89, No. 19, pp. 195112(12), (2014).

[44] J. Heyd and G. E. Scuseria, *Efficient hybrid density functional calculations in solids: Assessment of the Heyd–Scuseria–Ernzerhof screened Coulomb hybrid functional*, J. Chem. Phys., Vol. 121, No. 3, pp. 1187(6), (2004).

Chapter III

The Full Potential-Linearized Augmented Plane Wave (FP-LAPW) method

Chapter III

III.1. Introduction

To understand the different properties of solids, it is necessary to study the behavior of electrons in the latter. There are many *ab initio* methods that physicists and chemists use to calculate the electronic structure. All *ab initio* methods have been continuously refined over recent years and all have benefited from the availability of increasingly powerful computers. Most methods can now model to study extended systems like solids (See Fig. III.1). The most common and widely used method, which will be used in this work, is "The Full-Potential Linearized Augmented Plane Wave Method". The LAPW method is fundamentally a modification of the original augmented plane wave (APW) method of Slater.

The full-potential linearized augmented plane wave (FP-LAPW) method has emerged as a widely used very robust and precise state-of-the-art *ab initio* electronic structure technique with reasonable computational efficiency to simulate the electronic properties of materials based on density-functional theory (DFT). The FP-LAPW method is an all-electron algorithm, which is universally applicable to all atoms of the periodic table in particular to transition metals and rare earths and to multi-atomic systems with compact as well as open structures. Due to the all-electron nature of the method, magnetism and nuclear quantities are included rigorously. In addition, open structures such as surfaces, clusters, organic and inorganic molecules as well as wires can be treated

without problems. The capability of calculating atomic forces exerted on the atoms opens the path to structure optimization.

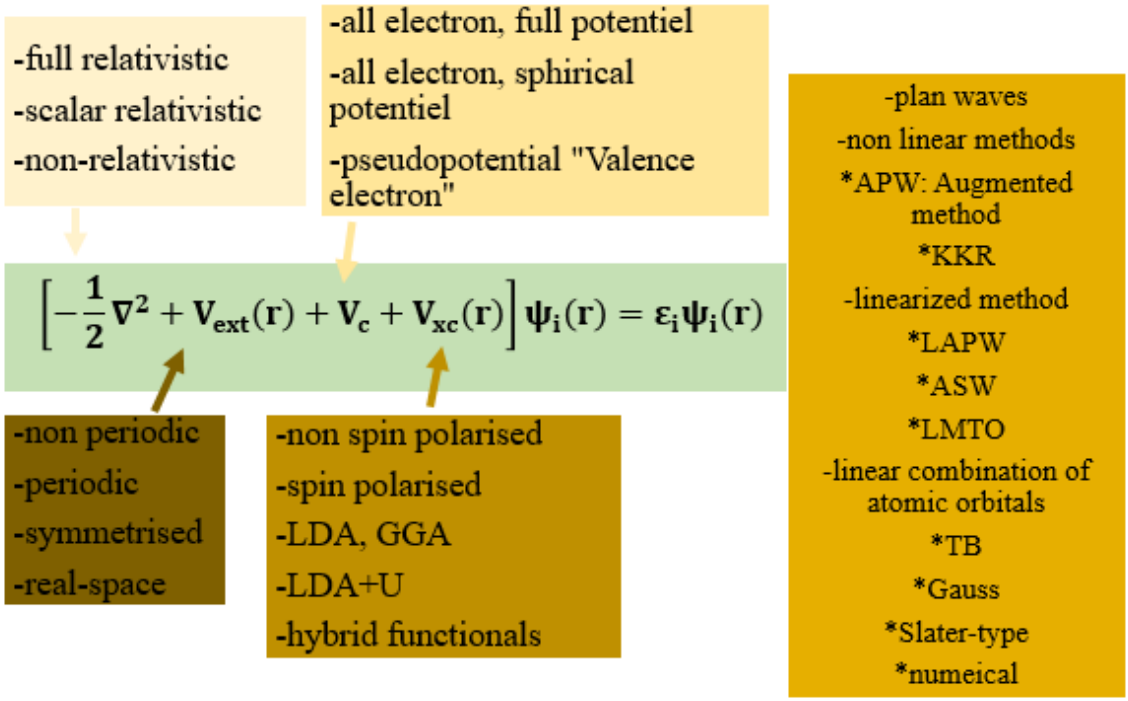

Figure III.1: Overview of electronic structure calculations [1].

III.2. The APW method

The APW method was developed by Slater in 1937 [2, 3]. Near an atomic nucleus the potential and wave functions are similar to those in an atom "they are strongly varying but nearly spherical. Conversely, in the interstitial space between the atoms both the potential and wave functions are smoother. Accordingly, space is divided into two regions and different basis expansions are used in these regions: radial solutions of Schrodinger's equation inside non-overlapping atom centered spheres and plane waves in the remaining interstitial region (Fig. III.2) [4]. The crystalline potential $U(\vec{r})$ and the wave function $\phi(\vec{r})$ are written as:

$$U(\vec{r}) = \begin{cases} U(\vec{r}) & \vec{r} \in \text{I} \\ 0 & \vec{r} \in \text{II} \end{cases} \qquad \text{(III. 1)}$$

$$\phi(\vec{r}) = \begin{cases} \sum_{lm} A_{lm} U_l(\vec{r}) Y_{lm}(\vec{r}) & \vec{r} \in \text{I} \\ \frac{1}{\sqrt{\Omega}} \sum_G C_G \, e^{i(\vec{K}+\vec{G})\vec{r}} & \vec{r} \in \text{II} \end{cases} \qquad \text{(III. 2)}$$

where $\vec{K}$ is Bloch vector, Ω is the cell volume, $\vec{G}$ is a reciprocal lattice vector, Y_{lm} is the spherical harmonics, C_G and A_{lm} are expansion coefficients (l and m are quantum numbers). $U_l(\vec{r})$ is the regular solution of the radial Schrodinger equation defined by:

$$\left(-\frac{\hbar^2}{2m}\frac{d^2}{dr^2} + \frac{\hbar^2}{2m}\frac{l(l+1)}{r^2} + V(\vec{r}) - E_l\right) r U_l(\vec{r}) = 0 \qquad \text{(III. 3)}$$

where E_i is an energy parameter, V is the spherical component of the potential in the sphere. The radial functions $U_l(\vec{r})$ defined by (Eq. II.3) are automatically orthogonal to any eigenstate of the same Hamiltonian that vanishes on the sphere boundary [4]:

$$(E_2 - E_1) r U_1(\vec{r}) U_2(\vec{r}) = u_2 \frac{d^2 r U_1(\vec{r})}{dr^2} - u_1 \frac{d^2 r U_2(\vec{r})}{dr^2} \qquad \text{(III. 4)}$$

where $U_1(\vec{r})$ and $U_2(\vec{r})$ are radial solutions at different energies E_1 and E_2. The overlap is constructed using this relation and integrating by parts; the surface terms vanish if either $U_1(\vec{r})$ or $U_2(\vec{r})$ vanish on the sphere boundary, while the other terms cancel.

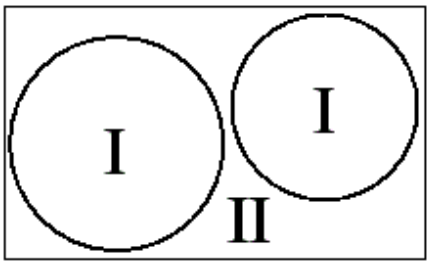

Figure III.2: The division of space in the APW method. The muffin-tin spheres "I" are surrounded by the interstitial region "II".

The problem of this method lies in (Eq. III.2), which does not ensure the continuity of the kinetic energy at the boundary of the sphere. So, it is essential to impose this constraint in the method, by defining the coefficients A_{lm} as a function of C_G through the development in spherical harmonics of the plane waves. The coefficient of each component (lm) being given by [4, 5]:

$$A_{lm} = \frac{4\pi i^{l}}{\sqrt{\Omega}U_{l}(R)} \sum_{G} C_{G}\, j_{l}\left(\left|\vec{K}+\vec{G}\right|R\right) Y_{lm}^{*}(\vec{K}+\vec{G}) \qquad \text{(III. 5)}$$

where j_l is the Bessel function of order 1 and R is the sphere radius.

If the E_l's were fixed, used only as a parameter during the construction of the basis, the Hamiltonian could be set up in terms of this basis. This would lead to a standard secular equation for the band energies. Unfortunately, it turns out, that the APW basis does not offer enough variational freedom if the E_l's are kept fixed. An accurate description can only be achieved if they are set to the corresponding band energies. However, requiring the E_l's to be equal to the band energies, the latter can no longer be determined by a simple diagonalization of the Hamiltonian matrix. Since the U_l's depend on the band energies, the solution of the secular equation becomes a nonlinear problem, which is computationally much more demanding than a secular problem.

Another disadvantage of the APW method is, that it is difficult to extend beyond the spherically averaged muffin-tin potential approximation, because in the case of a general potential the optimal choice of El is no longer the band energy. And finally, but less serious, if, for a given choice of E_l's, the radial functions u_l vanish at the muffin-tin radius, the boundary conditions on the spheres cannot be satisfied, i.e., the plane-waves and the radial functions become decoupled. This is called the asymptote problem. It can already cause numerical difficulties if U_l becomes very small at the sphere boundary [5]. To overcome these difficulties, several modifications have been made to the APW method, notably those proposed by Anderson [6], as well as that of Koelling and Abrman [7].

In 1975, Anderson proposed a method in which the basic functions $U_l(\vec{r})$ and their derivatives are continued for a given energy. This choice solves the problems encountered in the APW method thus giving a band structure method, flexible and precise. This method is called the linear LAPW augmented plane wave method.

III.3. The FP-LAPW method

In the original APW formulation introduced by Slater, the plane-waves are augmented to the exact solutions of the Schrödinger equation within the MT at the calculated eigenvalues. This approach is computationally expensive because it leads to an explicit energy dependence of the basis functions (and consequently of the Hamilton- and overlap-matrices) and thus to a non-linear eigenvalue problem. Instead of performing a single diagonalization to solve the KS equation one repeatedly needs to evaluate (for many trial energies) the determinant of the secular equation in order to find its zeros and thus the single particle eigenvalues ε_i [8, 9].

For a crystal, the space is divided into two regions: the first region is the Muffin-tin sphere, and the second is the remaining space that represents the interstitial region. The basic functions of the FP-LAPW are plane waves in the interstitial region and spherical harmonics multiply by the radial functions in the muffin-tin spheres .In the FP-LAPW method, the basic functions in the MT spheres are linear combinations of the radial functions $U_l(\vec{r})Y_{lm}$ and their derivatives $\dot{U}_l(\vec{r})Y_{lm}(\vec{r})$.

The functions U_l are defined exactly as in the APW method but with a fixed E_l. The Function U_l satisfies the following equation:

$$\left(-\frac{\hbar^2}{2m}\frac{d^2}{dr^2}+\frac{\hbar^2}{2m}\frac{l(l+1)}{r^2}+V(\vec{r})\ -E_l\right)r\dot{U}_l(\vec{r})=rU_l(\vec{r}) \qquad \text{(III. 6)}$$

where the combination of the radial functions U_l and $\dot{U}_l$ ensures continuity with the plane waves of the interstitial region on the surface of the sphere MT.

The augmented wave functions are then used as basic functions of the FP-LAPW method, so we have:

$$\phi(\vec{r})=\begin{cases}\sum_{lm}\left[A_{lm}U_l(\vec{r})+B_{lm}\dot{U}_l(\vec{r})\right]\ Y_{lm}(\vec{r}) & r\in \text{I}\\ \frac{1}{\sqrt{\Omega}}\sum_G C_G\ e^{i(\vec{K}+\vec{G})\vec{r}} & r\in \text{II}\end{cases} \qquad \text{(III. 7)}$$

where A_{lm} : are coefficients corresponding to the function $U_l(\vec{r})$.

B_{lm} : are coefficients corresponding to the function $\dot{U}_l(\vec{r})$.

Inside the spheres, the LAPWs functions are better adapted than the APWs functions, in fact if E_l differs a little from the band energy E, the linear combination of the (Eq. III.7) will better reproduce the function radial than the APWs functions taken alone:

$$U_l(E,\vec{r}) = U_l(E_l,\vec{r}) + (E - E_l)\,\dot{U}_l(E_l,\vec{r}) + O((E - E_l)^2) \qquad \text{(III. 8)}$$

where $O((E - E_l)^2)$ represents the quadratic error in energy.

In this method, the calculations lose some precision compared to the APW method whose wave functions are more correct. The FP-LAPW method causes an error $O(E - E_l)^2$ of order on the wave functions and another on the band energy of order $O(E - E_l)^4$. Despite these minor drawbacks, the LAPWs functions form a good basis for -with a single E_l- to get all the valence bands in a fairly wide energy range. However, it is possible to divide the energy interval into several energy windows, each of which corresponds to an energy E_l where the solution will be obtained separately [10].

III.4. Construction of the Radial Functions

III.4.1. Non-relativistic Radial Functions

The differential equations (Eq. III.6) may be solved on the radial mesh using standard methods [11]. However, since (Eq. III.3) is linear, the norm of U_l is undetermined, and furthermore, given a solution, $\dot{U}_l$ of (Eq. III.6), $\dot{U}_l + cU_l$ with arbitrary c is also a solution. In practice, it is convenient to enforce the normalization,

$$\int_0^{r_\alpha} [rU_l(\vec{r})]^2 d\vec{r} = 1 \qquad \text{(III. 9)}$$

and to orthogonalize U_l and $\dot{U}_l$

$$\int_0^{r_\alpha} r^2 U_l(\vec{r})\dot{U}_l(\vec{r})d\vec{r} = 0 \qquad \text{(III. 10)}$$

where r_α is the location of the sphere "atom" α,

With this choice, the norm of $\dot{U}_l$ ($\|\dot{U}_l\|$) provides an indication as to the range over which the energy linearization is a reasonable approximation. In particular, the linearization errors are acceptable for most purposes when $\|\dot{U}_l\| \times E_l - \varepsilon \leq 1$, where E_l is/are the energy parameter(s) for those "l" for which the band in question has significant

character and "ε" is the band energy.

Several options are available if a choice of E_l that satisfies the above criterion cannot be determined. These are (i) to divide the energy range into windows (also known as panels) and treat each window separately with E_l appropriate for the states in it, (ii) to relax the linearization using a local orbital extension (this is effectively a quadratic method), or (iii) to reduce the sphere sizes, thereby reducing $\|\dot{U}_l\|$. The first two options are commonly used. The latter, while generally applicable, results in substantial increases in the basis set size, and these increases are often computationally prohibitive and further may exacerbate problems due to high lying extended core states (e.g., ghost bands). However, iterative implementations of the LAPW method impose smaller penalties for increased basis set size, and in these methods (iii) may be a reasonable alternative [4, 12].

II.4.2. Relativistic Radial Functions

Relativistic corrections are important only when the kinetic energy is large. Since the band energies of interest in solids are small, this means that relativistic effects need only be incorporated in regions where the potential is strongly negative, i.e., near the nuclei. In the LAPW method, this means that relativistic effects can be safely neglected in the interstitial region, and the only modifications are to the radial functions in the spheres and the components of the Hamiltonian that operate on them.

The relativistic modification is, therefore, to replace (Eq. III.3) and (Eq. III.6) by the corresponding Dirac equation and its energy derivative, and retain the relativistic terms when evaluating the sphere contribution to the Hamiltonian matrix elements. It is, however, convenient to neglect spin-orbit effects at this stage (the scalar relativistic approximation), since otherwise the size of the secular equation is doubled. If important, spin-orbit effects can be taken account of latter using the low lying band wave functions as the basis for a second variational step. The exception is for calculations with non-collinear magnetism, in which case the secular equation is doubled regardless. Koelling and Harmon [13] have presented a technique for solving the Dirac equation in a spherically symmetric potential, in which spin-orbit effects are initially neglected, but may be incorporated afterward [4].

The solution of the Dirac equation is conventionally written as, [4, 13]

$$\psi_{k\mu} = \begin{bmatrix} g_k \chi_{k\mu} \\ -if_k \sigma_r \chi_{k\mu} \end{bmatrix} \qquad \text{(III. 11)}$$

Where *K* is the relativistic quantum number, $\chi_{k\mu}$ is a two-component spinor and the radial coordinate has been suppressed.

Koelling and Harmon [13] define a new function,

$$\phi_k = \frac{1}{2MC} g_k' \qquad \text{(III. 12)}$$

Here the prime denotes the radial derivative, m is the mass, C is the speed of light and

$$M = m + \frac{1}{2C^2}(E - V) \qquad \text{(III. 13)}$$

at energy, *E*. Dropping the spin-orbit term, the solution is rewritten with the usual non-relativistic "*lm*" quantum numbers as:

$$\phi_{lms} = \begin{bmatrix} g_l Y_{lm} \chi_s \\ \frac{i}{2MC} \sigma_r \left(-g_l' + \frac{1}{r} g_l \sigma \right) Y_{lm} \chi_s \end{bmatrix} \qquad \text{(III. 14)}$$

Where χ_s is the usual non-relativistic spinor. Defining $P_l = r g_l$ and $Q_l = rC\phi_l$, the scalar relativistic equations become:

$$P_l' = 2MQ + \frac{1}{2} P_l \qquad \text{(III. 15)}$$

and

$$Q_l' = -\tfrac{1}{2} Q + \left[\tfrac{l(l+1)}{2Mr^2} + (V - E_l) \right] P_l \qquad \text{(III. 16)}$$

These can be solved numerically in the same way as the non-relativistic Schrodinger equation (e.g., standard predictor-corrector), given the boundary condition,

$$\lim_{r \to 0} \frac{Q}{P} = C \frac{[l(l+1) + 1 - (2Z/C)^2]^{1/2} - 1}{(2Z/C)} \qquad \text{(III. 17)}$$

The spin-orbit term (note that there are higher order terms in M^{-1} that have been neglected) may be included by adding $-\left(\frac{V'}{4M^2C^2}\right)(k+1)P$ to the right hand side of (Eq.

III.16). The energy derivatives, needed for the linearization, are analogous to the non-relativistic case.

$$\dot{P}_l' = 2\left(\dot{M}Q_l + M\dot{Q}_l\right) + \frac{1}{r}\dot{P}_l \qquad \text{(III. 18)}$$

and

$$\dot{Q}_l = -\frac{1}{r}\dot{Q}_l\left[\frac{l(l+1)}{2Mr^2} + (V - E_l)\right]\dot{P}_l - \left[\frac{l(l+1)\dot{M}}{2M^2r^2} + 1\right]P_l \qquad \text{(III. 19)}$$

From the solution. P_l and Q_l, the large and small components, g_l and f_l can be determined via the definitions of P_l, Q_l and ϕ_k. Both the large and small components are to be used in constructing the charge density or evaluating matrix elements. Thus the quantity replacing U_l^2 in the normalization equation (Eq. III.9) is $g^2 + f^2$.

III.5. Semi-core states problem

The FP-LAPW method generally gives accurate band energies in the vicinity of the linearization energies E_l and in most materials it is sufficient to choose these energies near the center of the bands. However, this is not always possible and in some cases the choice of a single value of E_l is not sufficient for the calculation of all energy bands. This kind of problem is encountered, for example, with the orbital materials 4f, as well as with the elements of the transition metals. This is the fundamental problem of the so-called semi-core state: An intermediate state between the state of valence and the state of heart. In this case, the difficulty is overcome by (i) using the multiple energy windows or (ii) the (LAPW + LO) method of Singh [14-18].

III.5.1. Multiple energy windows

In the two window treatment (See Fig. III.3), a division is made into semi-core and valence energy regions. A different set of E_l is chosen for each window to treat the states in it as accurately as possible. Separate calculations are then performed for the two windows and the relevant bands are used to construct semi-core and valence charge densities. This amounts to two independent LAPW calculations, with the exception that the potential is the same and the charge densities are combined.

Although this approach does solve many of the problems associated with the linearization and permits full relaxation of semi-core states, it is not fully satisfactory. First of all, there is a substantial overhead because separate calculations are being done for each window. When multiple windows are used for the conduction bands, the cost of a two window calculation is almost twice that of a one window calculation. For the more common application to semi-core states, the overhead is lower because these states are almost dispersionless and so only a very small number (typically only one) of k-points is needed for the lower window [4].

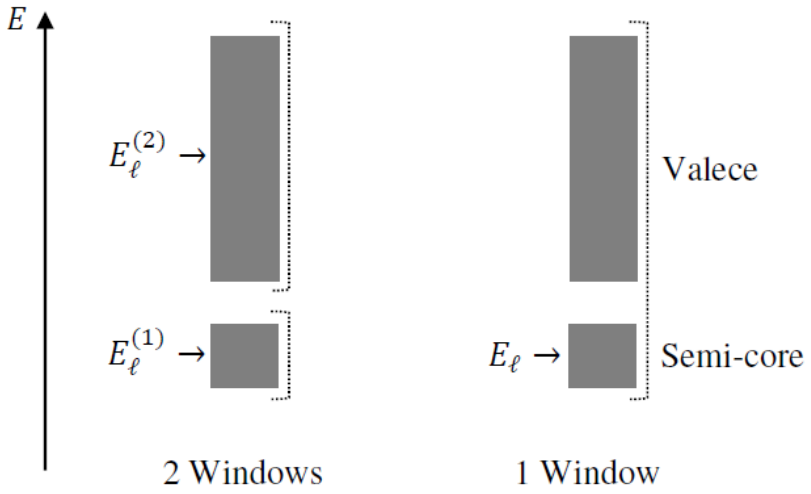

Figure III.3: Example of windows with a semi-core state. The E_l corresponding to the semi-core angular momentum is set low in the single window case [4].

III.5.2. LAPW+LO method

The main idea of this method is the treatment of all energy states with a single energy window. A linear combination of two radial functions are proposed [19-21]; the derivatives of these functions with respect to energy are equal, but the corresponding linearization energies are different. The proper function has the following form:

$$\phi_{lm}^{LO} = \left[A_{lm}U_l(\vec{r}, E_{1,l}) + \dot{U}_l B_{lm}\left(\vec{r}, E_{1,l}\right) + C_{lm}U_l(\vec{r}, E_{2,l})\right]Y_{lm}(\vec{r}) \qquad \text{(III. 20)}$$

The coefficients A_{lm}, B_{lm} and C_{lm} are determined by the requirements that ϕ_{lm}^{LO} should be normalized and has zero value and slope at the sphere boundary.

References

[1] S. Blugel, G. Bihlmayer, *Full-Potential Linearized Augmented Plane wave Method*, Comput. Nanosci.: Do It Yourself!, Vol. 31, pp. 85-129, (2006).

[2] J. C. Slater, *Wave functions in a periodic potential*. Physical Review, Vol. 51, No. 10, pp. 846(6), (1937).

[3] J. C. Slater, *An Augmented Plane Wave Method for the Periodic Potential Problem*, Phys. Rev., Vol. 92, No. 3, pp.603(6), (1953).

[4] D. J. Singh, L. Nordstrom, *plane waves, pseudopotentials and the LAPW method*,2nd Edition, U.S.A, (2006).

[5] Y. Mokrousov, *Ab initio All-electron Full-potential Linearized Augmented Plane-wave Method for One-dimensional Systems*, Master of Science, Rheinisch-West fälischen Technischen Hochschule Aachen (Germany), (2005).

[6] O. K. Andersen, *Linear methods in band theory*, Phys. Rev. B ,Vol. 12, No. 8, pp. 3060-3083, (1975).

[7] D. D. Koelling and G. O. Arbman, *Use of energy derivative of the radial solution in an augmented plane wave method: application to copper*. J. Phys. F: Metal Phys., Vol. 5, No. 11, p. 2041, (1975).

[8] M. Petersen, F. Wagner, L. Hufnagel, M. Scheffler, P. Blaha and K. Schwarz, Improving the efficiency of FP-LAPW calculations, Comput. Phys. Commun., Vo. 126, No. 3, pp. 294–309, (2000).

[9] H. Bross, and G. M. Fehrenbach, *The spline augmented plane wave method*. Z. Phys. B: Condens. Matter, Vol. 81, No 2, pp. 233-243, (1990).

[10] L. F Mattheiss and D. R. Hamann, *Linear augmented-plane-wave calculation of the structural properties of bulk Cr, Mo, and W*, Phys. Rev. B, Vol. 33, No. 2, pp. 823-840, (1986).

[11] M. Planitz, *Numerical recipes-the art of scientific computing*, by W. H. Press, B. P. Flannery, S. A. Teukolsky and W. T. Vetterling, (Cambridge University Press). The Mathematical Gazette, Vol. 71, No. 457, pp. 245-246, (1987).

[12] S. Goedecker, *Treatment of semicore states in the linearized augmented-plane-wave method and other linearized electronic-structure methods*. Phys. Rev. B, Vol. 47, No. 15, pp. 9881-9883, (1993).

[13] D. D. Koelling, and B. N. Harmon, *A technique for relativistic spin-polarised calculations*, J. Phys. C: Solid State Phys., Vol. 10, No. 16, pp. 3107-3114, (1977).

[14] D. D. Koelling, *Approximate treatment for semi-core states*, Solid State Commun., Vol. 53, No. 11, pp. 1019-1021, (1985).

[15] S. Goedecker and K. Maschke, *Alternative approach to separable first-principles pseudo-potentials*, Phys. Rev. B, Vol. 42, No. 14, pp. 8858-8863, (1990).

[16] P. Blaha, D. J. Singh, P. I. Sorantin, and K. Schwarz, *Electric-field-gradient calculations for systems with large extended-core-state contributions*, Phys. Rev. B, Vol. 46, No. 3, pp. 1321-1325, (1992).

[17] D. J. Singh, and J. Ashkenazi, *Magnetism with generalized-gradient-approximation density functionals*, Phys. Rev. B, Vol. 46, No. 18, pp. 11570-11577, (1992).

[18] D. J. Singh, W. E. Pickett and H. Krakauer, *Gradient-corrected density functionals: Full-potential calculations for iron*, Phys. Rev. B, Vol. 43, No. 14, pp. 11 628-11 634, (1991).

[19] T. Takeda, and J. Kubler, *Linear augmented plane wave method for self-consistent calculations*, J. Phys. F: Metal Phys., Vol. 9, No. 4, pp. 661-672, (1979).

[20] L. Smrčka, *Linearized augmented plane wave method utilizing the quadratic energy expansion of radial wave functions*, Czech. J. Phys. B, Vol. 34, No 7, pp. 694-704, (1984).

[21] J. Petrů, J. and L. Smrčka, *Quadratic augmented plane wave method for self-consistent band structure calculations*, Czech. J. Phys. B, Vol, Vol. 35, No. 1, pp. 62-71, (1985).

Chapter IV

Results and Discussion

Chapter IV

IV.1. Structural properties of the BaFAg*Ch* (*Ch* = S, Se and Te) compounds

It is well known that the physical properties of crystals depend strongly on their structural properties. Therefore, as first step of the present work, we have determined the optimized (equilibrium) structural parameters of the three studied compounds accurately. In order to obtain the optimized structural parameter values that are in good agreement with the available experimental ones, the calculation parameters should be well chosen. The following calculation parameters were used to calculate the optimized structural parameters:

- Three different functionals, namely the local density approximation (LDA) [1], generalized gradient approximation (GGA) parametrized by Perdew *et al*. [2] (the so-called GGA-PBE or GGA96) and an another version of the GGA parametrized by Perdew *et al*. [3] (the so-called GGA-PBEsol or GGA08) were used to model the exchange-correlation.
- The Ba: $5s^2 5p^6 6s^2$, F: $2s^2 2p^5$, Ag: $4p^6 5s^1 4d^{10}$, S: $3s^2 3p^4$, Se: $4s^2 3d^{10} 4p^4$ and Te: $5s^2 4d^{10} 5p^4$ orbitals were treated as valence electron states.
- The muffin-tin radii for the Ba, F, Ag and *Ch* atoms were chosen to be respectively 2.4, 2.5, 2.5, 2.24 *a.u.* in BaFAgS, 2.42, 2.5, 2.5, 2.5 in BaFAgSe and 2.44, 2.5, 2.5, 2.5 in BaFAgTe.
- The energy convergence criterion was set to 10^{-5} Ry.
- To achieve the total energy convergence, the plane wave cut-off parameter $R_{MT}^{\min} K_{\max}$ is chosen to be equal to 10.
- For the *k*-space integration over the Brillouin zone (BZ), a 16×16×7 Monkhorst-Pack [4, 5] *k*-point mesh was used.
- The geometry optimization was performed with a full structural relaxation of the volume and shape of the unit cell and the atomic positions until the maximum force on any atom should be smaller than 0.5 mRy/*a.u*.
- The calculations were performed with and without including the spin-orbit coupling effect.

The BaFAg*Ch* (*Ch* = S, Se and Te) compounds crystallize in a tetragonal layered structure of the LaOAgS-type with the space group P4/*nmm* (n. 129) [6]. There are two chemical formulas in the unit cell (Z = 2), e.g., the BaFAg*Ch* unit cell contains 2 Ba, 2 F, 2

Ag and 2 *Ch* atoms. The Wyckoff positions of the four inequivalent atomic positions in the BaFAg*Ch* compounds are Ba: 2c (0.25, 0.25, zBa), Ag: 2b (0.75, 0.25, 0.5), Ch: 2c (0.25, 0.25, z_{Ch}) and F: 2a (0.75, 0.25, 0), where z_{Ba} and z_{Ch} are respectively the internal coordinates along the *c*-axis of the Ba and *Ch* atoms. Each Fluoride (Silver) atom is contouring by four barium (Chalcogenide) atoms as showed in Fig. IV.1. The BaFAg*Ch* (*Ch* = S, Se, Te) compounds may be schematically viewed as an alternating stacking of quasi two-dimensional [BaF] and [Ag*Ch*] layers along the *c*-axis. Therefore, the BaFAg*Ch* (*Ch* = S, Se, Te) compounds are a natural superlattice structure.

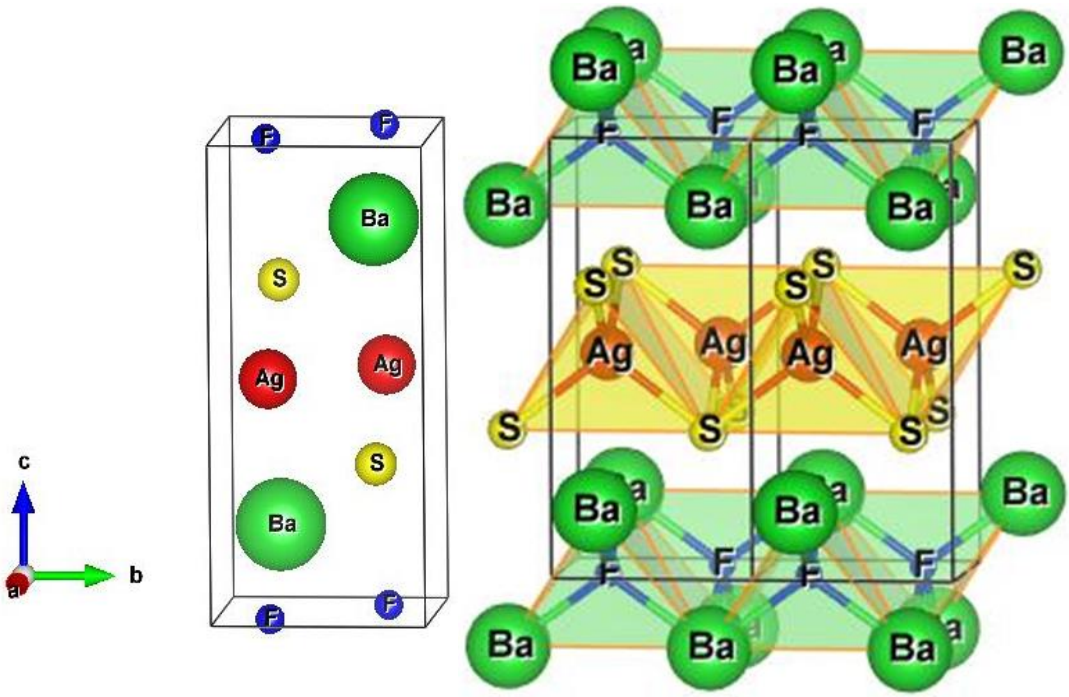

Figure IV.1: The unit-cell crystalline structure (left) and polyhedrons on the 1x2x1 super cell (right) of BaFAgS.

The BaFAg*Ch* (*Ch* = S, Se and Te) compounds are characterized by four structural parameters that are not fixed by the symmetry group, namely the lattice parameters: *a* and *c*, and the internal coordinates z_{Ba} and z_{Ch}, which need to be optimized. To obtain the optimized crystalline structure, i.e., the structural parameters that correspond to the total energy minimum, i.e., equilibrium state, we proceeded as follows:

(i) Calculate the total energy (E_{tot}) for a set of unit cell volumes ($V = 0.9V_{expt}$, 0.95 V_{expt}, V_{expt}, 1.05 V_{expt} and 1.10 V_{expt}), which were chosen around the experimental value of the unit cell (V_{expt}) (or the equilibrium one if the experimental one is not available), where the *c/a* ratio and the atomic positions were optimized for each volume

(ii) Fit the obtained E_{tot}-V data to the Birch–Murnaghan equation of state (*EOS*) [7]:

$$E(V) = E_0 + \frac{9V_0B_0}{16}\left\{\left[\left(\frac{V_0}{V}\right)^{\frac{3}{2}} - 1\right]^3 B_0' + \left[\left(\frac{V_0}{V}\right)^{\frac{2}{3}} - 1\right]^2\left[6 - 4\left(\frac{V_0}{V}\right)^{\frac{2}{3}}\right]\right\} \qquad \text{(IV. 1)}$$

Here V_0 is the equilibrium volume of the unit cell and E_0 is the corresponding total energy (the minimum of the total energy), B_0 is the equilibrium bulk modulus and *B'* is its pressure derivative. The mentioned procedure to calculated the optimized structural parameters is implemented in a special package developed by Jamal Morteza [8] which is implemented in the Wien2K code. The calculated equilibrium unit-cell parameters (*a* and *c*) and internal atomic coordinates (z_{Ba} and z_{Ch}) for each considered compound and the corresponding measured and previously calculated values (when available) are collected in Tab. IV.1. From Tab. IV.1, one can note the following:

➢ Owing to the fact that measures of the lattice parameters were performed at room temperature whereas our results are predicted for zero temperature, one will expect that correct calculated values for the lattice parameters will be slightly smaller than their corresponding measured ones. From Tab. IV.1, one can note that the GGA96-calculated (LDA-calculated) lattice parameters of the three considered compounds are somewhat larger (somewhat smaller) than the measured ones. This stems from the well-known fact that the LDA tends to slightly underestimate the interatomic distances and the GGA96 tends to slightly overestimate them. However, from Tab. IV.1, one can appreciate that the GGA08 calculated lattice parameters are practically equal to the arithmetic averages of the GGA96 and LDA-calculated values and are slightly smaller than their corresponding

experimental ones as expected. It is worth to note that the GGA08 [3] has been developed specifically to improve the description of the exchange-correlation effects in solids. The maximum relative deviation of our calculated structural parameters values from the experimental ones ($d(\%) = ((x - x_{expt}) / x_{expt}) \times 100$), where $x = a, c$, does not exceed 1%, which demonstrates the reliability of the obtained results. Therefore, the GGA08 optimized structural parameters were adopted for the calculations of the remaining investigated properties.

- The lattice parameters increase when substituting the *Ch* atom in the following sequence: $S \rightarrow Se \rightarrow Te$, which can be explained by the increase of the atomic radius (R) of the chalcogen atom *Ch*: R(S)=1.09 Å< R(Se)=1.22 Å< R(Te)=1.42 Å.
- The inclusion of the spin-orbit coupling leads to a non-significant effect on the lattice parameters values.
- The bulk modulus (*B*) value decreases when the *Ch* atom in the BaFAg*Ch* compound is replaced in the following sequence: $S \rightarrow Se \rightarrow Te$. This result is consistent with the fact that *B* is inversely proportional with the unit cell volume (*V*): ($B \sim 1/V$) [9, 10].

Table IV.1: Calculated lattice parameters (a and c, in Å), relative deviation from the experimental value $d(\%) = [(x - x_{expt})/x_{expt}] * 100$, ($x$ = a, c), internal atomic coordinates (z_{Ba} and z_{Ch}, dimensionless), unit-cell volume (V_0, in Å^3), bulk modulus (B_0, in GPa), cohesive energy (E_{Coh}, in eV) and formation enthalpy (ΔH, in eV) for the BaFAgCh (Ch = S, Se, Te) compounds, compared with the available experimental and theoretical data.

BaFAgS			
	Present	Expt. [6]	Other [11]
a	4.2035[a], 4.1963[a,*], 4.2880[b], 4.1523[c]	4.2406	4.280
d	-0.87[a], 1.04[a,*] +1.12[b],+2.08[c]	-	-
c	9.2423[a] ,9.2327[a,*] ,9.4537[b], 9.1114[c]	9.3029	9.411
d	-0.65[a], -0.75[a,*], +1.62[b] , -2.06[c]	-	-
z_{Ba}	0.1698[a] 0.1687[a,*] 0.1676[b] 0.1694[c]	0.1665	-
z_S	0.6745[a] 0.6752[a,*] 0.6750[b] 0.6750[c]	0.6760	-
V_0	163.306a, 162.578[a,*], 173.8246[b]157.0951[c]	167.2911	172.3945
B_0	61.1462[a] 51.4222[b], 70.3551[c]	-	-
E_{Coh}	-7.7244		
ΔH	-5.9081		
BaFAgSe			
	Present	Expt. [6]	Other [11]
a	4.3177[a], 4.3078[a,*], 4.4035[b], 4.2712[c]	4.3449	4.390
d	-0.63[a], -0.85 [a,*], +1.35[b], -1.70[c]	-	-
c	9.3327[a], 9.3349 [a*], 9.5701[b], 9.1604[c]	9.4018	9.558
d	-0.73[a], -0.71 [a,*], +1.80[b], -2.57[c]	-	-
z_{Ba}	0.1627[a], 0.1567 [a,*], 0.1603[b], 0.1622[c]	0.1598	-
z_{Se}	0.6803[a], 0.6819 [a,*], 0.6802[b], 0.6812[c]	0.6798	-
V_0	173,9852[a], 173.2290 [a,*], 185.4720[b], 167.1145[c]	177,4886	184.2027
B_0	55.0176[a], 45.7175[b], 63.1989[c]	-	-
E_{Coh}	-7.5893		
ΔH	-5.2899		
BaFAgTe			
	Present	Expt.	Other
a	4.4987[a], 4.5013[a,*], 4.5809[b], 4.4583[c]		
d	-		
c	9.5035[a], 9.4515 [a,*], 9.7991[b], 9.2773[c]		
d	-		
z_{Ba}	0.1497[a], 0.1452[a,*], 0.1474[b], 0.1468[c]		
z_{Te}	0.6849[a], 0.6859 [a,*], 0.6843[b], 0.6885[c]		
V_0	192,3347[a], 191.5035[a,*], 205.6306[b], 184.3997[c]		
B_0	46.9707[a], 40.5974[b], 53.0310[c]		
E_{Coh}	-7.4296		
ΔH	-5.2115		

[a] Present work using the GGA08, [b] Present work using the GGA96, [c] Present work using the LDA.
[a*] Present work using the GGA08 including the spin-orbit coupling (SOC).

To confirm the chemical and structural stabilities of the studied crystals, we calculated their cohesive energies (E_{Coh}) and formation enthalpies (ΔH). The cohesive energy, the energy that is required for the crystal to decompose into free atoms, is given by the following relationship:

$$E_{Coh} = \frac{1}{N_{Ba} + N_F + N_{Ag} + N_{Ch}} \left[E_{tot}^{BaFAgCh} - \left(N_{Ba} E_{tot}^{Ba(atom)} + N_F E_{tot}^{F(atom)} + N_{Ag} E_{tot}^{Ag(atom)} + N_{Ch} E_{tot}^{Ch(atom)} \right) \right] \quad \text{(IV. 2)}$$

The formation enthalpies (ΔH) is given by the following expression:

$$\Delta H = \frac{1}{N_{Ba} + N_F + N_{Ag} + N_{Ch}} \left[E_{tot}^{BaFAgCh} - \left(N_{Ba} E_{tot}^{Ba(solid)} + N_F E_{tot}^{F(gaz)} + N_{Ag} E_{tot}^{Ag(solid)} + N_{Ch} E_{tot}^{Ch(solid)} \right) \right] \quad \text{(IV. 3)}$$

Here N_{Ba}, N_F, N_{Ag} and N_{Ch} are the numbers of Ba, F, Na and *Ch* atoms, respectively, in the unit-cell of the BaFAg*Ch* compound; $E_{tot}^{Ba(atom)}$, $E_{tot}^{F(atom)}$, $E_{tot}^{Ag(solid)}$ *and* $E_{tot}^{Ch(atom)}$ are the total energies of the Ba, F, Ag and *Ch* isolated atoms, respectively; $E_{tot}^{Ba(solid)}$, $E_{tot}^{Ag(solid)}$ and $E_{tot}^{Ch(solid)}$ are the total energies per atom of the solid state of the Ba, Ag and *Ch* pure elements, respectively; $E_{tot}^{F(gaz)}$ is the total energy per atom of the gas state of the pure element F. The obtained values for the cohesive energies and formation enthalpies are listed in Tab. IV.1. The obtained results show that:

- Calculated cohesive energies and formation enthalpies are negative, confirming the chemical and structural stabilities of the studied compounds, including the hypothetical one; BaFAgTe.
- Both cohesive energy and formation enthalpy decrease when going from BaFAgS to BaFAgSe to BaFAgTe.

Variations of the bond lengths (*d*) and angles between atoms (See Fig. IV.2) when the chalcogenide element (*Ch*) is substituted in the BaFAg*Ch* compounds in the following sequence: $S \rightarrow Se \rightarrow Te$ are given in Tab. IV.2. Crystal structure drawings were produced using the program VESTA [12]. From Tab. IV.2 data, one can note:

- Variations of the α_2 and α_4 angles in the [BaF] block are more considerable than in the [Ag*Ch*] block; the α_2 (Ba-F-Ba) angle increases while α_4 (Ba-F-Ba) angle decreases, indicating that the block [BaF] will be more flat when going from BaFAgS to BaFAgSe to BaFAgTe. This result is consistent with the diminution of the *c*/*a* ratio in the same sequence.
- The bond length between Ba and F; $d_{\text{Ba-F}}$, increases slowly, by about 0.019 Å in average, when going from BaFAgS to BaFAgSe to BaFAgTe.
- The bond length between Ag and *Ch*; $d_{\text{Ag-}Ch}$, increases, by about 0.1025 Å in average, when the *Ch* atom is substituted in the sequence: $\text{S} \rightarrow \text{Se} \rightarrow \text{Te}$.
- Calculated bond lengths and angles between the constituent atoms of the BaFAg*Ch* (*Ch* = S, Se, Te) compounds are in good agreement with the available experimental findings [6].

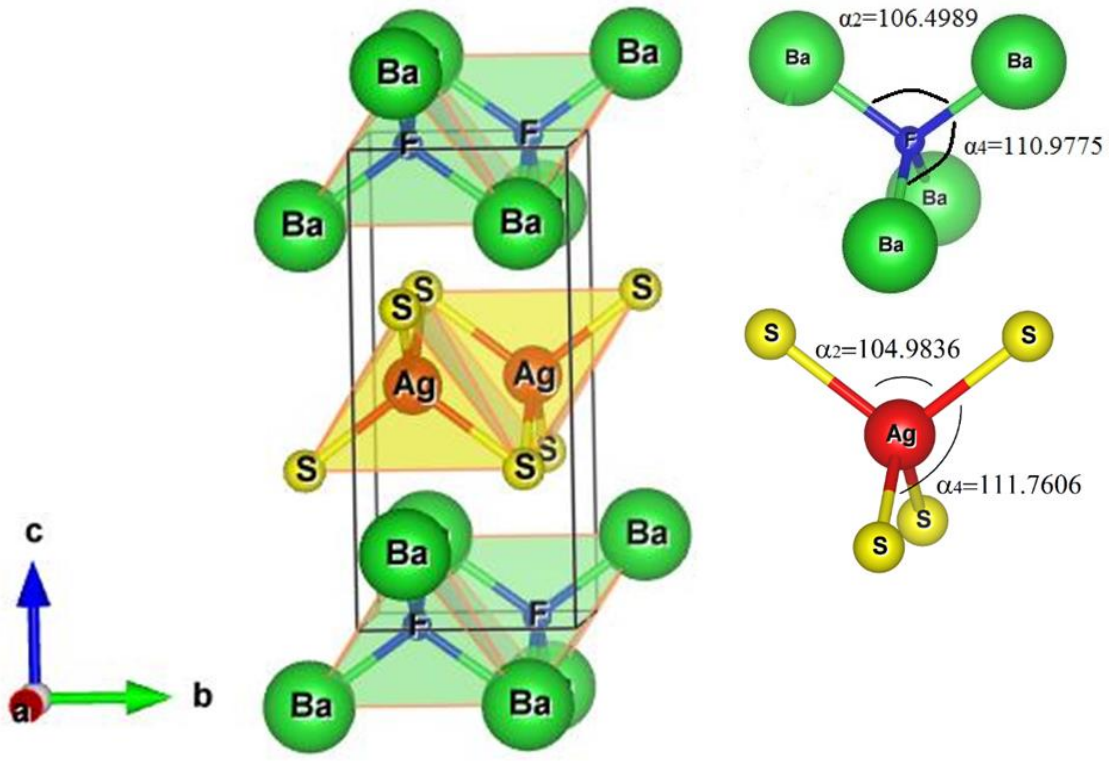

Figure IV.2: Bond lengths and angles between the constituent atoms of the BaFAgS compound.

Table IV.2: Bond lengths (*d*, in A˚) and angles (α , in degree) for the BaFAg*Ch* (*Ch* = S, Se, Te) compounds.

	BaFAgS		**BaFAgSe**		**BaFAgTe**	
	Pres.	Exp. [6]	Pres.	Exp. [6]	Pres.	Exp. [6]
$d_{\text{Ba-F}}$	2.623	2.626	2.639	2.642	2.661	2.668
$d_{\text{Ba-}Ch}$	3.302	3.337	3.387	3.422	3.548	3.586
$d_{\text{Ag-}Ch}$	2.649	2.679	2.737	2.753	2.854	2.879
$\boldsymbol{\alpha}_2$ (Ba-F-Ba)	106.5	107.69	109.77	110.65	115.38	116.15
$\boldsymbol{\alpha}_4$ (Ba-F-Ba)	110.98	110.37	109.32	108.88	106.60	106.24
$\boldsymbol{\alpha}_2$ (*Ch*-Ag-*Ch*)	104.98	104.65	104.14	104.22	104.01	103.69
$\boldsymbol{\alpha}_4$ (*Ch*-Ag-*Ch*)	111.76	111.93	112.20	112.16	112.27	112.43

IV.2. Elastic properties of the BaFAg*Ch* (*Ch* = S, Se and Te) compounds

IV.2.1. Preamble

All solid objects are deformable under the applied external forces; there is an internal force, which resists to this deformation. The resistance against deformation in crystals is greater than that in amorphous materials. The external forces can change size and shape of a solid. This change is called deformation. Elasticity is the physical property of a material that returns matter to its original form and dimensions after the removal of stresses (external forces) that affect the material and lead to its deformation (distortion). This means that the stress-strain response is reversible and consequently the material has a preferred natural state. In general, the relation between stress and strain is nonlinear, and the corresponding theory is called the nonlinear theory of elasticity. However, if the relationship between stress and strain is linear, the material is said to be linearly elastic, and the corresponding theory is called the linear theory of elasticity [13]. Fig. IV.3 shows the behaviour of a solid material under an applied force F that stretch the solid elastically from L_0 to $L_0 + \delta L$. The force is divided among chains of atoms that make the solid. Each chain carries a force δF_N [14].

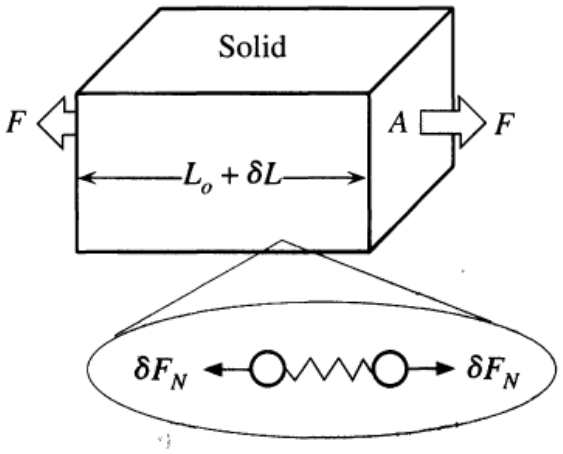

Figure IV.3: The behaviour of a solid material under an applied force *F* [14].

Hooke's law of elasticity [15, 16], established by the English scientist Robert Hooke in 1660, states that: «Forces can cause objects to deform (i.e., change their shape). The way in which an object is deformed depends on its dimensions, the nature of the

material of which it is made, the size of the force and direction of the force». That means, for relatively small deformations of an object, the displacement or size of the deformation is directly proportional to the deforming force or load. Under these conditions, the object returns to its original shape and size upon removal of the load. Elastic behaviour of solids according to Hooke's law can be explained by the fact that small displacements of their constituent molecules, atoms, or ions from normal positions is also proportional to the force *F* that causes the displacement *X*,

$$F = kX \qquad \text{(IV. 4)}$$

Here k is a constant known as the rate or spring constant. However, the strain state in a solid medium around some point, cannot be described by a single vector. The same parcel of material, no matter how small, can be compressed, stretched, and sheared at the same time, along different directions. The relevant state of the medium around a point must be represented by two-second-order tensors, the strain tensor ε (instead of the displacement *X*) and the stress tensor σ (replacing the restoring force *F*). The linear law for the relation between stress and strain is called the generalized Hooke's law. The general form of writing Hooke's law is as follows:

$$\sigma = C\varepsilon \qquad \text{(IV. 5)}$$

$$\sigma_{ij} = \sum_{kl}^{1,3} C_{ijkl}\varepsilon_{kl} \qquad \text{(IV. 6)}$$

C is a tensor of rank four, which is called the stiffness tensor or elasticity tensor; the quantities C_{ijkl} are called the elastic coefficients of a body. The stiffness tensor C is represented by a matrix of $3^4 = 81$ real numbers C_{ijkl}, however, this number is reduced in systems that exhibit symmetry. According to the Voigt notation, the single-crystal elastic constants are noted C_{ij} and the relation (IV.6) can be given as follows:

$$\sigma_i = \sum_{i}^{6} C_{ij}\varepsilon_j \qquad \text{(IV. 7)}$$

Here $\varepsilon_j (j = 1,2,..,6)$, $\sigma_i (i = 1,2,..,6)$ and C_{ij} are strain, stress, and single-crystal elastic (stiffness) constants, respectively.

Theoretically, there are two ways for calculating the possible 21 elastic constants C_{ij}:

(i) 1. Applying a set of strain patterns tensors ($\varepsilon_j (j = 1,2,..,6),$) that allows the calculations of the elastic constants of interest, 2. Calculating the corresponding stress tensors ($\sigma_i (i = 1,2,..,6)$) via first-principles calculations and then 3. Once the stress is calculated for each strain, the single-crystal elastic constants are retrieved by linear least-squares fitting.

(ii) 1. Applying a set of strain patterns, 2. Calculating the corresponding elastic potential energy (E) via first-principles calculations and then calculating the possible 21 elastic constants C_{ij} using the following expression:

$$C_{ij} = \frac{1}{V} \frac{\partial^2 E}{\partial \varepsilon_i \partial \varepsilon_j} \qquad \text{(IV. 8)}$$

Here V is the volume of the unit cell. In the present work, we used the second method (Total energy-stain) to calculate the elastic constants C_{ij}.

In addition to the single-crystal elastic constants, there are some other elastic moduli that are used usually to characterize the mechanical properties of solid, such as:

- Young's modulus (E), which describes the tensile elasticity or the tendency of an object to deform along an axis when opposing applied forces along that axis, is defined as the ratio of tensile stress to tensile strain:

$$E = \frac{\sigma}{\varepsilon} \qquad \text{(IV. 9)}$$

where σ is the uniaxial stress, or uniaxial force per unit surface, in Pascal, and ε is the strain; change in length divided by original length (dimensionless). In other words, E describes the material's strain response to uniaxial stress in the direction of this stress.

- The bulk modulus (B), which describes volumetric elasticity, or the tendency of an object to deform in all directions when uniformly loaded in all directions, is defined as volumetric stress over volumetric strain, and is the inverse of compressibility:

$$B = -V \frac{dV}{dP} \qquad \text{(IV. 10)}$$

where P is pressure, V is volume, and $\frac{dV}{dP}$ denotes the derivative of volume with respect to pressure. The bulk modulus is an extension of Young's modulus to three dimensions. In other words, B describes the material's response to (uniform) hydrostatic pressure.

- The shear modulus (G), which describes an object's tendency to shear (the deformation of shape at constant volume) when acted upon by opposing forces, is defined as shear stress over shear strain. In other words, G describes the material's response to shear stress.
- Poison's ratio (ν) is the ratio of transverse contraction strain to longitudinal extension strain in the direction of stretching force. Tensile deformation is considered positive and compressive deformation is considered negative. The definition of Poisson's ratio contains a minus sign so that normal materials have a positive ratio,

$$\nu = -\frac{\varepsilon_{transverse}}{\varepsilon_{longitudinal}} \qquad \text{(IV. 11)}$$

In other words, ν describes the response in the directions orthogonal to this uniaxial stress.

IV.2.2. Calculation method

To calculate the single-crystal elastic constants C_{ij} using the "Energy-strain" method, we proceeded as flows:

1. Optimize the crystalline structure with full relaxation.

2. Select the elastic constants C_{ij} of interest; choose the appropriate strain tensors that allow the calculation of the elastic constants of interest.

3. Deform the crystal according the chosen strain tensors.

4. Re-optimize the crystalline structure for each deformed crystalline structure.

5. Repeat step 3. for a set of similar deformations with different amplitudes, creating a Total Energy vs. ε curve (a parabola).

6. Fit the curve to extract the second derivative of the total energy and calculate elastic constants

More details for the procedure to calculate the elastic constants for some crystalline systems can be found in Ref. [17]

Polycrystalline solid is composed of randomly oriented crystalline regions; called crystallites; crystallite is a domain of solid-state matter that has the same structure as a single crystal. Theoretically, the isotropic polycrystalline elastic moduli *B* and *G* can be calculated from the single crystal elastic constants C_{ij} through the Voigt-Reuss approximations [18, 19]. The stress and strain are generally unknown in the composite and are expected to be no uniform. To calculate the *B* and *G* moduli for a polycrystalline solid, Voigt [20] assumed that the strain is everywhere uniform (See Fig. IV.4.a), so his approximation yields the upper bound (upper limit) for the *B* and *G* moduli, while Reuss [21] assumed that the stress is everywhere uniform (See Fig. IV.4.b), so his approximation yields the lower bound (lower limit). Hill [22, 23] proposed that the arithmetic average of the upper and lower bounds of the modulus yields the effective value.

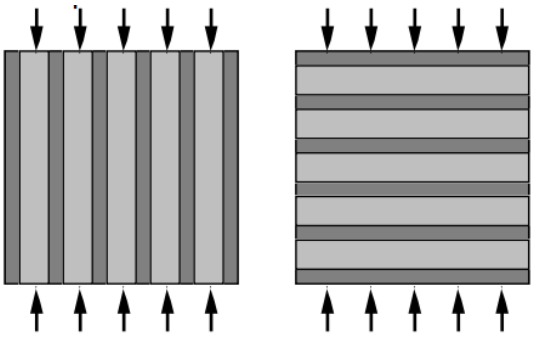

(a) (b)

Figure IV.4: Geometric interpretations of the stress and strain on a polycristallin, (a): Voigt iso-strain model, (b): Reuss iso-stress model.

The Voigt-Reuss-Hill (VRH) average provides a simple way to estimate the elastic moduli of a textured polycrystalline in terms of its crystallographic texture and the elastic constants of the constituting crystallites. According to the VRH approximations, Voigt *B* and *G* moduli (B_V and G_V), Reuss *B* and *G* moduli (B_R and G_R) and Hill *B* and *G* moduli (B_H and G_H) can be calculated from the single-crystal elastic constants using the following relationships [24, 25]:

$$\begin{cases} B_V = \frac{1}{9}\{2(C_{11}+C_{12})+4C_{13}+C_{33}\}, \\ G_V = \frac{1}{30}(M+3C_{11}-3C_{12}+12C_{44}+6C_{66}), \\ M = C_{11}+C_{12}+2C_{33}-4C_{13} \end{cases} \quad (IV.12)$$

$$\begin{cases} B_R = \frac{C^2}{M} \\ G_R = \frac{15}{\left\{\left[\frac{2(2(C_{11}+C_{12})+C_{33}+4C_{13})}{C^2}\right]+\frac{6}{(C_{11}-C_{12})}+\frac{6}{C_{44}}+\frac{3}{C_{66}}\right\}} \\ C^2 = (C_{11}+C_{12})C_{33}-2C_{13}^2 \end{cases} \quad (IV.13)$$

$$B_H = \frac{B_R + B_V}{2} \quad (IV.14)$$

$$G_H = \frac{G_R + G_V}{2} \quad (IV.15)$$

Furthermore, the calculated isotropic bulk moduli *B* and shear moduli *G* allow calculation of the Young's modulus *E* and Poisson's ratio ν via the following relationships [24, 25]:

$$E = \frac{9BG}{3B+G} \quad (IV.16)$$

and

$$\nu = \frac{3B-2G}{2(3B+G)} \quad (IV.17)$$

IV.2.3. Single-crystal elastic constants

A Tetragonal crystal has six independent second-order elastic constants, namely C_{11}, C_{33}, C_{44}, C_{66}, C_{12} and C_{13}. After determination of the lattice parameters that match the experimental value, we calculated the elastic constants for the title compounds using the "Energy–strain" method [17]. As there are no available data for the elastic constants of the

considered compounds in the literature to be compared with our results, we have calculated the elastic constants C_{ij} using the "stress-strain" method as implemented in the CASTEP code [26]. It is worth to note here that the CASTEP code is an implementation of the pseudopotential plane wave (PP-PW) method. The calculated values of the six C_{ij} elastic constants, namely C_{11}, C_{33}, C_{44}, C_{66}, C_{12} and C_{13}, for the title materials are listed in Tab. IV.3.

Table IV.3: Calculated single-crystal elastic constants (C_{ij}, in GPa) for the BaFAgS, BaFAgSe and BaFAgTe compounds obtained using both the "energy-stain" and "stress-strain" methods.

	BaFAgS		BaFAgSe		BaFAgTe	
	FP-LAPW [a]	PP-PW [b]	FP-LAPW	PP-PW	FP-LAPW	PP-PW
C_{11}	101.3	111.4	102.6	105.7	86.2	90.9
C_{33}	76.8	77.6	61.7	66.6	32.9	51.7
C_{44}	33.7	34.8	32.2	33.2	21.2	21.1
C_{66}	21.4	23.3	20.9	22.1	18.9	19.9
C_{12}	27.6	34.7	28.4	33.4	23.7	31.1
C_{13}	43.2	47.2	41.7	45.3	28.6	39.4

[a] : As implemented in the Wien2k code , [b] : As implemented in CASTEP code.

The obtained results for the C_{ij} allow us to make the following conclusions:

- Calculated elastic constants C_{ij} (Tab. IV.3) satisfy the mechanical stability criteria for tetragonal crystals [25]:

$$\begin{cases} C_{11} > 0, C_{33} > 0, C_{44} > 0, C_{66} > 0, \\ (C_{11} - C_{12}) > 0, (C_{11} + C_{33} - 2C_{13}) > 0, \\ 2(C_{11} + C_{12}) + C_{33} + 4C_{13} > 0, \end{cases} \qquad \text{(IV. 18)}$$

  Therefore, the examined compounds (including the hypothetical BaFAgTe compound) are mechanically stable.

- In a tetragonal system, the C_{11} characterizes the resistant to the compressional stress along the a-axis (b-axis) while the C_{33} characterizes the resistant to the

compressional stress along the *c*-axis. From Tab. IV.3, one can note that C_{11} is larger than C_{33}, indicating that the studied crystals are more resistant to compressional strains along the *a*-axis than that along the *c*-axis. This is in agreement with the layered nature of the studied compounds, where the bonding between the [Ag*Ch*] and [BaF] layers, stacked along the *c*-axis, is weaker than the intralayer bonding in the ab-plane. The difference between the values of C_{11} and C_{33}, characterizing the elasticity in the stacking plane (C_{11}) and in the perpendicular [001] direction (C_{33}), demonstrates also that the studied materials are elastically anisotropic.

- C_{11} and C_{33} are larger than C_{44} and C_{66}, demonstrating that the resistance of the examined materials against shear deformations is much weaker compared to that against t compressional deformations.
- Elastic constants calculated using the FP-LAPW method are slightly smaller than those obtained using the PP-PW one.

IV.2.4. Polycrystalline elastic properties

Calculated elastic moduli for the polycrystalline phases of the studied compounds through the Voigt–Reuss–Hill approximations are listed in Tab. IV.4. From the Tab. IV.4 data, the following conclusions can be made:

- Values of both *B* (which measures the resistance to volume change) and *G* (which measures the resistance to shear deformation) decrease when going from BaFAgS to BaFAgSe to BaFAgTe, indicating that the hardness of these compounds decreases in the same consequence.
- For each considered compound, the calculated *B* value from the single-crystal elastic constants through the Voigt-Reuss-Hill average is in good agreement with the corresponding one derived from the *EOS* fit. Therefore, this good agreement between the *B* values obtained via two different computational methods constitutes another proof of the reliability and accuracy of the computed elastic moduli.
- The considered compounds have a relatively small Young's modulus (*E*) value. This confirms the rather low stiffness of the considered compounds. As E characterizes the resistance of solid against uniaxial deformation, so it is related to C_{11} and C_{33} elastic constants, which explains the decrease of *E* when going from BaFAgS to BaFAgSe to BaFAgTe in the same sequence as C_{11} and C_{33}. The shear

modulus *G* decreases also when going from BaFAgS to BaFAgSe to BaFAgTe in accordance with the decrease of the C_{44}.

- The calculated values of the Poisson's ratio are smaller than ~ 0.33, which is typical of ductile metallic materials.
- For all examined systems, the bulk modulus *B* is larger than the shear modulus *G*; this implies that the parameter limiting the mechanical stability of these materials is the shear modulus.

Table IV.4: Calculated polycrystalline elastic moduli: bulk modulus (*B*, in GPa), shear modulus (*G*, in GPa), Young's modulus (*E*, in GPa), Poisson's coefficient (ν, dimensionless), longitudinal, transversal and average sound velocities (v_l, v_t and v_m, respectively, in m/s), Debye temperature (θ_D, in K), Pugh's indicator (*B/G*), universal anisotropy index A^U and melting temperature (T_m, in K) for the BaFAg*Ch* (*Ch* = S, Se, Te) compounds

	BaFAgS	BaFAgSe	BaFAgTe
B	56.365^{V}, 56.203^{R}, 56.284^{H}	54.502^{V}, 52.571^{R}, 53.536^{H}	40.818^{V}, 32.341^{R}, 36.579^{H}
G	28.773^{V}, 26.584^{R}, 27.678^{H}	27.411^{V}, 24.069^{R}, 25.740^{H}	20.582^{V}, 16.528^{R}, 18.555^{H}
E	73.766^{V},68.890^{R}, 71.340^{H}	70.426^{V}, 62.646^{R}, 66.553^{H}	52.861^{V}, 42.366^{R}, 47.614^{H}
ν	0.281^{V}, 0.295^{R}, 0.288^{H}	0.284^{V}, 0.301^{R}, 0.292^{H}	0.284^{V}, 0.281^{R}, 0.283^{H}
v_l	3932.8	3662.3	3010.6
v_t	2143.3	1982.3	1656.1
v_m	2390.7	2212.2	1845.9
θ_D	260.4	235.9	190.4
B/G	2.03	2.08	1.97
A^U	0.41	0.73	1.49
T_m	772.977 ± 300	754.520 ± 300	662.177 ± 300

Debye temperature θ_D is an important parameter in solids; it is the temperature of a crystal's highest normal mode of vibration, and it correlates the elastic properties with the thermodynamic properties such as phonons. Debye temperature can be calculated from the elastic constants using the followng relationship [27]:

$$\theta_D = \frac{h}{k_B}\left[\frac{3n}{4\pi V_a}\right]^{\frac{1}{3}} v_m \qquad \text{(IV. 19)}$$

Here, h is Plank's constant, k_B is Boltzmann's constant, n is the number of atoms in the molecule, and V_a is the atomic volume. The average sound wave velocity v_m in a polycrystalline material integrated over several crystal directions is given by the following expression [27]:

$$v_m = \left[\frac{1}{3}\left(\frac{2}{v_s^3} + \frac{1}{v_l^3}\right)\right]^{-1/3} \qquad \text{(IV. 20)}$$

Here, v_s and v_l are respectively the shear and longitudinal sound velocities, which can be calculated from the bulk (B) and shear (G) moduli using the Navier's equations [28]:

$$v_s = \left(\frac{G}{\rho}\right)^{1/2} \qquad \text{(IV. 21)}$$

$$v_l = \left(\frac{3B + 4G}{3\rho}\right)^{1/2} \qquad \text{(IV. 22)}$$

Here, ρ is the mass density. Calculated θ_D, v_m, v_s and v_l are listed in Tab. IV.4. From Tab. IV.4 data one can note:

- The longitudinal wave velocity is larger than the transverse one and both the longitudinal and transverse waves decrease when going from BaAgSF to BaAgSeF to BaAgTeF. This can be explained by the decrease of the single-crystal elastic constants in the same sequence; the elastic wave velocities are proportional to the square root of the corresponding elastic constants.
- The T_D value decreases when going from BaFAgS to BaFAgSe to BaFAgTe, which is in accordance with the decrease of the stiffness in the same sequence. This might indicate a decrease of the thermal conductivity when going from BaFAgS to BaFAgSe to BaFAgTe.

Brittle/ductile behavior is one of important mechanical characteristics of materials, which is closely related to their reversible compressive deformation and fracture ability. One of the most widely used malleability measures of materials is the Pugh's criterion (*B/G* ratio) [29]. The empirical Pugh's indicator stipulates that if *B/G* >1.75, the material behaves in a ductile manner, otherwise, it demonstrates brittleness. The *B/G* value is obviously greater than the critical value 1.75 for all studied compounds, suggesting that these compounds are ductile materials. A ductile material is resistant to thermal shocks. The bulk modulus *B* is two times the shear modulus *G*, indicating that the shear deformation is easier to occur in the considered compounds.

Most materials are elastically anisotropic; their stiffness depends on the direction in which the stress is applied. It is established that the anisotropy of the coefficient of thermal expansion and elastic anisotropy can cause microcracks in materials [30]. It is also accepted that the elastic anisotropy can significantly influence the nanoscale precursor textures in alloys [31]. Therefore, it becomes necessary and important to estimate the elastic anisotropy extent in solids. Some different indexes have been established to estimate the elastic anisotropy degree in crystals. To evaluate the elastic anisotropy degree in the considered BaFAg*Ch* compounds, two different approaches were employed.

(i) Ranganathan and Ostoja-Starzewski [32] proposed a universal index A^U, defined as follows $A^U = 5G_V/G_R + B_V/B_R - 6$, to quantify the elastic anisotropy extent in a crystal. An isotropic crystal is characterized by $A^U = 0$. Any deviation of A^U from zero indicates the presence of an elastic anisotropy and the degree of this deviation gives extent of this elastic anisotropy. The computed values of the A^U (Tab. IV.4) demonstrate that the considered compounds exhibit a noticeable elastic anisotropy and its degree increases when going from BaFAgS to BaFAgSe to BaFAgTe.

(ii) A more used tool to visualize the elastic anisotropy extent of crystals is by plotting three-dimensional (3-D) representations of the directional dependence of their elastic moduli. 3-D representations of the directional dependence of the Young's modulus *E* and compressibility β ($\beta = 1/\beta$) were used in the present work. For a tetragonal crystal, the crystallographic direction dependence of the Young's modulus *E* and compressibility β are expressed by the following relations [33]:

$$\frac{1}{E} = (l_1^4 + l_2^4)S_{11} + l_3^4 s_{33} + l_1^2 l_2^2(2s_{12} + s_{66}) + l_3^2(1 - l_3^2)(2s_{13} + s_{44}) \qquad (\text{IV. } 23)$$

$$\beta = (s_{11} + s_{12} + s_{13}) + l_3^2(s_{11} + s_{12} - s_{13} - s_{33}) \qquad (IV.24)$$

In Eqs. 23 and 24, S_{ij}s are the elastic compliance constants and l_1, l_2 and l_3 are the directional cosines with respect to the *x*-, *y*- and *z*-axes, respectively. In a closed 3D-representation, the distance from the origin of the coordination system to the surface gives the value of the represented modulus in a given direction. Thus, for an isotropic material, the representative closed surface should exhibit a spherical shape. Any deviation of the representative closed surface from the spherical shape announces the presence of an elastic anisotropy. From Figs. IV.5 and IV.6, one can appreciate that the shape of the 3D-closed surfaces for E and β are considerably different from the spherical shape, suggesting a strong elastic anisotropy of the examined materials. The cross-sections of the 3D-closed surface of the E modulus in the *xy* and *xz* planes are also represented in Fig. IV.6 in order to more visualizing the elastic anisotropy. These 2D-representations clearly show the pronounced elastic anisotropy of the considered systems. The highest value of the Young's modulus (E_{max}) is realized for applied external stress along the [100] and [010] crystallographic directions and the lowest value of the Young's modulus E_{min} is along the [001] direction, which is consistent with the fact that the *a*-axis is more resistant against compression than the *c*-axis. The E_{min} is approximately 57% E_{max} in BaFAgS, 49% E_{max} in BaFAgSe and 43% E_{max} in BaFAgTe, which indicates that the elastic anisotropy degree increases when going from BaFAgS to BaFAgSe to BaFAgTe.

Another important parameter, which can be estimated from the elastic constants C_{ij}, is the melting point T_m, which is the temperature at which a substance changes from solid to liquid state. T_m can be calculated through the following the empirical formula [34]:

$$T_m = 354 + 4.5\frac{2C_{11} + C_{33}}{3} \qquad (IV.25)$$

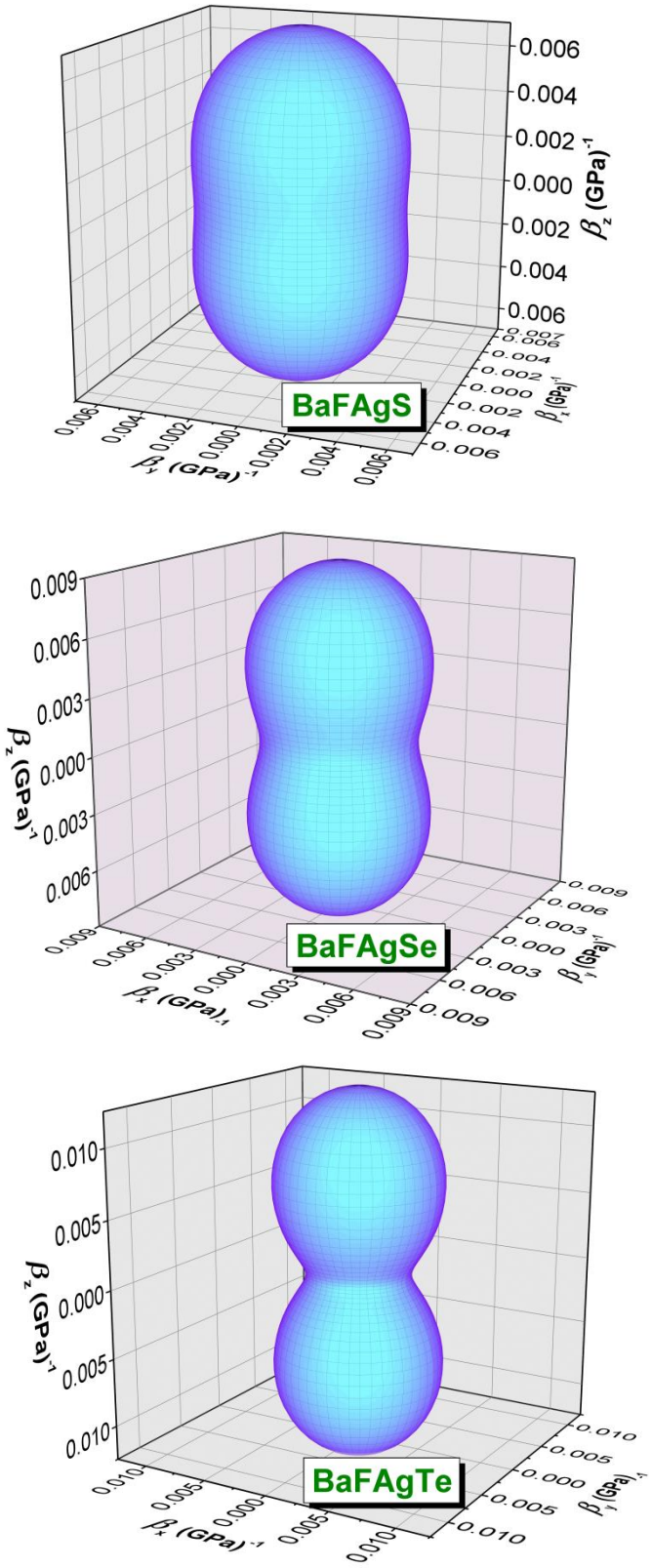

Figure IV.5: The compressibility (β) 3D-representation for the BaFAgS, BaFAgSe and BaFAgTe compounds.

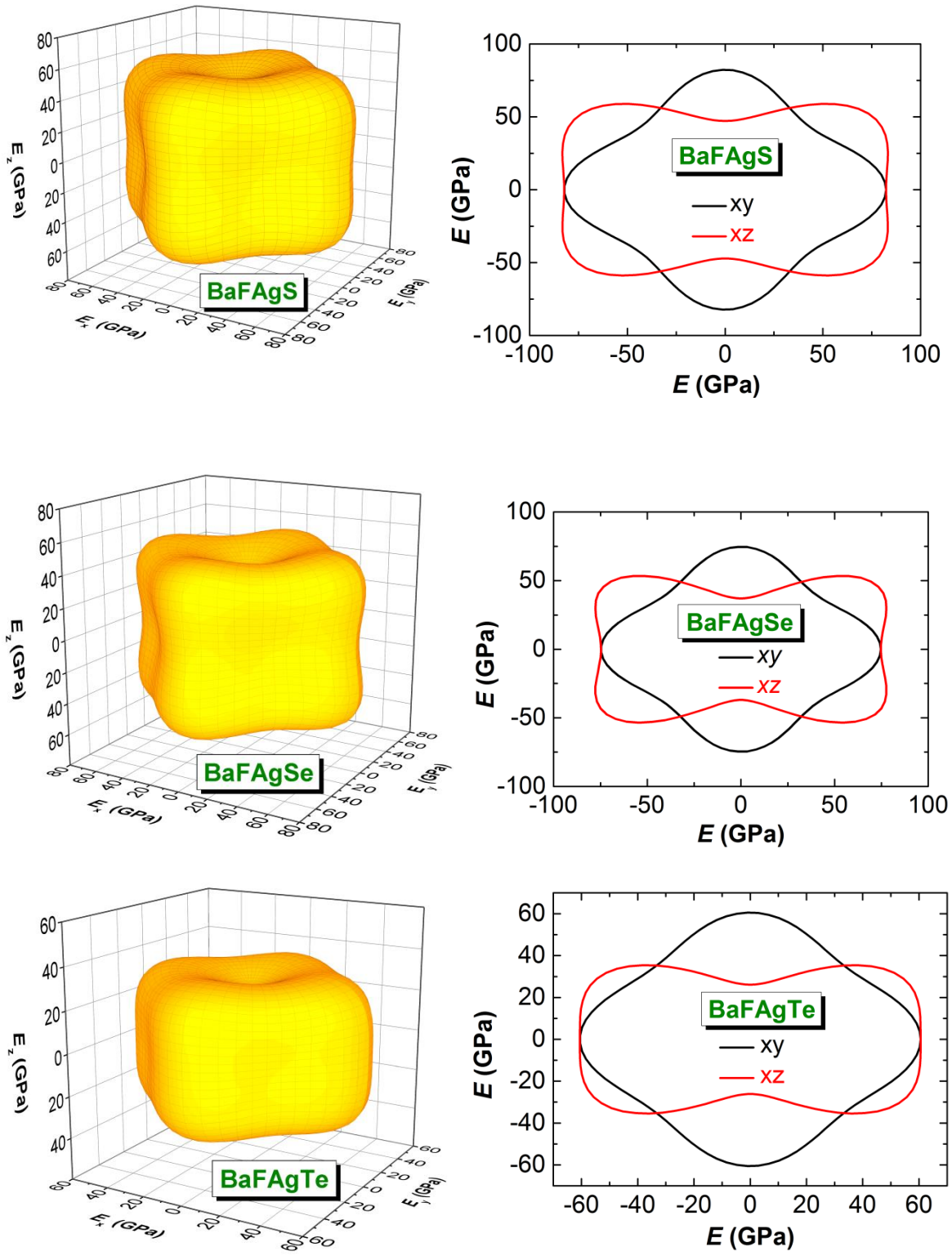

Figure IV.6: The Young's modulus 3D-representations and their cross-section in the *xy* and *xz* planes for the BaFAgS, BaFAgSe and BaFAgTe compounds.

IV.3. Electronic properties of the BaFAg*Ch* (*Ch*=S, Se and Te) compounds

IV.3.1. Preamble

The electrons of a single and isolated atom occupy atomic orbitals where each one has a discrete energy level. When two or more atoms join together to form into a molecule, their atomic orbitals overlap. The Pauli exclusion principle dictates that no two electrons can have the same quantum numbers in a molecule. So, if two identical atoms combine to form a diatomic molecule, each atomic orbital splits into two molecular orbitals of different energy, allowing the electrons in the former atomic orbitals to occupy the new orbital structure without any having the same energy. Similarly, if a large number N of identical atoms come together to form a solid, the atoms' orbitals overlap. Since the Pauli exclusion principle dictates that no two electrons in the solid will have the same quantum numbers, each atomic orbital splits into *N* discrete molecular orbitals, each one with a different energy. Since the number of atoms in a macroscopic piece of solid is a very large number (N~10^{22}), the number of orbitals is very large and thus they are very closely spaced in energy (of the order of 10^{-22} eV). The energy of adjacent levels is so close together that they can be considered as a continuum, an energy band [35, 36]. This formation of bands is mostly a feature of the outermost electrons (valence electrons) in the atom, which are the ones involved in chemical bonding and electrical conductivity. The inner electron orbitals do not overlap to a significant degree, so their bands are very narrow.

The band structure plays critical roles in assisting scientists to interpret the structural stability and correlate crystal structures with physical properties such as electronic conductivity, optical and magnetic properties. The electronic properties of a crystalline material are generally determined by its electronic band structure. Valence band is the highest energy band, which is completely occupied by electrons. The next higher lying energy band is the conduction band. The electrical conductivity of a material is determined by the distribution of electrons in the conduction and valence bands. In a metal, the conduction band is partially occupied. These high-energy electrons can be easily scattered into unoccupied states on application of an external electric field resulting in the good electrical conductivity of metals. In an insulator, the highest energy electron is in the valence band, which is completely filled. As a result, there is no scope for the intra-band scattering of electrons on the application of an external electric field and insulators do not

conduct electricity. The conduction and valence bands in an insulator are separated by an energy gap, known as the band gap energy. The situation for a semiconductor is very similar to that in an insulator. However, the band gap in case of a semiconductor is much less than that in insulators (< 6 eV). As a result, electrons can be excited from the valence band to the conduction band by absorption of light in the visible and near infra-red region of the electromagnetic spectrum, which results in many interesting properties of semiconductors [37]. Electronic transitions between the valence and conduction bands shown in crystal start at the absorption edge, which corresponds to the minimum energy difference between the lowest minimum of the conduction and the highest maximum of the valence band. If these extremes lie at the same point in the *K*-space, the transitions are called direct and if this is not the case, the transitions are possible only when phonon–assisted and are called indirect transitions [38].

IV.3.2. Scalar relativistic electronic band structure

Firstly, scalar relativistic (SR; without including spin-orbit coupling) electronic energy band dispersions at the optimized structural parameters (Tab. IV.1) of the BaFAgS, BaFAgSe and BaFAgTe systems were calculated using the full potential-linearized augmented plane wave (FP-LAPW) method within both the GGA08 and TB-mBJ functionals along the high symmetry lines of the BZ (See Fig. IV.7) and depicted in Fig. IV.8.

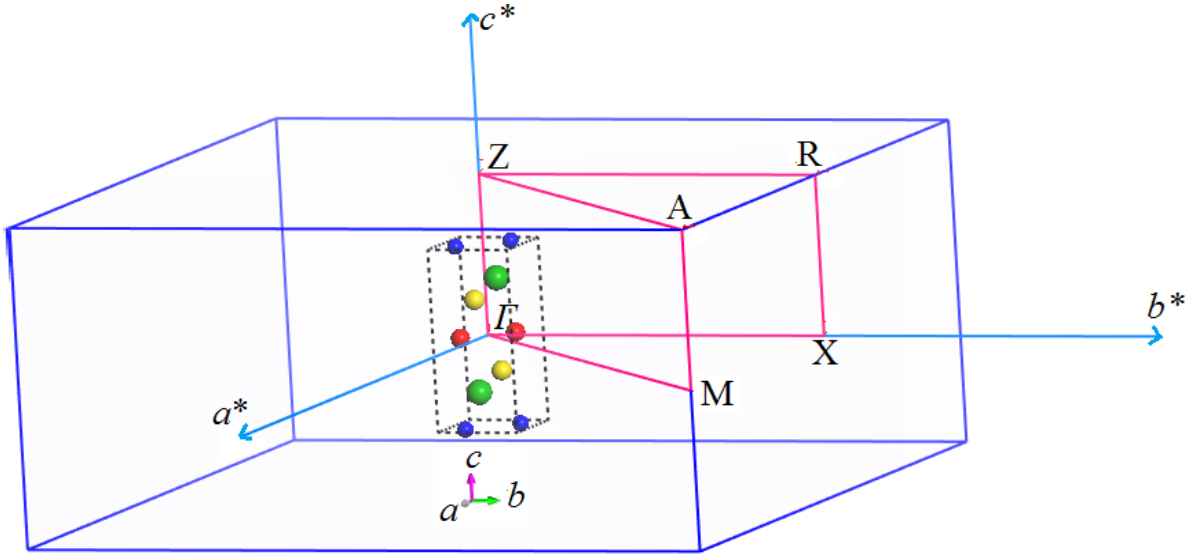

Figure IV.7: High-symmetry points and lines in the Brillouin zone, A (0.5, 0.5, 0.5), M (0.5, 0.5, 0), Γ (0, 0, 0), Z (0,0,0.5), R (0, 0.5, 0.5) and X (0, 0.5, 0).

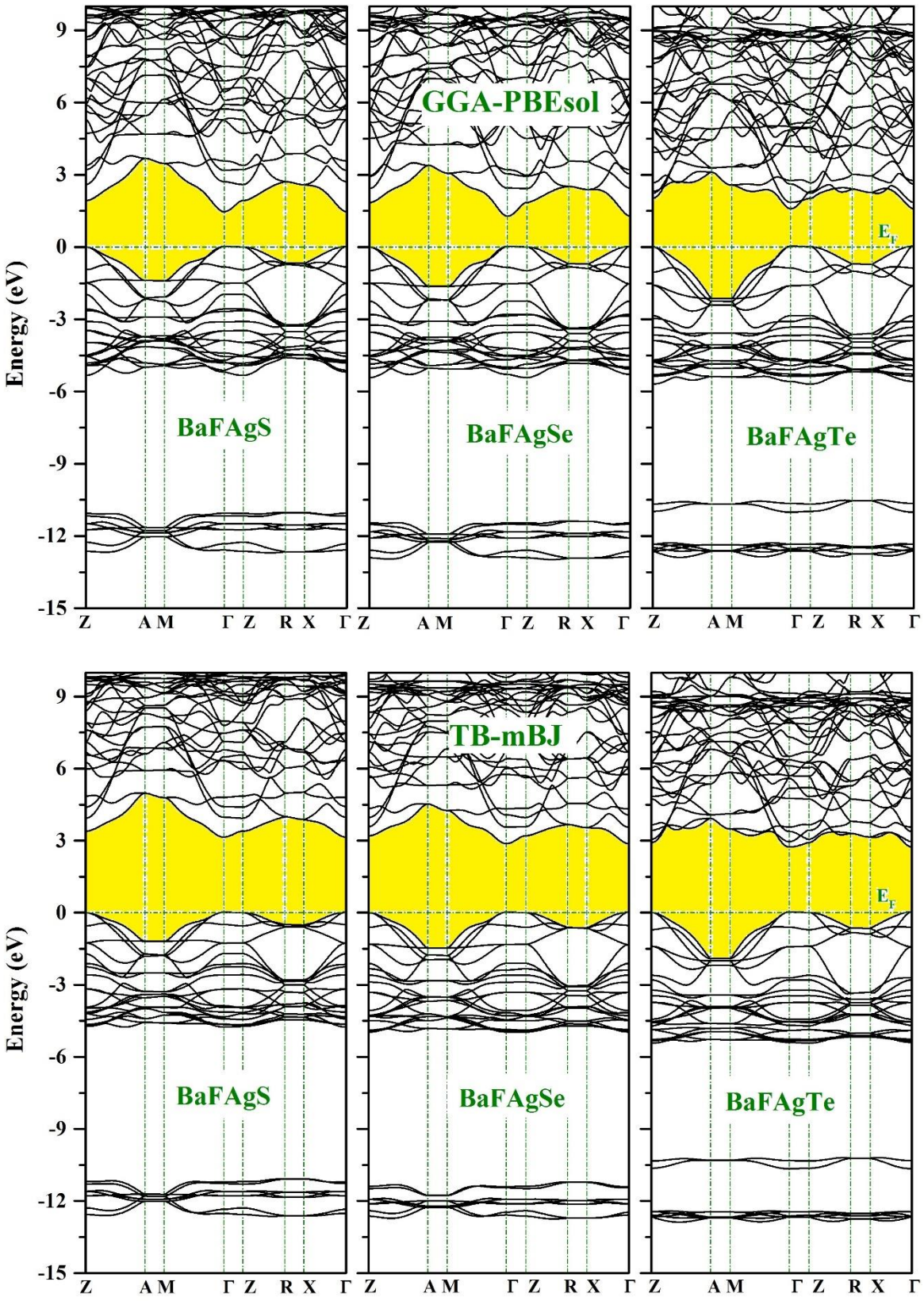

Figure IV.8: Scalar relativistic (without including the spin-orbit coupling) GGA-PBEsol and TB-mBJ band structures of the BaFAgS, BaFAgSe and BaFAgTe compounds. The energy zero level corresponds to the Fermi level.

Our obtained results reveal that:

- The barium silver fluoride chalcogenides BaFAg*Ch* (*Ch* = S, Se, Te) compounds have similar electronic structure.
- The valence band maximum (VBM) and the conduction band minimum (CBM) are both located at the Γ point, therefore these compounds are direct band gap $(\Gamma - \Gamma)$ semiconductors).
- The energy band gap decreases when moving from BaFAgS to BaFAgSe to BaFAgTe, due to the decrease of the ionization potential when moving in the same sequence.
- For all investigated compounds, the overall profile of the GGA08 band structure is almost similar to that of the TB-mBJ one, but there is an important quantitative difference between the TB-mBJ band gap and the GGA08; the obtained TB-mBJ (GGA08) fundamental band gap is 3.13 eV (1.44 eV) for BaFAgS, 2.85 eV (1.25 eV) for BaFAgSe and 2.71 eV (1.55 eV) for BaFAgTe. The use of the TB-mBJ approximation leaded to the displacement of the conduction bands towards higher energies with respect to the top of the valence band, resulting in a considerable opening of the energy band gap. The TB-mBJ approach improves the band gap values of BaFAgS, BaFAgSe and BaFAgTe by approximately 117%, 128%, and 75%, respectively, compared to the corresponding GGA08 ones
- The substitution of the *Ch* atom in the BaFAgCh series in the sequence $S \rightarrow Se \rightarrow Te$ leads to a monotonously narrowing of the TB-mBJ fundamental band gap; it is not the case when using the GGA08.
- One can observe the presence of quasi flat valence bands along the $\Gamma \rightarrow Z$, $R \rightarrow X$ and $M \rightarrow A$ directions in the Brillouin zone, along with highly dispersive valence bands in the other high symmetry directions. This noticeable dependence of the dispersion of the valence bands on the crystallographic directions is an indicative of a highly bonding anisotropy in the layered BaFAg*Ch*. The bonds along the *c*-axis (interlayer bonding; the inter-adjacent-blocks bonding between the [BaF] and [Ag*Ch*] blocks) should differ considerably from those in the *ab*-plane (intralayer bonding; the chemical bonding inside the blocks [BaF] and [Ag*Ch*]). The simultaneous presence of large and small hole effective masses is a favourable indicator of thermoelectric performance; small hole effective mass is favourable for

good electrical conductivity, while large hole effective mass is favourable for large Seebeck coefficient for *p*-type compounds.

- The dispersion of the valence bands around the VBM is highly anisotropic; the upper valence bands show a large dispersion around the VBM along the $\Gamma \rightarrow M$ and $\Gamma \rightarrow X$ directions in the reciprocal space (*k*-space) and a pronounced flatness along the $\Gamma \rightarrow Z$ direction. The flatness of the upper valence bands along the $\Gamma \rightarrow Z$ direction in the *k*-space promotes a large hole effective mass along the *c*-axis direction, while their large dispersions along the $\Gamma \rightarrow M$ and $\Gamma \rightarrow X$ directions in the *k*-space reveal a small hole mass along the *a*-axis direction and in the *ab*-plane.
- The conduction bands exhibit a pronounced dispersion along all the considered directions in the BZ, suggesting that the *n*-type compounds should show less thermoelectric performance than the *p*-type ones.

IV.3.3. Full relativistic electronic band structure

Full relativistic (with including the spin-orbit coupling) calculation of the energy band dispersions along the lines of high symmetry of the BZ using TB-mBJ for the BaFAgS, BaFAgSe and BaFAgTe compounds are presented in Fig. IV.9. We limited the energy range between -6 eV and 6 eV for the clarity of the figure. Spin-orbit coupling effect on the BaFAg*Ch* (*Ch*=S, Se and Te) band structures can be summarized as follows:

- Inclusion of the spin-orbit coupling causes the splitting of bands at the valence band maximum. The SOC band splitting at the valence band maximum is 25 meV in BaFAgS, 108 meV in BaFAgSe and 269 meV in BaFAgTe. The SOC effect increases with the increase of chalcogenide atom weight.
- The TB-mBJ-SOC energy band gaps of BaFAgS, BaFAgSe and BaFAgTe are reduced by approximately 0.97%, 2.44% and 7.54%, respectively, compared to the corresponding ones obtained using the TB-mBJ-SR.
- The SOC effect increases when going from BaAgSF to BaAgSeF to BaAgTeF. This trend may be attributed to the increase of the atomic number of the chalcogen atoms; $Z^{(S)} = 16$, $Z^{(Se)} = 34$ and $Z(Te) = 52$.

- The substitution of the *Ch* atom in the BaFAg*Ch* series in the sequence $S \rightarrow Se \rightarrow Te$ leads to a monotonously narrowing of the TB-mBJ fundamental band gap. It is not the case when using the GGA08.
- There is no experimental data for the energy band gaps of the BaFAg*Ch* (*Ch* = S, Se, Te) compounds to be compared with our results. The TB-mBJ-SOC band gaps of the BaFAg*Ch* (*Ch* = S, Se, Te) compounds, which range from 2.52 eV to 3.10 eV, are comparable with the measured band gaps for some isostructural compounds SrFCuS (3.0 eV) [39], SrFCuSe (2.7 eV) [39], BaFCuS (3.2 eV) [40], BaFCuSe (3.0 eV) [40] and BaFCuTe (2.3 eV) [41].

To facilitate the comparison between band gap values obtained using different approachs, we visualize the calculated energy band gap values using the GGA08-SR, GGA08-SOC, TB-mBJ-SR and TB-mBJ-SOC in Fig. IV.10 and Tab. IV.5.

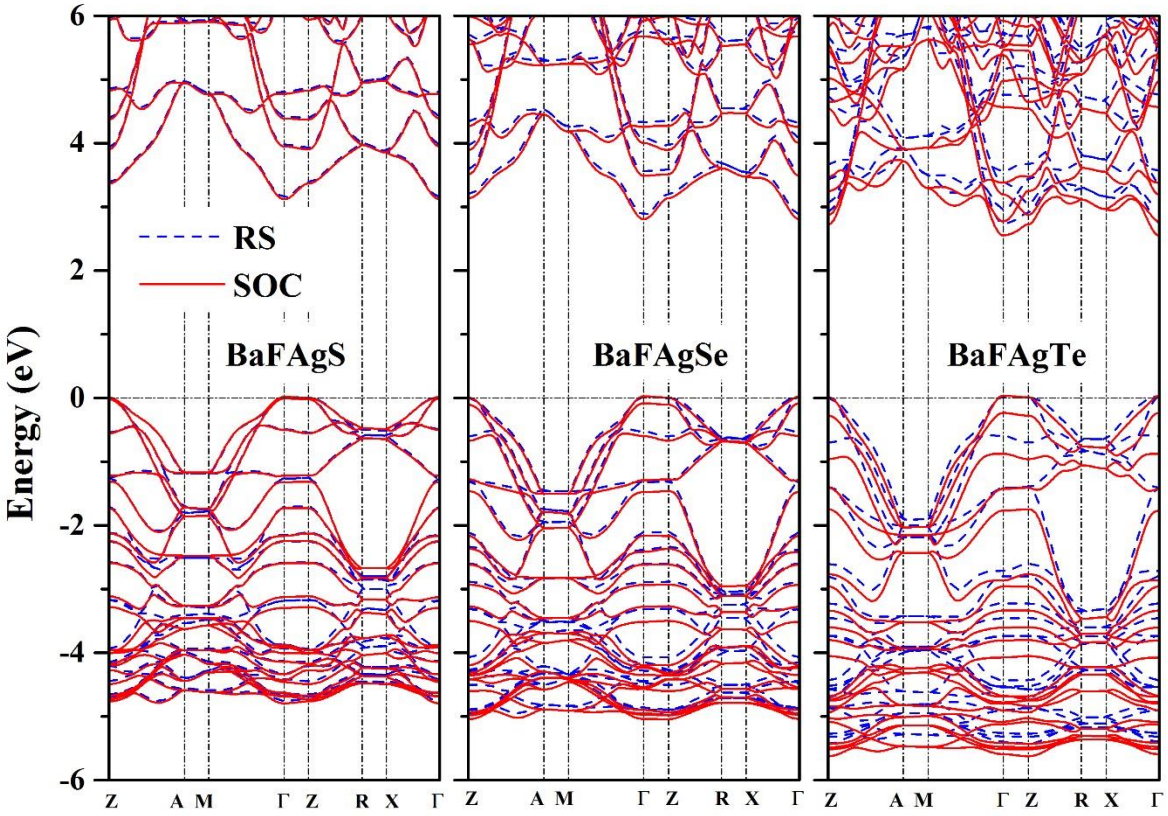

Figure IV.9: Calculated energy band structure for the BaFAg*Ch* (*Ch* = S, Se, Te) compounds using the TB-mBJ-SR (Red dashed lines) and the TB-mBJ-SOC (Black solid lines).

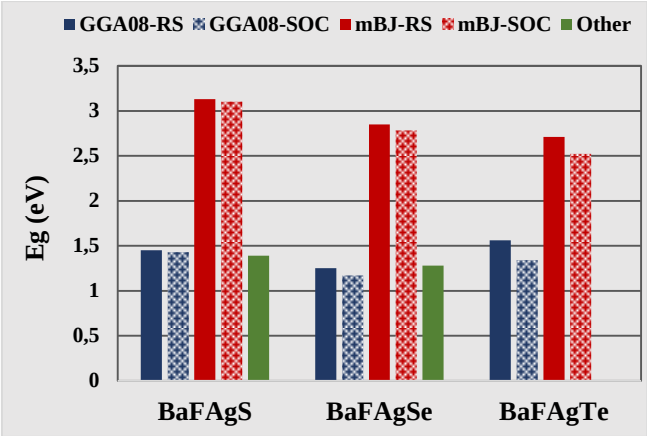

Figure IV.10: Comparison between the calculated fundamental band gap ($\Gamma-\Gamma$) values (Eg, in eV) obtained using different approaches: GGA08-SR, GGA08-SOC, mBJ-SR and mBJ-SOC for the BaFAg*Ch* (*Ch* = S, Se, Te) compounds.

Table IV.5: Calculated fundamental energy band gap (Γ- Γ) for the BaFAg*Ch* (*Ch*=S, Se, Te) compounds.

System	Present cal.				Previous cal.
	GGA08-SR	GGA+SOC	TB-mBJ+SR	TB-mBJ+SOC	
BaFAgS	1.44	1.43	3.13	3.10	1.387[11]
BaFAgSe	1.25	1.17	2.85	2,78	1.278[11]
BaFAgTe	1.55	1.34	2.71	2.52	

IV.3.4. Effective mass

Transport properties in semiconductors are principally controlled by the effective masses of charge-carriers [42]. Therefore, it becomes necessary to evaluate the electron and hole effective masses of the investigated compounds at the band edges. To calculate the hole effective mass m_h^* (electron effective mass m_e^*), we first fit the dispersion ($E(k)$) of the topmost valence band (lowest conduction band) around the VBM (around the CBM) to a quadratic polynomial in the reciprocal lattice vector k ($E(k)=Ak^2$), then the

effective mass m^* (in unit of m_0, where m_0 denotes the electron rest mass) can be estimated using the following expression:

$$\frac{1}{m^*} = \frac{m_0}{h^2}\left(\frac{\partial^2 E(k)}{\partial k^2}\right)\Bigg|_{k=k_0} \qquad \text{(IV. 26)}$$

The predicted effective masses of holes m_h^* at the valence band topmost and of electrons m_e^* at the conduction band bottom towards three different directions in the k space; $\Gamma \rightarrow Z$, $\Gamma \rightarrow X$ and $\Gamma \rightarrow M$, for the title compounds are listed in Tab. IV.6. To facilitate the comparison between the values of m_h^* and m_e^*, the obtained results are visualized in Fig. IV.11. It is apparent that both m_h^* and m_e^* exhibit noticeable dependences on the crystallographic directions. The values of m_h^* and m_e^* along the *c*-axis ($\Gamma \rightarrow Z$ direction in the *k*-space) are significantly larger than the corresponding ones in the *ab*-plane ($\Gamma \rightarrow M$ direction in the *k*-space) and along the *a*-axis ($\Gamma \rightarrow X$ direction in the *k*-space). According to these results, the mobility of charge-carries along the *a*-axis should be significantly larger than that along the *c*-axis, while the Seebeck coefficient will be larger along the *c*-axis. The obtained results reveal also that the hole effective mass is more dependent on the crystallographic direction than the electron one, demonstrating that the anisotropy of the effective mass and its related properties, such as Seebeck coefficient and electrical conductivity, should be more pronounced in the *p*-type compounds than in the *n*-type ones.

Table IV.6: Calculated hole and electron effective masses of the BaFAg*Ch* (*Ch* = S, Se, Te) compounds along different directions at the Γ-point in the BZ. The values are given in the unit of free electron mass (m_0).

Carrier type	m_h^*			m_e^*		
directions	Γ-X	Γ -Z	Γ-M	Γ-X	Γ -Z	Γ-M
BaFAgS	1.00	14.14	0.95	0.57	0.79	0.57
BaFAgSe	0.64	9.31	0.63	0.45	0.61	0.45
BaFAgTe	0.42	7.63	0.41	0.32	1.82	0.32

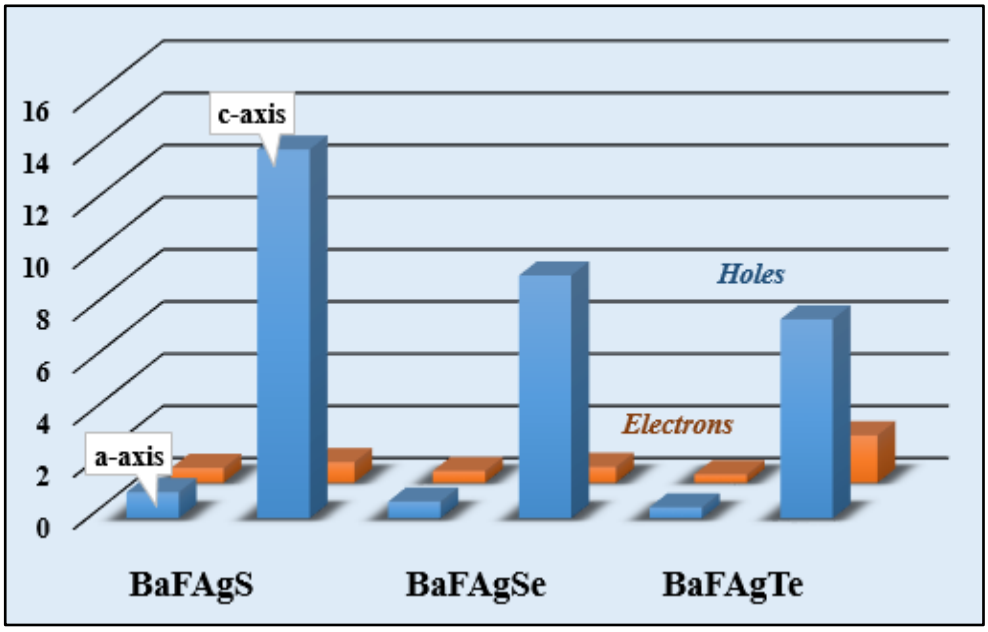

Figure IV.11: Representation of the calculated hole and electron effective masses of the BaFAg*Ch* (*Ch* = S, Se, Te) compounds along different directions at Γ-point in the BZ. The values are given in the unit of free electron mass (m_0).

IV.3.5. Total and partial density of states

Total (TDOS) and atomic-resolved *l*-projected (PDOS) densities of electronic states diagrams help to assign the electronic states of the electronic energy bands. Calculated TDOS PDOS with a dense *k*-mesh (50x50x23) for the BaFAgS, BaFAgSe and BaFAgTe compounds are shown in Fig. IV.12. From the calculated DOS diagrams, one can make the following conclusions:

- Three narrow band valence groups centered at about ~ -54, ~ -26 and ~ -24 eV, which are not shown in Fig. IV.12 for clarity of the diagrams, are mainly formed from the 4*p*-Ag, 5*s*-Ba and 2*s*-F states, respectively.
- The lower valence band group in Fig. IV.12 are made predominantly of the *5p*-Ba and *ns*-chalcogen states (n = 3 for S, n = 4 for Se and n = 5 for Te) with a small contribution from the *2p*-F states. In the BaFAgTe DOS diagram, this valence band group splits into two groups clearly separated by an energy gap because the *5s*-Te states are located somewhat higher in energy than the 5*p*-Ba ones.
- The upper part (from about -5 eV to the Fermi level) is mainly composed of 4*d*-Ag states hybridized with *np*-*Ch* states, and *2p*-F states (fine and high pick around -5eV). The hybridization of the *np*-*Ch* and *4d*-Ag states suggests that the *Ch*-Ag bonds inside the blocks [Ag*Ch*] are mainly covalent.
- The width of the near-Fermi level valence band group increases slightly when the chalcogen atom in the BaFAg*Ch* series is replaced in the following sequence: $\mathrm{S} \rightarrow \mathrm{Se} \rightarrow \mathrm{Te}$, indicating the decrease of hybridization between *np*-*Ch* and *4d*-Ag states inside the blocks [Ag*Ch*]
- The bottom of the conduction band is composed from an admixture of the *ns*-*Ch*, *4s*-Ag and *5d*-Ba states.

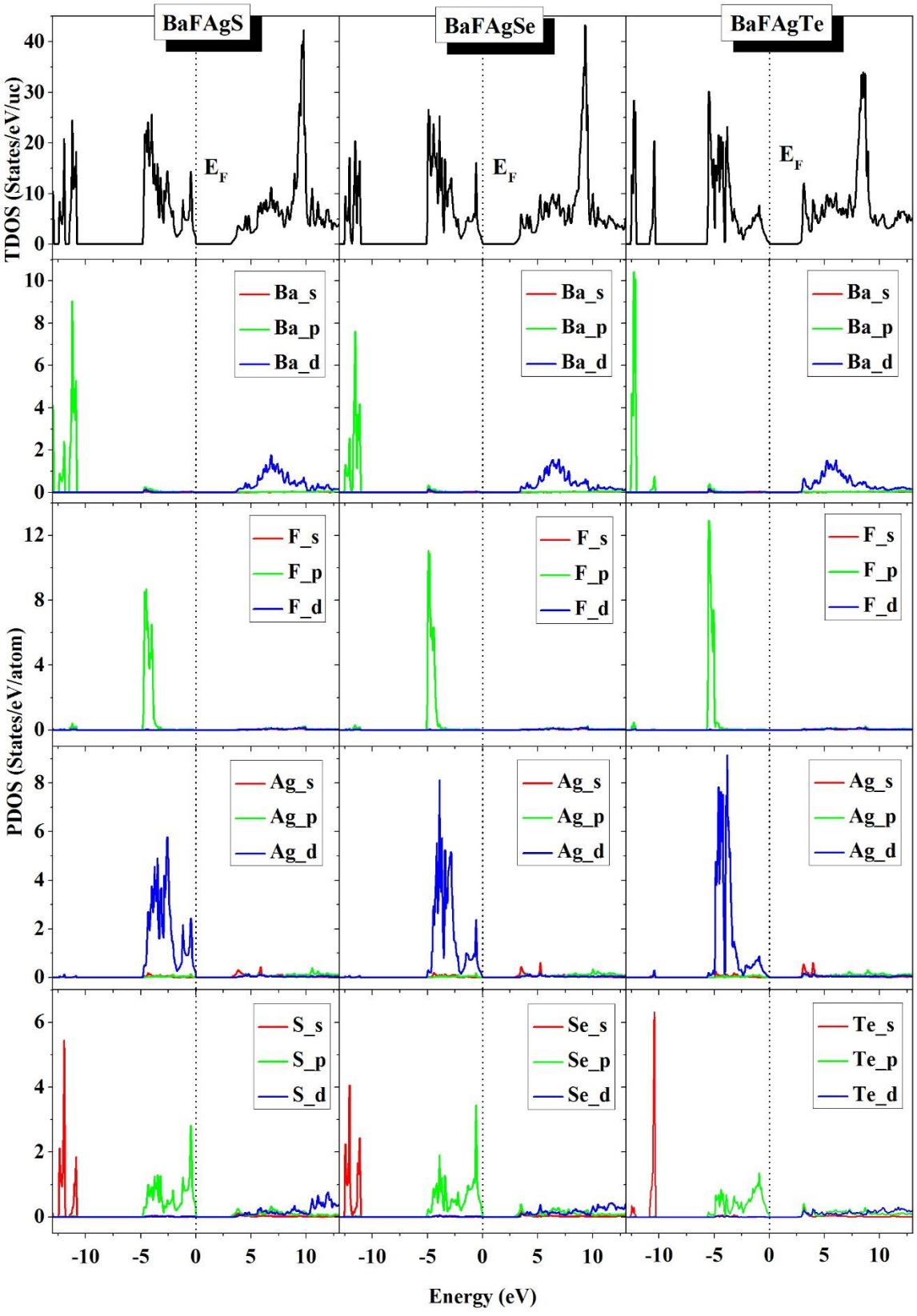

Figure IV.12: Total and atomic-resolved *l*-decomposed densities of states (TDOS and PDOS, respectively) for the BaFAgS, BaFAgSe and BaFAgTe systems. The energy zero level corresponds to the Fermi level.

IV.3.6. Electronic charge density

Chemical structure and bonding are key features and concepts in chemical systems, which are used in deriving structure–property relationships, and hence in predicting physical and chemical properties of compounds. Atoms sticking together in molecules or crystals are said to be bonded with one another. A chemical bond is a lasting attraction between atoms, ions or molecules that enables the formation of chemical compounds. It can be covalent bond, ionic bond, Hydrogen bond, Van der Waals force or metallic bonding. The bond may result from the electrostatic force of attraction between oppositely charged ions as in ionic bonds, or through the sharing of electrons as in covalent bonds. When a chemical bond is formed between two elements, the differences in the electronegativity of the atoms determine where on the sliding scale the bond falls. Large differences in electronegativity favour ionic bonds, and relatively small differences cause the formation of covalent bonds [43]. More than simple attraction and repulsion, the energies and distributions characterize the availability of an electron to bond to another atom.

The electronic charge density distributions (in the unit eV/Å^3) in the [Ag*Ch*] block and in (400) plane are plotted in Fig. IV.13. From Fig. IV.13, the following conclusions can be made:

- For the tree studied compounds, the bonding in the [Ag*Ch*] and [BaF] blocks are of mixed ionic and covalent nature. The Ag-*Ch* bond inside the [Ag*Ch*] layer is predominantly of covalent character, which is due to the strong hybridization between the Ag: 4d and *Ch*: np states, while the Ba-F bond in the layer [BaF] is predominantly ionic. This can be predicted by the periodic table of the elements, where the barium atom is located on the left and the fluorine atom on the right, so the difference in the electronegativity is very clear. As for the elements Ag and *Ch*, the relatively small differences cause the formation of covalent bonds.
- The electronic charge density around the chalcogen atom become less localized in the sense of $S \rightarrow Se \rightarrow Te$. This is consistent with the results obtained through the study of the nature of the chemical bonding from the density of states.
- The substitution of S by Se and Te leads to the decrease the degree of covalency.

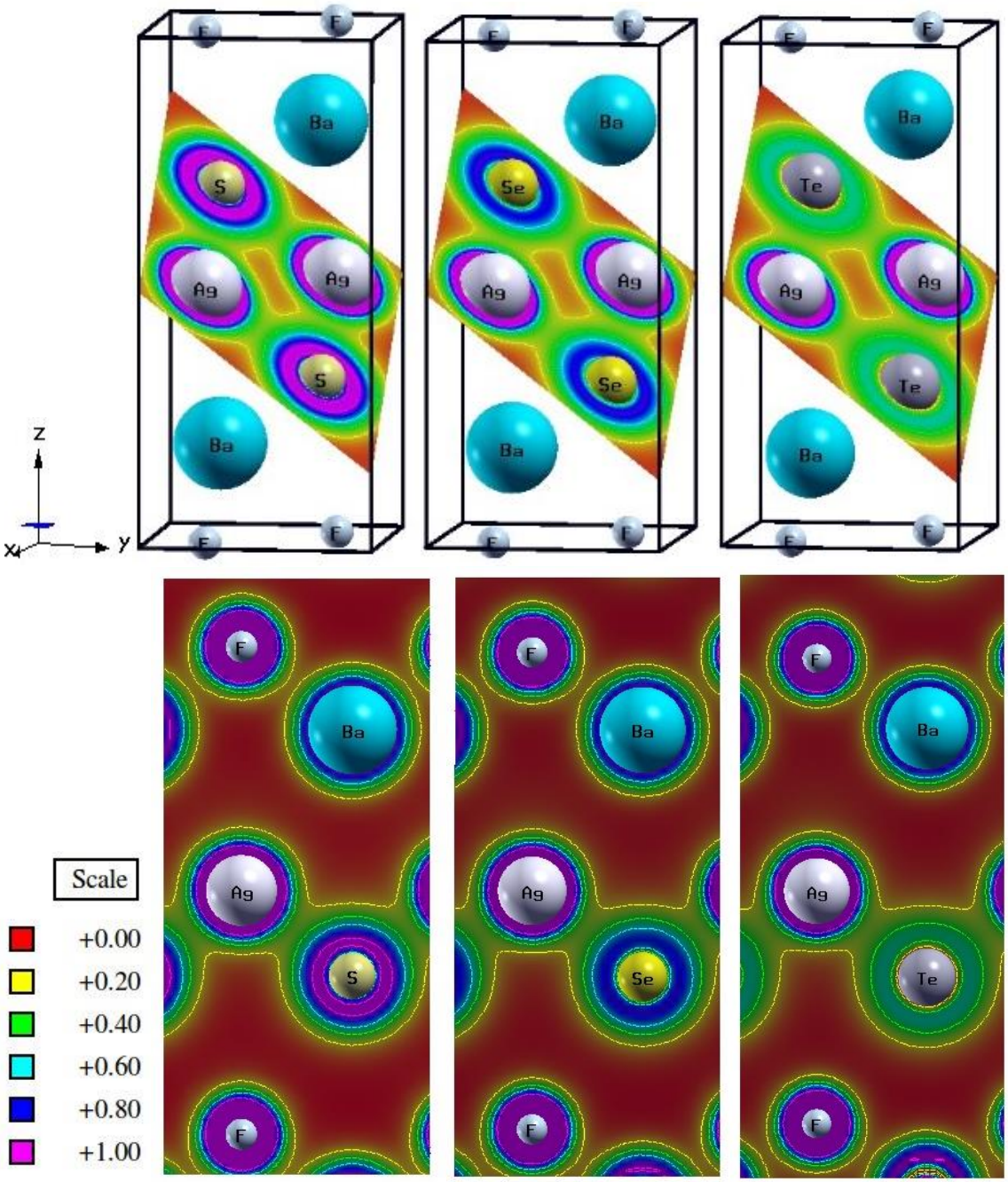

Figure IV.13: Electronic charge density of BaFAg*Ch* (*Ch*=S, Se and Te): in the [Ag*Ch*] block (a) and in the (400) crystallographic plane (b).

IV.4 Optical properties of BaFAg*Ch* (*Ch* = S, Se and Te)

Optical properties of materials are those characteristic properties that determine how the matter interact with light. Light is not only the electromagnetic radiation that we can see; wavelengths in the visible range, typically 400 to 700 nm, in many applications, light is the electromagnetic radiation that can have somewhat shorter or longer wavelengths such as ultraviolet (UV) and infrared (IR) light

Interaction of light with a material leads to a number of phenomena: The photons that constituting the light may give their energy to the material (absorption); photons give their energy, but photons of identical energy are immediately emitted by the material (reflection); photons may not interact with the material structure (transmission); or during transmission photons change their velocity (refraction). At any instance of light interaction with a material, the total intensity of the incident light (I_0) striking a surface is equal to sum of the absorbed (I_A), reflected (I_R), and transmitted (I_T) intensities, i.e., $I_0=I_A+I_R+I_T$.

Optical properties of materials depend on the dielectric polarization mechanisms as well as the wavelength of the radiation [14]. The dielectric polarization is given by the dielectric function ($\mathcal{E}(\omega)$). The dielectric function ($\mathcal{E}(\omega)$) describes the response of materials to an external electromagnetic field. The dielectric function of an anisotropic material is a complex symmetric tensor; $\mathcal{E}(\omega) = \mathcal{E}_1(\omega) + i\mathcal{E}_2(\omega)$. The imaginary part ($\mathcal{E}_2(\omega)$) of the dielectric function ($\mathcal{E}(\omega)$) characterizes the absorption of the incident light by the matter - it is directly related with the absorption spectrum -, so sometimes; it is called the absorptive part and can be computed by summing all allowed electronic transitions from occupied to unoccupied states. The real part ($\mathcal{E}_1(\omega)$) characterizes the dispersion of the incident radiation when it traverses a medium, so sometimes; it is called the dispersive part. In the limit of the linear optics, in the case of non-spin polarization, and within the independent particle approximation, random phase approximation, the imaginary part of the dielectric tensor ($\mathcal{E}_2(\omega)$) can be computed from knowledge of the electronic band structure of a solid from the well-known relation [44, 45]:

$$Im\ \mathcal{E}_{\alpha\beta}(\omega) = \mathcal{E}_2^{\alpha\beta}(\omega)$$
$$= \frac{4\pi e^2}{m^2\omega^2}\sum_{i,f}\int \langle f|P^{\alpha}|i\rangle\langle i|P^{\beta}|f\rangle W_i(1-W_f)(E_f - E_i - \hbar\omega)\, d^3k \qquad (A.27)$$

In this expression, $\langle f|P^{\alpha}|i\rangle$ and $\langle i|P^{\beta}|f\rangle$ are the dipole matrix elements corresponding to the α and β directions of the crystal (x, y or z), and f, i are the final and initial states, respectively. W_n is the Fermi distribution function for the n th state, and E_n is the electron energy in the nth state. The real part $(\mathcal{E}_1(\omega))$ of the frequency-dependent dielectric function expression $\mathcal{E}_{\alpha\beta}(\omega)$ is computed from $\mathcal{E}_2^{\alpha\beta}(\omega)$ using the Kramers-Kronig relations in the form [46, 47]:

$$\mathcal{E}_1^{\alpha\beta}(\omega) = \delta_{\alpha\beta} + \frac{2}{\pi} P \int_0^{\infty} \frac{\omega' \mathcal{E}_2^{\alpha\beta}(\omega')}{\omega'^2 - \omega^2} d\omega' \qquad \text{(IV. 28)}$$

where P is the Cauchy principal value of the integral. Optical constants, such as the refractive index $n(\omega)$, extinction coefficient $k(\omega)$, reflectivity $R(\omega)$, coefficient of absorption $\alpha(\omega)$ and the loss function $L(\omega)$, can be calculated from the dielectric function $\mathcal{E}(\omega) = \mathcal{E}_1(\omega) + i\mathcal{E}_2(\omega)$ using the well known relations:

$$\alpha(\omega) = \frac{\sqrt{2}}{c} \omega \sqrt{-\mathcal{E}_1(\omega) + \sqrt{\mathcal{E}_1(\omega)^2 + \mathcal{E}_2(\omega)^2}} \qquad \text{(IV. 29)}$$

$$n(\omega) = 1 + P \int_0^{+\infty} \frac{\omega' k(\omega')}{\omega'^2 - \omega^2} d\omega' \qquad \text{(IV. 30)}$$

$$k(\omega) = -\frac{2\omega}{\pi} P \int_0^{+\infty} \frac{n(\omega') - 1}{\omega'^2 - \omega^2} d\omega' \qquad \text{(IV. 31)}$$

$$R(\omega) = \left(\frac{\mathcal{E}_1(\omega)}{2} + \frac{\sqrt{\mathcal{E}_1(\omega)^2 + \mathcal{E}_2(\omega)^2}}{2} \right)^2 \qquad \text{(IV. 32)}$$

$$L(\omega) = -Im\left(\frac{1}{\mathcal{E}(\omega)}\right) = \frac{\mathcal{E}_2(\omega)}{\mathcal{E}_1^2(\omega) + \mathcal{E}_2^2(\omega)} \qquad \text{(IV. 33)}$$

For the tetragonal symmetry only the diagonal dielectric tensor components, namely $\mathcal{E}^{xx} = \mathcal{E}^{yy}$ and $\mathcal{E}^{zz}$, are non-zero. The dielectric tensor component $\mathcal{E}^{xx}(\mathcal{E}^{yy})$ corresponds to the electric fields $\vec{E}$ of the incident radiation parallel to the x-axis (y-axis) (i.e., $\vec{E}//\vec{a}$ ($\vec{E}//\vec{b}$)) and to the z-axis (i.e., $\vec{E}//\vec{c}$).

Calculated frequency-dependent dispersive ($\mathcal{E}_1(\omega)$) and absorptive ($\mathcal{E}_2(\omega)$) parts of the dielectric function ($\mathcal{E}(\omega)$) for the BaFAgS, BaFAgSe and BaFAgTe systems are depicted in Fig. IV.14. In view of Fig. IV.14, one can observe the following features:

(i) There are noticeable differences between the magnitudes, shapes and locations of the main peaks in the $\mathcal{E}_2^{xx}(\omega)$ ($\vec{E}//\vec{a}$) and $\mathcal{E}_2^{zz}(\omega)$ ($\vec{E}//\vec{c}$), revealing a strong anisotropy of the dielectric response of the examined systems to the incident radiation.

(ii) Tthe overall shape of the dielectric function spectra of BaFAgS and BaFAgSe are almost similar, whereas that of BaFAgTe is somewhat different from them. This difference can be attributed to the fact that the energy band dispersion of BaFAgTe is somewhat different from those of BaFAgS and BaFAgSe.

(iii) The intensity of the peaks increases when we move in the following sequence: $BaFAgS \rightarrow BaFAgSe \rightarrow BaFAgTe$. The $\mathcal{E}_2^{xx}(\omega)$ and $\mathcal{E}_2^{zz}(\omega)$ spectra start at the same energy (E_0), indicating an isotropic energy gap. However, $\mathcal{E}_2^{xx}(\omega)$ and $\mathcal{E}_2^{zz}(\omega)$ grow with different rates.

To access the electronic transitions that are responsible for the peaks observed in the $\mathcal{E}_2(\omega)$ spectra, the $\mathcal{E}_2(\omega)$ spectrum is decomposed to the individual contribution from each electronic transition from occupied valence band V_i to unoccupied conduction band C_j, i.e., determination of the contribution of each allowed electronic transition ($V_i \rightarrow C_j$) to the $\mathcal{E}_2(\omega)$ spectrum. To determine which electronic states of the bands V_i and C_j are involved in the $V_i \rightarrow C_j$ transition, the electronic transition energies $E_{ij}(k)$ ($E_{ij}(k) = E_{C_j}(k) - E_{V_i}(k)$) are plotted along the high-symmetry directions of the BZ. For sake of brevity, only decomposition of the $\mathcal{E}_2(\omega)$ spectrum of BaFAgS to individual contributions of the electronic transitions ($V_i \rightarrow C_j$) and the corresponding transition energy $E_{ij}(k)$ dispersion are shown in Fig. IV.15, as representative for the other studied systems. The first threshold energy E_0 of $\varepsilon_2(\omega)$, termed also fundamental absorption edge, is originated from the direct electronic transition between the topmost valence band V_1 and the bottommost conduction band C_1 ($V_1 \rightarrow C_1$). It is to note that the bands counting is up (down) from the bottommost (topmost) of the conduction (valence) band. The locations of the major peaks E_i (i =1, 2…etc.) and the origin of the dominant optical transitions in an energy range up to 10 eV are listed in Tabs. IV.7-12. The obtained electronic static

dielectric constant $\mathcal{E}^{e}(0) = \mathcal{E}_1(\omega \to 0)$, which is a parameter of fundamental importance in many aspects of material properties, are given in Tab. IV.13. Our results are in agreement with the available theoretical results for BaFAgS [11]. The $\mathcal{E}_1(O)$ increases in the following sequence: $BaFAgS \to BaFAgSe \to BaFAgTe$ and the $\mathcal{E}_1^{xx}(\omega \to 0)$ component is larger than the$\mathcal{E}_1^{zz}(\omega \to 0)$ component. The $\mathcal{E}_1(O)$ value increases when the energy gap E_g decreases. This is in accordance with the Penn model [48]: $\mathcal{E}_1(O) \approx 1 + \left(\hbar\omega_p/E_g\right)^2$; $\mathcal{E}_1(O)$ is inversely proportional with E_g , i.e., smaller E_g yields larger $\mathcal{E}_1(O)$.

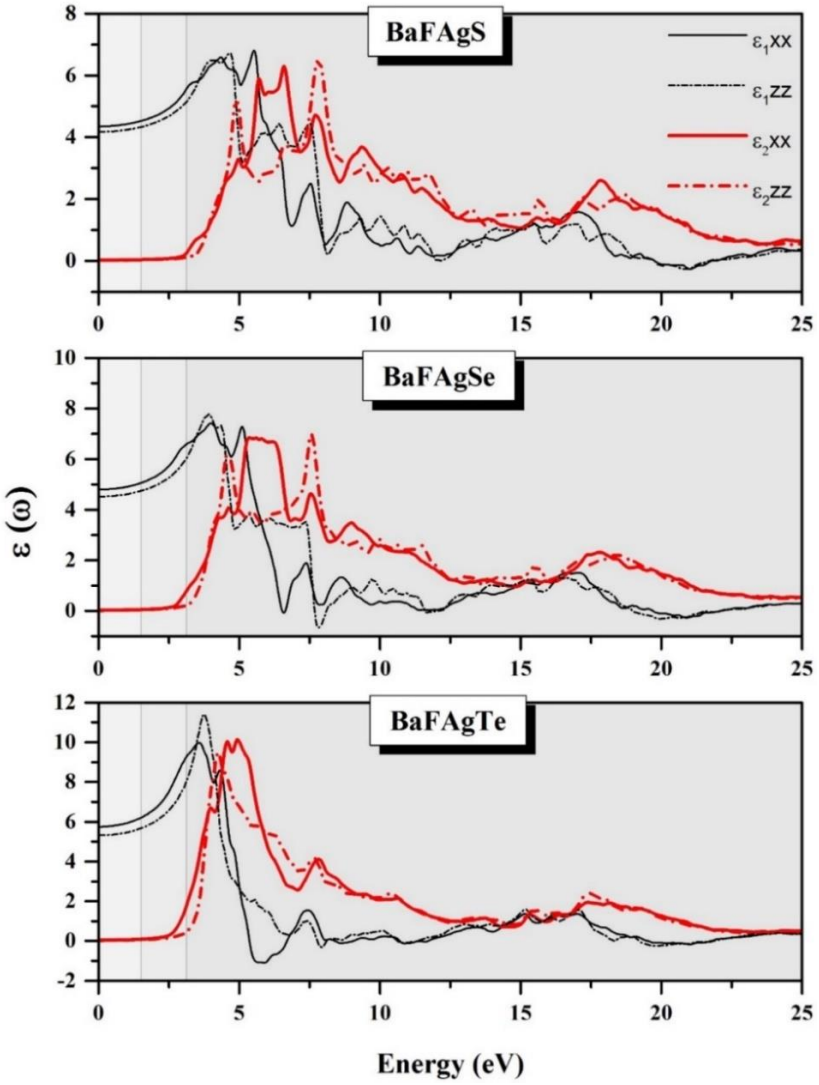

Figure IV.14: Frequency-dependent imaginary ($\mathcal{E}_2^{xx}(\omega)$ and $\mathcal{E}_2^{zz}(\omega)$; red line) and real ($\mathcal{E}_1^{xx}(\omega)$ and $\mathcal{E}_1^{zz}(\omega)$; black line) parts of the dielectric function tensor components for the BaFAg*Ch* (*Ch* = S, Se and Te) compounds.

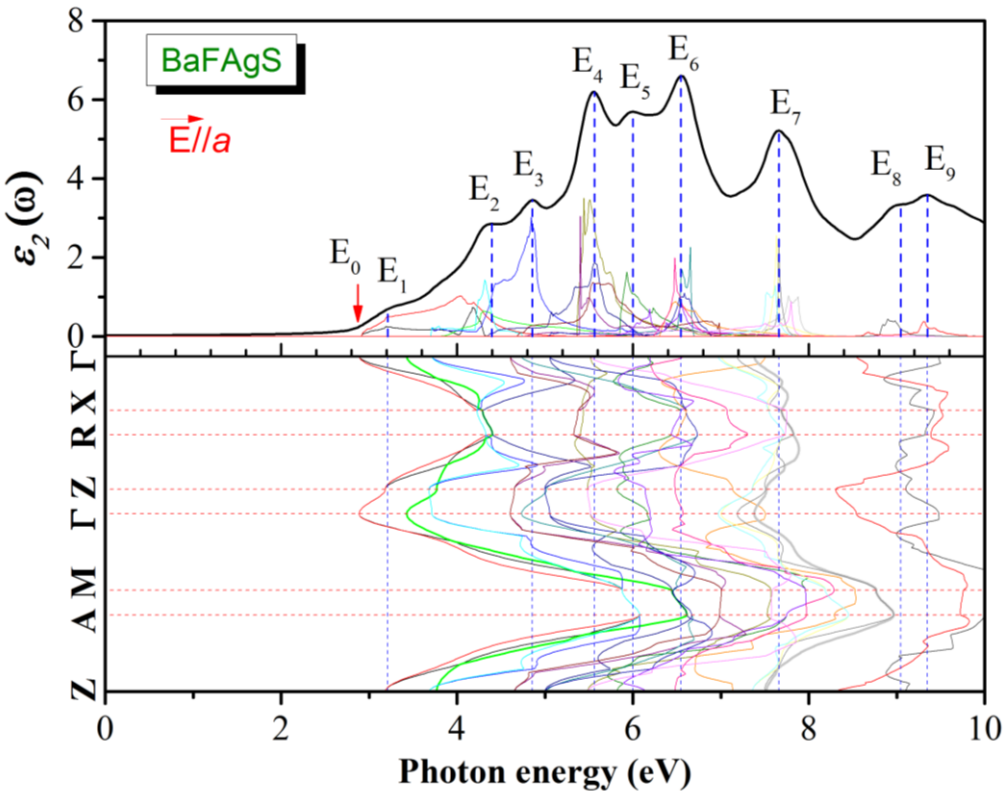

Figure IV.15: Decomposition of the imaginary part of the dielectric function $\mathcal{E}_2^{xx}(\omega)$ into band-to-band contribution (upper panel (a)) and the transition energy band structure (lower panel (b)) for BaFAgS. The counting of the bands is down (up) from the top (bottom) of the valence (conduction) band.

Table IV.7: Peak positions of the $\mathcal{E}_2^{xx}(\omega)$ spectrum together with the dominant interband transition contributions to every peak and their location in the Brillouin zone for the BaFAgS compound.

Optical structures		Dominant interband transition contributions		
Structure	Peak position	Transition	Region	Energy (eV)
E_1	3.21	V2-C1	Z, M-Γ, Z-R, X-Γ	3.21
		V1-C1	Z, M-Γ, Z-R, X-Γ	3.19
E_2	4.39	V1-C2	Z-A, M-Γ	4.30
		V1-C2	Z-A, M-Γ	4.29
E_3	4.86	V2-C2	Z-A, M-Γ	4.85
E_4	5.56	V4-C3	Z-A, M-Γ, X-Γ	5.51
		V4-C2	Z-A, M-Γ	5.57
		V2-C4	Z-A, M-Γ, Z-R	5.51
		V1-C4	Z-A, M-Γ, Z-R	5.53
E_5	6.00	V2-C5	Z-A, M-Γ, Γ-Z, Z-R, X-Γ	5.94
E_6	6.54	V6-C1	Z-A, A-M, M-Γ, Z-R, X-Γ	6.64
		V5-C2	Z-A, A-M, M-Γ, Z-R, X-Γ	6.60
		V4-C5	Z-R, R-X, X-Γ	6.49
		V1-C6	Z-A, M-Γ, Z-R, R-X, X-Γ	6.56
		V1-C8	Z-A, M-Γ, Γ-Z, Z-R, X-Γ	6.47
E_7	7.66	V16-C1	Z-A, M-Γ, Z-R, X-Γ	7.78
		V15-C1	Z-A, M-Γ, Z-R, X-Γ	7.68
		V14-C1	Z-A, M-Γ, Z-R, R-X, X-Γ	7.63
		V13-C1	Z-A, M-Γ, Z-R, R-X	7.62
		V5-C3	Z-A, M-Γ, Z-R, X-Γ	7.79
E_8	9.05	V10-C5	Z-A, M-Γ, Z-R, X-Γ	8.88
E_9	9.35	V1-C16	Z-A, M-Γ, Z-R, X-Γ	9.31

Table IV.8: Peak positions of the $\mathcal{E}_2^{zz}(\omega)$ spectrum together with te dominant interband transition contributions to every peak and their location in the Brillouin zone for the BaFAgS compound.

Optical structures		Dominant interband transition contributions		
Structure	Peak position	Transition	Region	Energy (eV)
E_1	7.69	V2-C1	Z-A, M-Γ, Z-R, X-Γ	4.17
		V3- C2	Z-A, M-Γ, Z-R, X-Γ	4.04
E_2	4.78	V1-C2	Z-A, M-Γ, Z-R, X-Γ	4.90
		V1-C3	Z-A, M-Γ	4.70
		V4-C4	Z-A, M-Γ, Z-R, X-Γ	4.78
E_3	5.86	V1-C5	Z-A, M-Γ	5.94
		V1-C6	Z-A, M-Γ, Γ-Z, Z-R, X-Γ	5.79
		V2-C5	Z-R, X-Γ	5.86
		V4-C5	Z-A, M-Γ, Γ-Z, Z-R, X-Γ	5.90
E_4	6.46	V2-C7	M-Γ, Z-R, X- Γ	6.47
		V3-C6	Z-A, M-Γ, Γ-Z, Z-R, X-Γ	6.43
		V3-C5	Z-A, M-Γ, Z-R, X- Γ	6.42
		V3-C7	Z-A, M-Γ, Γ-Z, Z-R, X-Γ	6.41
		V7-C4	Z-A, Z-R	6.45
E_5	6.87	V6-C2	Z-A, M-Γ	6.87
		V2-C8	Z-A, M-Γ	6.79
		V3-C8	Z-A, M-Γ, Z-R, X-Γ	7.12
		V1-C9	Z-A, M-Γ, Z-R, X-Γ	6.74
		V15-C1	Z-A, M-Γ, Z, Z-R	6.87
E_6	7.69	V14-C1	Z-A, M-Γ, Z-R, X	7.64
		V13-C1	Z-A, M-Γ, Z-R, R-X	7.63
		V5-C4	Z-A, M-Γ, Z-R, R-X	7.73
		V5-C6	Z-A, M-Γ, Z-R, X-Γ	7.82
E_7	8.64	V12-C3	Z-A, M-Γ, Z-R, X-Γ	8.65
E_8	9.35		Z-A	9.29

Table IV.9: Peak positions of the $\mathcal{E}_2^{xx}(\omega)$ spectrum together with the dominant interband transition contributions to every peak and their location in the Brillouin zone for the BaFAgSe.

Optical structures		Dominant interband transition contributions		
Structure	Peak position	Transition	Region	Energy (eV)
E_1	4.15	V3-C1	Z-A, M-Γ, Z-R, R-X, X-Γ	4.19
		V2-C2	Z-A, M-Γ, Z-R, R-X, X-Γ	4.11
		V1-C1	Z-A, M-Γ, Z, R-X	4.13
E_2	4.59	V3-C2	Z-A, M-Γ, Z-R, X-Γ	4.65
		V2-C2	Z-A, M-Γ, Z-R	4.57
E_3	5.21	V4-C2	Z-A, M-Γ, Z-R	5.20
		V4-C3	Z-A, Γ-Z, Z-R, X-Γ	5.16
		V2-C3	Z-A, M-Γ	5.19
		V1-C4	Z-A, M-Γ, Z-R, X-Γ	5.18
E_4	5.65	V4-C4	Z-A, M-Γ, Z-R, X-Γ	5.60
		V3-C5	Z-A, Z-R, X-Γ	5.71
		V2-C5	Z-A, M-Γ, Γ-Z, Z-R, X-Γ	5.62
		V1-C3	Z-A, M-Γ	5.64
E_5	6.25	V5-C2	Z-A, M-Γ, Z-R, X-Γ	6.31
		V4-C5	Z-R, R-X, X	6.27
		V1-C6	Z-A, M- Γ, Z-R, R-X, X-Γ	6.24
E_6	6.98	V5-C5	Z-A, M-Γ, Γ-Z, Z-R, X-Γ	6.95
		V3-C3	Z-A, M-Γ	6.98
E_7	7.55	V15-C2	R-X, X-Γ	7.59
		V14-C1	Z-A, M-Γ, Z-R, R-X, X-Γ	7.60
		V13-C1	Z-A, M-Γ, Z-R, R-X	7.49
E_8	8.99	V13-C3	Z-A, A-M, M-Γ	9.00
		V1-C15	Z-A, M-Γ, Z-R, X-Γ	9.01

Table IV.10: Peak positions of the $\mathcal{E}_2^{zz}(\omega)$ spectrum together with the dominant interband transition contributions to every peak and their location in the Brillouin zone for the BaFAgSe compound.

Optical structures		Dominant interband transition contributions		
Structure	Peak position	Transition	Region	Energy (eV)
E_1	3.99	V1-C2	Z-A, M-Γ, Z-R, X-Γ	4.00
		V2-C1	Z-A, M-Γ, Z-R, X-Γ	4.03
E_2	4.03	V3-C2	Z-A, M-Γ, Z-R, X-Γ	4.62
		V1-C2	Z-A, M-Γ	4.42
		V2-C3	Z-A, M-Γ, Z-R, X-Γ	4.44
E_3	5.43	V2-C4	Z-A, M-Γ, Z-R	5.41
		V2-C5	Z-A	5.54
		V1-C5	Z-A, Z-R, X-Γ	5.40
		V1-C6	Z-R, X-Γ	5.45
E_4	6.19	V3-C4	Z-A, M-Γ	6.22
		V3-C5	Z-A, M-Γ, Z-R, R, X-Γ	6.22
		V3-C6	Z-A, M-Γ, Z-R, R, X-Γ	6.21
		V3-C7	M-Γ, Z-R	6.19
E_5	6.49	V6-C2	Z-A, M-Γ	6.76
		V3-C8	Z-A, M-Γ, Z-R, X-Γ	6.44
		V2-C8	Z-A, M-Γ, Z-R, X-Γ	6.48
		V1-C9	Z-A, M-Γ, Z-R, X-Γ	6.48
E_6	6.82	V7-C4	Z-A, M-Γ, Z-R, X-Γ	6.78
		V2-C9	Z-A, M- Γ, Z-R, X- Γ	6.76
		V1-C10	Z-A, M-Γ, Z-R, X-Γ	6.84
E_7	7.55	V15-C1	Z-A, M-Γ, Z-R, R-X, X-Γ	7.60
		V14-C1	Z-A, M-Γ, Z-R, R-X, X-Γ	7.58
		V13-C1	Z-A, M-Γ, Z-R, R-X	7.54
		V5-C4	Z-A, Z-R, R-X, X-Γ	7.49
E_8	8.37	V4-C12	Z-A, Z-R, X-Γ	8.39
E_9	8.88	V12-C3	Z-A, M-Γ, Z-R	8.95
		V11-C3	Z-A, M-Γ	8.87
		V11-C5	Z-A, M-Γ, Z-R, R-X, X-Γ	8.95
		V3-C16	Z-A, M-Γ, Z-R, X-Γ	8.89
E_{10}	9.21	V5-C11	Z-A, M-Γ, Z-R, X-Γ	9.23

Table IV.11: Peak positions of the $\mathcal{E}_2^{xx}(\omega)$ spectrum together with the dominant interband transition contributions to every peak and their location in the Brillouin zone for the BaFAgTe compound.

Optical structures		Dominant interband transition contributions		
Structure	Peak position	Transition	Region	Energy (eV)
E_1	3.88	V2-C1	Z-A, M-Γ, Z-R, X-Γ	3.81
		V2-C2	Z-A, M-Γ, Z-R, X-Γ	3.89
		V1-C2	Z-A, M-Γ	3.86
		V1-C1	Z-A, M-Γ	3.86
E_2	4.50	V4-C3	Z-R, X-Γ	4.45
		V4-C2	Z-A, M-Γ, Z-R, X-Γ	4.51
		V3-C3	Γ-Z	4.44
		V2-C3	Z-A, M-Γ	4.50
		V1-C4	Z-A, M-Γ, Z-R, X-Γ	4.55
E_3	5.05	V3-C4	Z-A, M-Γ, Z-R, X-Γ	4.99
		V3-C3	Z-A, M-Γ	5.04
		V2-C3	Z-A, M-Γ	5.04
		V2-C5	Z-A, M-Γ, Z-R, X-Γ	5.13
		V1-C7	M-Γ, Z-R, X-Γ	5.13
E_4	7.74	V16-C1	Z-A, M-Γ, Z-R, X-Γ	7.83
		V16-C2	Z-A, M-Γ, Γ-Z, Z-R, X-Γ	7.78
		V15-C1	Z-A, M-Γ, Z-R, X-Γ	7.78
		V15-C2	Z-A, M-Γ, Z-R, X-Γ	7.72

Table IV.12: Peak positions of the $\mathcal{E}_2^{zz}(\omega)$ spectrum together with the dominant interband transition contributions to every peak and their location in the Brillouin zone for the BaFAgTe compound.

Optical structures		Dominant interband transition contributions		
Structure	Peak position	Transition	Region	Energy (eV)
E_1	4.15	V4-C1	M-Γ, Γ-Z, Z-R, X-Γ	4.07
		V2-C2	Z-A, M-Γ	4.13
		V2-C1	Z-A, M-Γ	4.15
		V2-C3	Z-A, M-Γ, Z-R, X-Γ	4.18
		V1-C2	Z-A, M-Γ	4.14
E_2	4.59	V4-C3	Γ-Z, Z-R, X-Γ	4.55
		V3-C3	Z-A, M-Γ	4.60
		V1-C5	Z-R, X-Γ	4.53
		V1-C4	Z-A, M-Γ, Z-R	4.60
		V1-C2	Z-A, M-Γ	4.56
E_3	5.05	V2-C6	Z-A, M-Γ, Γ-Z, Z-R, X-Γ	5.06
		V2-C1	Z-A, M-Γ	5.08
		V1-C5	Z-A, M-Γ, Z-R, X-Γ	5.06
E_4	5.51	V3-C6	Z-A, M- Γ, Γ -Z, Z-R, R-X, X- Γ	5.47
		V3-C3	Z-A, M-Γ	5.50
		V3-C7	Z-A, M-Γ, Z-R, X-Γ	5.49
		V2-C7	Z-A, M-Γ, Z-R, X-Γ	5.51
		V2-C8	Z-A, M-Γ, Γ-Z, Z-R, X-Γ	5.57
E_5	6.16	V3-C3	Z-A, M-Γ	6.19
		V3-C4	Z-A, M-Γ	6.19
		V2-C9	Z-A, M-Γ, Z-R, R-X, X-Γ	6.15
E_6	7.52	V15-C1	Z-A, M-Γ, Z-R, R, X-Γ	7.48
		V14-C2	A-M, M-Γ, Γ-Z, Z-R, X-Γ	7.63
		V14-C1	Z-A, A-M, M-Γ, Z-R, X-Γ	7.47
		V13-C1	Z-A, A-M, M-Γ, Z-R, X-Γ	7.56
		V13-C2	A-M, M-Γ, Γ-Z, Z-R, X-Γ	7.47

Table IV.13: Calculated static dielectric constant $\varepsilon_1(0)$ and, static refractive index and static optical reflectivity for BaFAgS, BaFAgSe and BaFAgTe as calculated using the TB-mBJ for two different polarizations of the incident radiations, compared with the available data in the scientific literature.

System	$\varepsilon_1^{xx}(0)$	$\varepsilon_1^{zz}(0)$	$n^{xx}(0)$	$n^{zz}(0)$	$R^{xx}(0)$	$R^{zz}(0)$
BaFAgS	4.53 5.22 [11]	4.17 4.89 [11]	2.08	2.04	12.4	11.7
BaFAgSe	4.80	4.53	2.19	2.13	13.9	13.0
BaFAgTe	5.75	5.31	2.40	2.31	16.9	15.6

Figs. IV.16-19 presents the frequency-dependent coefficient of absorption $\alpha(\omega)$, index of refraction $n(\omega)$, coefficient of extinction $k(\omega)$, reflectivity $R(\omega)$ and electron energy-loss function $L(\omega)$ for incident radiation polarized both along the *a*-axis ($\vec{E}//\vec{a}$) and *c*-axis ($\vec{E}//\vec{c}$) in a wider spectral region up to 25 eV. The optical spectra for $\vec{E}//\vec{a}$ are quite different from those for $\vec{E}//\vec{c}$, implying the optical anisotropy of these systems. The optical absorption coefficient $\alpha(\omega)$, which defines the amount of light absorbed by the matter, is an important criterion to judge if a material could have an eventual application in the photoelectric field. The examined compounds exhibit a high coefficient of absorption (higher than 10^4 cm^{-1}) in a large energy range extending from the absorption edge E_g (from ~2.6 to 2.9 eV) up to 30 eV, suggesting that they could be suitable absorber layers for photovoltaic applications. Obviously, these materials with a band gap higher than 2.6 eV may absorb the blue and violet rays of the visible spectrum. The calculated refractive index spectra for the three examined materials are given in Fig. IV.17. The refractive index reaches its maximum in the near ultra-violet (~3.8 ─ 5eV). One can note the refractive index value increases when going from BaFAgS to BaFAgSe to BaFAgTe, which is in accordance with the usual trend of the refractive index, i.e., the refractive index increases when the band gap decreases. The calculated static refractive index ($n(0)$), which is a very important physical quantity for semiconductors, is listed in Tab. IV.13. From Fig. IV.18, one can observe that the title systems exhibit a weak reflectivity at low

energies and the magnitude of the reflectivity increases slightly when going from BaFAgS to BaFAgSe to BaFAgTe. Calculated static reflectivity coefficients ($R(0)$) of the three studied systems are given in Tab. IV.13. The energy loss-function $L(\omega)$ spectra are depicted in Fig. IV.19. $L(\omega)$ is an important factor describing the energy loss of a fast electron traversing in a material. The peaks in $L(\omega)$ spectra represent the characteristic associated with the plasma resonance and the corresponding frequency is the so called plasma frequency ω_p. The peaks of $L(\omega)$ correspond to the trailing edges in the reflection spectra., for instance, the peak of $L(\omega)$ is at about 12 eV corresponding to the abrupt reduction of $R(\omega)$.

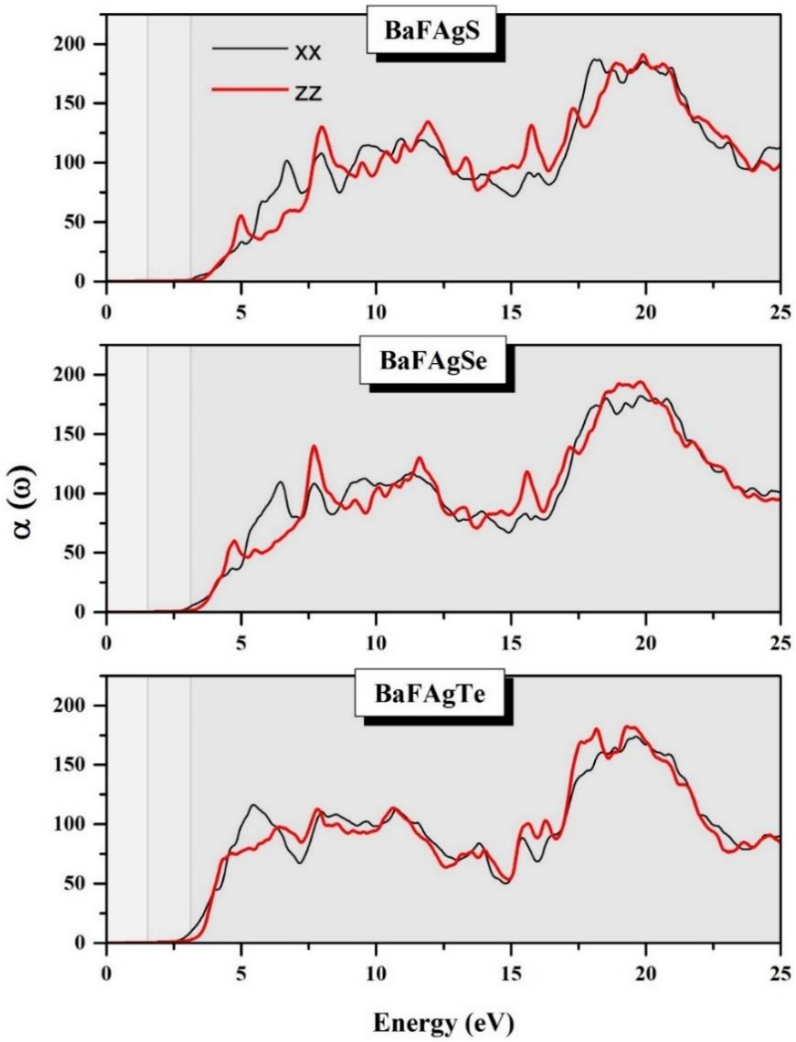

Figure IV.16: Calculated absorption coefficient (α (ω)) for the BaFAg*Ch* (*Ch* = S, Se and Te) compounds for two different applied light polarizations ($\vec{E}//\vec{a}$; black line, and $\vec{E}//\vec{c}$; red line).

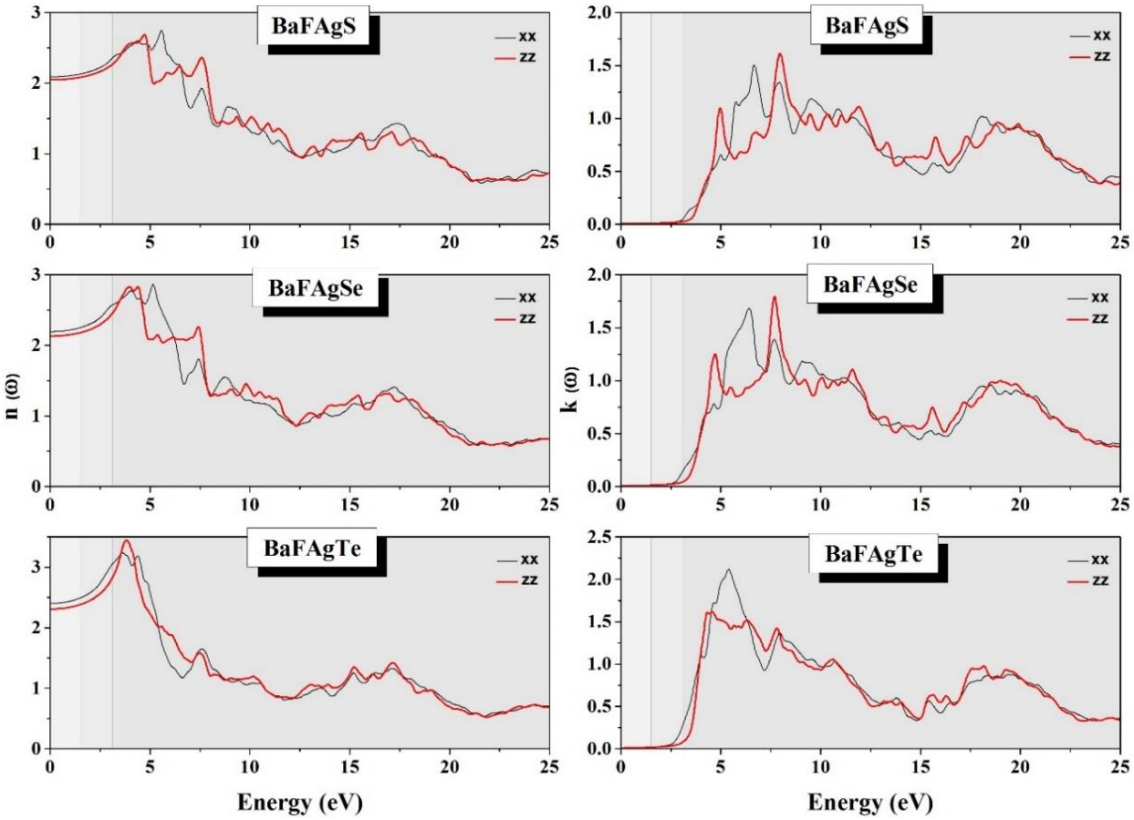

Figure IV.17: Calculated refractive index (*n (ω)*; left panels) and extinction coefficient (*k (ω)*; right panels) of BaFAg*Ch* (*Ch* = S, Se and Te) for two different applied light polarizations ($\vec{E}//\vec{a}$; black line, and $\vec{E}//\vec{c}$; red line).

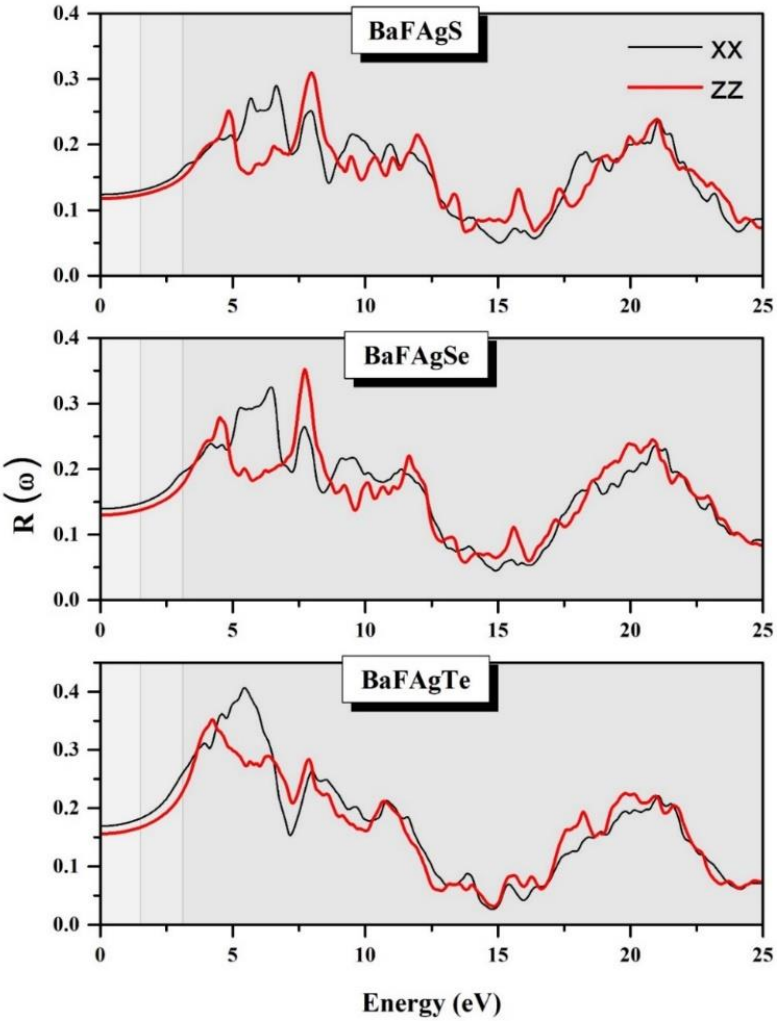

Figure IV.18: Calculated optical reflectivity *R (ω)* of BaFAg*Ch* (*Ch*=S, Se and Te) for two different applied light polarizations ($\vec{E}//\vec{a}$; black line, and $\vec{E}//\vec{c}$; red line).

.

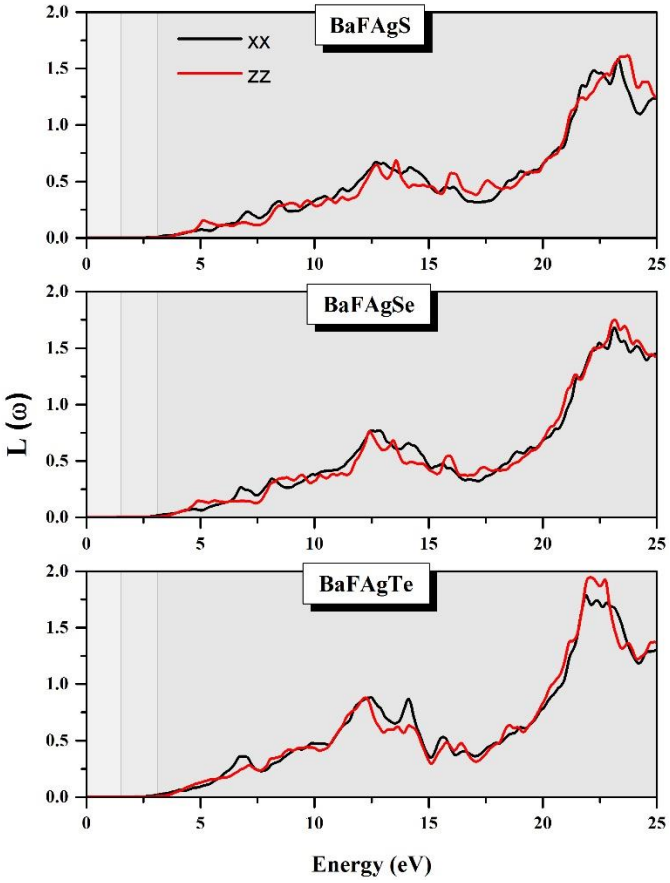

Figure IV.19: Calculated energy-loss function *L (ω)* of BaFAg*Ch* (*Ch*=S, Se and Te) for two different applied light polarizations ($\vec{E}//\vec{a}$; black line, and $\vec{E}//\vec{c}$; red line).

.

IV.5. Thermoelectric properties of BaFAg*Ch* (*Ch*=S, Se and Te)

IV.5.1. Thermoelectricity

Transport phenomena refer to physical phenomena resulting from the motion of charge carriers under the action of internal or external fields or temperature gradients. They include electric and thermal conductivities, galvanomagnetic, thermomagnetic and thermoelectric phenomena. Thermoelectric phenomena refer to the direct conversion of heat into electricity [49].

Early, peoples know the heat and use it in different ways to facility live. Heat is a form of energy that flows between two samples of matter due to their difference in temperature. However, the electricity would remain little more than an intellectual curiosity for millennia until 1600, when the English scientist ***William Gilbert*** made a careful study of electricity and magnetism [50]. Electricity is a form of energy that are produced fundamentally by the movement of electrical charges in the material and that provides power to devices that create light, heat…etc. [51]. Both, heat and electricity express or exhibit the energy that could be storing in material or flowing between two materials. However, the amount of energy that lost during production, transport and using the electricity has been very considerable. Furthermore, the global energy crisis and environmental impact of fossil fuels led us to thinking to conserve energy and recover lost ones. Renewable energy sources [52] are important for the production of energy (electricity) to address the needs of a growing population without destroying the environment. Thermoelectricity is one of the simplest technologies applicable to energy conversion; thermoelectric materials can generate electrical power from heat, and use electricity to function as heat pumps providing active cooling or heating [53]. For example, in a car, the maximum efficiency of an internal combustion engine ranged 40 to 50%; means that 50 to 60% of energy that producing from the motor is lost, However, it is a useful energy that could be used to operate the car parts and reduce the load on the motor [54] .

In 1831, the German scientist Thomas Seebeck (1770-1831) discovered the Thermoelectric effect; he found that a closed loop formed by two different metals (Copper and Bismuth) joined in two places (See Fig. IV.20)", with a temperature difference between the joints generates a magnetic field around them. Seebeck did not recognize there was an electric current involved, so he called the phenomenon "*thermomagnetic effect*".

Danish physicist Hans Orsted has been able to explain this phenomenon and attributed it to the generation of an electric voltage between the two nodes coined the term "thermoelectricity", contrary to what Seebeck thought was that magnetism resulted from the join of the two metals. This phenomenon has been used in the measurement of temperature in so-called thermocouples.

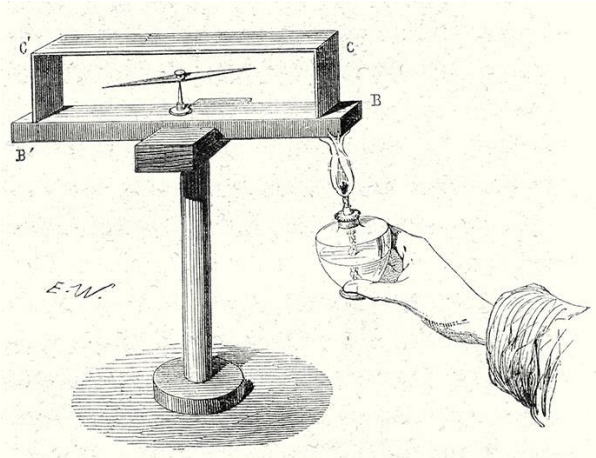

Figure IV.20: Schematic illustration of Seebeck effect (original experience with **B**ismuth and **C**opper).

In general, the Seebeck effect is described locally by the creation of an electromotive force ***(emf).*** The value of this thermal ***emf*** depends on the temperature difference between the cold and the hot side (junction) and may be expressed as:

$$E_{emf} = S\Delta T \qquad (IV.34)$$

Or $$\Delta V = -S\Delta T \qquad (IV.35)$$

S is the thermoelectric coefficient or Seebeck coefficient (also called thermo-power) expressed as the potential difference (i.e., $\Delta V = V_h - V_c$) per degree change in temperature between the cold (c) junction and the hot (h) junction (*i.e.*, $\Delta T = T_h - T_c$) [55].

We notice that for thermocouples, Seebeck coefficient given as [56] :

$$S = \frac{S_n\sigma_n + S_p\sigma_p}{\sigma_n + \sigma_p} \qquad (IV.36)$$

Here S_p (S_n) is the Seebeck coefficient of holes (electrons), σ_p (σ_n) is the electrical conductivity of holes (electrons).

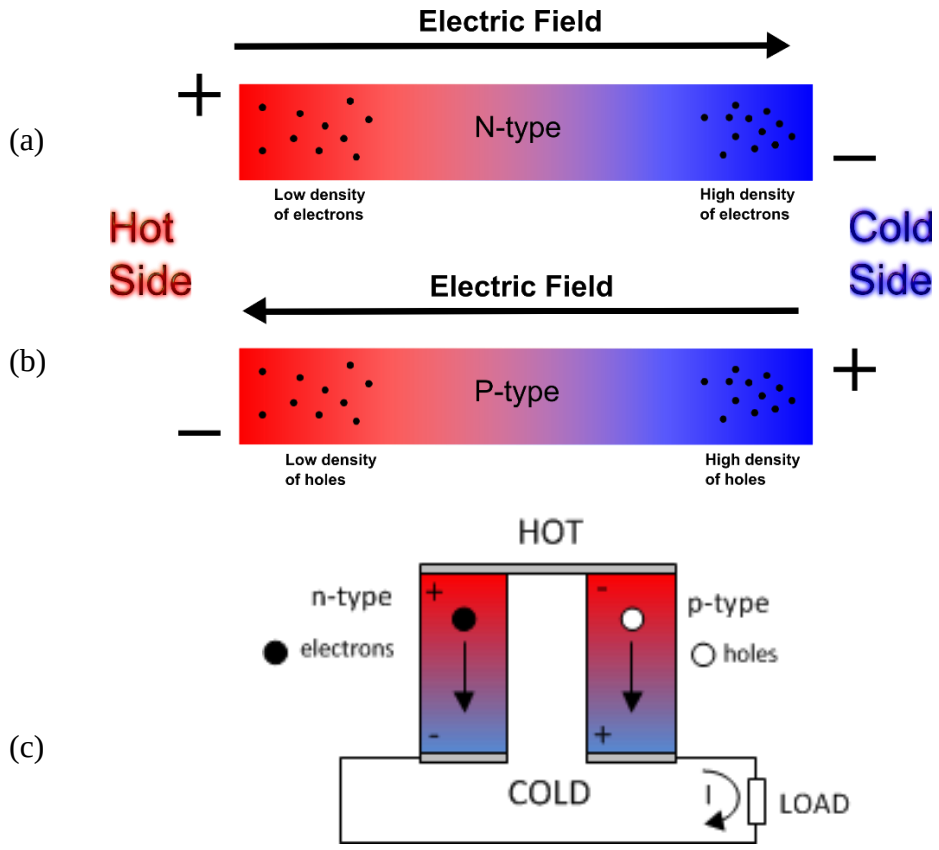

Figure IV.21: Diagram illustrating the Seebeck effect: *n*-type semiconductor (a), *p*-type semiconductor (b) and thermocouples (c).

In the same period, French scientist Jean Peltier was able to discover the reverse phenomenon; when an electric current is passed in the circuit, one of the two nodes produces heat and the other absorbs the heat. In reverse, the opposite occurs. Similar to Seebeck, Peltier didn't completely understand the physics of this phenomenon [57], and it was Emil Lenz who recognized the reversibility of this effect and demonstrated that the rate of heat ejection or absorption Q was proportional to the electrical current I with the proportionality coefficient Π that was subsequently named after J. Peltier.

$$Q = \Pi I \qquad (\text{IV}.37)$$

In 1851, William Thomson, famously known as Lord Kelvin , was able to discover the Thomson effect that single material carrying an electric current could absorb or release heat if it had a temperature difference over its length. Absorbing or evolving heat Q will

depend on direction of current and proportional to the electrical current i and the temperature gradient through a proportionality coefficient τ (Thomson coefficient):

$$Q = \tau i(-\Delta T) \qquad \text{(IV. 38)}$$

In 1840, the English physicist Joule suggested that heat could be generated by an electrical current. Electric energy is converted to heat through resistive losses in the material. It is generated on the micro-scale when the conduction electrons transfer energy to the conductor's atoms by way of collisions. Joule deduced that the heat produced was proportional to the square of the current multiplied by the electrical resistance:

$$Q = R \int_{t_1}^{t2} i^2 \, dt \qquad \text{(IV. 39)}$$

In a conductor subject to a temperature gradient, the increase of its cold end temperature is always observed as a result of heat conduction, which is expressed as following:

$$Q = -AK \frac{dT}{dX} \qquad \text{(IV. 40)}$$

Here *A* is the cross-section area of the conductor and k is material's thermal conductivity, the expression is known as Fourier law. The thermoelectric efficiency loss caused by heat conduction is directly proportional to *K*, hence the materials with low thermal conductivity are required for efficient energy conversion.

Thermoelectric conversion technology, which can realize the direct and reversible conversion between heat and electricity without moving parts, offers a promising solution to critical energy and environmental challenges.

IV.5.2. Electrical and thermal conduction

Electrical conduction involves the motion of charges in a material under the influence of an applied electric field [14]. Solid-state materials can be classified into three groups: insulators, semiconductors and conductors. Fig. IV.22 shows typical conductivities for metals, semiconductors and insulators. Semiconductors can be seen lying between metals and insulators, one important difference is that semiconductor conductivities are

shown varying over several orders of magnitude. This is a very important property of semiconductors. We can vary the conductivity of semiconductors by doping the semiconductor, in a controlled fashion, with minute amounts of impurity atoms [58].

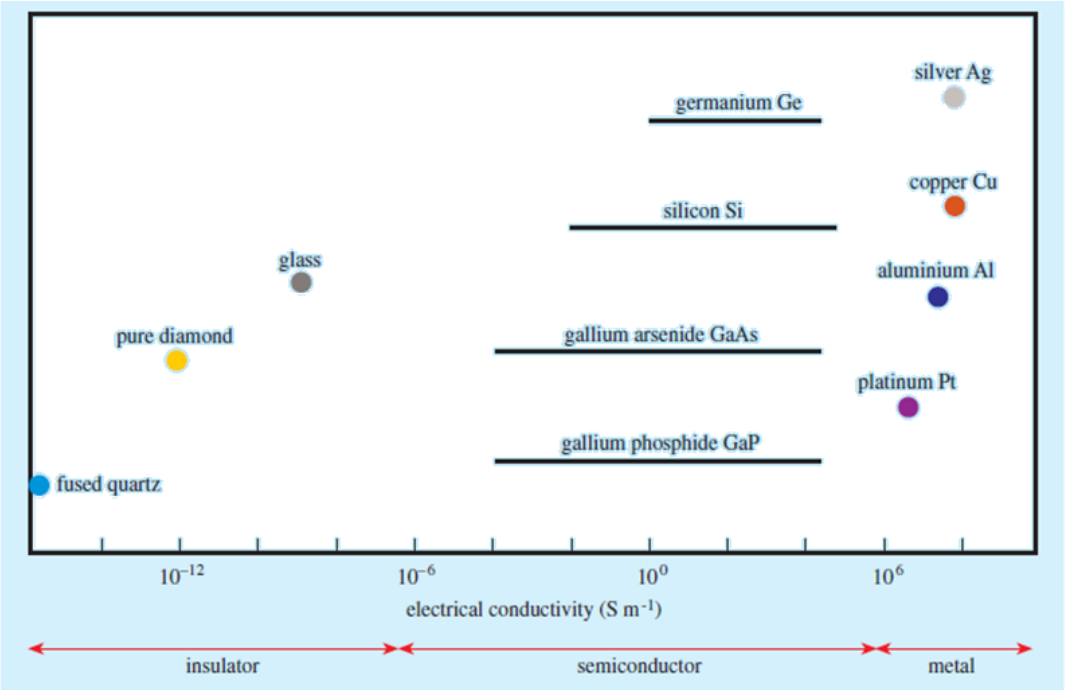

Figure IV.22: Comparison of electrical conductivities for insulators, metals and semiconductors [58].

Good electrical conductors, such as metals, are also known to be good thermal conductors (See Fig. IV.23). The conduction of thermal energy, which is one of the three forms of heat transfer (conduction, conversion and radiation), from higher to lower temperature regions in a metal involves the conduction electrons carrying the energy. Consequently, there is an innate relationship between the electrical and thermal conductivities, which is supported by theory and experiment. The early studies of electrical conduction in metals were done in the nineteenth centuries, where Physicists have tried to construct simple models to explain qualitatively and even quantitatively the characteristic properties of metals.

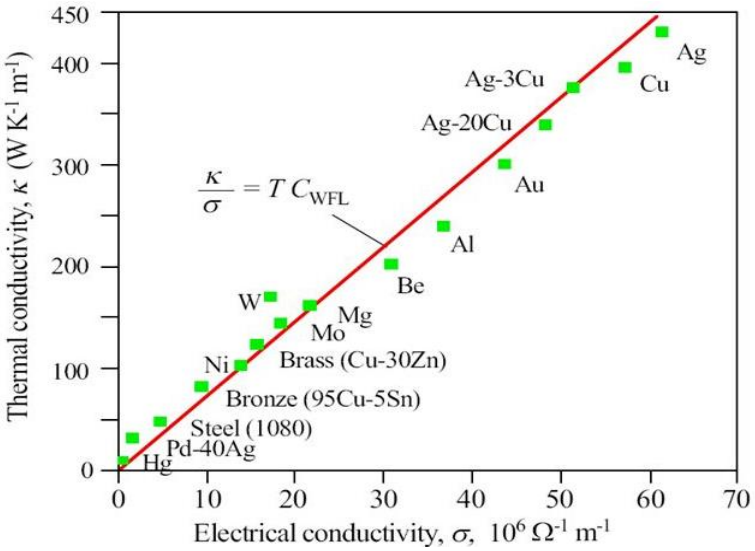

Figure IV.23: Thermal conductivity κ versus electrical conductivity σ for various metals (elements and alloys) at 20 ℃. The solid line represents the *WFL* law with $C_{WFL} = 2.44 \times 10^{-8}(W.\Omega.K^{-2})$ [14]

IV.5.3. Optimisation of thermoelectric materials

The performance of thermoelectric compounds is defined by their figure of merit ZT that given as: [55]

$$ZT = \frac{S^2\sigma}{\kappa}T = \frac{S^2\sigma}{\kappa_{el} + \kappa_l}T \qquad (IV.41)$$

The thermal conductivity κ includes two parts: the electronic thermal conductivity κ_{el} (i.e., the carriers consisted of electrons and holes transporting heat) and the lattice thermal conductivity κ_l (i.e., phonon transporting heat). The fundamental problem in creating efficient thermoelectric materials is that they need to be good at conducting electricity, but not at conducting thermal energy. That way, one side can get hot while the other gets cold, instead of the material quickly equalizing the temperature. However, in most materials, electrical and thermal conductivity go hand in hand [59]. Fig. IV.24 shows the compromise between high thermo-power and large electrical conductivity in potential thermoelectric materials that must be achieved to maximize the thermoelectric figure of merit. The optimal temperature at which the figure of merit peaks is achieved at carrier concentration between 10^{18} and 10^{21} carrier per cm^3. This type of carrier concentration is found in

common metals and heavily doped semiconductors. Insulators and semiconductors are both low carrier concentration and show large Seebeck coefficients (See Tab. IV.24). However, low carrier concentration materials result in low electrical conductivity.

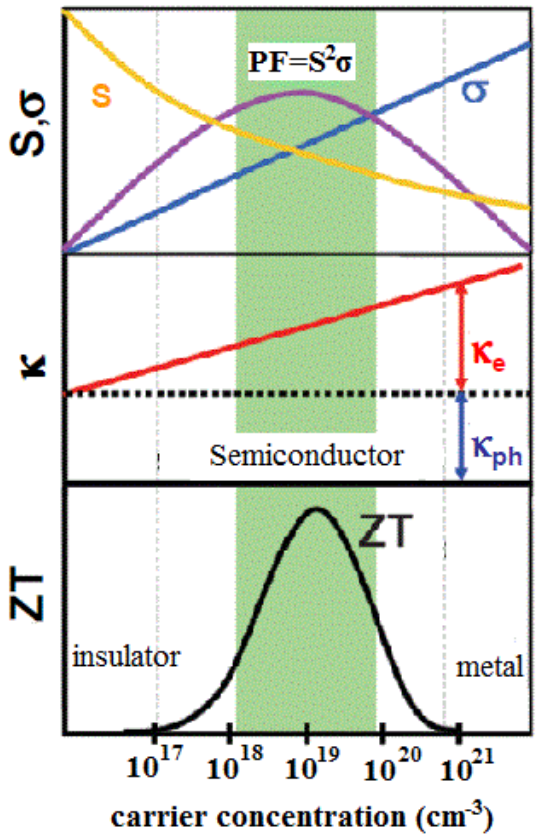

Figure IV.24: Evolution of the figure merit value ZT and the different electrical and thermal properties as a function of charge carrier concentration [60].

The increase in ZT is due to the introduction of interfaces created by the lattice mismatches of the bulk materials that make up the superlattice. These interfaces serve to scatter the phonons reducing the thermal conductivity while not adversely affecting the electrical conductivity.

Table IV.14: Electronics transport properties of Metals, semi-conductors and isolates at 300 K [60].

Properties	Metals	Semiconductors	Isolates
S ($\mu V.K^{-1}$)	~ 5	~ 200	~ 10^3
σ ($\Omega^{-1}.cm^{-1}$)	~ 10^6	~ 10^3	~ 10^{-12}
Z (K^{-1})	~ $3x10^{-6}$	~ $2x10^{-3}$	~ $5x10^{-17}$

IV.5.4. From conventional to new thermoelectric materials

Over the past few years, thermoelectric materials are of renewed interest for applications as heat pumps and power generators. Bismuth telluride (Bi_2Te_3) is a well-known narrow bandgap semiconductor, this compound has been widely studied principally for its thermoelectric properties. It currently stands as one of the best room-temperature thermoelectric materials (See Fig. IV.25 and Tab. IV.15) [61]. Low-dimensional systems allow for the alteration of the electronic structure through the choice of dimensionality, 3D to 0D. In 1993, L.D. Hicks and M.S. Dresselhaus published theoretical results exploring the effects of a 2D system on the thermoelectric figure-of-merit. The theoretical investigation proposed that a 2D quantum well structure could increase *ZT* of bismuth telluride (Bi_2Te_3).

Table IV.15: Thermoelectric coefficients of conventional materials.

	Temperature for maximum *ZT* (K)	Effective mass (m_0)	Mobility ($m^2/V.s$)	Lattice thermal conductivity ($W/m.K$)	*ZT*
Bi_2Te_3	300	0.2	0.12	1.5	1.3
PbTe	650	0.05	0.17	1.8	1.1
$Si_{1-x}Ge_x$	1100	1.06	0.01	4.0	1.3

Recently, many semiconductors have already been tested as potentially appropriate materials for thermoelectric applications, such as Skutterudites [62], Clathrates « Phonon-glass electron-crystal » [63], Heusler compounds and their alloys [64], Tetrahedrite and Tennantite materials [65], Zintl phases [66], layered compounds [67]…. etc. There is much

excitement about layered structure material for high-density applications and for replacing conventional material.

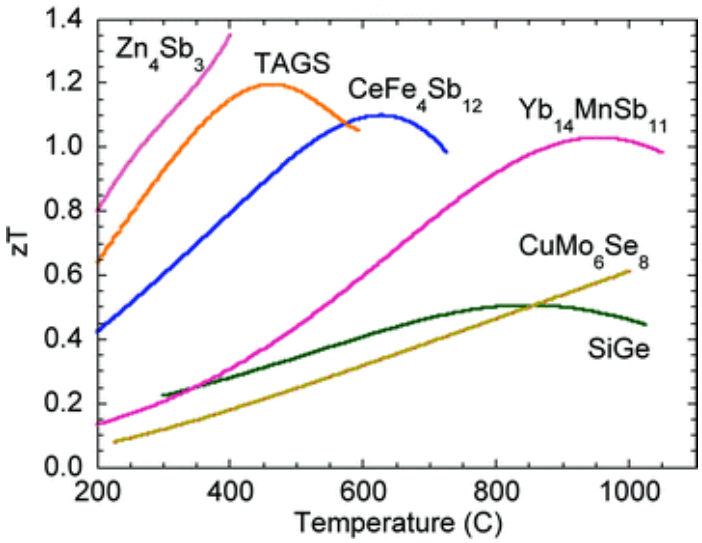

Figure IV.25: Figure of merit as a function of temperature for a number of some *p*-type materials [68].

The best thermoelectric materials commercially available today are alloys of bismuth telluride.

IV.6.5. Chemical potential

Chemical potential was first, described by the American engineer, chemist and mathematical physicist ***Josiah Willard Gibbs***. He defined it for a thermodynamic system as the total change in free energy per extra mole of substance; it is measured in units of energy/particle or, equivalently, energy/mole: [69, 70]

$$\mu_i = \left(\frac{\partial U}{\partial N_i}\right)_{S,V,N_{j\neq i}} \qquad (\mathrm{V}.42)$$

Here ∂U is the infinitesimal change of internal energy U, and ∂N is the infinitesimal change of particle number N_i of species i as particles are added or subtracted. Respectively, S and V is the entropy and volume for a thermodynamic system in thermal equilibrium.

More specifically chemical potential called total chemical potential. If two locations have different total chemical potentials for a species, some of it may be due to potentials associated with "external" force fields, while the rest would be due to "internal". Therefore, the total chemical potential can be split into internal chemical potential and external chemical potential:

$$\mu_{tot} = \mu_{int} + \mu_{ext} \qquad \text{(IV. 43)}$$

The term "chemical potential" sometimes means "total chemical potential", but that is not universal. In some fields, such us solid-state physics, the term "chemical potential" means internal chemical potential. In the case of semiconductor, the temperature witch considering us an external field, lead to electron transition from the valence band to the conduction band and generation of free holes on the valence band. Resulting non-current state.

$$\mu_{tot} = \mu_{int} \qquad \text{(IV. 44)}$$

The intrinsic chemical potential is an increasing function of the carrier concentration provided the physical system is stable.

$$(\mu_{int})_{ext} = (E_F)_{ext} = (E_F)_{int} \pm \frac{\partial U}{\partial N} \qquad \text{(IV. 45)}$$

Respectively, $(E_F)_{ext}$ and $(E_F)_{int}$ are the Fermi levels of an extrinsic and intrinsic semiconductors.

In semiconductor physics, the chemical potential of a system of electrons at a temperature of zero Kelvin is known as the Fermi energy. The Fermi level expresses the work required to add an electron to it, or equally the work obtained by removing an electron.

Assuming the electron transport in the material is due to a single parabolic band, the density of states scales as square root of energy. Further, as electrons are Fermions, only a small bandwidth of energy (few k_BT, where k_B is Boltzmann constant and T is temperature) close to the chemical potential is relevant for electron transport. As one shifts the chemical potential further into a band from an energy gap, the carrier concentration increases. As one know, as the chemical potential increases and lies deeper into the band, the electrical conductivity increases, explaining why metals are good conductors compared to semiconductors. On the other hand, electrical conductivity is directly related to thermo-

power; hence, this value decreases as the chemical potential moves further deep into the band. This explains the origin of low thermo-power of metals as compared to semiconducting materials. This conflicting nature of thermo-power and electrical conductivity evolution with carrier concentration is the key reason why carrier concentration is used as an optimization parameter to achieve high figure of merit *ZT* [71].

IV.5.6. Chemical potential dependence of TE properties of BaFAg*Ch* (*Ch* = S, Se and Te)

The band structure calculation for BaFAg*Ch* (*Ch* = S, Se and Te) shows that the three investigated compounds have high densities of states near the band gap and a flat band dispersion on the valence band, especially along the z directions, suggesting the high thermoelectric efficiency of these compounds. The BoltzTraP code based on the semi-classical Boltzmann theory are used to investigate the thermoelectric coefficients of the BaFAg*Ch* (*Ch* = S, Se and Te) compounds. Respecting to the relaxation time, the BoltzTraP code gives the electronic transport versus three variable:

- Temperature.
- Carrier concentration.
- Chemical potential.

Together, temperature and carrier concentration, provide an understanding of how the matter behave. In Fig. IV.26, the Seebeck tensor S and the power factor ($PF = S^2\sigma/\tau$) are plotted with respect to the chemical potential μ at three fixed temperatures: 300, 600 and 900 K. The total density of state is also displayed in Fig. IV.26; this can explain which bands are contributing more towards the thermoelectric coefficients. According to the obtained results, the following points can be concluded:

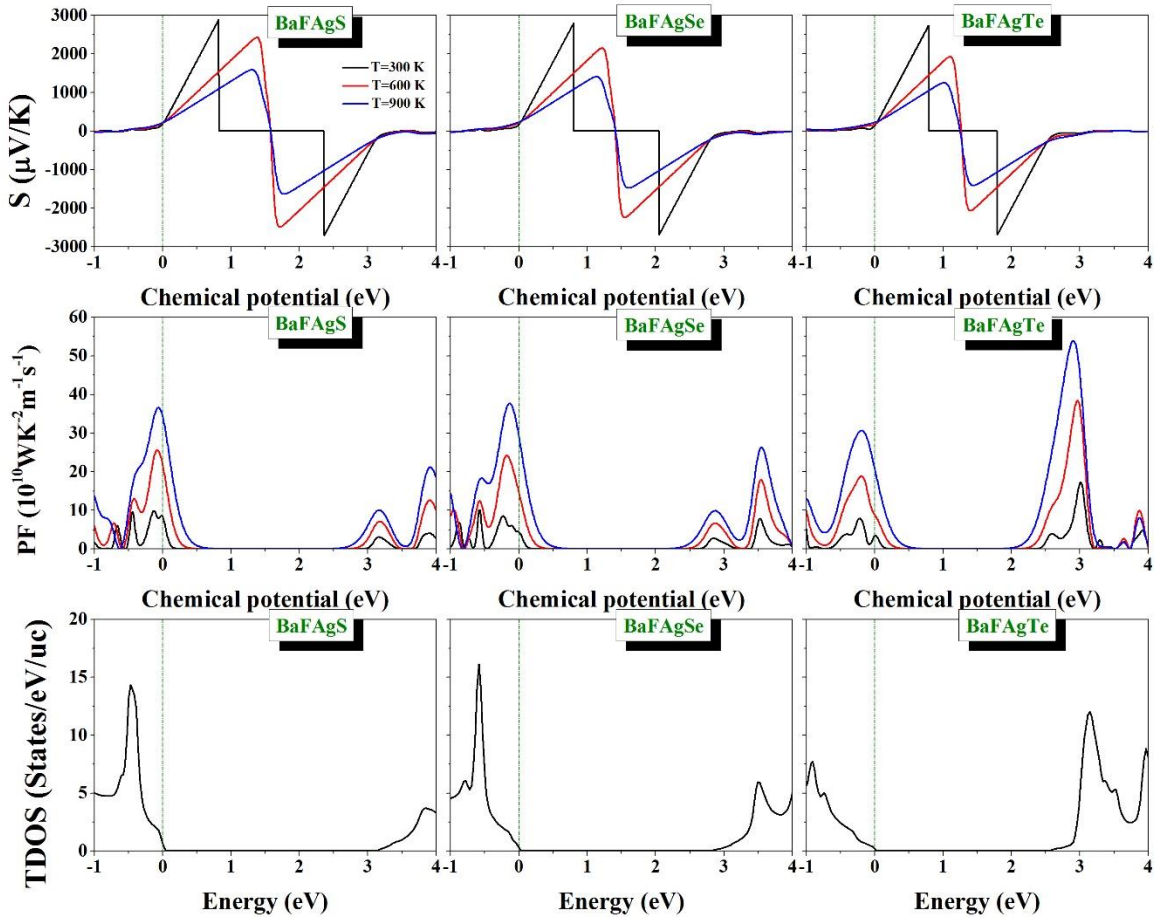

Figure IV.26: Variation of Seebeck coefficient (in the unit of μV/K) and Power factor (in the unit of W/(K^{2}ms)) vs chemical potential at three fixed temperatures: T = 300 K, T = 600 K, and T = 900 K. The total density of state is also plotted for a direct comparison. The Fermi energy is plotted as a dashed line.

- At Fermi level, the Seebeck coefficient show positive values, indicating that the majority charge carriers are holes, for the three compounds.
- Near the Fermi level, the power factor is more dominate in the negative chemical potential region, suggesting that doping with holes might will be more favourite for thermoelectric efficiency than doping with electrons.
- Both Seebeck coefficient and power factor of the BaFAg*Ch* (*Ch* = S, Se and Te) increase with increasing temperature.
- Both Seebeck coefficient and power factor of BaFAg*Ch* (*Ch* = S, Se and Te) decrease when the *Ch* atom is substituted in the following sequence $S \rightarrow Se \rightarrow Te$.

- The needed hole concentration to obtain the maximum power factor increases when going from of length from BaFAgS than BaFAgSe and BaFAgTe.

IV.5.7. Relaxation time and lattice thermal conductivity

Within the constant relaxation time approximation (CRTA), the Seebeck coefficient can be calculated without any adjustable parameters; however, the electrical conductivity has to be calculated with respect to the relaxation time, therefore it is crucial to determine τ to estimate the electrical conductivity and thermal conductivity. Generally, two ways are proposed to determine the τ value: (i) from the experimental value of the resistivity, or (ii) from a theoretical calculation. As there are no experimental data that allow the calculation of the τ values of the considered compounds, a theoretical method was used to estimate τ. An approximation that has a large success for calculating τ is based on the deformation potential theory developed by Bardeen and Shockley [72-74]:

$$\tau = \frac{2\sqrt{2\pi}\, C_\beta \hbar^4}{3(m^* K_B T)^{\frac{3}{2}} E_\beta^2} \qquad \text{(IV. 46)}$$

where C_β is the 3D elastic constant, E_β is the 3D deformation potential and m^* is the charge-carrier effective mass. The method to calculate E_β and C_β can be found in Ref. [75]. The necessary parameters to calculate τ are listed in Tab. IV.16. The variation of τ as function of temperature is depicted in Fig. IV.27. Practically, temperature dependence of the relaxation time is similar in the three studied compounds; the relaxation time d ecreases with increasing temperature. When temperature increases, the thermal speed of electrons increases and consequently collisions between electrons become more considerable, and the vibration amplitude of atoms around their mean positions increases; all these decrease the relaxation time.

Thermal conductivity describe the capacity of matter to transport the heat energy under applied gradient temperature, it consist from two part; the first one (κ_{el}), it has their origin from the motion of electrons, called electronic thermal conductivity, lattice thermal conductivities (κ_l) is the second part which express the vibration response of the lattice (i.e., phonons). Meanwhile, the BoltzTraP code gives just the electronic part. For more accurate calculation, it is necessary to calculate the contribution of the lattice vibration to the thermal conductivity. Usually, the best values of the figure of merit of materials occur

at mid or high temperature, and at this range of temperature, their lattice thermal conductivities (κ_l) are comparable to their minimum lattice conductivities (κ_{min}). At high temperature, the lattice thermal conductivity deceases to a lower limit (κ_{min}) with increasing temperature. The minimum lattice thermal conductivity (κ_{min}) can be calculated using Cahill model [76, 77], which gives a good estimation of the minimum lattice thermal conductivity for a large class of materials [78, 79]. The calculated values of the minimum lattice thermal conductivity $\kappa_{\min}$ for the considered compounds are listed in Tab. IV.16. The calculated κ_{min} of the three studied compounds are smaller than unity, suggesting that these compounds might be good TE candidates

Table IV.16: Calculated 3D elastic constant (C_β, in GPa unit), 3D deformation potential (E_β, in eV unit) and the minimum lattice thermal conductivity (k_{min}, in $Wm^{-1}K^{-1}$ unit) using Cahill model for the BaFAg*Ch* (*Ch* = S, Se and Te) compounds.

properties	C_β		E_β				k_{min}
Direction	*a*-axis	*c*-axis	*a*-axis		*c*-axis		
Carrier			h	e	h	e	
BaFAgS	110.32	77.78	9.35	11.83	10.98	13.94	0.612
BaFAgSe	103.60	62.92	9.70	12.40	9.88	12.97	0.544
BaFAgTe	94.26	50.53	10.59	13.37	9.78	12.80	0.420

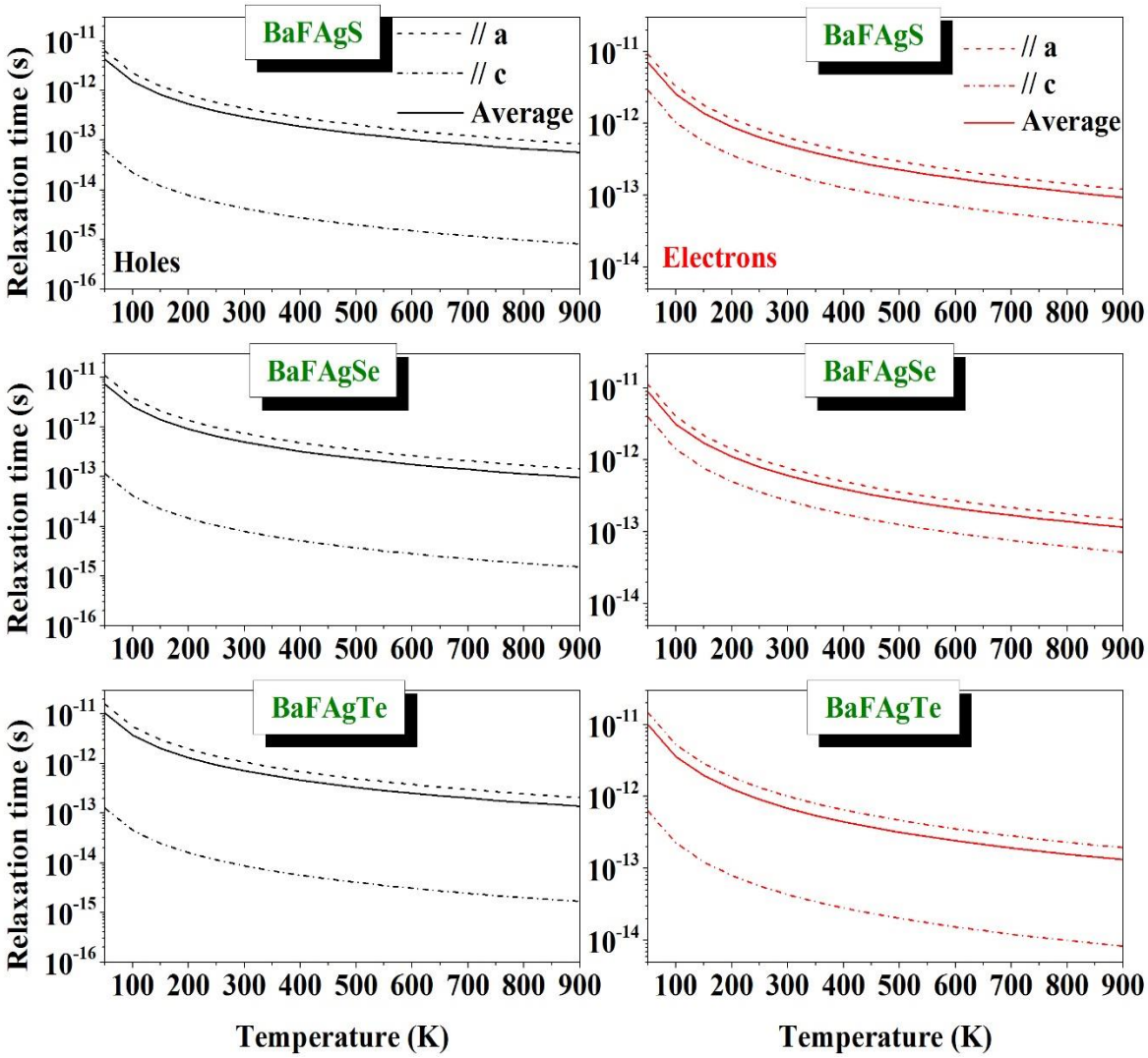

Figure IV.27: Temperature dependence of the relaxation *time (τ)* for the BaFAg*Ch* (*Ch* = S, Se and Te) compounds.

IV.5.8. Carrier concentration and temperature dependence of TE properties for BaFAg*Ch* (*Ch* = S, Se and Te)

Variation of the Seebeck coefficient, electrical conductivity, thermal conductivity and figure of merit as functions of carrier concentration for both ***p***-type and ***n***-type BaFAgS, BaFAgSe and BaFAgTe in the range 10^{16} - 10^{20} cm^{-3} along the [100] (a-axis) and [001] (c-axis) crystallographic directions at T = 900 K are plotted in Fig. IV.28. From this curves, the following conclusions can be made:

- The absolute value (magnitude) of the Seebeck coefficient (*S*) decreases with increasing carrier concentration and increases with increasing temperature for both the *n*-type and *p*-type compounds.
- The magnitude of S for the *p*-type system is higher than that of the *n*-type one throughout the considered concentration range of charge carriers. This result is consistent with the already predicted result from the calculated charge-carrier masses; large effective masses of charge-carriers translates to a high Seebeck coefficient.
- The thermo-power (*S*) shows practically the same behaviour regarding the variation of carrier concentration and temperature for the three studied compounds. This behaviour is attributed to the similarity of their energy band dispersions around the Fermi level.
- For the charge-carrier concentration, the value of (*S*) decreases when we move from BaFAgS to BaFAgSe to BaFAgTe. This might be due to the decrease of the charge-carrier effective masses when we move in the same sequence.
- Seebeck coefficient has almost an isotropic behaviour along the different crystallographic directions.

The *p*-type BaFAgS, BaFAgSe and BaFAgTe compounds are more favourable for TE performance than the *n*-type ones.

- The electrical conductivity, electronic thermal conductivity and figure of merit are considerably anisotropic, which is consistent with the layered structure of the title compounds.
- The electrical conductivity, thermal conductivity and figure of merit of the *p*-type compounds along the a-axis and in the *ab*-plane are considerably larger than the corresponding ones along the *c*-axis. This might be because the lower hole effective mass along the a-axis and in the *ab*-plane compared to the corresponding one along the *c*-axis.
- The anisotropy of the electrical and thermal conductivities in the *n*-type compounds is less pronounced than that in the *p*-type one. This might be due to the almost equal values of the electron effective masses along the different crystallographic directions.
- To facilities the comparison, all the numerical values were listed in Tab. IV.17.
- We note that curves corresponding to 300 K and 600 K are similar to those obtained at T = 900 K.
- Our results compare favourably with the values of order reported for the Cu-based *p*-type transparent conductors.

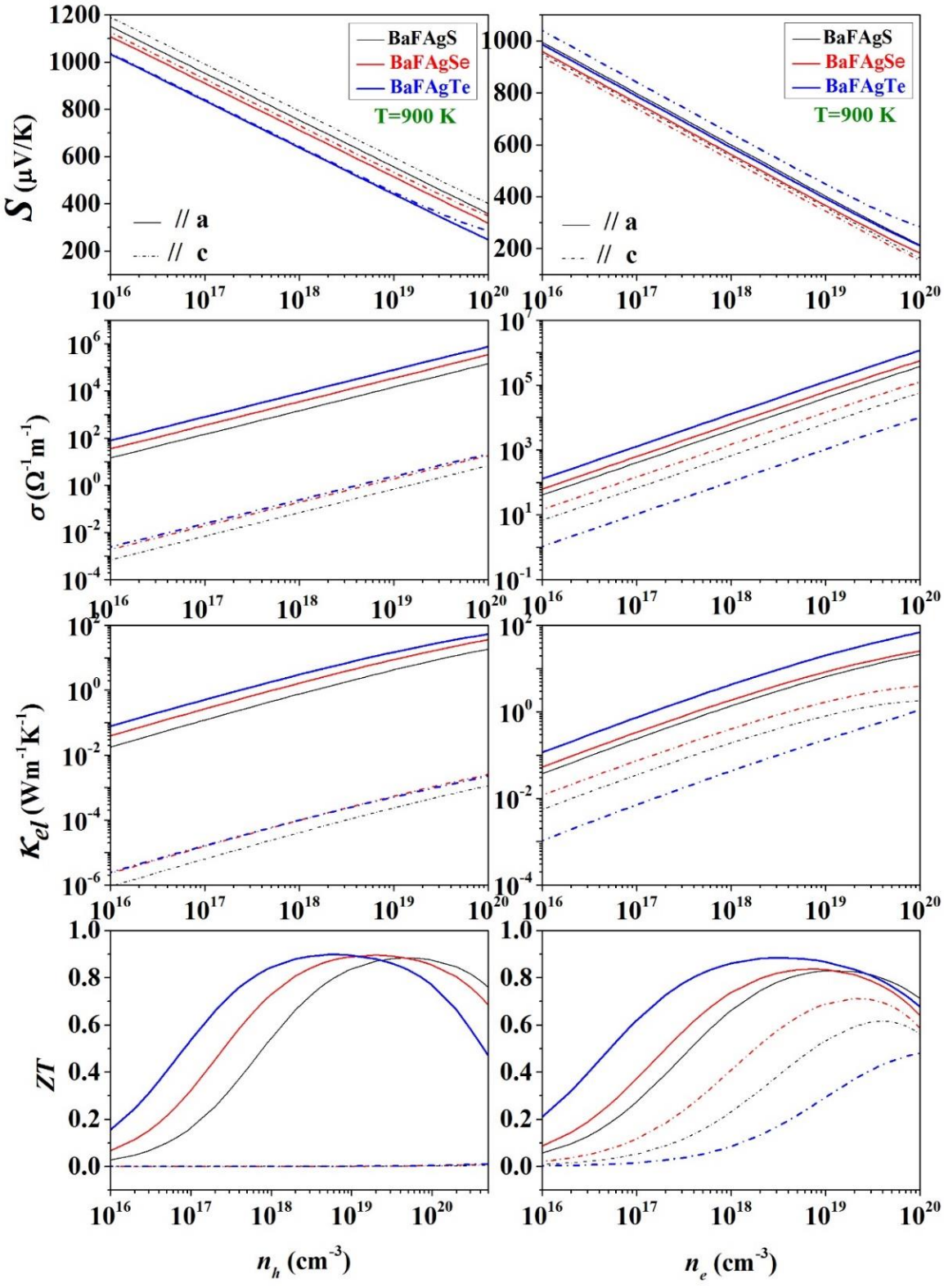

Figure IV.28: Charge carrier concentration dependence of the Seebeck coefficient, electrical conductivity, electronic thermal conductivity and figure of merit at T = 900 K for the BaFAg*Ch* (*Ch* =S, Se, Te) compounds.

Table IV.17: Calculated thermoelectric properties (S (μV/K), σ($\Omega^{-1}m^{-1}$), κ ($WK^{-1}m^{-1}$), PF ($WK^{-2}m^{-1}$) and ZT) of BaFAg*Ch* (*Ch* = S, Se and Te) along the two axis ***a*** and ***c*** at fixed (hole/electrons) doping $n = 10^{19}$ cm^{-3}.

		300				600				900			
		n_h		n_e		n_h		n_e		n_h		n_e	
System		***a***	***c***	***a***	***c***	***a***	***c***	***a***	***c***	***a***	***c***	***a***	***c***
BaFAgS	***S***	451.4	357.6	248.8	241.7	515.4	495.3	343.8	318.1	556.4	595.0	402.0	357.9
	σ	9.8*10	7.389	2.8*10	6.0*10	3.2*10	1.417	8.7*10	1.7*10	1.5*10	0.696	4.0*10	6.6*10
	κ	6.484	$3*10^{-4}$	6.780	1.359	5.304	2.3*10	7.106	1.132	4.262	2.4*10	6.473	0.811
	PF	$2*10^{-2}$	$9*10^{-7}$	1.7*10	3.5*10	8.4*10	3.5*10	1.0*10	1.7*10	4.5*10	2.5*10	6.5*10	8.4*10
	ZT	0.85	$4*10^{-4}$	0.70	0.53	0.85	3.4*10	0.80	0.58	0.84	3.6*10	0.83	0.53
BaFAgSe	***S***	363.0	273.1	217.1	215.9	460.4	408.2	307.4	298.0	513.9	533.7	366.0	343.6
	σ	2.4*10	25.920	4.3*10	1.1*10	7.3*10	4.321	1.3*10	3.4*10	3.5*10	1.912	6.2*10	1.4*10
	κ	10.860	6.6*10	8.541	2.172	10.125	5.0*10	9.097	2.099	8.840	5.5*10	8.449	1.690
	PF	3.2*10	1.9*10	2.0*10	5.2*10	1.5*10	7.2*10	1.3*10	3.0*10	9.3*10	5.4*10	8.3*10	1.7*10
	ZT	0.84	1.1*10	0.67	0.57	0.88	7.9*10	0.79	0.68	0.89	9.0*10	0.83	0.69
BaFAgTe	***S***	311.8	209.6	229.0	226.3	385.8	309.7	319.9	320.3	440.3	447.66	392.6	448.1
	σ	5.7*10	41.005	8.610^{5}	6.6*10	1.7*10	5.982	2.9*10	2.1*10	7.9*10	2.389	1.3*10	1.0*10
	κ	19.082	6.1*10	18.537	0.137	16.705	4.2*10	21.004	0.162	15.039	5.1*10	20.146	0.229
	PF	7.2*10	1.6*10	4.5*10	3.4*10	2.5*10	5.7*10	2.9*10	2.2*10	1.5*10	4.8*10	2.0*10	2.1*10
	ZT	0.74	1.3*10	0.71	0.18	0.88	8.2*10	0.82	0.22	0.89	1.0*10	0.83	0.37

It is very important to know the best ranges of the charge carrier concentration and temperature where the TE efficiency is high. High TE efficiency requires a high Seebeck coefficient, high electrical conductivity and low thermal conductivity. Fig. IV.29 shows the Seebeck coefficient (*S*), electrical conductivity (σ), electronic thermal conductivity (κ_{el}) and factor of merit (*ZT*) maps as functions of temperature and carrier concentration along the *a*-direction for the *p*-type BaFAgS, BaFAgSe and BaFAgTe. Fig. IV.29 and Tab. IV.17 show that the Seebeck coefficient increases with increasing temperature and decreases with increasing hole concentration, but at high hole concentration, it saturates at high temperatures. The electrical conductivity decreases with increasing temperature for a fixed hole concentration. The thermal conductivity remains approximately constant with increasing temperature for a fixed hole concentration. However, at a fixed temperature, both the electrical and thermal conductivities increase sharply with increasing hole concentration.

The influence of carrier concentration on the figure of merit is much more evident than that of the temperature. The high values of the figure of merit are found for carrier concentration around 10^{19} cm^{-3} with a large range of temperature from 300 K to 900 K. For BaFAgS, *ZT* along the *a*-axis = 0.88 at T = 900 K and hole concentration of $5\times10^{19}cm^{-3}$, for BaFAgSe, *ZT* along the *a*-axis = 0.89 at T = 900 K and hole concentration of $2\times10^{19}cm^{-3}$ and for BaFAgTe, *ZT* along the *a*-axis = 0.90 at T = 900 K and hole concentration of $6\times10^{18}cm^{-3}$. It is worth to note here that *ZT* of the considered compounds attains a value slightly higher than the aforementioned ones for temperature higher than 900 K. The thermoelectricity efficiency of the studied compounds can be enhanced if one could reduce the lattice thermal conductivity κ_l by introducing further phonon scattering centres by alloying or doping by chemical elements that reduce the lattice thermal conductivity.

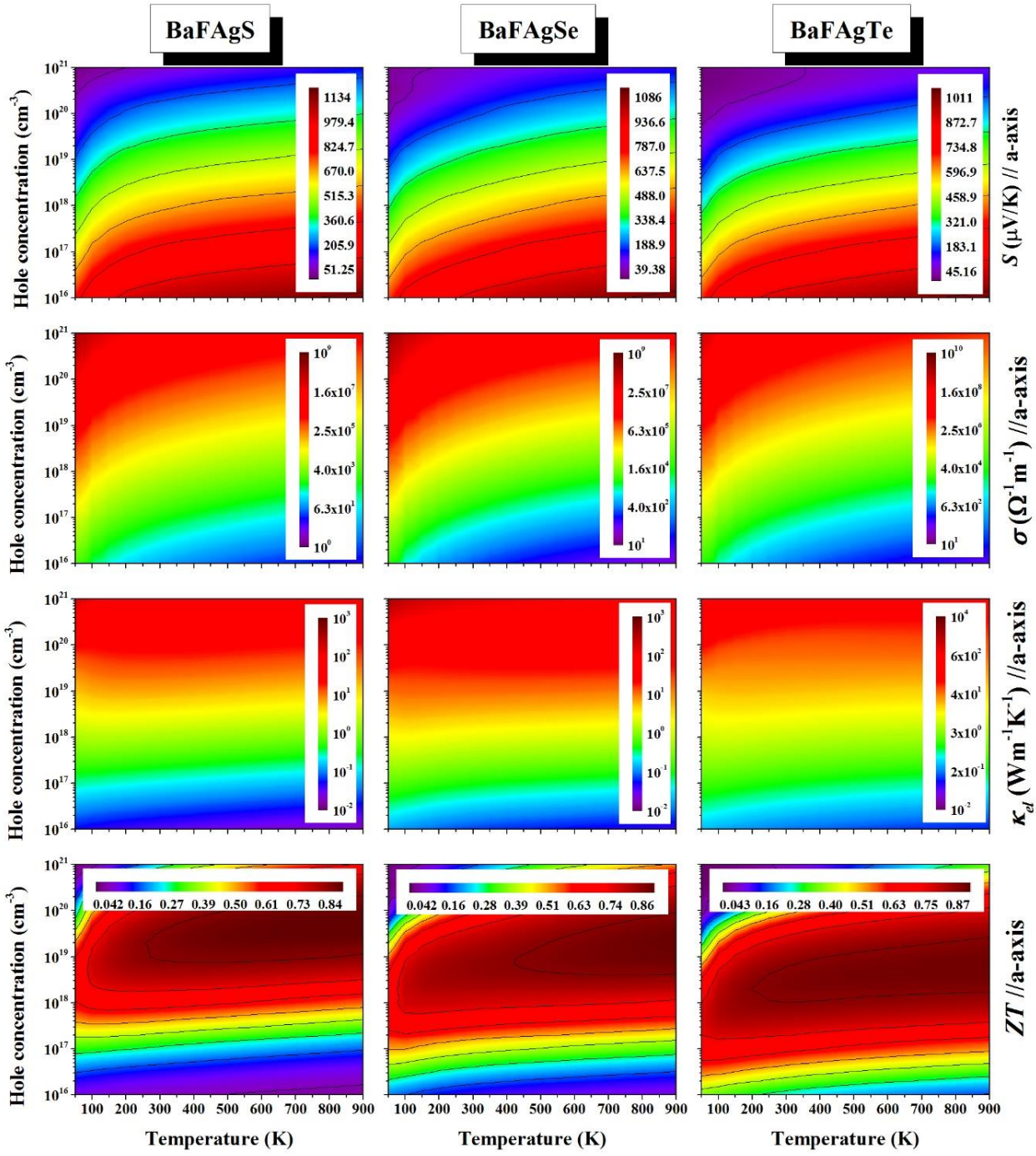

Figure IV.29: Maps of the calculated hole concentration and temperature dependences of the Seebeck coefficient (S, in μV/K unit), electrical conductivity (σ in ($\Omega^{-1}m^{-1}$) unit), electronic thermal conductivity (κ_{el} in ($WK^{-1}m^{-1}$) unit) and figure of merit (ZT, dimensionless) for the BaFAg*Ch* (*Ch* = S, Se, Te) compounds.

IV.6. Thermodynamic properties of BaFAg*Ch* (*Ch* = S, Se and Te)

Thermodynamics [80], is the branch of physics concerned with pressure and temperature and their relation to energy and work. The behaviour of these quantities is governed by the four laws of thermodynamics, irrespective of the composition or specific properties of the material or system in question. The laws of thermodynamics are explained in terms of macroscopic constituents by statistical mechanics. Thermodynamic properties (including heat capacity, thermal expansion coefficients, Debye temperature…etc.) is a very useful tool in science and engineering, including geophysics, physical chemistry, chemical engineering and mechanical engineering.

Many physical properties of an atomic crystalline lattice can be successfully determined from first principles within the static approximation at zero temperature. However, the crystal lattice is not just a rigid collection of atoms under symmetry constraints. On the contrary, it is in a continuous dynamical state, with atoms vibrating around their respective equilibrium positions. Thermodynamic properties related directly with the atomic vibration witch can be expressed as energy or the wavy nature of energy. At 0 K, the atoms have the minimum energy. When heat is supplied to the material, the atoms gain heat energy and vibrate at a particular amplitude and frequency. This vibration produces an elastic wave called a "*phonon*". The phonon energy can be expressed as a function of wavelength or frequency, in much the same way as that of a photon, using the Planck relation ($E = h\nu = {}^{hc}/_{\lambda}$). Thus, the material gains or lose heat by gaining or losing phonons [81].

Previously, we have carried out detailed studies concerning the ground states of the quaternary compounds. The data computed through the equation of state (i.e., Energy versus volumes data that obtained using GGA08) are employed to evaluate pressure and temperature dependences of thermodynamic properties of BaFAg*Ch* (*Ch* = S, Se and Te). In our study, the quasi-harmonic Debye model that implemented in the Gibbs2 code (See Appendix) was used to study the variation of some fundamental physical properties with both temperature (from 0 to 900 K) and hydrostatic pressure (from 0 to 35 GPa).

From the macroscopic vision, the volume of matter (primitive cell volume) is strongly related to the temperature and pressure; the increase of the first one lead to increase of inter atomic distance; consequently the lattice parameters (volume), however the increasing of the second one reduce all the lattice parameters. The variation of the

primitive cell volume in (Bohr^3) with temperature at four fixed pressures: 0 GPa, 5 GPa, 10 GPa and 15 GPa, and with pressure at four fixed temperatures: 0 K, 300 K, 600 K and 900 K for BaFAgS, BaFAgSe and BaFAgTe are shown in Fig. IV.30. From Fig. IV.30 one can note the following:

✓ Qualitatively, temperature (T) and pressure (P) dependencies of the volume for the three investigated compounds are similar. For low temperature; less than 100 K ($T < 100\,K$), the volume is practically constant, but it increases remarkably with increasing temperature for temperatures $T > 100\,K$. On the next, we interesting by analysis of BaFAgS results.

- At a pressure equal to 0 GPa, the BaFAgS unit cell volume is equal to 1130.65 Bohr^3 at T = 300 K and 1162.98 Bohr^3 at T= 600 K, which corresponds to an increase of 2.86%.
- At pressure equal 5 GPa, the BaFAgS unit cell volume is equal to 1047.44 Bohr^3 at T = 300 K and 1066.48 Bohr^3 at T= 600 K, which corresponds to an increase of 1.82%.
- At pressure equal 10 GPa, the BaFAgS unit cell volume is equal to 990.52 Bohr^3 at T = 300 K and 1004.14 Bohr^3 at T= 600 K, which corresponds to an increase of 1.38%.
- At pressure equal 15 GPa, the BaFAgS unit cell volume is equal to 947.29 Bohr^3 at T = 300 K and 957.91 Bohr^3 at T= 600 K, which corresponds to an increase of 1.05%.

The volume increases practically linearly with temperature, and the increase becomes slower with increasing pressure.

✓At a fixed temperature, the volume decreases with pressure.

- At temperature equal 0 K, the BaFAgS unit cell volume is equal to 1111.52 Bohr^3 at P = 0 GPa and 1035.99 Bohr^3 at P = 5 GPa, which corresponds to an decrease of 6.80%, indicating that the influence of the pressure on the volume is much more evident than that of the temperature.

Fig. IV.31 and Fig. IV.32 gives respectivly the variation of the adiabatic bulk modulus B_S and the isothermal bulk modulus B_T with temperature and pressure for BaFAg*Ch* (*Ch* = S, Se and Te). It is noted from the figure that the relationship between bulk modulus and pressure (temperature) is nearly linear at fixed temperature (pressure).

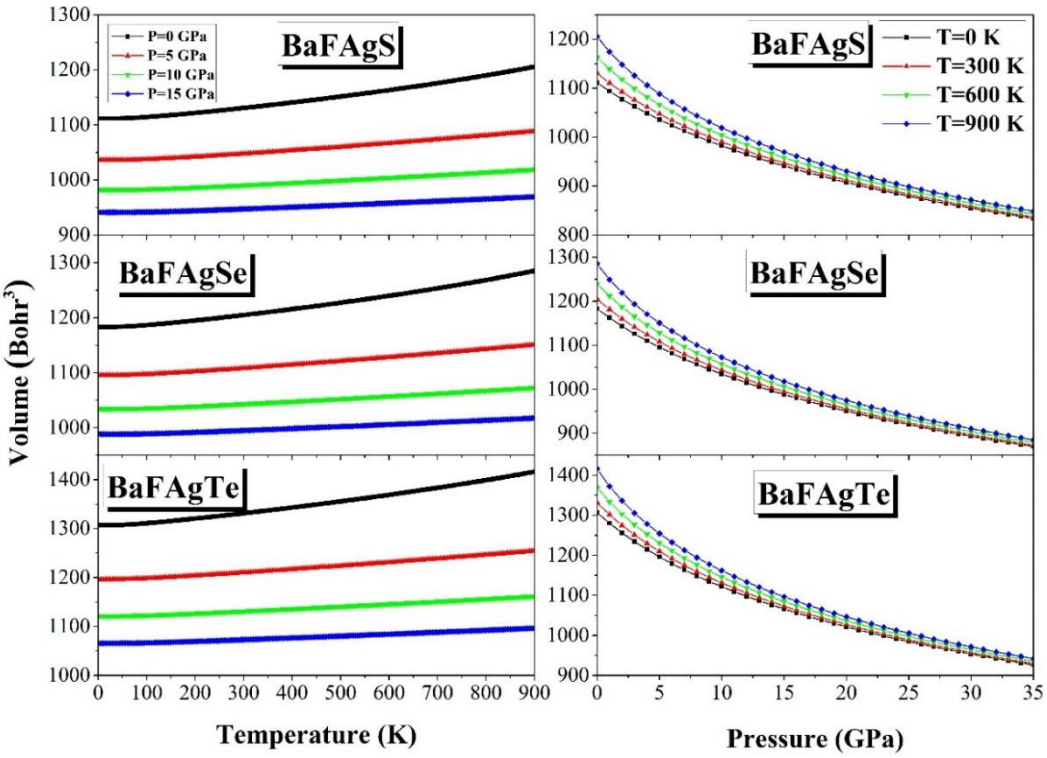

Figure IV.30: Variation of the primitive cell volume with temperature and pressure for BaFAg*Ch* (*Ch*=S, Se and Te).

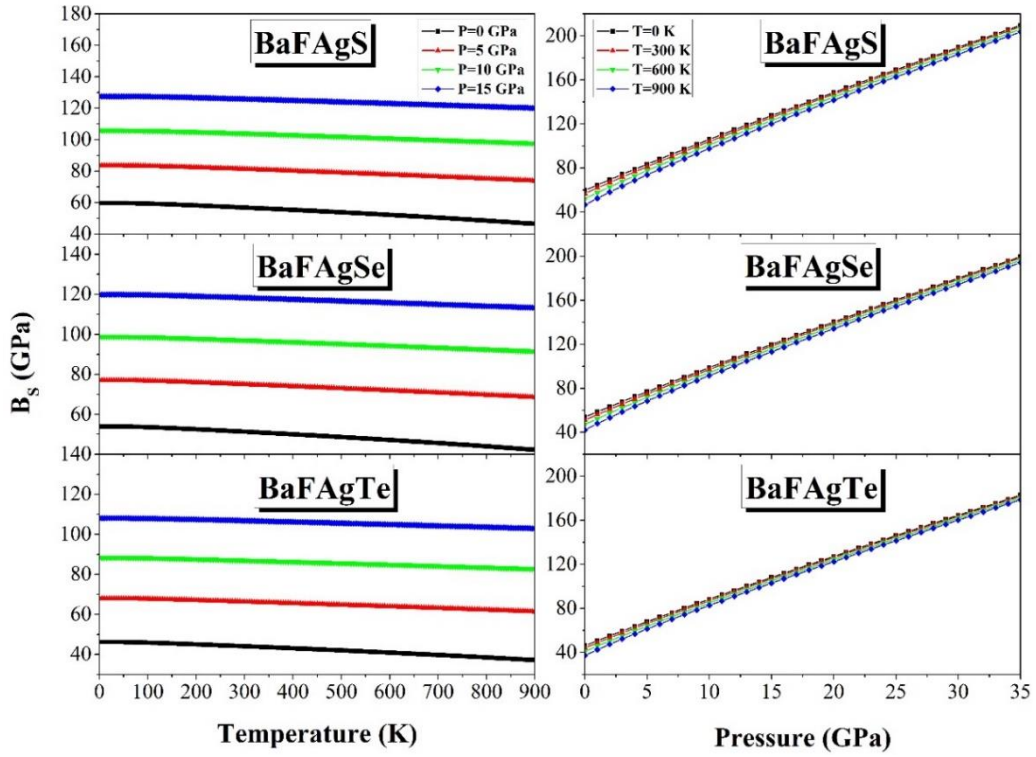

Figure IV.31: Variation of the adiabatic bulk modulus B_S with temperature and pressure for BaFAg*Ch* (*Ch* = S, Se and Te).

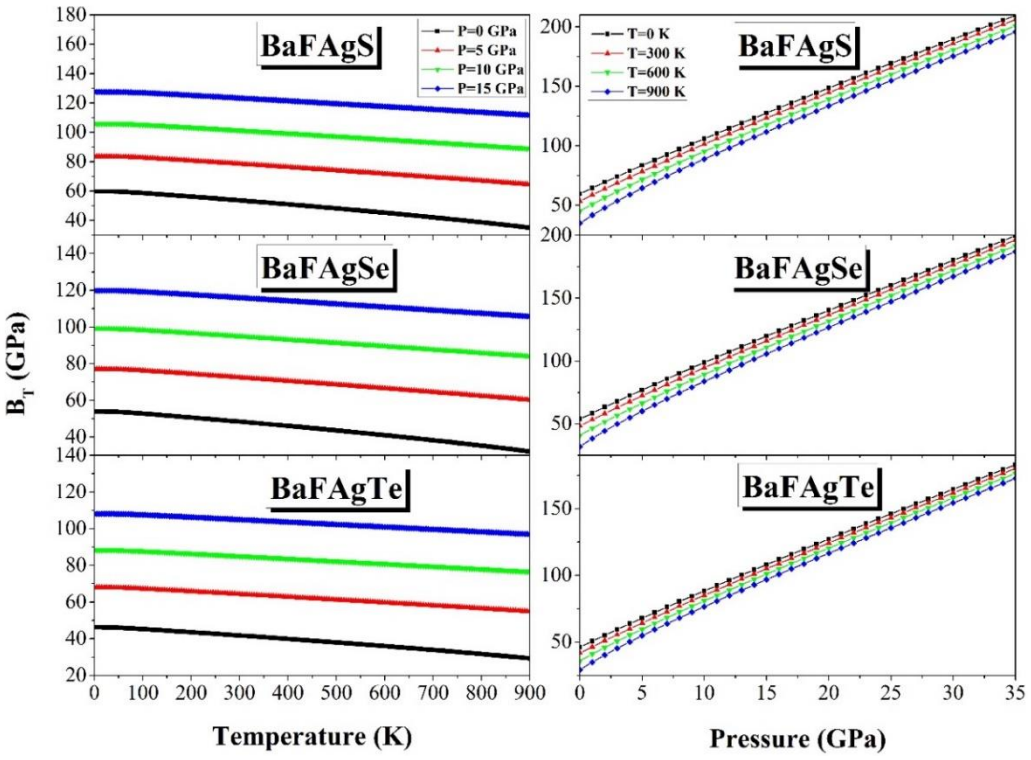

Figure IV.32: Variation of the isothermal bulk modulus B_T versus temperature and pressure for BaFAg*Ch* (*Ch* = S, Se and Te).

Heat capacity or thermal capacity [80, 82] is a measurable physical quantity equal to the ratio of the heat added to (or removed from) an object to the resulting temperature change. The unit of heat capacity is joule per kelvin (J/K). Measuring the heat capacity, sometimes referred to as specific heat, at constant volume can be prohibitively difficult for liquids and solids. That is, small temperature changes typically require large pressures to maintain a liquid or solid at constant volume, implying that the containing vessel must be nearly rigid or at least very strong (see coefficient of thermal expansion and compressibility). Instead, it is easier to measure the heat capacity at constant pressure (allowing the material to expand or contract freely) and solve for the heat capacity at constant volume using mathematical relationships derived from the basic thermodynamic laws. Starting from the fundamental thermodynamic relation one can show that:

$$C_P - C_V = T\left(\frac{\partial P}{\partial T}\right)_{V,n}\left(\frac{\partial V}{\partial T}\right)_n \qquad \text{(III. 47)}$$

where the partial derivatives are taken at constant volume and constant number of particles, and constant pressure and constant number of particles, respectively. This can also be rewritten as:

$$C_p - C_V = VT\frac{\alpha^2}{K} \qquad \text{(III. 48)}$$

Constant volume heat capacity C_V for the three compounds under different pressures and temperatures is curved in Fig. IV.33. At sufficiently low temperature, the changing C_V values under given pressures is proportional to T^3, then at high temperature, the amplification of C_V slows down evidently, and it tends towards a limited value when temperature keeps increasing, namely, Dulong-Petit limit. C_V decreases with increasing pressure; it can be easily found that C_V is more sensitive to the temperature than the pressure. Variations of the constant volume heat capacity C_P versus temperature and pressure are presented in Fig. IV.34.

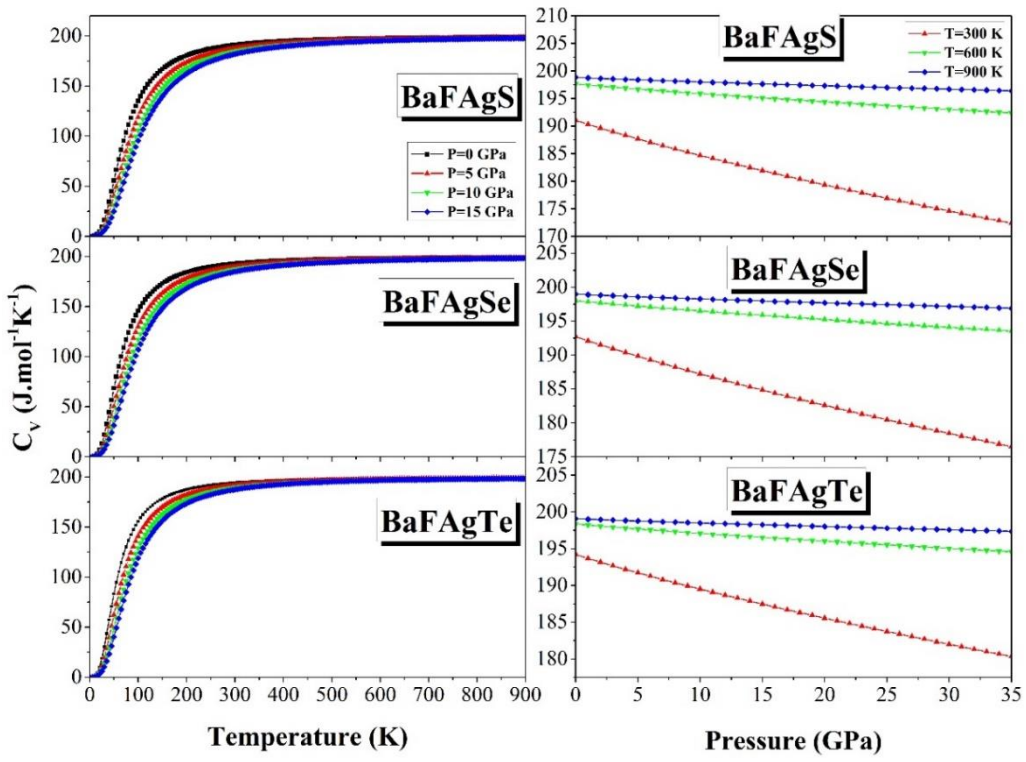

Figure IV.33: Calculated constant volume heat capacity C_V versus temperature and pressure for BaFAg*Ch* (*Ch* = S, Se and Te).

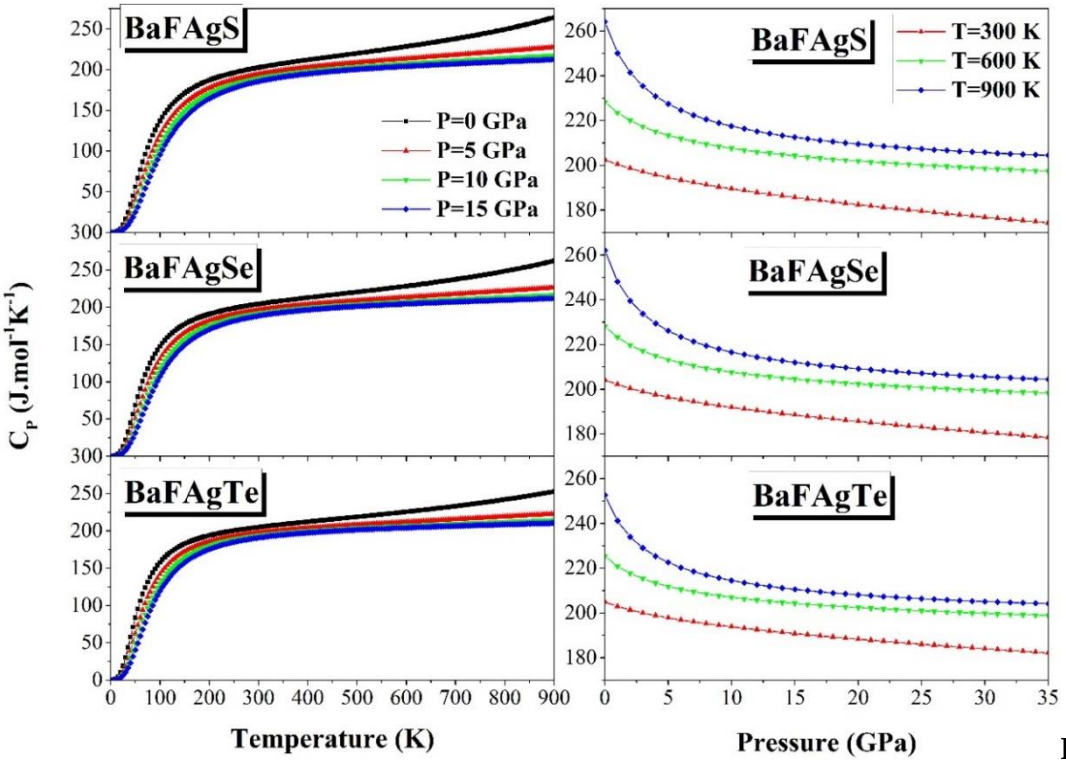

Figure IV.34: Calculated constant pressure heat capacity C_P versus temperature and pressure for BaFAg*Ch* (*Ch* = S, Se and Te).

Thermal expansion coefficient is an important parameter as it enters into many thermodynamic formulas and is expressed as the tendency of matter to change in volume in response to a change in temperature, typically represented by the symbol α:

$$\alpha_l = (l_T - l_0)/l_0(T - T_0) \qquad \text{(III. 49)}$$

Or

$$\alpha_V = (V_T - V_0)/V_0(T - T_0) \qquad \text{(III. 50)}$$

Where l_T (V_T) is the length (volume) of material at given temperature T. For a cubic material, $\alpha_l = 1/3\alpha_V$, where "*l*" is the length of an isotropic material.

From another side it's given as:

$$\alpha = \frac{\gamma C_V K}{V} \qquad \text{(III. 51)}$$

Where γ, C_V and K are the Gruneisen parameter (typically in the range of 1 to 3), specific heat at constant volume and isothermal compressibility, respectively.

With:

$$K = -(1/V)(\partial V/\partial P)_T \qquad \text{(III. 52)}$$

There are many potential applications for materials with controlled thermal expansion properties, as thermal expansion causes many problems in engineering, and indeed in everyday life. Within small temperature changes, the change in the length of a material is proportional to its change in temperature. The vast majority of materials have a positive coefficient of thermal expansion and their volume increases on heating and different materials expand by different amounts as shown in the table below. However, negative or even zero values could be observed in some cases: Zero expansion composites can be employed, for example, in high precision optical mirrors, where thin metallic layers are coated on a substrate; the use of a zero expansion substrate leads to a mirror whose optical properties do not degrade as temperature is varied. Perhaps the best known examples of materials with a negative thermal expansion coefficients are the ZrW_2O_8, ZrP_2O_7 and $Sc_2(WO_4)_3$ families [83-87]. Fig. IV.35 shows that for a two-coordinate bridging atom a longitudinal vibration will lead to an expansion of the interatomic distances, so the length will be increase. During a transverse vibration, however, if the interatomic distances remains essentially unchanged, the length will decrease.

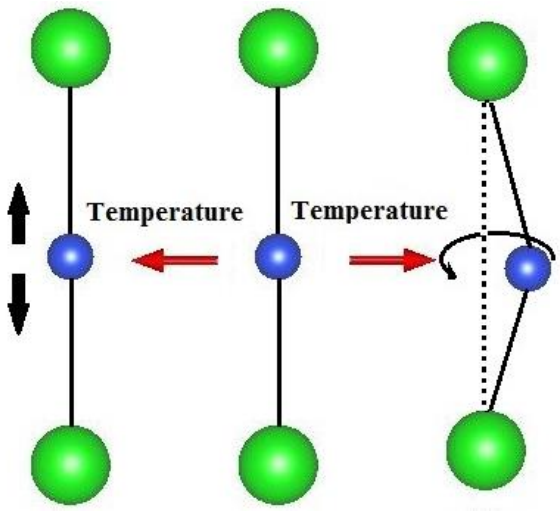

Figure IV.35: Schematic representation of the effect of different types of vibrational mode on thermal expansion. Transverse "*guitar string*" vibrations tend to lead to negative thermal expansion [83].

The thermal expansion coefficient α of the quaternary compounds BaFAg*Ch* (*Ch* = S, Se and Te) as a function of temperature at different pressures is curved in Fig. IV.36, left panel. From the α(T) curves we can observe that α increases rapidly with temperature at the range of low temperatures, then gradually show a linear smoothly increasing trend when the temperature increases. The thermal expansion coefficient α decreases with increasing pressure; Fig. IV.36, right panel.

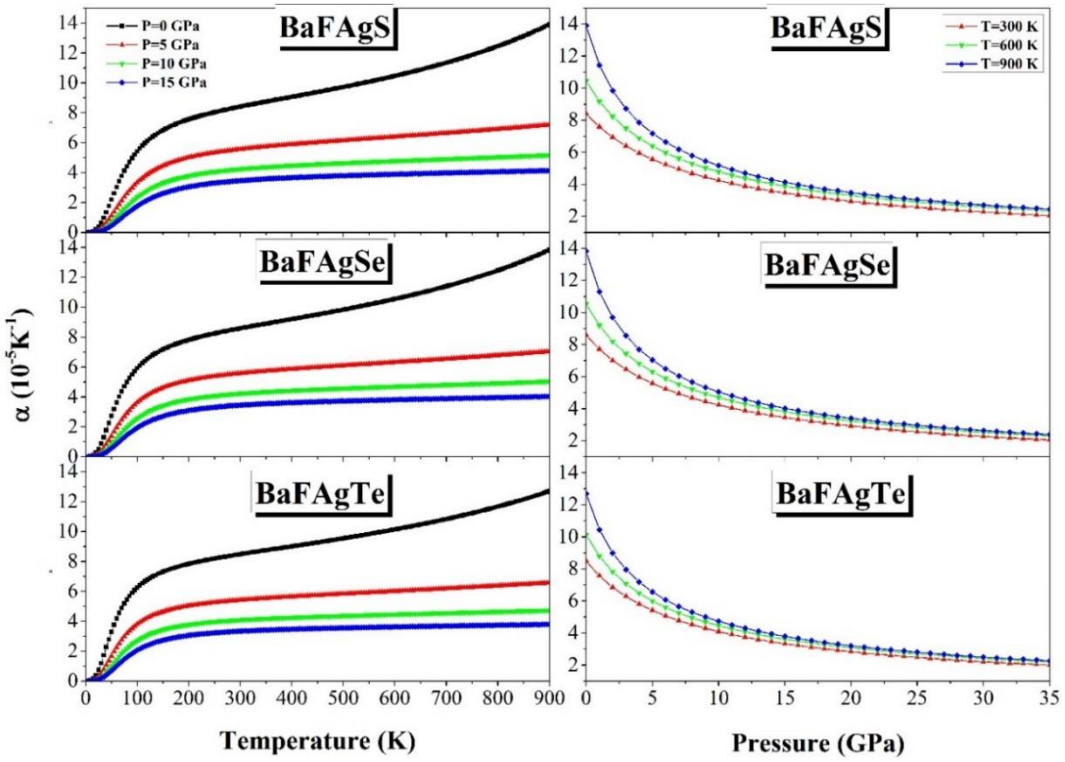

Figure IV.36: Variations of the thermal expansion coefficient α versus temperature and pressure for BaFAg*Ch* (*Ch* = S, Se and Te).

Grüneisen parameter is an extremely useful quantity in high-pressure physics. This parameter allows the extraction of a maximum of information from a minimum of data, which is a special virtue for experimental conditions where data are often difficult to obtain. Variations of the Grüneisen parameter γ versus pressure and temperature for the three considered compounds are shown in Fig. IV.37. From these curves one can observe

that γ increases linearly with temperature, especially at low pressures. Grüneisen parameter decreases slowly and smoothly with increasing pressure.

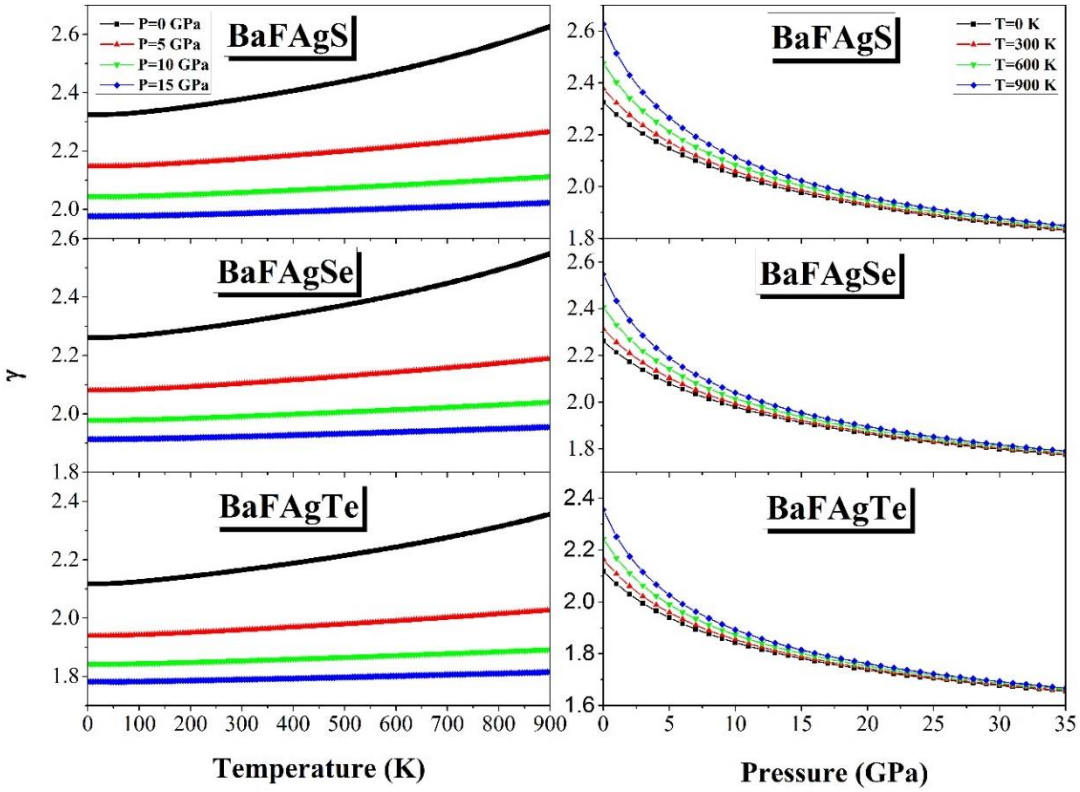

Figure IV.37: Variations of the Grüneisen parameter γ versus temperature and pressure for the BaFAg*Ch* (*Ch* = S, Se and Te) compounds.

In Debye theory, the Debye temperature θ_D is the temperature of a crystal's highest normal mode of vibration, i.e., the highest temperature that can be achieved due to a single normal vibration. The Debye temperature is given by:

$$\theta_D = \frac{h\nu_m}{k_B} \qquad \text{(IV. 53)}$$

Here, h is Planck's constant, k_B is Boltzmann's constant, and ν_m is the Debye frequency. Fig. IV.38 displays the variations of Debye temperature versus temperature at some fixed pressures for the three studied compounds. It can be seen that θ_D is nearly constant at low

temperature and decreases linearly with increasing temperature. With increasing pressure the slope of the $\theta_D(T)$ curve becomes gentler. Debye temperature θ_D increases almost linearly with increasing pressure at fixed temperature.

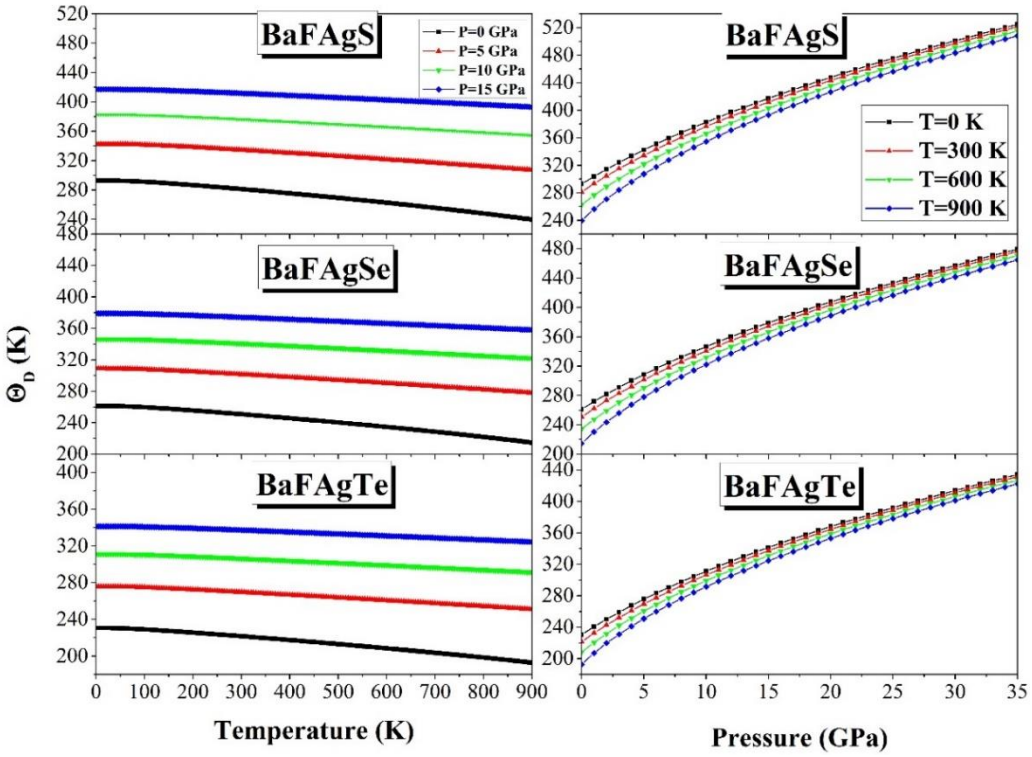

Figure IV.38: Variations of Debye temperature θ_D versus temperature and pressure for the BaFAg*Ch* (*Ch* = S, Se and Te) compounds.

References

[1] M. Gell-Mann, K. A. Bruegkner, *Correlation Energy of an Electron Gas at High Density*, Phys. Rev., Vol. 106, No. 2, pp. 364-368, (1957).

[2] J. P. Perdew, K. Burke, and M. Ernzerhof, *Generalized gradient approximation made simple*, Phys. Rev. Lett., Vol. 77, No. 18, pp. 3865(4), (1996).

[3] J. P. Perdew, A. Ruzsinszky, G. I. Csonka, O. A. Vydrov, G. E. Scuseria, L. A. Constantin, X. Zhou, K. Burke, *Restoring the Density-Gradient Expansion for Exchange in Solids and Surfaces*, Phys. Rev. Lett., Vol. 100, No. 13, pp. 136406(4), (2008).

[4] H. J. Monkhorst and J. D. Pack, *Special points for Brillonin-zone integrations*, Phys. Rev. B, Vol. 13, No. 12, pp. 5188(5), (1976).

[5] J. D. Pack and H. J. Monkhorst, *Special points for Brillouin-zone integrations- a reply*, Phys. Rev. B, Vol. 16, No. 4, pp. 1748-1749, (1977).

[6] D.O. Charkin, A.V. Urmanov, and S.M. Kazakov, *Preparation and crystal structures of novel LaOAgS-type copper and silver fluoride chalcogenides*, J. Alloys Compd., Vol. 516, pp.134, (2012).

[7] F. Birch, *Finite Elastic Strain of Cubic Crystals*, Phys. Rev., Vol. 71, No. 11,pp. 809(16), (1947).

[8] A. H. Reshak and Morteza Jamal, *Calculation of the lattice constant of hexagonal compounds with two dimensional search of equation of state and with Semilocal functionals a new package (2D-optimize)*, J. Alloys Compd., Vol. 555, pp. 362–366, (2013).

[9] M. Gaith and I. Alhayek , *Correlation between overall elastic stiffness, bulk modulus and interatomic distance in anisotropic materials: semiconductors*, Reviews on Advanced Materials Science, Vol. 21, No. 2, pp. 183-191, (2009).

[10] T. H. Courtney, *Mechanical Behavior of Materials* (2nd ed.), Waveland Pr Inc (2005).

[11] V. V. Bannikov, I. R. Shein and A. L. Ivanovskii, *Electronic, optical properties and chemical bonding in six novel 1111-like chalcogenide fluorides AMChF (A=Sr, Ba; M=Cu, Ag and Ch=S, Se,Te) from first principles calculations*, J. Solid State Chem., Vol. 196,No.5, pp. 601–606, (2012).

[12] K. Momma, F. Izumi, *VESTA: A Three-Dimensional Visualization System for Electronic and Structural Analysis*, Japan, (2014).

[13] Yu. A. Amenzade, *Theory of Elasticity*, Mir Publishers Moscow, (1976).

[14] S. O. Kasap, *Principles of electronic materials and devices*, 3rd Ed, The McGraw-Hill, (2006).

[15] Yu. A. Amenzade, *Theory of Elasticity*, Mir publishers Moscow, (1979).

[16] A. Love, *A treatise on the mathematical theory of elasticity*, Cambridge "the university press, (1892).

[17] A. H. Reshak and M. Jamal, *DFT Calculation for Elastic Constants of Tetragonal Structure of Crystalline Solids with WIEN2k Code: A New Package (Tetra-elastic)*, Int. J. Electrochem. Sci., Vol. 8, No. 11, pp. 12252, (2013).

[18] L. Zuo, M. Humbert and C. Esling. *Elastic properties of polycrystals in the Voigt-Reuss-Hill approximation*. J. Appl. Crystallogr., Vol. 25, No. 6, pp. 751-755, (1992).

[19] C-S. Man and M. Huang, *A Simple Explicit Formula for the Voigt-Reuss-Hill Average of Elastic Polycrystals with Arbitrary Crystal and Texture Symmetries*, Journal of Elasticity, Vol.105, Nos. 1–2, pp. 29-48, (2011).

[20] W. Voigt, *Lehrbuch der Kristallphysik*, Vieweg+Teubner Verlag, (1928).

[21] A. Reuss, *Berechnung der Fließgrenze von Mischkristallen auf Grund der Plastizitätsbedingung für Einkristalle*, Z. angew. Math. Mech., Vol. 9, No. 1, pp. 49-58, (1929).

[22] R. Hill, *The elastic behaviour of a crystalline aggregate*. Proc. Phys. Soc. Section A, Vol. 65, No. 5, pp. 349-354, (1952).

[23] R. Hill, *Elastic properties of reinforced solids: some theoretical principles*, J. Mech. Phys. Solids, Vol. 11, No. 5, pp. 357-372, (1963)

[24] V.V. Bannikov, I.R. Shein, A.L. Ivanovskii, *Structural, elastic, electronic properties and stability trends of 1111-like silicide arsenides and germanide arsenides MCuXAs (M = Ti, Zr, Hf; X = Si, Ge) from first principles*, J. Alloys Compd., Vol. 533, pp. 71– 78, (2012).

[25] H. Zhai, X. Li, J. Du, Mater. Trans, *First-Principles Calculations on Elasticity and Anisotropy of Tetragonal Tungsten Dinitride under Pressure*, Mater. Trans., JIM, Vol. 53, No. 7, pp. 1247-1251, (2012).

[26] S.J. Clark, M.D. Segall, C.J. Pickard, P.J. Hasnip, M.J. Probert, K. Refson, M. C. Payne, *First principles methods using CASTEP*, Z. Kristallogr., Vol. 220, Nos. 5-6, pp. 567-570, (2005).

[27] O. L. Anderson, *A simplified method for calculating the Debye temperature from elastic constants*, J. Phys. Chem. Solids, Vol. 24, No. 7, pp. 909-917, (1963).

[28] E. Schreiber, O. L. Anderson, N. Soga, *Elastic Constants and their Measurements* , McGraw-Hill , New York , (1973).

[29] S.F. Pugh, *Relations between the elastic moduli and the plastic properties of polycrystalline pure metals*, Philos. Mag., Vol. 45, No. 367, pp. 823-843, (1954).

[30] F. Delale and H. Boduroglu, *Effect of thermal expansion anisotropy on microcracking in ceramic composites*, Eng. Fract. Mech., Vol. 39, No. 1, pp. 45-60, (1991).

[31] P. Lloveras, T. Casta´n, M. Porta, A. Planes and A. Saxena, *Influence of Elastic Anisotropy on Structural Nanoscale Textures*, Phys. Rev. Lett., Vol. 100, No. 16, pp. 165707(4), (2008).

[32] S. I. Ranganathan and M. Ostoja-Starzewski, *Universal Elastic Anisotropy Index*, Phys. Rev. Lett., Vol. 101, No. 5, pp. 055504(4), (2008).

[33] J. F. Nye, *Properties of Crystals*, Oxford: Clarendon Press,(1985).

[34] M. Alouani, R. C. Albers, and M. Methfessel, *Calculated elastic constants and structural properties of Mo and* $MoSi_2$, Phys. Rev. B, Vol. 43, No 8, pp. 6500, (1991).

[35] S. L. Altmann, *Band Theory of Solids - An Intro. from the Point of View of Symmetry*, Oxford University Press Inc., New York (USA), (1991).

[36] J. Singleton, *Band Theory and Electronic Properties of Solids*, Oxford University Press Inc., New York (USA), (2001).

[37] R. Singh, *Excitons in Semiconductor Quantum Wells Studied Using Two Dimensional Coherent Spectroscopy*, Doctorat these, University of Colorado Boulder, (2013).

[38] M. Labidi, *Etude des propriétés structurales, électroniques des quaternaires*, thèses de Doctorat, Universite Badji Mokhtar, (2011).

[39] E. Motomitsu, H. Yanagi, T. Kamiya, M. Hirano, H. Hosono, *Synthesis, structure and physical properties of layered semiconductors MCuFCh (M = Sr, Eu, Ch = S, Se)*, J. Solid State Chem., Vol. 179, No. 6, pp. 1668-1673, (2006).

[40] H. Yanagi, J. Tate, S. Park, C. Park and A. Keszler, *p-type conductivity in wide-band-gap BaCuQF (Q = S, Se)*, Appl. Phys. Lett., Vol. 82, No17, pp. 2814, (2003).

[41] C, Park, R. Kykyneshi, A. Yokochic, J. Tateb, D. A. Keszlera, *Structure and physical properties of BaCuTeF*, J. Solid State Chem., Vol .180, No. 5, pp. 1672–1677 (2007).

[42] U. K. Mishra, J. Singh, *Semiconductor Device Physics and Design*, Springer, Netherlands, (2008).

[43] A. H. Reshak, *Electronic structure and transport properties of Ba2Cd2Pn3 (Pn = As and Sb): An efficient materials for energy conversion*, J. Alloys Compd., Vol. 670, pp. 1-11, (2016).

[44] T. S. Moss, *Optical properties of semi- conductors (Semi- conductor monographs)*, Butterworths Scientific Publications, New York, (1959).

[45] L. V. Keldysh, D. A. Kirzhnitz, A. A. Maradudin, *The dielectric function of condensed systems*, Modern Problems in Condensed Matter Sciences 24, North- Holland, (1989).

[46] R.L. Kronig, *On the theory of dispersion of X- Rays*, J. Opt. Soc. Am, Vol. 12, No. 6, pp. 547–556, (1926).

[47] V. Lucarini, K- E. Peiponen, J. J. Saarinen, E. M. Vartiainen, *Kramers- Kronig Relations in Optical Materials Research*, Springer- Verlag Berlin Heidelberg, (2005).

[48] D. R. Penn, *Wave-number-Dependent Dielectric Function of Semiconductors*, Phys. Rev., Vol. 128, No. 5, pp. 2093- 2097, (1962).

[49] P.S. Kireev, *Semiconductor Physics*, Vysshaya Shkola, Moscow, (1975).

[50] https://en.wikipedia.org/wiki/Electricity.

[51] http://dictionary.cambridge.org.

[52] S. Bensalem, *Contribution to the study of physical properties of CZTX (X=S, Se) solar materials*, Doctorat thesis, Département de Physique, Universite Ferhat Abbas - Setif 1, (2015).

[53] J. P. Heremans, *Low-Dimensional Thermoelectricity*, Acta Phys. Pol., A, Vol. 108, No. 4, pp. 609-634, (2005).

[54] http://www.syr-res.com.

[55] V. stupelman and G. Filaretov, *semiconductor devices*, Mir publishers Moscow, (1976).

[56] X. Zhang, C. Wang, Y. X. Wang, *Influence of the elements (Pn = As, Sb, Bi) on the transport properties of p-type Zintl compounds Ba2ZnPn2*, Comput. Mater. Sci., Vol. 127, pp. 8–14, (2017).

[57] O. Bubnova, *Thermoelectric properties of conducting polymers*, Doctorate these, Department of science and technology (ITN), Linköping University, Sweden, (2013).

[58] T. Jenkins, *A brief history of . . . semiconductors*, Phys. Educ., Vol. 40, No. 5, pp. 430-439, (2005).

[59] http://news.mit.edu

[60] L. Andrea, *Modelisation du transport thermique dans des materiaux thermoelectriques*, These de Doctorat, Universite Pierre et Marie Curie - Paris VI, (2016).

[61] W. Ibarra-Hern´andez, M. J. Verstraete and J-Y. Raty, *Effect of hydrostatic pressure on the thermoelectric properties of Bi2Te3*, Phys. Rev. B, Vol. 90, No.24, pp. 245204(7), (2014).

[62] G. S. Nolas, D. T. Morelli, T. M. Tritt, *SKUTTERUDITES: A Phonon-Glass-Electron Crystal Approach to Advanced Thermoelectric Energy Conversion Applications*, Annu. Rev. Mater. Sci, Vol. 29, pp. 89–116, (1999).

[63] T. Takabatake, K. Suekuni, T. Nakayama, E. Kaneshita, *Phonon-glass electroncrystal thermoelectric clathrates: Experiments and theory*, Rev. Mod. Phys., Vol. 86, No. 2, pp. 669(48), (2014).

[64] M. K. Yadav, B. Sanyal, *First principles study of thermoelectric properties of Li-based half-Heusler alloys*, J. Alloys Compd., Vol. 622 pp. 388–393, (2015).

[65] Y. Bouyrie, C. Candolfi, B. Vaney, A. Dauscher and B. Lenoir, *High Temperature Transport Properties of Tetrahedrite* $Cu_{12-x}M_xSb_{4-y}Te_yS_{13}$ *(M = Zn, Ni) Compounds*, J. Electron. Mater., Vol. 45, No. 3, pp. 1601–1605, (2016).

[66] X. Zhang, C. Wang, Y. X. Wang, *Influence of the elements (Pn = As, Sb, Bi) on the transport properties of p-type Zintl compounds Ba2ZnPn2*, Comput. Mater. Sci., Vol. 127, pp. 8–14, (2017).

[67] L. E. Shelimova, O. G. Karpinskii, P. P. Konstantinov, M. A. Kretova, E. S. Avilov, and V. S. Zemskov, *Composition and Properties of Layered Compounds in the GeTe–Sb2Te3 System*, Neorg. Mater., Vol. 37, No. 4, pp. 421–427, (2001).

[68] S. M. Kauzlarich, S. R. Brown and G. J. Snyder, *Zintl phases for thermoelectric devices*, Dalton Trans., pp. 2099–2107, (2007).

[69] R. Baierlein, *The elusive chemical potential*, Am. J. Phys., Vol. 69, pp. 423- 434, (2001).

[70] G. Job and F. Herrmann, *Chemical potential- a quantity in search of recognition*, Eur. J. Phys., Vol. 27, pp. 353–371, (2006).

[71] J. Ravichandrana, *Thermoelectric and thermal transport properties of complex oxide thin films, heterostructures and superlattices*, J. Mater. Res., Vol. 32, No. 1, pp. 183-203, (2017).

[72] S. Lemal, J. Varignon, D.I. Bilc, P. Ghosez, *Thermoelectric properties of layered calcium cobaltite Ca3Co4O9 from hybrid functional first-principles calculations*, Phys. Rev. B, Vol. 95, No. 7, pp. 075205(14). (2017),

[73] J. Bardeen, W. Shockley, *Deformation potentials and mobilities in non-polar crystals*, Phys. Rev., Vol. 80, No. 1, pp. 72-80, (1950).

[74] F. B. Beleznay, F. Bogàr, J. Ladik, *Charge Carrier mobility in quasi-onedimensional systems: application to a guanine stack*, J. Chem. Phys, Vol. 119, No. 11, pp. 5690-5695, (2003).

[75] J. Xi, M. Long, L. Tang, D. Wang and Z. Shuai, *First-principles prediction of charge mobility in carbon and organic nanomaterials*, Nanoscale, Vol. 4, No. 15, pp. 4348-4369, (2012).

[76] D. G. Cahill, R. O. Pohl, *Heat flow and lattice vibrations in glasses*, Solid State Commun., Vol. 70, No 10, pp. 927-930, (1989).

[77] D. G. Cahill, S. K. Watson, R. O. Pohl, *Lower limit to the thermal conductivity of disordered crystals*. Phys. Rev. B, Vol. 46, No 10, pp. 6131, (1992).

[78] A. Zevalkink, S. P. Gregory, S. Johnson, J. Swallow, Z. M. Gibbs and G. J. Snyder, *Influence of the Triel Elements (M= Al, Ga, In) on the Transport Properties of Ca5M2Sb6 Zintl Compounds*, Chem. Mater., Vol. 24, No. 11, pp. 2091-2098, (2012).

[79] J. Wang, Z. Chen, C. Ii, et al. *Electronic structures, elastic properties, and minimum thermal conductivities of cermet M3AlN*, J. Solid State Chem., Vol. 216, pp. 1-8, (2014).

[80] M. Kaufman, *Principles of Thermodynamics*, Marcel Dekker, Inc, New York, (2002).

[81] K. Haddadi, *Etude des propriétés structurales, élastiques et électroniques des composes antiperovskites de type XNCa3*, doctoral thesis, Faculty of Science, University of Setif 1, Algeria, (2013).

[82] N. W. Ashcroft, N, D, Mermin, *Solid state physics*, Harcourt College Publishers, (1976).

[83] J. S. O. Evans, *Negative thermal expansion materials*, J. Chem. Soc., Dalton Trans., pp. 3317–3326, (1999).

[84] Z. Peng, Y.Z. Sun, L.M. Peng, *Hydrothermal synthesis of ZrW2O8 nanorods and its application in ZrW2O8/Cu composites with controllable thermal expansion coefficients*, Mater. Des., Vol. 54, pp. 989–994, (2014).

[85] A. W. Sleight, *Isotropic negative thermal expansion*, Annul. Rev. Mater. Sci., Vol. 28, pp. 29–43, (1998).

[86] X. Shen, C. Viney, E. R. Johnson, C. Wang and J. Q. Lu, *Large negative thermal expansion of a polymer driven by a submolecular conformational change*, Nat. Chem., vol. 5, pp. 1035-1041, (2013).

[87] M. P. Attfield and A. W. Sleight, *Strong negative thermal expansion in siliceous faujasite*, Chem. Commun., pp. 601-602, (1998).

CONCLUSION

In the present work, we have studied in details the structural, elastic, electronic, optical and thermoelectric properties of three quaternary layered LaOAgS-type compounds, namely BaFAgS, BaFAgSe and BaFAgTe, using the Full Potential-Linearized Augmented Plane Wave (FP-LAPW) method in the framework of density functional theory (DFT) as implemented in the WIEN2k package. The main obtained results can be summarized as follows.

1. **Structural properties**

Calculated structural parameters, including lattice parameters and atomic coordinates, are in good agreement with available experimental data. Relative deviations between calculated lattice parameters (*a* and *c*) and the corresponding experimental ones are less than 1%, confirming the reliability of the performed calculations. Calculated cohesive energies and formation enthalpies confirm the chemical and structural stabilities of the title compounds.

2. **Elastic properties**

Calculated single-crystal elastic constants, using the energy-strain method, satisfy the mechanical stability criteria. The noticeable difference between C_{11} and C_{33} values indicates the strong elastic anisotropy. This is in agreement with the layered structure of the studied compounds.

Polycrystalline elastic moduli were calculated from the calculated single-crystal elastic constants through the Voigt–Reuss–Hill (VRH) approximations. One notes:

- ✓ Calculated bulk modulus (*B*) values from the *EOS* fitting are in good agreement with the corresponding ones derived from the calculated single-crystal elastic constants. This constitutes a proof of the reliability of the performed calculations.
- ✓ Young's modulus (*E*) values are relatively small, confirming the rather low stiffness of the considered compounds. The value of *E* decreases when one moves in the following sequence BaFAgS → BaFAgSe → BaFAgTe.
- ✓ The bulk modulus (*B*) value is approximately the double of the shear modulus (*G*) one, indicating that the shear deformation is easier to occur in the considered compounds than the compression one.
- ✓ Based on the Pugh's empirical criterion, the considered compounds are ductile.
- ✓ The studied compounds exhibit a noticeable elastic anisotropy and its degree increases when one moves from BaFAgS to BaFAgSe to BaFAgTe.

- ✓ Debye temperature (θ_D) value decreases when going from BaFAgS to BaFAgSe to BaFAgTe, which is in accordance with the stiffness trend. This indicates the decrease of the thermal conductivity when going from BaFAgS to BaFAgSe to BaFAgTe.

3. Electronic properties

The LDA and GGA functionals underestimate the band gaps of semiconductors and isolators. Therefore, to improve the calculated band structures of the investigated compounds, the TB-mBJ functional was used to model the exchange-correlation potential. Both scalar relativistic (without inclusion of the spin-orbit coupling) and full relativistic calculation (with inclusion of the spin-orbit coupling) calculations were performed for the electronic properties. The obtained results reveal:

- ✓ The studied compounds have similar band structure features. They are wide direct band gap (Γ-Γ) materials, which range from 2.52 to 3.10 eV.
- ✓ Qualitatively, the GGA08 band structure profile is almost similar to the corresponding TB-mBJ one, but quantitatively, there is an important difference between the TB-mBJ band gap and the GGA08 one. The TB-mBJ approach improves the band gap value of BaFAgS, BaFAgSe and BaFAgTe by approximately 117%, 128%, and 75%, respectively, compared to the corresponding GGA08 one.
- ✓ The dispersion of the valence bands around the VBM is highly anisotropic; the upper valence bands show a large dispersion around the VBM along the $\Gamma \rightarrow \mathrm{M}$ and $\Gamma \rightarrow \mathrm{X}$ directions in the *k*-space and a pronounced flatness along the $\Gamma \rightarrow \mathrm{Z}$ direction. In consequence, the hole effective mass value along the *c*-axis ($\Gamma \rightarrow Z$ direction) should be significantly larger than the corresponding ones in the *ab*-plane ($\Gamma \rightarrow M$ direction) and along the *a*-axis ($\Gamma \rightarrow X$ direction).
- ✓ The spin-orbit coupling has an important effect on the electronic properties:
  - (i) Splitting of the energy bands, especially, the valence bands near to Fermi level at Γ point,
  - (ii) Reduction of the band gap value.
  - (iii) Spin-orbit coupling effect becomes more important when one moves from BaFAgS to BaFAgSe to BaFAgTe.
- ✓ The assignments of the energy band electronic states and chemical bonding characters were accomplished with the help of the calculated DOS diagrams and electronic charge density maps. The bonding in the [Ag*Ch*] and [BaF] blocks are of mixed ionic and covalent nature. The Ag-*Ch* bond inside the [Ag*Ch*] layer is predominantly of covalent

character, which is due to the strong hybridization between the Ag: 4*d* and *Ch*: n*p* states, while the Ba-F bond in the layer [BaF] is predominantly ionic.

4. Optical properties

Based on the band structure obtained using the TB-mBJ with including SOC, the absorptive and dispersive parts of the dielectric function, absorption coefficient, refractive index, extinction coefficient, optical reflectivity and energy-loss function spectra were calculated for the [100] and [001] polarized incident radiation in a wide energy range up to 25 eV.

- ✓ The calculated optical spectra show a noticeable anisotropy.
- ✓ The magnitude of the peaks of the optical spectra increase with increasing atomic number of the *Ch* element.
- ✓ The origins of the electronic transitions that are responsible of the observed structures in the optical spectra were assigned in terms of the calculated energy band structure.
- ✓ The zero-frequency limit of the real part of the dielectric function $\varepsilon_1(\omega)$ increases when the energy band gap value decreases.

5. Thermoelectric properties

The semi-classical Boltzmann transport theory was used to investigate charge-carrier (holes and electrons) concentration and temperature dependences of the thermoelectric parameters, including Seebeck coefficient, electrical conductivity and thermal conductivity, along the two principal crystallographic directions, i.e., *a* and *c* axes. The obtained results show:

- ✓ The Seebeck coefficient (*S*) increases with increasing temperature and decreases with increasing charge-carrier concentration, but at high hole concentration, it saturates at high temperatures.
- ✓ The electrical conductivity (σ) decreases with increasing temperature for a fixed hole concentration.
- ✓ The thermal conductivity remains approximately constant with increasing temperature for a fixed hole concentration. However, at a fixed temperature, both the electrical and thermal conductivities increase sharply with increasing charge-carrier concentration.
- ✓ Thermoelectric parameter values of the for the *p*-type compounds are larger than that of the *n*-type ones.
- ✓ The studied thermoelectric parameters exhibit a strong degree of anisotropy.

- ✓ The minimum lattice thermal conductivity of the studied materials was evaluated from the elastic properties, using Cahill's model. It is found that the minimum lattice thermal conductivity is relatively small and decrease when one moves from BaFAgS to BaFAgSe to BaFAgTe.
- ✓ Finally, calculated thermoelectric efficiency, given by the dimensionless figure of merit ZT, indicates that the studied compounds show a high performance along the *a*-axis for a large range of temperature.

6. Thermodynamic properties

Using the quasi-harmonic Debye model, temperature (from 0 to 900 K) and pressure (from 0 to 35 GPa) dependences of the heat capacity, thermal expansion, Debye temperature, bulk modulus and Grüneisen parameter were predicted. The obtained results reveal:

- ✓ Temperature effect on the aforementioned parameters decreases with increasing pressure.
- ✓ The pressure influence on the volume and bulk modulus is much more evident than that of the temperature.
- ✓ At low temperature, the constant volume heat capacity curve C_V(T) is proportional to T^3. At high temperature, it tends towards a limited value, the so-called Dulong-Petit limit. In addition, C_V and the pressure constant heat capacity (C_p) are more sensitive to temperature than to pressure.
- ✓ The thermal expansion coefficient α increases with increasing temperature (sharply at low temperatures, and slowly at high temperature) and decreases with increasing pressure.
- ✓ Debye temperature (θ_D) is more sensitive to temperature than to pressure. The θ_D value decreases when going from BaFAgS to BaFAgSe to BaFAgTe.

APPENDIX

Appendix

A.1. Wien2k Code

First principles calculations are mainly performed within Density Functional Theory (DFT). In the framework of DFT, the many-body problem of interacting electrons and nuclei is mapped to a series of one electron equation, the so-called Kohn–Sham (KS) equations. Several methods have been developed for the solution of KS equations. The Linearized Augmented Plane-Wave (LAPW) method is one among the most accurate ones for solving the KS equations. One successful implementation of the full-potential LAPW (FP-LAPW) method is the program package WIEN2k, which is developed by Blaha and co-workers [1, 2]. It has been successfully applied to a wide range of crystal properties. Minimizing the total energy of a system by relaxing the atomic coordinates for complex systems became possible by the implementation of atomic forces, and even molecular dynamics became feasible. Also, relativistic correction terms are included [3]:

- The scalar-relativistic corrections: mass-velocity correction and Darwin correction,
- The spin-orbit coupling correction.

A.1.1. Description of general input and output files

- **The master input file "case.struct"**

"case.struct" is the file that defines the crystal structure and is the main input file that is required for all programs of the WIEN2k code.

- **The history file "case.scf"**

During the self-consistent field (SCF) cycle, the essential data are appended to the file "case.scf" in order to generate a summary of previous iterations. For an easier retrieval of certain quantities, the essential lines are labelled with: LABEL, which can be used to

monitor these quantities during self-consistency as explained below. The most important: LABELs are [4]:

:ENE: total energy (Ry).

:DIS: charge distance between last 2 iterations ($\int|\rho_n - \rho_{n-1}|dr$).

:FER: Fermi energy.

:FORxx: force on the atom xx in mRy/Bohr.

:FGLxx: force on the atom xx in mRy/Bohr.

:DTOxx: total difference charge density for the atom xx between last 2 iterations.

:CTOxx: total charge in the sphere xx (mixed after MIXER).

:NTOxx: total charge in the sphere xx (new (not mixed) from LAPW2+LCORE).

:QTLxx: partial charges in the sphere xx.

:EPLxx: *l*-like partial charges and ``mean energies" in the lower (semi core) energy window for the atom xx used as energy parameters in case.in1 for next iteration.

:EPHxx: *l*-like partial charges and ``mean energies" in higher (valence) energy window for the atom xx used as energy parameters in case.in1 for next iteration.

:EFGxx: Electric field gradient (EFG) V_{zz} for the atom xx.

:ETAxx: Asymmetry parameter of EFG for the atom xx.

:RTOxx: Density for the atom xx at the nucleus (first radial mesh point).

:VZERO: Gives the total, Coulomb and xc-potential at z=0 and z=0.5 (meaningful only for slab calculations).

- ✓ To check to which type of calculation a scf file corresponds, we use:

:POT: Exchange-correlation potential used in this calculation.

:LAT: Lattice parameters in this calculation.

:VOL: Volume of the unit cell.

:POSxx: Atomic positions for the atom xx (as in case.struct).

:RKM: Actual matrix size and resulting RK_{max}.

:NEC: Normalization check of electronic charge densities. If a significant amount of electrons is missing, one might have core states, whose charge density is not completely confined within the respective atomic sphere. In such a case the corresponding states should be treated as band states (using LOs).

- ✓ For spin-polarized calculations:

:MMTOT: Total spin magnetic moment/cell.

:MMIxx: Spin magnetic moment of the atom xx. Note, that this value depends on RMT.

:CUPxx: spin-up charge (mixed) in the sphere xx.

:CDNxx: spin-dn charge (mixed) in the sphere xx.

:NUPxx: spin-up charge (new, from lapw2+lcore) in the sphere xx.

:NDNxx: spin-dn charge (new, from lapw2+lcore) in the sphere xx.

:ORBxx: Orbital magnetic moment of the atom xx (needs SO calculations and LAPWDM).

:HFFxx: Hyperfine field of the atom xx (in kGauss).

- ✓ One can monitor the energy eigenvalues (listed for the first k-point only), the Fermi-energy or the total energy. Often the electronic charges per atom reflect the convergence. Charge transfer between the various atomic spheres is a typical process during the SCF cycles: large oscillations should be avoided by using a smaller mixing parameter; monotonic changes in one direction suggest a larger mixing parameter.
- ✓ In spin-polarized calculations the magnetic moment per atomic site is an additional crucial quantity which could be used as convergence criterion.
- ✓ If a system has electric field gradients and one is interested in that quantity, one should monitor the EFGs, because these are very sensitive quantities.
- ✓ It is better to monitor several quantities, because often one quantity is converged, while another still changes from iteration to iteration. The script run_lapw has three different convergence criteria built in, namely the total energy, the atomic forces and the charge distance.

- ✓ We recommend the use of UNIX commands like: grep: ENE case.scf or use "Analysis"' from the graphical user interface w2web for monitoring such quantities.

A.1.2. Flow of programs

As a starting point of the calculation, one needs to check the convergence of the results with respect to *k*-points, Radius of Muffin-Tin spheres (R_{MT}) and cut-off energy. The initialization consists of running a series of small auxiliary programs which generates the inputs for the main programs (See Fig. A.1). One starts by defining the structure in "case.struct". The initialization can be invoked by the script "**init_lapw"** and consists of running [2-6]:

NN: a program, which lists the nearest neighbour distances up to a specified limit (defined by a distance factor f) and thus helps to determine the atomic sphere radii. In addition it is a very useful additional check of your "case.struct" file (equivalency of atoms).

SGROUP: determines the space group of the structure defined in your "case.struct" file.

SYMMETRY: generates from a raw "case.struct" file the space group symmetry operations, determines the point group of the individual atomic sites, generates the LM expansion for the lattice harmonics and determines the local rotation matrices.

LSTART: generates free atomic densities and determines how the different orbitals are treated in the band structure calculations (i.e., as core or band states, with or without local orbitals...).

KGEN: generates a *k*-mesh in the irreducible part of the BZ.

DSTART: generates a starting density for the scf cycle by a superposition of atomic densities generated in LSTART.

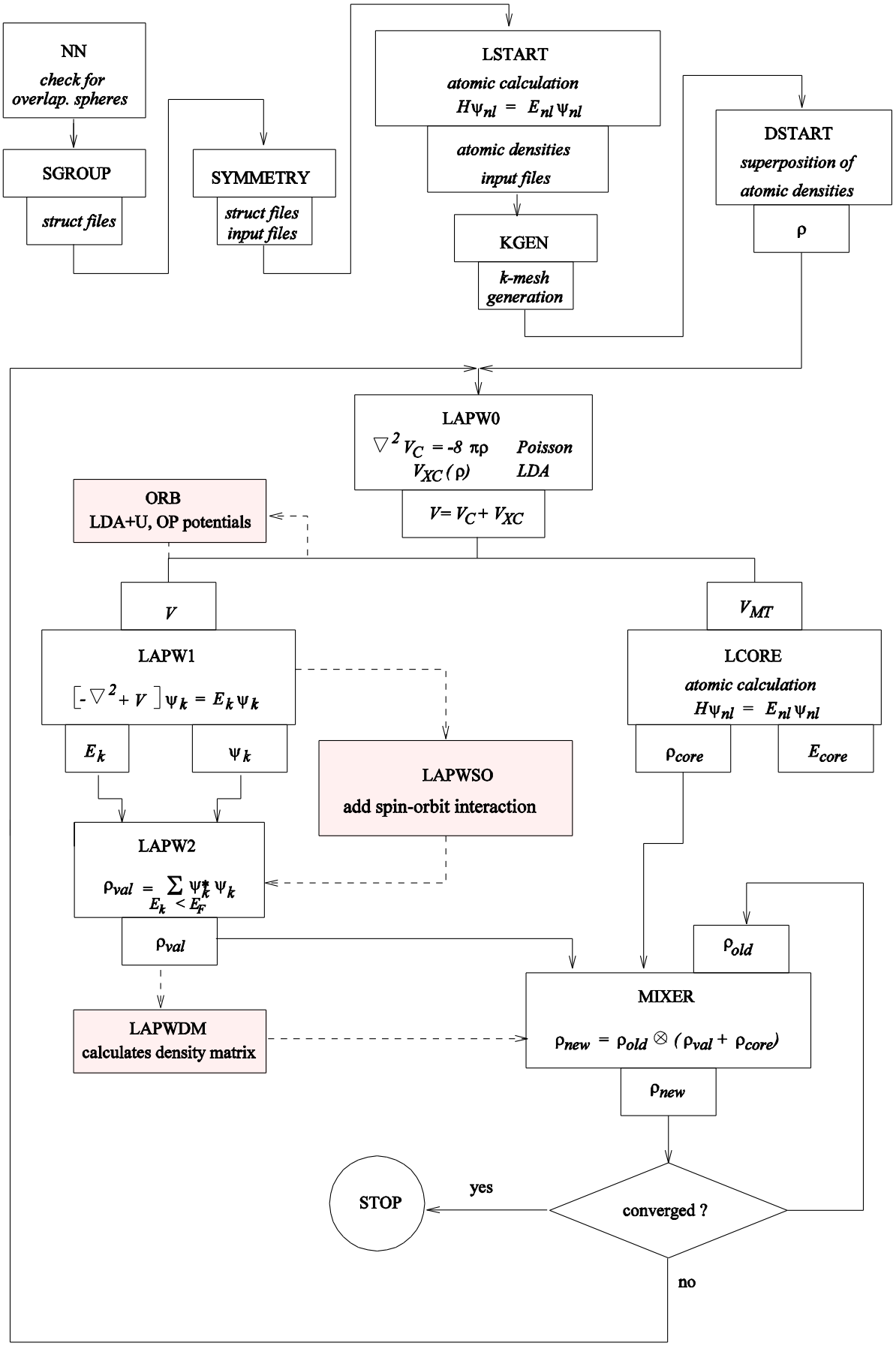

Figure A.1: Program flow in WIEN2k. [1]

Then a self-consistency cycle is initiated and repeated until convergence criteria are met (See Chap. II). This cycle can be invoked with a script **run_lapw**, and consists of the following steps:

LAPW0: (POTENTIAL) generates the potential from a given charge density.

LAPW1: (BANDS) calculates valence bands (eigenvalues and eigenvectors).

LAPW2: (RHO) computes valence densities from eigenvectors.

LCORE: computes core states and densities.

MIXER: mixes the densities generated by LAPW2 and CORE with the density of the previous iteration to generate a new charge density.

LAPW1 and LAPW2 programs are the most time consuming, while the time needed to run CORE and MIXER are basically negligible.

In order to calculate physical properties of solid, equilibrium DFT crystal lattice parameters have to be used, and they are different for GGA and for LDA. Within the defect calculation, all the atoms must be allowed to relax without any symmetry constrains.

A.2. Spin-Orbit Coupling

A.2.1. Definition

Spin-Orbit Coupling (SOC) is defined as the interaction of the electron spin magnetic moment with magnetic field due to the motion of the electron in the electrostatic field of the proton. This interaction leads to the splitting of atomic energy levels; it's usually known in atomic physics and spectroscopy by the name of fine structure of levels (spectral lines). The origin of the spin-orbital splitting is the same as of the splitting of energy level of isolated atoms, which results in the formation of energy bands when the atoms interact with one another [7-9].

In states subject to spin-orbit coupling, in the atomic limit, spin and orbital angular momenta (S and L) are not good quantum numbers; total angular momentum J is instead the conserved quantity. The total angular momentum operator defined as:

$$J = S + L \qquad (A.1)$$

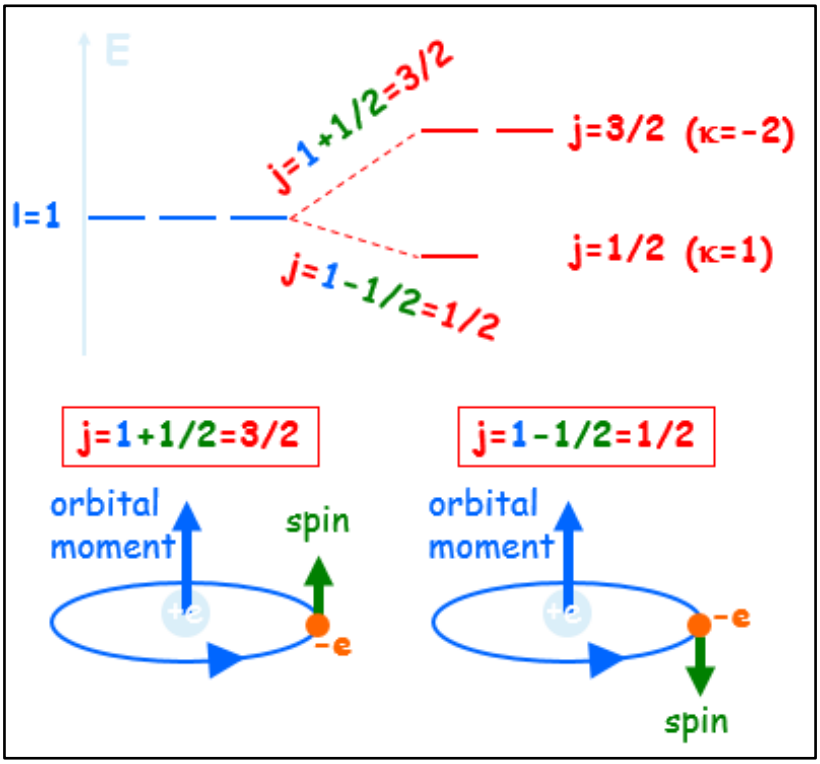

Figure A.2: Spin-orbit splitting of *l*-quantum number. [8, 9]

Scalar-relativistic *p*-orbital is similar to $p^{3/2}$ wave function thus ψ does not contain $p^{1/2}$ basis, so we need to add 'local orbital with $p^{1/2}$.

In quantum physics, the spin–orbit interaction is a relativistic interaction of a particle's spin with its motion inside a potential. So, the Schrödinger equation became [7]:

$$H\Psi = E\Psi + H_{So}\Psi \qquad (A.2)$$

Where H_{So} is the energy of the interaction between spin and the orbital moment.

In mathematical physics and mathematics, the Pauli matrices are a set of three 2x2 complex matrices which are Hermitian and unitary [10]. These matrices are named after the physicist Wolfgang Pauli. In quantum mechanics, they occur in the Pauli equation which takes into account the interaction "H_{SO}" of the spin of a particle with an external electromagnetic field.

$$H_{SO} = \frac{(Z - \sigma_n)e^2\hbar^2}{4m_0^2c^2r^3}(\sigma L) \qquad (A.3)$$

Where:

- σ_n is the screening constant.
- $(Z - \sigma_n)|e|$is the charge of the nucleus screened by the inner electron shells.
- L is the orbital mechanical angular momentum M in unit of $\hbar$ $(M = \hbar L)$.

The spin-orbital should be observed for all states except the s-states ($L = 0$) where the orbital angular momentum ($M = \hbar L$) is zero.

A.2.2. Implementation of SOC in Wien2K

The FP-LAPW method divide the solid into two regions: (i) Muffin-Tin spheres, and (ii) interstitial region. In the interstitial region, the valence electrons are not relativistic, while in the MT spheres, core states are fully-relativistic (include SOC), and the valence electrons are treated classically [8, 9]:

- Fully-relativistic core,
- Scalar-relativistic valence,
- Mass-velocity and Darwin s-shift,
- No spin-orbit interaction.

In the Fully-relativistic calculation, several levels of treating are illustrated in (Fig.A.3), we use the scalar-relativistic (pure-spin) eigenstates Ψ as basis and add the Spin-Orbit interaction:

- adding SO in “second variation” (using previous eigenstates as basis).
- adding $p^{1/2}$ LOs to increase accuracy.
- x lapw1 (increase E-max for more eigenvalues, to have basis for lapwso).
- x lapwso
- x lapw2 –so –c (SO always needs complex lapw2 version).

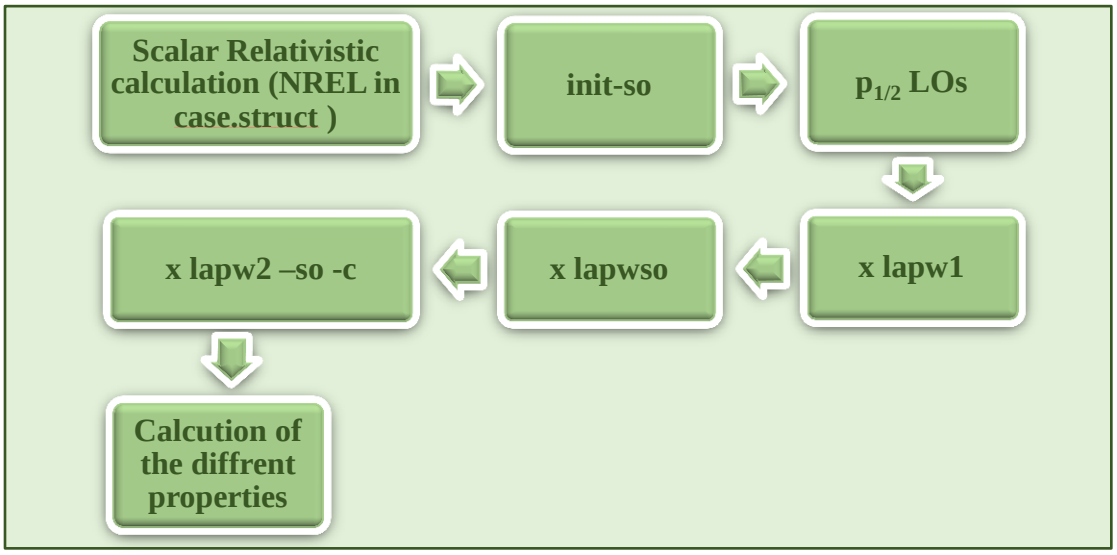

Figure A.3: Including the Spin-Orbit coupling for calculating the physical properties in the WIEN2k code. [8, 9]

A.2.3. Spin-orbit effect

Many results about the electronic structure of solids with and without including the SOC interaction are presented in the scientific literature as a comparative study. The important observed effects of SOC are: (i) reducing the energy band gap [11-13] and (ii) splitting of the first degenerated conduction levels [14-16]. However, Spin-orbit effects generally give small corrections to the non-relativistic band structure, except near *k*-points where bands are degenerate in the non-relativistic structure.

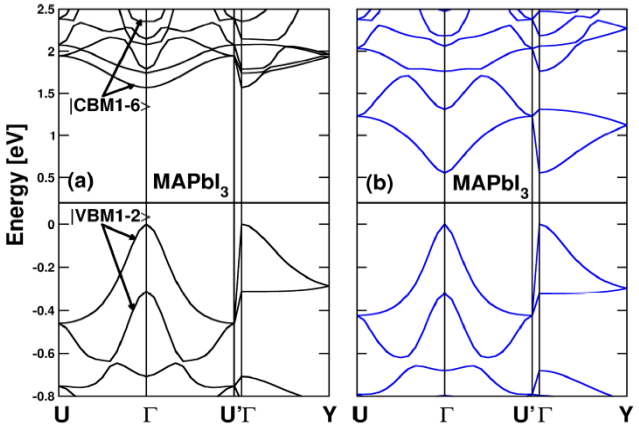

Figure A.4: Electronic band structure of $CH_3NH_3PbI_3$, without (a) and with (b) the spin−orbit coupling interaction. The origin of the energy scale is taken at the top of the VB. [11]

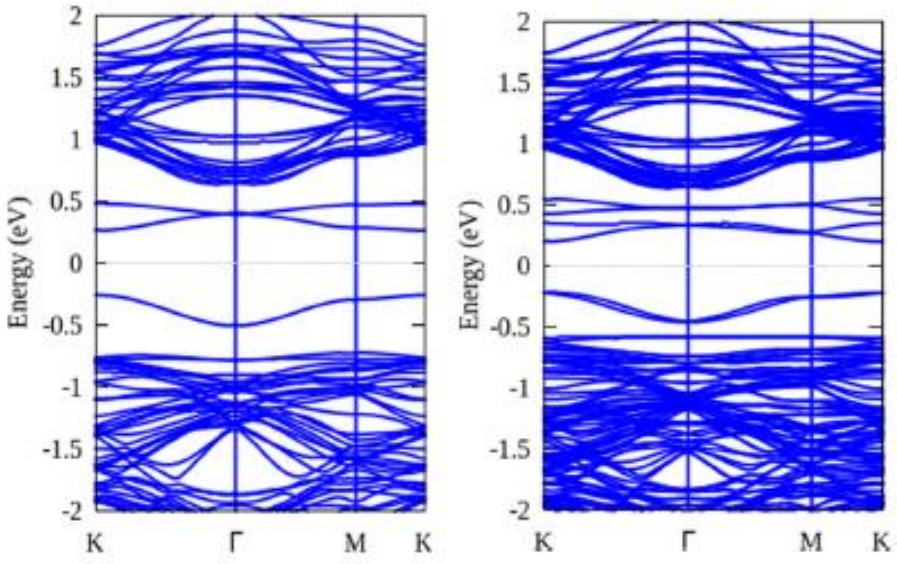

Figure A.5: Electronic band structure of the VSe without inclusion of the spin-orbit coupling (SOC), "left panel", and with inclusion of the SOC, "right panel". [14]

The major role of spin−orbit coupling (SOC) that significantly reduces the band gap by inducing a large splitting of the first degenerated conduction levels.

A.3. BoltzTraP Code

A.3.1. Description and method

Boltzmann **Tra**nsport **P**roperties (BoltzTraP) is a program for calculating the semi-classic transport coefficients. It uses a mesh of band energies and is interfaced to the WIEN2k, ABINIT, SIESTA, VASP and Quantum Espresso programs. The program is based on a smoothed Fourier interpolation of the bands. From this analytical representation we calculate the derivatives necessary for the transport distributions. The method is compared to earlier calculations, which in principle should be exact within Boltzmann theory, and a very convincing agreement is found [17]. The idea of this procedure was developed in 1986 by Koelling and Wood [18] and implemented in a code by Madsen and Singh in 2006 [17] for solving the Boltzmann equation. BoltzTraP code calculates electronic transport coefficients depending on the chemical potential, i.e. charge carrier densities and temperature. Only an energy independent relaxation time is assumed so far. Transport coefficients for phonons are not calculated. BoltzTraP code relies on a Fourier expansion of the band energies where the space group symmetry is maintained by using star functions. The idea of the Fourier expansion is to use more star functions than band energies, but to constrain the fit so that the extrapolated energies are exactly equal to the calculated band-energies and use the additional freedom to minimize a roughness function and thereby suppress oscillations between the data points. Using the analytical representation of the bands it is then a reasonable simple procedure to calculate band-structure dependent quantities as mentioned in Fig. A.6.

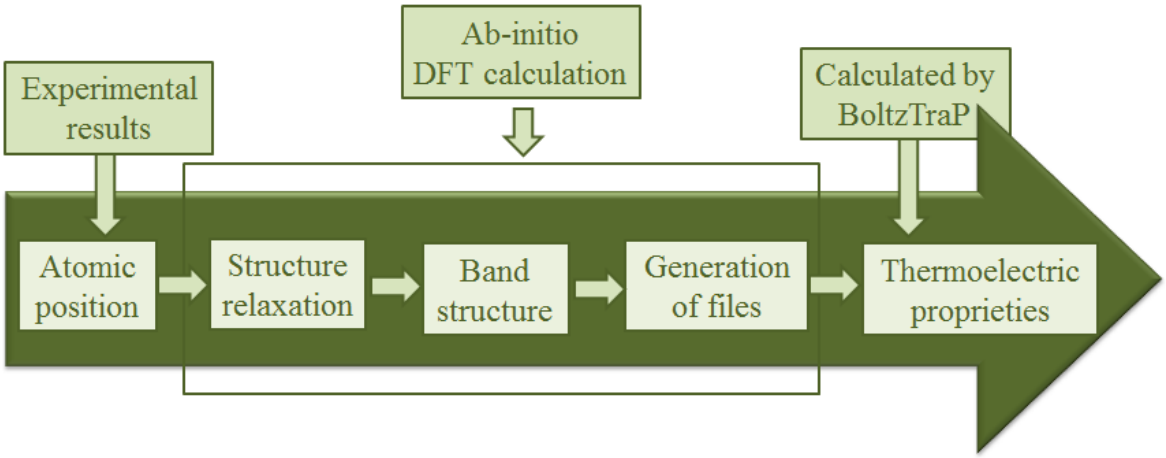

Figure A.6: Flowchart illustrating the calculation scheme used to calculate and store transport properties.

The input data needed to run BoltzTraP are the crystal structure and the electronic band structure on a uniform grid. More than 10 output files are being generated, they allow the user to check the results on a more detailed level. The traces of the conductivity tensors are written as a function of μ and T in the file called case.trace (See Tab. A.1).

Table A.1: Output in case.trace.

Column	1	2	3	4	5	6	7	8	9	10
Quantity	μ	T	N	n	S	σ/τ	R_H	κ^0	C	$\varkappa$
unit	Ry	K	e/u.c.	e/u.c.	V/K	1/(Ωms)	m^3/C	W/(mKs)	J/(molK)	m^3/mol

The program outputs the individual components of the conductivity tensors (files case.condtens and case.halltens). The first three columns are like in the case.trace file. In case.condtens next nine columns are the σ/τ components (3x3 tensor). These are followed by the nine Seebeck components and finally the nine κ^0 components. In case.halltens 27 columns follow (The Hall tensor is 3x3x3 tensor). The coordinate-system used is defined so that the x-axis is parallel to the crystallographic a-axis (of the conventional cell). The y-axis lies in the crystallographic ab plane and is orthogonal to the x-axis and the z-axis is orthogonal to the x and y axes.

BoltzTraP is a computer code to calculate transport properties of materials from First Principles electronic band structures.

A.3.2. Semi-classical Boltzmann theory

In order to evaluate transport phenomena occurring at the electronic level, a microscopic model of the transport process is needed to assess the transport coefficients of materials. The basic transport equation of the current density *j*, in presence of an electrical field *E* and magnetic field *B*, and a temperature gradient ΔT, is, [17,19]

$$j_i = \sigma_{ij}E_j + \sigma_{ijk} + \nu_{ij}\nabla_j T + \cdots \qquad \text{(A. 4)}$$

A semi-classical approach based on solving Boltzmann's equation, within the relaxation time approximation, is commonly used to describe the conductivity tensors. This model evaluates the electrical conductivity introducing a lifetime, τ, for an electron that

encapsulates all the different scattering mechanisms that it can undergo. The conductivity tensors can be written as:

$$\sigma_{\alpha\beta}(i,K) = e^2 \tau_{i,K} v_\alpha(i,K) v_\beta(i,K) \qquad (A.5)$$

and using the Levi-Civita tensor ε_{ijk}:

$$\sigma_{\alpha\beta\gamma}(i,K) = e^3 \tau_{i,K}^2 \varepsilon_{\gamma uv} v_\alpha(i,k) M_{\beta u}^{-1} \qquad (A.6)$$

in terms of the group velocity and the inverse mass tensor:

$$v_\alpha(i,k) = \frac{1}{\hbar} \frac{\partial \varepsilon_{i,k}}{\partial k_\alpha} \qquad (A.7)$$

$$M_{\beta u}^{-1}(i,k) = \frac{1}{\hbar} \frac{\partial^2 \varepsilon_{i,k}}{\partial k_\beta \partial k_u} \qquad (A.8)$$

The relaxation time, τ, in principle is dependent on both the band index and the k vector direction. However detailed studies of the direction dependence of τ have shown that, to a good approximation, τ is direction independent and that even in the superconducting cuprates, that have substantially anisotropic conduction and cell-axes, the τ is almost isotropic.

The three main transport tensors depending on the temperature T and the Fermi level (or chemical potential) of the electrons μ are:

$$\sigma_{\alpha\beta}(T,\mu) = \frac{1}{\Omega} \int \sigma_{\alpha\beta}(\varepsilon) \left[-\frac{\partial f_\mu(T,\varepsilon)}{\partial \varepsilon} \right] d\varepsilon \qquad (A.9)$$

$$v_{\alpha\beta}(T,\mu) = \frac{1}{eT\Omega} \int \sigma_{\alpha\beta}(\varepsilon)(\varepsilon - \mu) \left[-\frac{\partial f_\mu(T,\varepsilon)}{\partial \varepsilon} \right] d\varepsilon \qquad (A.10)$$

$$\kappa_{\alpha\beta}^0 = (T,\mu) = \frac{1}{e^2 T\Omega} \int \sigma_{\alpha\beta}(\varepsilon)(\varepsilon - \mu)^2 \left[-\frac{\partial f_\mu(T,\varepsilon)}{\partial \varepsilon} \right] d\varepsilon \qquad (A.11)$$

$$\sigma_{\alpha\beta\gamma}(T,\mu) = \frac{1}{\Omega} \int \sigma_{\alpha\beta\gamma}(\varepsilon) \left[-\frac{\partial f_\mu(T,\varepsilon)}{\partial \varepsilon} \right] d\varepsilon \qquad (A.12)$$

where κ^0 is the electronic part of the thermal conductivity. The Seebeck and Hall coefficients can then easily be calculated:

$$S_{ij} = E_i \left(\nabla_j T \right)^{-1} = (\sigma^{-1})_{\alpha i} v_{\alpha j} \qquad (A.13)$$

$$R_{ijk} = \frac{E_j^{ind}}{j_i^{appl} B_k^{appl}} = (\sigma^{-1})_{\alpha i}\sigma_{\alpha\beta k}(\sigma^{-1})_{i\beta} \qquad (A.14)$$

A.4. Gibbs2 program

A.4.1. Description and method

Thermodynamic properties of solids are among the fundamental properties in condensed matter physics, materials science, and geophysics, where the ability of using materials in different devices and applications does not related only by the characteristic of matter, the dependence on the environment condition is very important to evaluate the efficiency of materials in given condition. Hence, the study of pressure and temperature dependence of thermodynamic properties is very helpful.

Gibbs2 program [20-22] derives thermal behaviour out from energy versus volume data obtained from ab initio calculations. Gibbs2 code does not give just pressure and temperature dependence of the thermodynamic properties, it could be also used to study the phase transitions of a solid. Gibbs2 reads one main input file (the case.ing) that contain the *E(V)* data and basic properties of the crystal (i.e., atomic mass), and generates the main output that have the same root. Fig. A.7 illustrate the calculation scheme used to calculate the Pressure *P(GPa)* and Temperature *T(K)* (those given by the user) dependence of thermodynamic properties. Among them: equilibrium volume *V(bohr^3)*, static energy E_{static} (Hy), Gibbs free energy *G* (kJ/mol), Isothermal bulk modulus *B* (GPa), Constant volume heat capacity C_V (J/molK), Debye temperature $\theta_D(T)$, Grüneisen parameter γ, Volumetric thermal expansion coefficient α, Adiabatic bulk modulus B_s(GPa), Constant pressure heat capacity C_p (J/molK), Vibrational contribution to the Helmholtz free energy F_{vib} (kJ/mol), Vibrational contribution to the internal energy U_{vib} (kJ/mol), Vibrational contribution to the entropy S_{vib} (J/molK).

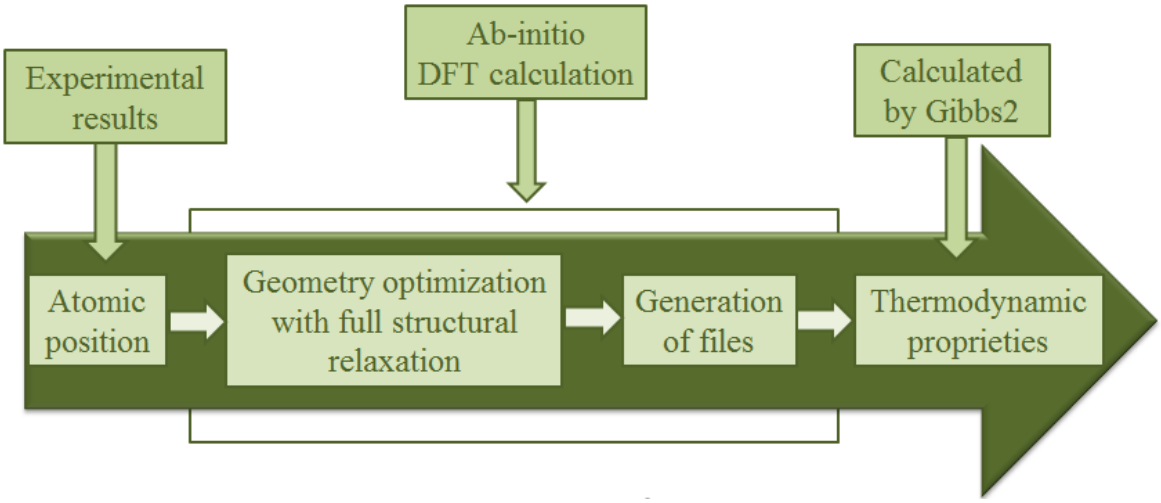

Figure A.7: Flowchart illustrating the calculation scheme used to calculate and store thermodynamic properties.

A.4.2. Thermal models

The effect of pressure is accounted for in a simple way by adding a $+PV$ term. The effect of temperature, however, requires a thermal model: a way of including the thermal contribution of the crystal degrees of freedom to the free energy. These contributions are dominated, in general, by the vibrational free energy, so the bulk of the gibbs2 program deals with how to incorporate the vibrational effects. Several thermal models with increasing complexity have been implemented [22]:

- Static: no temperature effects.
- Debye and Debye-Grüneisen: require the knowledge of the static energy. Optionally, the Poisson ratio and the Grüneisen gamma can also be input.
- Debye-Einstein: in addition, requires the vibrational frequencies at the gamma point of the first Brillouin zone (1BZ).
- Quasi-harmonic approximation (QHA): together with the static energy curve, either the phonon density of states or the frequencies on a grid sampling the 1BZ are required at each volume.

A.4.3. Quasi-harmonic Debye Model

It is known that all thermodynamic quantities of a crystal can be obtained from the vibrational density of states, $g(w)$. This function gives the number of normal modes of vibration between ω and $\omega + d\omega$. Debye model starts from the hypothesis that the crystal

can be modelled as a continuous medium, such that normal vibrations are stationary elastic waves. With this condition, you can calculate wavenumber whose frequency is in the range $(\omega, \omega + d\omega)$, providing the density of states corresponding to the model [23].

Within the Debye model, the force constants are evaluated from a harmonic-approximation consideration of the potential energy. This amounts that θ_D, Debye temperature, is constant, and that it must be obtained from the elastic constants of the same geometry. However, this purely harmonic model lacks one of the most important experimental characteristics of the crystals, such as the thermal expansion. Indeed, since the temperature only influences the Helmholtz function through the vibrational term, and this in turn depends on the force constants (or elastic constants) that are being considered constant, there is no relation between temperature and geometry of the system (volume). To overcome this deficiency, it is necessary to introduce interdependence between *T* and *V* in the model. One possible treatment is the quasi-harmonic approximation, which assumes harmonic vibrations, at positions different from the equilibrium positions. Hence, vibration frequencies are dependent on the crystal geometry (volume), being evaluated as related to the corresponding second derivatives of the potential energy surface at off-equilibrium position. Clearly, under static conditions, these do not produce real frequencies of vibration, the vibration must be around a minimum. However, in the presence of external conditions, such as pressure, which act such as generalized forces on the crystal, the equilibrium geometry displaces up to the situation in which external forces cancel the gradient of the static potential energy surface [24].

Recently, thanks to the advent of very efficient methods of computing the vibrational dispersion relations of a crystal, The QHA considered as the highly popular method. The function that controlling the geometry and phase stability of a solid under a given pressure and temperature is the non-equilibrium Gibbs free energy, [20]

$$G^*(x, V; P, T) = E_{stat}(x, V) + PV + F^*(x, V; T) \qquad (A.15)$$

where *x* represents the internal geometry of the solid (i.e., the independent unit cell lengths and angles of this phase, and all the free crystallographic coordinates of the atoms in non-fixed Wyckoff positions), $E_{stat}(x, V)$ is the static energy that obtained directly from the ab-initio calculation (i.e., null temperature and absence of zero point vibrational energy) and F^* is the Helmholtz free energy, which is defined as :

$$F^* = F^*_{el} + F^*_{vib} \qquad (A.16)$$

where F_{el} and F_{vib} are electronic excitations and ionic vibrations, respectively. Because of the difficulty of calculating G^*, a usual approach is restricting the internal variables to those resulting of a minimization of the static energy at any given volume (i.e., $E_{stat}(V) = min_x E_{sta}(x,V)$), that transforms Eq. A.15 to:

$$G^*(V;P,T) = E_{stat}(V) + PV + F^*_{vib}(\theta_D(V);T) \qquad (A.17)$$

The vibrational Helmholtz free energy, $F^*(\theta(V);T)$ can be written as: [25]

$$F^*_{Vib}(\theta_D;T) = nkT\left[\frac{9\theta_D}{8T} + 3\,ln\left(1 - e^{-\theta_D/T}\right) - D\left(\frac{\theta_D}{T}\right)\right] \qquad (A.18)$$

where $D(\theta_D/T)$ is the debye integral, and is defined as:

$$D(\theta_D/T) = \frac{3}{(\theta_D/T)^3}\int_0^{\theta_D/T}\frac{x^3}{e^x - 1}dx \qquad (A.19)$$

where n represents the number of atoms per formula unit. Debye temperature θ is described as:

$$\theta_D = \frac{\hbar}{k}\left[6\pi^2 V^{1/2} n\right]^{1/3} f(\nu)\sqrt{\frac{B_S}{M}} \qquad (A.20)$$

where M is the mass of per formula unit, ν Poisson ration and B_S the adiabatic bulk modulus that is approximated as:

$$B_S \approx B(V) = V\left(\frac{d^2E(V)}{dV^2}\right) \qquad (A.21)$$

and the *f(ν)* is given by:

$$f(\nu) = \left\{3\left[2\left(\frac{2}{3}\frac{1+\nu}{1-2\nu}\right)^{3/2} + \left(\frac{1}{3}\frac{1+\nu}{1-\nu}\right)^{3/2}\right]^{-1}\right\}^{1/3} \qquad (A.22)$$

Therefore, for the given pressure P and temperature T with respect to the volume V, the nonequilibrium Gibbs function merely depends on *V(P,T)* and can be solved as:

$$\left(\frac{\partial G^*(V;P,T)}{\partial V}\right)_{P,T} = 0 \qquad (A.23)$$

As a result, the heat capacity C_V (at constant volume), and the heat capacity C_P (at constant pressure), and the thermal expansion are given by:

$$C_V = nkT\left[4D(\theta_D/T) - \frac{3\,\theta_D/T}{e^{-\theta/T} - 1}\right] \qquad (A.24)$$

$$C_P = C_V(1 + \alpha\gamma T) \qquad (A.25)$$

$$\alpha = \frac{\gamma C_V}{B_T V} \qquad (A.26)$$

where the Grüneisen parametercis is defined as:

$$\gamma = -\frac{d(\ln \theta_D(V))}{d(lnV)} \qquad (A.27)$$

References

[1] P. Blaha, K. Schwarz, G. Madsen, D. Kvasnicka, J. Luitz, *WIEN2k: An Augmented Plane Wave Plus Local Orbitals Program for Calculating Crystal Properties; User's Guide, WIEN2k 14.2*, Vienna University of Technology, Inst. of Physical and Theoretical Chemistry, Austria, (2014).

[2] K, Schwarz, P. Blaha, G. K. H. Madsen, *Electronic structure calculations of solids using the WIEN2k package for material sciences*. Comput. Phys. Commun., Vol. 147, No 1-2, pp. 71-76, (2002).

[3] K. Schwarz, P. Blaha and S.B. Trickey, *Electronic structure of solids with WIEN2k*, Vol. 108, Nos. 21–23, pp. 3147–316, (2010).

[4] http://euler.phys.cmu.edu/cluster/WIEN2k/2Detailed_description.html.

[5] P. Blaha, K. Schwarz, P. Sorantin, S. B. Trickey, *Full-potential, linearized augmented plane wave programs for crystalline systems*, Comput. Phys. Commun., Vol. 59, No. 2, pp. 399-415, (1990).

[6] M. Petersen, F. Wagner, L. Hufnagel, M. Scheffler, P. Blaha, K. Schwarz, *Improving the efficiency of FP-LAPW calculations*, Comput. Phys. Commun., Vol. 126, No. 3, pp. 294–309, (2000).

[7] P.S. Kireev, *Semiconductor Physics*, Vysshaya Shkola, Moscow, (1975).

[8] X. Rocquefelte, *Relativistic effects and Non-collinear magnetism, 20th WIEN2k Workshop,* Penn State University, (2013).

[9] X. Rocquefelte, *Relativistic effects and magnetism in WIEN2k, 24th WIEN2k Workshop*, Vienna, (2017).

[10] R. L. Liboff, *Introductory Quantum Mechanics*, Addison-Wesley, (1980).

[11] J. Even, L. Pedesseau, J. M. Jancu, and C. Katan, *Importance of spin–orbit coupling in hybrid organic/ inorganic perovskites for photovoltaic applications*, J. Phys. Chem. Lett. Vol. 4, No. 17, pp. 2999–3005, (2013).

[12] J. A. Reyes-Retana, and F. Cervantes-Sodi, *Spin-orbital effects in metal-dichalcogenide semiconducting monolayers*, Scientific reports, Vol. 6, pp. 24093(10), (2016).

[13] S-D. GUO, *Importance of spin–orbit coupling in power factor calculations for half-Heusler ANiB (A= Ti, Hf, Sc, Y; B=Sn, Sb, Bi)*, J. Alloys Compd., Vol. 663, pp. 128-133, (2016).

[14] M. A. U. Absor, I. Santoso, Harsojo, and K. Abraha, *Defect-induced large spin-orbit splitting in monolayer PtSe2*, Phys. Rev. B, Vol. 96, No. 11, pp. 115128(6), (2017).

[15] M. Cardona, N. E. Christensen, and G. Fasol, *Relativistic band structure and spin-orbit splitting of zinc-blende-type semiconductors*, Phys. Rev. B, Vol. 38, No. 3, pp. 1806-1827, (1988).

[16] W-F. Li, C. Fang, and M. A. van Huis, *Strong spin-orbit splitting and magnetism of point defect states in monolayer WS2*, Phys. Rev. B, Vol. 94, No. 19, pp. 195425(8), (2016).

[17] G.K.H. Madsen, D.J. Singh, *BoltzTraP. A code for calculating band-structure dependent quantities*, Comput. Phys. Commun., Vol. 175, No. 1, pp. 67-71, (2006).

[18] D. D. Koelling, J. H. Wood, *On the interpolation of eigenvalues and a resultant integration scheme*, J. Comput. Phys., Vol. 67, No. 2, pp. 253-262, (1986).

[19] F. Ricci, W. Chen, U. Aydemir, G. J. Snyder, G-M Rignanese, A. Jain, G. Hautier. *An ab-initio electronic transport database for inorganic materials*. Scientific data, Vol. 4, pp. 170085, (2017).

[20] M.A. Blanco, E. Francisco, V. Luaña, *GIBBS: isothermal-isobaric thermodynamics of solids from energy curves using a quasi-harmonic Debye model*, Comput. Phys. Comm., Vol. 158, No. 1, pp. 57–72, (2004).

[21] A. Otero-de-la-Roza, V. Luana, *Gibbs2: A new version of the quasi-harmonic model code. I. Robust treatment of the static data*, Comput. Phys. Comm., Vol. 182, No. 8, pp.1708–1720, (2011).

[22] A. Otero-de-la-Roza, D. Abbasi-Pérez, V. Luaña, *Gibbs2: A new version of the quasiharmonic model code. II. Models for solid-state thermodynamics, features and implementation*, Comput. Phys. Comm., Vol. 182, No. 10, pp. 2232-2248, (2011).

[23] Daniel V. Schroeder. *An Introduction to Thermal Physics*. Addison-Wesley, San Francisco, 2000. Section 7.5.

[24] A. Breidi, *Quasiharmonic Debye Model*, researchgate.net, (2016).

[25] S. Feng, Sh. Li, H. Fu, *First-principle calculation and quasi-harmonic Debye model prediction for elastic and thermodynamic properties of* Bi_2Te_3, Comput. Mater. Sci., Vol. 82, pp. 45–49, (2014).

Journal of ELECTRONIC MATERIALS
DOI: 10.1007/s11664-017-5452-6

Structural, Elastic, Electronic and Optical Properties of LaOAgS-Type Silver Fluoride Chalcogenides: First-Principles Study

K. BOUDIAF,[1] A. BOUHEMADOU,[1,6] O. BOUDRIFA,[1] K. HADDADI,[1] F. SAAD SAOUD,[2] R. KHENATA,[3] Y. AL-DOURI,[4] S. BIN-OMRAN,[5] and M.A. GHEBOULI[1]

1.—Laboratory for Developing New Materials and Their Characterization, Department of Physics, Faculty of Science, University of Setif 1, 19000 Setif, Algeria. 2.—Department of Science and Technique, Faculty of Sciences and Technology, University of Bordj Bou-Arreridj, LMRN, 34000 Bordj Bou-Arreridj, Algeria. 3.—Laboratoire de Physique Quantique et de Modélisation Mathématique (LPQ3 M), Département de Technologie, Université de Mascara, 29000 Mascara, Algeria. 4.—Institute of Nano Electronic Engineering, Universiti Malaysia Perlis, 01000 Kangar, Perlis, Malaysia. 5.—Department of Physics and Astronomy, College of Science, King Saud University, P.O. Box 2455, Riyadh 11451, Saudi Arabia. 6.—e-mail: a_bouhemadou@yahoo.fr

First-principles density functional calculations were performed to investigate the structural parameters, elastic moduli and related properties, electronic band structure and optical properties of three LaOAgS-type barium silver fluoride chalcogenides BaAg*Ch*F (*Ch* denotes the chalcogenides S, Se and Te). The calculated structural parameters are in good accordance with the existing experimental data. The single-crystal and polycrystal elastic moduli were determined via the strain–stress technique. The investigated compounds show a strong anisotropic behaviour of the structural and elastic parameters. The calculated electronic band structure using the Tran–Blaha modified Becke–Johnson potential reveals that the three considered systems are large direct band gap semiconductors. The assignments of the energy band electronic states and chemical bonding character were accomplished with the help of the *l*-decomposed atomic densities of states diagrams. Frequency-dependent polarized optical functions were computed for an energy range from 0 eV to 30 eV. The microscopic origin of the electronic states that is responsible for the optical spectra structures were determined. The optical spectra exhibit a considerable anisotropy. Several trends in the variation of the considered physical properties with the atomic number *Z* of the chalcogenide *Ch* element in the BaAg*Ch*F series are observed.

Key words: 1111-like systems, first-principles calculations, elastic constants, electronic band structures, optical spectra

INTRODUCTION

The quaternary equiatomic LaOAgS-like systems, named also 1111 phases, form large family members (more than 200 compounds) in the crystal world.[1–8] This large class of quaternary materials exhibits some interesting physical properties, such as thermoelectricity,[6] transparency,[9] degenerate *p*-type electrical conductivity,[5] ferromagnetic response,[10] ionic conductivity[8] and medium-temperature superconductivity.[11,12] Owing to these outstanding physical properties, these 1111-like systems have various technological applications, such as *p*-type transparent semiconductors,[7,13] thermoelectrics,[14] optoelectronic devices[15] and photovoltaics.[16] The whole set of the 1111-like systems can be classified into two main

(Received November 26, 2016; accepted March 13, 2017)

Published online: 23 March 2017

subgroups.[3,12] The first one comprises metallic-like phases, which attract the attention of researchers for their superconductivity and magnetic properties.[11,17] The second one comprises the 1111-like systems exhibiting semiconducting behavior, which possess some interesting optical properties.[9,18–21] The 1111-like materials show a high flexibility to a large variety of constituent elements. The 1111-like oxychalcogenides have attracted the main attention of the researchers; however, much less investigations have been performed on the 1111-like chalcogenide fluorides.[12,21]

Recently, quaternary barium silver fluoride chalcogenides BaAg*Ch*F (*Ch* = S and Se) have been synthesized by Charkin et al.[2] via solid-state reactions of powdered Ba*Ch*, BaF_2 and Ag_2Ch (or Ba, BaF_2, Ag and *Ch*). Synthetic details, XRD characterisations and structural properties of the above-mentioned materials can be found in Ref. 2 These systems adopt the tetragonal $P4/nmm$ (No. 129) crystalline structure, $Z = 2$.[2] On the theoretical side, Bannikov et al.[12] calculated the electronic structures and optical spectra of BaAgSF and BaAgSeF employing the full-potential linearized augmented plane wave (FP-LAPW) method within the Perdew–Burke–Ernzerhof version of the generalized gradient approximation (GGA-PBE).[22] However, the GGA is well known by its misjudgment of the energy band gaps for semiconducting and insulating compounds. Typically, the energy band gap calculated through density functional theory (DFT) within the standard GGA/LDA is underestimated by approximately 30–50% compared to the measured one.[23–25] Accurate determination of the energy band dispersion and optical spectra of materials are especially required for eventual applications in the optoelectronic devices.[26] This constitutes the first objective of the present work. For technological applications in the optoelectronic field, the semiconductor materials are generally grown as thin films on substrates. However, the lattice mismatch and difference in thermal expansion coefficients between the epitaxial layer and substrate can produce large stresses in the grown layer.[27] Hence, it is of extreme importance to estimate the elastic moduli that describe the response of materials to external stresses. To the best knowledge of the authors, there is no available data in the literature on the elastic constants (C_{ij}s) of the studied BaAg*Ch*F crystals. Therefore, it becomes necessary and important to calculate the C_{ij}s of the BaAg*Ch*F compounds in order to disclose their elastic properties. Prediction of the elastic moduli and related properties of the BaAg*Ch*F series constitutes the second objective of the present work. A third objective of the present work is the investigation of the aforementioned properties for the hypothetical compound BaAgTeF, which is still completely unexplored to the best of our knowledge.

COMPUTATIONAL DETAILS

Two complementary codes based on the density functional theory were employed for a complete investigation of the structural parameters, elastic moduli, electronic properties and optical spectra of the barium silver fluoride chalcogenides BaAg*Ch*F (*Ch* = S, Se, Te).

The first part of the present work, namely, the structural optimization and elastic constants, was performed using the first-principles plane wave pseudopotential (PW-PP) approach as implemented in the CASTEP suite of programs.[28] The exchange–correlation functional was treated through the local density approximation (LDA)[29] and two different parameterizations of the GGA, namely, the GGA-PBE (termed also GGA96)[22] and the GGA-PBEsol (labelled also GGA08).[30] The GGA08 functional has been especially elaborated in order to improve the exchange–correlation potential modelling in solids. The Vanderbilt ultrasoft pseudopotentials[31] were used to model the interaction of the valence electrons with the nucleus and frozen core electrons. The electronic configurations for pseudo-atoms are Ba: $5s^25p^66s^2$, Ag: $3d^{10}5s^1$, F: $2s^22p^5$, S: $3s^23p^4$, Se: $4s^24p^4$ and Te: $5s^25p^4$. A kinetic energy cut-off of 400 eV and a Monkhorst–Pack algorithm[32] with a $12 \times 12 \times 5$ k-point mesh to sample the Brillouin zone (BZ) were used to ensure a total energy convergence of 10^{-6} eV/atom. The following convergence criteria: total energy variation smaller than 5.0×10^{-6} eV/atom, maximum force on any atom smaller than 0.01 eV/Å^{-1}, stress smaller than 0.02 GPa and atomic displacement smaller than 5.0×10^{-4} Å were used to perform the full geometry optimization via the BFGS minimization algorithm.[33] The six single-crystal independent elastic constants, namely C_{11}, C_{33}, C_{44}, C_{66}, C_{12} and C_{13}, were determined by means of a linear fitting of the stress–strain data obtained from first-principles calculations.[28] The polycrystalline aggregate elastic moduli, namely the bulk (B) and shear (G), were derived from the single-crystal elastic constants via the Voigt–Reuss–Hill approach.[34]

Generally, the common GGA and LDA yield unsatisfactory band gap values compared to the corresponding measured ones for semiconductors and insulators. This is because the standard GGA/LDA cannot describe accurately the excited electronic states. Some functionals beyond the GGA/LDA are developed in order to improve the treatment of the exchange–correlation potential and consequently better describing the electronic structures of semiconductors and insulators. Among these functionals, which yield an improved band gap compared to the standard functionals, we find the Tran–Blaha modified Becke–Johnson (TB-mBJ) potential.[35–37] The TB-mBJ functional yields accurate fundamental band gap values for large families of semiconductors and isolators.[38] The predicted band gap values using the TB-mBJ are almost comparable with the experimental ones but with

much less computing time compared to the sophisticated hybrid functionals and GW method. For this reason, the electronic and optical properties of the examined systems were studied using the TB-mBJ functional as implemented in the WIEN2k package[39] in order to provide electronic structure data more accurate than those reported previously.[12] The WIEN2k code[39] is an implementation of the full-potential linearized augmented plane wave (FP-LAPW) formalism based on the DFT. It is worth to note that the TB-mBJ potential functional is optimized to reproduce the energy band gaps of semiconducting and isolating materials and cannot be used for structural and elastic properties.[6] For the structural and elastic properties, we used the GGA-PBEsol, which is well tested for solids.[30]

The complex dielectric function: $\varepsilon(\omega) = \varepsilon_1(\omega) + i\varepsilon_2(\omega)$ characterizes the linear response of matter to incident radiation. The imaginary part ($\varepsilon_2(\omega)$) of the dielectric function ($\varepsilon(\omega)$) characterizes the absorption of the incident light by matter and can be computed by summing all allowed electronic transitions from occupied to unoccupied states. The real part ($\varepsilon_1(\omega)$) characterizes the dispersion of the incident radiation when it traverses a medium and can be derived from $\varepsilon_2(\omega)$ via the Kramer–Kronig transformation. The knowledge of both $\varepsilon_1(\omega)$ and $\varepsilon_2(\omega)$ permits one to compute all other macroscopic optical constants. To obtain accurate results for the optical constants, a dense k-point set is necessary. A $24 \times 24 \times 11$ k-point mesh was employed to calculate the dipole matrix element, which is the key for the optical spectra.

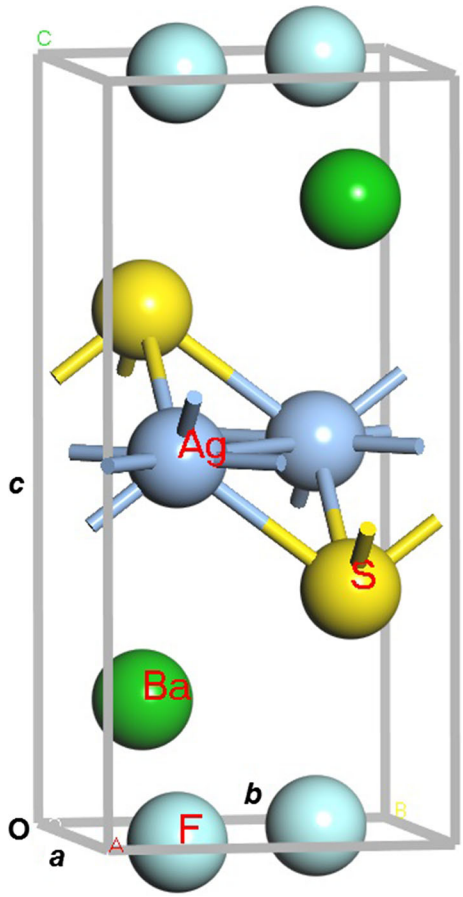

Fig. 1. The unit-cell crystalline structure of BaAgSF layered structure.

RESULTS AND DISCUSSION

Structural Properties

One conventional cell of the BaAgSF compound is depicted in Fig. 1 as a prototype for the BaAg*Ch*F series. As described elsewhere,[2] the barium silver fluoride chalcogenides BaAg*Ch*F (*Ch* = S, Se, Te) crystalize in a tetragonal layered structure of the LaOAgS-type with the space group $P4/nmm$ and may be schematically viewed as an alternating stacking of quasi two-dimensional [BaF] and [Ag*Ch*] layers along the c-axis.[21] The Wyckoff positions of the four inequivalent atomic positions in the BaAg*Ch*F compounds are Ba: 2c (0.25, 0.25, z_{Ba}), Ag: 2b (0.75, 0.25, 0.5), *Ch*: 2c (0.25, 0.25, z_{Ch}) and F: 2a (0.75, 0.25, 0), where z_{Ba} and z_{Ch} are the internal z-coordinates of the Ba and chalcogen *Ch* atoms, respectively. The calculated equilibrium unit-cell parameters (a and c) and internal atomic coordinates (z_{Ba} and z_{Ch}) for each considered compound and the corresponding measured and previously calculated values (when available) are collected in Table I. Owing to the fact that the experiments were performed at room temperature whereas our results are predicted for zero temperature, one would expect that correct calculated values for the lattice parameters will be slightly smaller than their corresponding measured ones. From Table I, one can note that the GGA96-calculated (LDA-calculated) lattice parameters of the three considered compounds are somewhat larger (somewhat smaller) than the measured ones. This stems from the well-known fact that the LDA tends to slightly underestimate the interatomic distances, and the GGA96 tends to slightly overestimate them. However, from Table I, one can appreciate that the GGA08 calculated lattice parameters are practically equal to the arithmetic averages of the GGA96 and LDA-calculated values and are slightly smaller than their corresponding experimental ones, as expected. It is worth to note that the GGA08[30] has been developed specifically to improve the description of the exchange–correlation effects in solids. The maximum discrepancy between the GGA08-calculated structural parameters and the experiment is about 1.5% for the c parameter and less than 1% for the remaining parameters, which demonstrates the reliability of the obtained results. Therefore, the GGA08 optimized structural parameters were adopted for the calculations of the remaining investigated properties. The unit-cell parameters, a and c, increase when the chalcogenide atom *Ch* is substituted in the following sequence:

Table I. Calculated lattice parameters (a and c, in Å), internal atomic coordinates (z_{Ba} and z_{Ch} (*Ch* = S, Se and Te), dimensionless), unit-cell volume (V, in (Å^3)), cohesion energy (E_{coh}, in eV), formation enthalpy (ΔH, in eV) for the BaAg*Ch*F compounds, compared with available experimental and theoretical data

	BaAgSF			BaAgSeF			BaAgTeF
Property	**This work**	**Expt.[A]**	**Other[B]**	**This work**	**Expt.[A]**	**Other[B]**	**This work**
a	4.2047[a]	4.2406	4.280	4.2982[a]	4.3449	4.345	4.5015[a]
	4.1420[b]			4.2463[b]			4.4332[b]
	4.2785[c]			4.3679[c]			4.5018[c]
	4.2047[d]			4.3108[d]			4.5078[d]
c	9.1718[a]	9.3029	9.411	9.2690[a]	9.4018	9.558	9.5170[a]
	9.0004[b]			9.0849[b]			9.2666[b]
	9.3918[c]			9.5186[c]			9.5164[c]
	9.2365[d]			9.3203[d]			9.5024[d]
V	162.15[a]	167.29		171.24[a]	177.49		192.85[a]
z_{Ba}	0.1676[a]	0.1665		0.1616[a]	0.1598		0.1472[a]
	0.1693[d]			0.1624[d]			0.1494[d]
z_{Ch}	0.6743[a]	0.6760		0.6796[a]	0.6798		0.6859[a]
	0.6747[d]			0.6809[d]			0.6846[d]
E_{Coh}	−5.0056[a]			−4.8942[a]			−4.6850[a]
ΔH	−2.0536[a]			−2.4271[a]			−1.9476[a]

[a]Present, using GGA08 (PP-PW).[b]Present, using LDA.[c]Present, using GGA-PBE.[d]Present, using GGA08 (FP-LAPW).[A]Ref. 2.[B]Ref. 11.

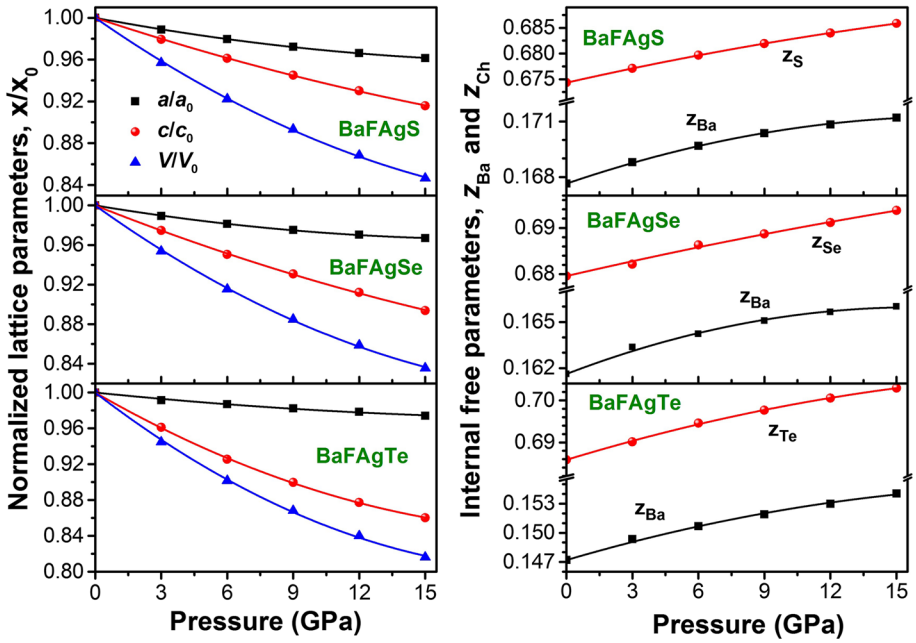

Fig. 2. Pressure dependence of the lattice parameters (a and c) and internal coordinates (Z_{Ba} and Z_{Ch}) for BaAgSF, BaAgSeF and BaAgTeF.

S → Se → Te in the BaAg*Ch*F series. This is a consequence of the increase of the *Ch* atomic radii (R); R(S) = 1.09 Å < R(Se) = 1.22 Å < R(Te) = 1.42 Å. One can appreciate that the calculated cohesive energy and formation energy (see Table I) are negative for each investigated compound, indicating that all studied compounds (including the hypothetical one; BaFAgTe) are chemically stable, confirming the fact that these compounds can be easily synthesized.

Pressure dependence of the relative shrinkage of the lattice parameters (a/a_0 and c/c_0) and unit-cell volume (V/V_0) and the internal atomic coordinates (z_{Ba} and z_{Ch}) are visualized in Fig. 2 (V, a, c, z_{Ba} and z_{Ch} are the values of the corresponding parameters at a fixed pressure P, whereas V_0, a_0 and c_0 are the corresponding values at zero pressure). In Fig. 2, the symbols represent the calculated results and solid lines represent the fits of these results to a second-order polynomial. One can appreciate that the

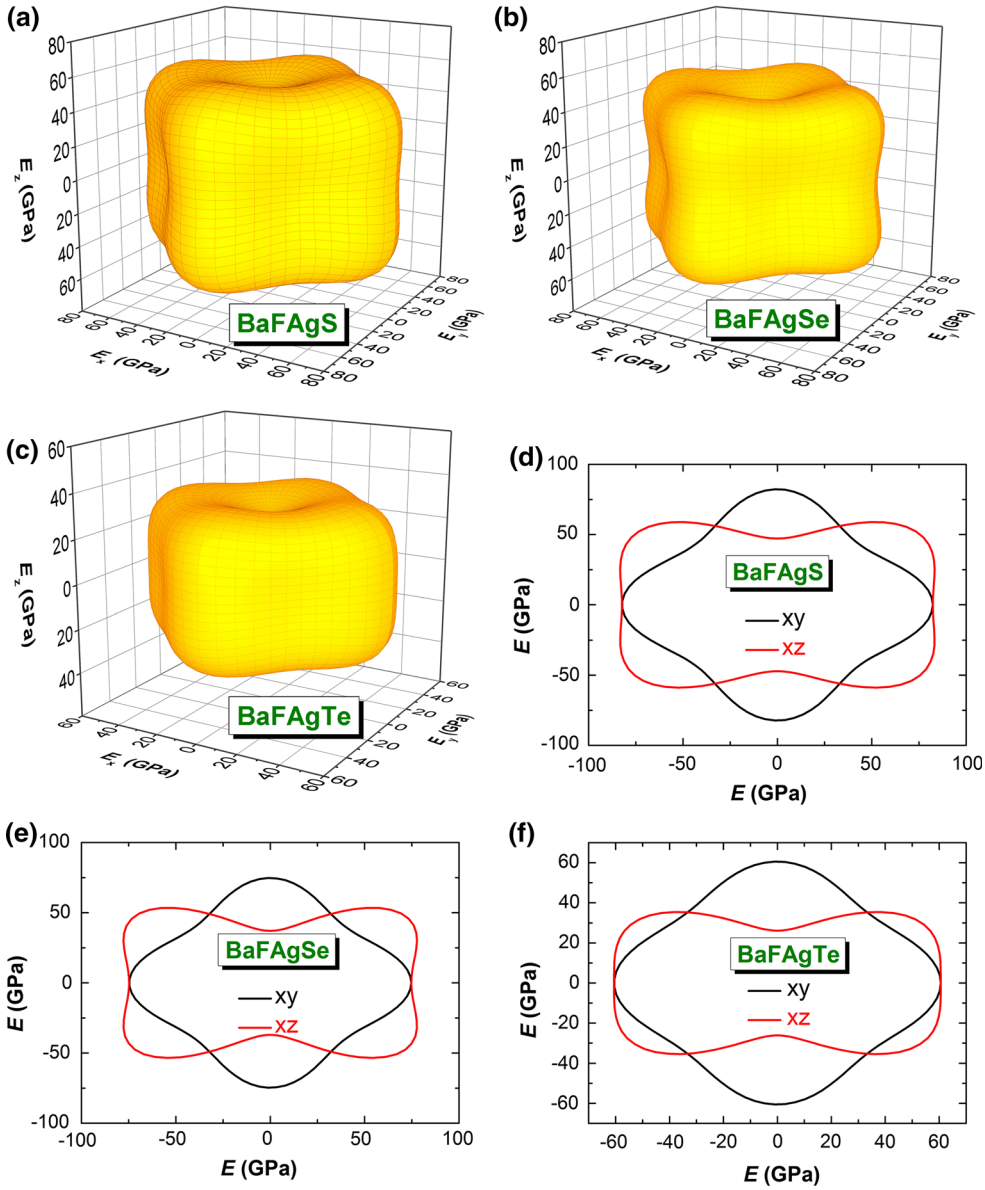

Fig. 3. The Young's modulus 3-D-representation for BaAgSF (a), BaAgSeF (b) and BaAgTeF (c) and their cross-section in the *xy* and *xz* planes (BaAgSF (d), BaAgSeF (e) and BaAgTeF (f)).

shrinkage along the *c*-axis is faster than that along the *a*-axis, indicating that the chemical bonding between the blocks [Ag*Ch*] and [BaF] along the *c*-axis are weaker than those between atoms inside these blocks along the *a*-axis. This demonstrates the chemical bonding anisotropy of the studied materials.

The calculated primitive-cell volume (V) versus pressure (P) and total energy (E) versus primitive-cell volume were fitted to some different equations of states (*EOS*) to determine the bulk modulus (B) and its pressure derivative (B') for the examined systems. Figure 3 presents the fit curves of the calculated E–V and P–V data to the corresponding Birch–Murnaghan *EOS*[40] as a prototype. The obtained values of B and B' from the fitting of the calculated E–V and V–P data with the Birch–Murnaghan,[40] Murnaghan[41] and Vinet[42] *EOSs* are collected in Table II. One can appreciate the good consistency between the values of B obtained via these different versions of *EOS*. It can be observed that the value of B decreases in BaAg*Ch*F series when going in the sequence BaAgSF → BaAgSeF → BaAgTeF. This is in agreement with the known fact that the bulk modulus is inversely proportional to the primitive-cell *volume*, i.e., $B \sim V^{-1}$. The relatively small values of B of the considered materials indicate that these compounds possess a high compressibility. The computed bulk modulus values from the *EOS* fits will be employed later to examine the consistency and accuracy of the present work results by comparing them to the corresponding ones that will be

Table II. The bulk modulus (B_0, in GPa) and its pressure derivative (B′, dimensionless) as extracted from Birch-Murnaghan (B.M.), Murnaghan (M.) and Vinet equation of states (*EOS*) for BaAgSF, BaAgSeF and BaAgTeF

		B.M. *EOS* fit		M. *EOS* fit		Vinet EOS fit	
Systems	**Property**	***E–V* EOS**	***P–V* EOS**	***E–V* EOS**	***P–V* EOS**	***E–V* EOS**	***P–V* EOS**
BaAgSF	B_0	60.87	61.82	60.32	62.40	61.77	61.50
	B'	4.70	4.49	4.59	4.17	4.085	4.67
BaAgSeF	B_0	55.37	56.36	54.78	56.94	55.67	56.04
	B'	4.58	4.36	4.47	4.03	4.605	4.55
BaAgTeF	B_0	46.34	45.49	45.54	46.18	46.72	45.11
	B'	4.51	4.734	4.44	4.31	4.529	4.97

Table III. Calculated single-crystal elastic constants (C_{ij}, in GPa), Bulk modulus (B, in GPa), shear modulus (G, in GPa), Young's modulus (E, in GPa), Poisson's coefficient (σ, dimensionless), Pugh's indicator (B/G), longitudinal, transversal and average sound velocities (V_l, V_t and V_m, respectively, in m/s) and Debye temperature (T_D, in K) for BaAgSF, BaAgSeF and BaAgTeF. The subscript V, R and H stand to Voigt, Reuss and Hill approximations. The compliance tensor S (S_{ij}) was calculated as the inverse of the stiffness matrix C ($S = C^{-1}$)

Property	**BaAgSF**	**BaAgSeF**	**BaAgTeF**
C_{11} (S_{11})	111.4 (0.0121457)	105.7 (0.0133843)	90.94 (0.0165082
C_{33} (S_{33})	77.62 (0.021210)	66.59 (0.0269921)	51.67 (0.0382949)
C_{44} (S_{44})	34.82 (0.0287206)	33.24 (0.0300857)	21.07 (0.0497541)
C_{66} (S_{66})	23.31 (0.0428973)	22.19 (0.0450560)	19.91 (0.0502173)
C_{12} (S_{12})	34.66 (−0.0008780)	33.44 (−0.0004625)	31.12 (−0.0003468)
C_{13} (S_{13})	47.18 (−0.0068492)	45.33 (−0.0087960)	39.43 (−0.0123439)
B_V	62.06	58.46	50.39
B_R	61.16	56.65	47.24
B_H	61.61	57.55	48.82
G_V	30.02	27.99	20.65
G_R	27.71	24.88	18.31
G_H	28.87	26.43	19.48
B_H/G_H	2.134	2.177	2.506
E	74.90	68.77	51.57
σ	0.2974	0.3008	0.3239
V_l	4062	3734	3329
V_t	2181	1993	1699
V_m	2435	2226	1904
T_D	266.1	238.9	196.3

derived from the single-crystal elastic parameters (C_{ij}s).

Elastic Constants and Related Properties

The calculated values of the six C_{ij} elastic constants, namely C_{11}, C_{33}, C_{44}, C_{66}, C_{12} and C_{13}, and the corresponding elastic compliances S_{ij}s for the title materials are listed in Table III. From Table III data, the following conclusions can be made:

I The computed C_{ij}s satisfy the well-known mechanical stability restrictions for tetragonal crystals.[42] Therefore, the examined compounds (including the hypothetical BaAgTeF compound) are mechanically stable.

II The difference between the values of C_{11} and C_{33} characterizes the elastic anisotropy in the stacking plane (C_{11}) and in the perpendicular [001] direction (C_{33}) in the studied systems. C_{11} is larger than C_{33}, indicating that these crystals are more resistant to compressional strains along the a-axis than that along the c-axis. This is in agreement with the fact that the bonding between the [AgCh] and [BaF] layers, stacked along the c-axis, is weaker than the intralayer bonding in the ab plane, discussed above in the "Structural properties" section. On the other hand, this result demonstrates that these materials are elastically anisotropic. One can also observe that C_{11} and C_{33} are larger than C_{44} and C_{66}, demonstrating that the resistance of the examined materials against the shear deformations is much weaker compared to that against the compressional deformations.

Table IV. Calculated acoustic wave velocities (in m/s) propagating along the [100], [110] and [001] directions in the BaAgSF, BaAgSeF and BaAgTeF systems

Direction	Polarisation	BaAgSF	BaAgSeF	BaAgTeF
[100]	[100]: υ_l	4286	3984	3671
	[010]: υ_{t1}	2395	2235	1767
	[001]: υ_{t2}	1960	1826	1718
[001]	[001]: υ_l	3577	3163	2767
	[100]: υ_{t1}	1960	1826	1718
	[001]: υ_{t2}	1960	1826	1718
[110]	[110]: υ_l	3985	3713	3464
	[1-10]: υ_{t1}	2395	2235	1767
	[001]: υ_{t2}	2515	2329	2106

III Theoretically, the macroscopic mechanical properties of polycrystals, which are expressed by B and G, can be evaluated from a proper averaging of the C_{ij}s via the Voigt–Reuss–Hill approach.[34] The Voigt and Reuss averages represent the extreme limits of B and G and according to Hill,[34] the effective values of B and G can be expressed by the arithmetic mean of these two limits. The expressions of Voigt (V) and Reuss (R) approximations of B (B_R, B_V) and G (B_R, G_V) for a tetragonal structure can be found in Refs. 43 and 44. The orientation-averaged Young's modulus E and the Poisson's ratio σ can be calculated from B and G using the well-known relations.[26] The predicted values for the B, G, E and σ moduli are listed in Table IV. From Table IV data, the following conclusions can be made:

A For each considered compound, the calculated B value from the single-crystal elastic constants through the Voigt-Reuss-Hill average is in good agreement with the corresponding one derived from the *EOS* fit. Therefore, this good agreement between the B values obtained via two different computational methods constitutes another proof of the reliability and accuracy of the computed elastic moduli.

B The considered compounds have a relatively small Young's modulus (E) value. This confirms the rather low stiffness of the considered compounds. As E characterizes the resistance of a solid against uniaxial deformation, so it is related to C_{11} and C_{33} elastic constants, which explains the decrease of E when going from BaAgSF to BaAgSeF to BaAgTeF in the same sequence as C_{11} and C_{33}. The shear modulus G decreases also when going from BaAgSF to BaAgSeF to BaAgTeF in accordance with the decrease of the C_{44}.

C According to an empirical criterion by Pugh,[45] a solid is brittle (ductile) if the B/G ratio is smaller (greater) than 1.75. The B/G ratios of all herein studied compounds are greater than 1.75, suggesting their ductile behaviour. A ductile material is resistant to thermal shocks. The bulk modulus B is two times the shear modulus G, indicating that the shear deformation is easier to occur in the considered compounds.

IV It is established that the anisotropy of the coefficient of thermal expansion and elastic anisotropy can cause microcracks in materials.[46] It is also accepted that the elastic anisotropy can significantly influence the nanoscale precursor textures in alloys.[47] Therefore, it becomes necessary and important to estimate the elastic anisotropy extent in solids. Some different indices have been established to estimate the elastic anisotropy degree in crystals. To evaluate the elastic anisotropy degree in the considered BaAg*Ch*F compounds, two different approaches were employed.

1. Ranganathan and Ostoja-Starzewski[48] proposed a universal index A^U, defined as follows $A^U = 5G_V/G_R + B_V/B_R - 6$, to quantify the elastic anisotropy extent in a crystal. An isotropic crystal is characterized by $A^U = 0$. Any deviation of A^U from zero indicates the presence of an elastic anisotropy and the degree of this deviation gives the extent of this elastic anisotropy. The computed values of the A^U ($A^U = 0.43$ for BaAgSF, $A^U = 0.66$ for BaAgSeF and $A^U = 0.71$ for BaAgTeF) demonstrate that the considered compounds exhibit a noticeable elastic anisotropy and its degree increases when going from BaAgSF to BaAgSeF to BaAgTeF.
2. A more used tool to visualize the elastic anisotropy extent of crystals is by plotting three-dimensional (3-D) representations of the directional dependence of their elastic moduli. 3-D representations of the directional dependence of the Young's modulus E and compressibility β ($\beta = 1/B$) were used in the present work. For a tetragonal

crystal, the crystallographic direction dependence of the Young's modulus E and compressibility β are expressed by the following relations[49]:

$$\frac{1}{E} = (l_1^4 + l_2^4)s_{11} + l_3^4 s_{33} + l_1^2 l_2^2(2s_{12} + s_{66}) + l_3^2(1 - l_3^2)(2s_{13} + s_{44}) \quad (1)$$

$$\beta = (s_{11} + s_{12} + s_{13}) + l_3^2(s_{11} + s_{12} - s_{13} - s_{33}). \quad (2)$$

In Eqs. 1 and 2, S_{ij}s are the elastic compliance constants and l_1, l_2 and l_3 are the directional cosines with respect to the x-, y- and z- axes, respectively. In a closed 3D-representation, the distance from the origin of the coordination system to the surface gives the value of the represented modulus in a given direction. Thus, for an isotropic material, the representative closed surface should exhibit a spherical shape. Any deviation of the representative closed surface from the spherical shape announces the presence of an elastic anisotropy.[50] From Figs. 3 and 4, one can appreciate that the shape of the 3D-closed surfaces for E and β are considerably different from the spherical shape, suggesting a strong elastic anisotropy of the examined materials. The cross-sections of the 3D-closed surface of the E modulus in the xy and xz planes are also represented in Fig. 3 in order to more visualize the elastic anisotropy. These 2D-representations clearly show the pronounced elastic anisotropy of the considered systems. The highest value of the Young's modulus (E_{max}) is realized for applied external stress along the [100] and [010] crystallographic directions, and the lowest value of the Young's modulus E_{min} is along the [001] direction, which is consistent with the fact that the a-axis is more resistant against compression than the c-axis. The E_{min} is approximately 57% E_{max} in BaAgSF, 49% E_{max} in BaAgSeF and 43% E_{max} in BaAgTeF, which indicates that the elastic anisotropy degree increases when going from BaAgSF to BaAgSeF to BaAgTeF.

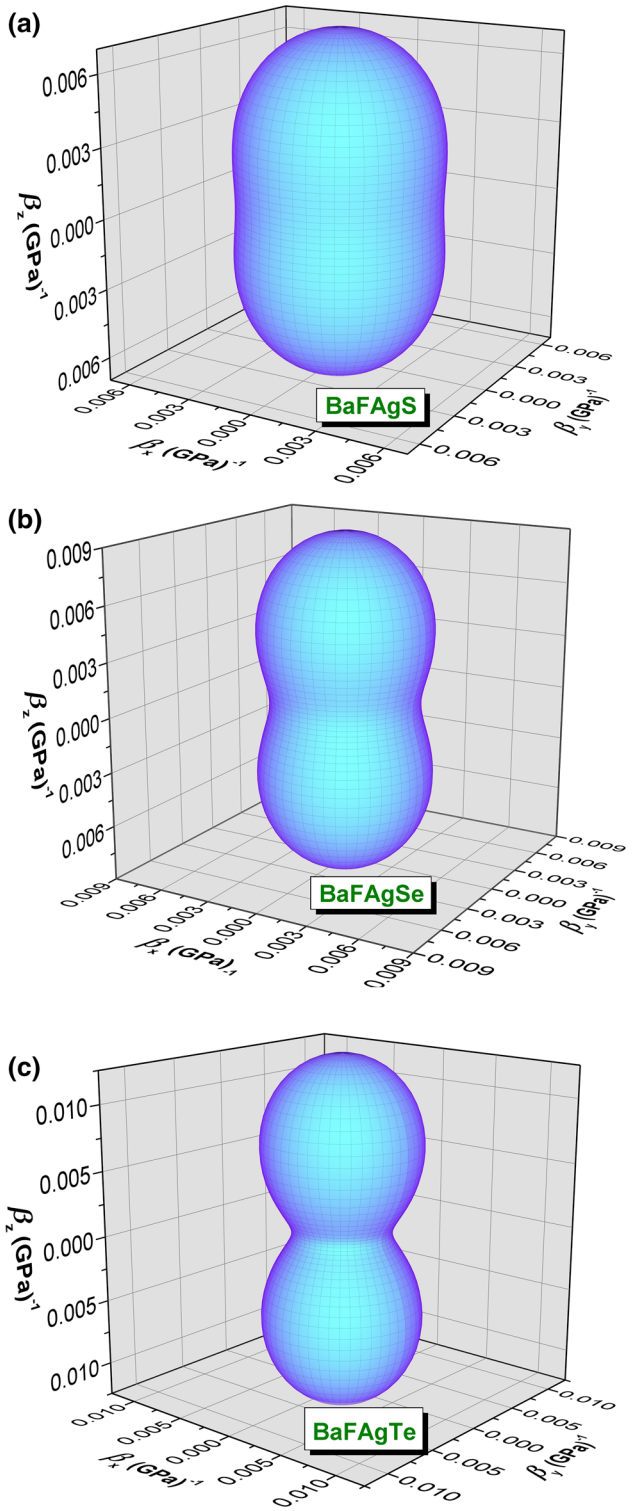

Fig. 4. The compressibility (β) 3D-representation for BaAgSF (a), BaAgSeF (b) and BaFAgTe (c).

V One can calculate the Debye temperature (T_D), which is correlated with many important fundamental physical properties of solids, from the computed B and G moduli as follows[51]:

$$T_D = \frac{h}{k_B}\left[\frac{3n}{4\pi V_a}\right]^{1/3} V_m. \quad (3)$$

Here, h is Plank's constant, k_B is Boltzmann's constant, n is the number of atoms in the molecule, and V_a is the atomic volume. The average sound wave velocity V_m in a polycrystalline material is given by[52]:

$$V_m = \left[\frac{1}{3}\left(2V_t^{-3} + V_l^{-3}\right)\right]^{-1/3}. \quad (4)$$

In Eq. 4, V_l and V_t are the transverse and longitudinal elastic waves in the polycrystalline phase of material, respectively, which are given by the Navier's equations:

$$V_l = \left(\frac{3B + 4G}{3\rho}\right)^{1/2}, \quad V_t = \left(\frac{G}{\rho}\right)^{1/2}. \quad (5)$$

Here, ρ is the mass density. Calculated T_D and average sound wave velocities (V_l, V_t and V_m) values are listed in Table III. The T_D value decreases when going from BaAgSF to BaAgSeF to BaAgTeF, which is an accordance with the decreases of the stiffness in the same sequence. This might indicate a decrease of the thermal conductivity when going from BaAgSF to BaAgSeF to BaAgTeF.

VI The sound wave velocities are related to some physical properties of crystals such as the thermal conductivity. In a tetragonal crystal, the elastic wave velocities propagating along the [100], [001] and [110] crystallographic directions can be calculated using the known relationships given in Ref. 53. The obtained elastic wave velocities are gathered in Table IV. The longitudinal wave velocities are larger than the transverse ones and both the longitudinal and transverse waves decrease when going from BaAgSF to BaAgSeF to BaAgTeF. This can be explained by the decease of the single-crystal elastic constants in the same sequence; the elastic wave velocities are proportional to the square root of the corresponding elastic constants.

Electronic Band Dispersion and Density of States

Figure 5 shows the calculated GGA08 and TB-mBJ energy band dispersions along some high symmetry lines of the BZ for the BaAgSF, BaAgSeF and BaAgTeF systems at the equilibrium lattice parameters obtained using the FP-LAPW method with the GGA08 (see Table I). Both the upper valence band maximum (UVBMa) and lower conduction band minimum (LCBMi) occur at the center of the BZ, demonstrating that these compounds are direct energy band gap (Γ–Γ) semiconductors. For all investigated compounds, the overall profile of the GGA08 band structure is almost similar to that of the TB-mBJ one. There is an important quantitative difference between the TB-mBJ band gap and the GGA08 one; the obtained TB-mBJ (GGA08) fundamental band gap is 2.89 eV (1.47 eV) for BaAgSF, 2.66 eV (1.22 eV) for BaAgSeF and 2.56 eV (1.56 eV) for BaAgTeF. The TB-mBJ displaces the conduction bands toward higher energies with respect to the top of the valence band, so, the TB-mBJ band gap is larger than the GGA08 one. No experimental data concerning the band gaps of the title materials are available in the literature to be compared with our results. Our calculated GGA08 band gaps for BaAgSF and BaAgSeF are in acceptable agreement with the available theoretical results,[12] which were performed using the FP-LAPW method within the GGA96. If we bear in mind that the GGA DFT band gap is approximately 30–50% smaller than the corresponding experimental one,[23–25] we can expect that the real band gaps of the considered materials will be larger than those obtained using the GGA08. From Table V, one can appreciate that the TB-mBJ approach improves the band gap values of BaAgSF, BaAgSeF and BaAgTeF by approximately 49%, 54%, and 40%, respectively, compared to the corresponding GGA08 ones. Therefore, the calculated TB-mBJ band gaps might be expected to be in reasonable agreement with the real values. The TB-mBJ band gaps for the BaAg*Ch*F series, expanding in the energy interval from 2.6 eV to 2.9 eV, are comparable with the measured gaps for the isostructural SrCuSF (3.0 eV) and SrCuSeF (2.7 eV).[54] Owing to the advantages of the TB-mBJ, we report and discuss only the results obtained within the TB-mBJ potential in the rest of the manuscript. One can note that the overall profile of the band structure dispersions of the BaAgSF and BaAgSeF compounds are practically identical, whereas that of BaAgTeF is somewhat different; for example, the lower valence band group in BaAgSF and BaAgSeF (Fig. 5) splits into two distinct narrow band groups in BaAgTeF. The width of the near-Fermi level valence band group increases slightly when the *Ch* chalcogen atom in the BaAg*Ch*F series is replaced in the following sequence: S → Se → Te, indicating a slight increase of the ionic character. One can observe narrow quasi-flat valence bands along the Γ–Z, A–M and R–X lines of the BZ, which correspond to the crystallographic *c*-axis, and relatively broad large dispersive valence bands along the Z–A, Γ–M, Z–R and Γ–X directions of the BZ, which are in the *ab* plane of the crystal. These behaviours demonstrate the high anisotropy of the chemical bonding in the layered BaAg*Ch*F systems; the chemical bonding inside the blocks [BaF] and [Ag*Ch*] differs considerably from the inter-adjacent-blocks bonding. Similar behaviours of the high-energy valence bands, i.e., the coexistence of quasi-flat and relatively high dispersive valence bands, were reported for other 1111-like oxychalcogenides and fluorochalcogenides.[5,6,12,21,54] These features are considered as favourable indicators of high *p*-type conductivity, promoting a relatively high hole mobility and a high hole concentration.[12,54]

The total (TDOS) and atomic-resolved *l*-projected (PDOS) densities of electronic states diagrams help to assign the electronic states of the electronic energy bands. The calculated TDOS and PDOS diagrams for the BaAgSF, BaAgSeF and BaAgTeF

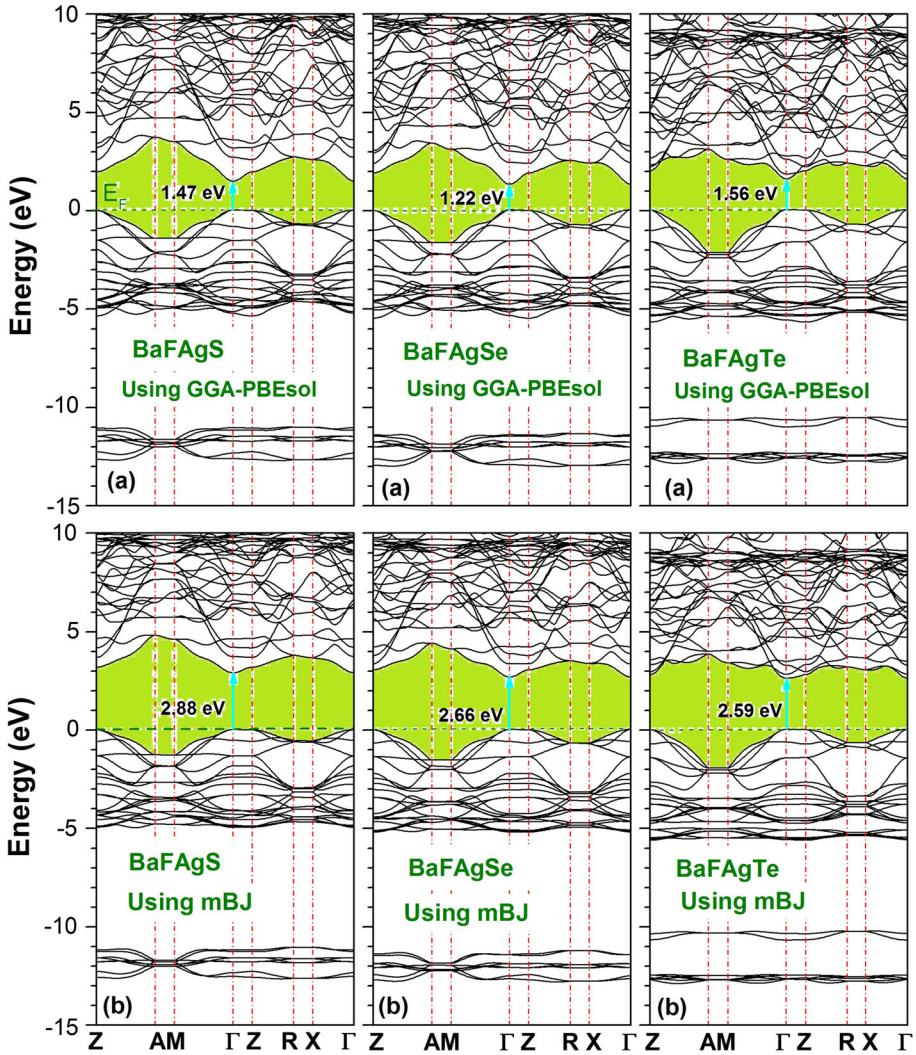

Fig. 5. GGA-PBEsol (a) and TB-mBJ (b) band structures of the BaAgSF, BaAgSeF and BaAgTeF systems along some high-symmetry lines in the Brillouin zone. The energy zero level corresponds to the Fermi level.

Table V. Calculated energy band gaps (E_g, in eV) within the GGA-PBEsol (GGA08) and TB-mBJ approximations compared to the available theoretical results

System	E_g (Γ–Z)	E_g (Γ–A)	E_g (Γ–M)	E_g (Γ–Γ)	E_g (Γ–R)	E_g (Γ–X)
BaFAgS						
GGA08[a]	2.002	3.674	3.427	1.516	2.742	2.605
GGA08[b]	1.939	3.700	3.477	1.468	2.800	2.571
TB-mBJ[b]	3.170	4.791	4.591	2.886	3.774	3.651
Other[12]				1.387		
BaFAgSe						
GGA08[a]	1.912	3.390	3.053	1.323	2.554	2.414
GGA08[b]	1.875	3.397	3.082	1.218	2.379	2.515
TB-mBJ[b]	3.025	4.364	4.099	2.663	3.486	3.351
Other[12]				1.278		
BaFAgTe						
GGA08[a]	1.999	2.989	2.438	1.534	2.346	2.202
GGA08[b]	1.974	3.070	2.551	1.557	2.364	2.227
TB-mBJ[b]	2.774	3.818	3.378	2.595	3.170	3.021

[a]Present, using CASTEP code.[b]Present, using WIEN2K code.

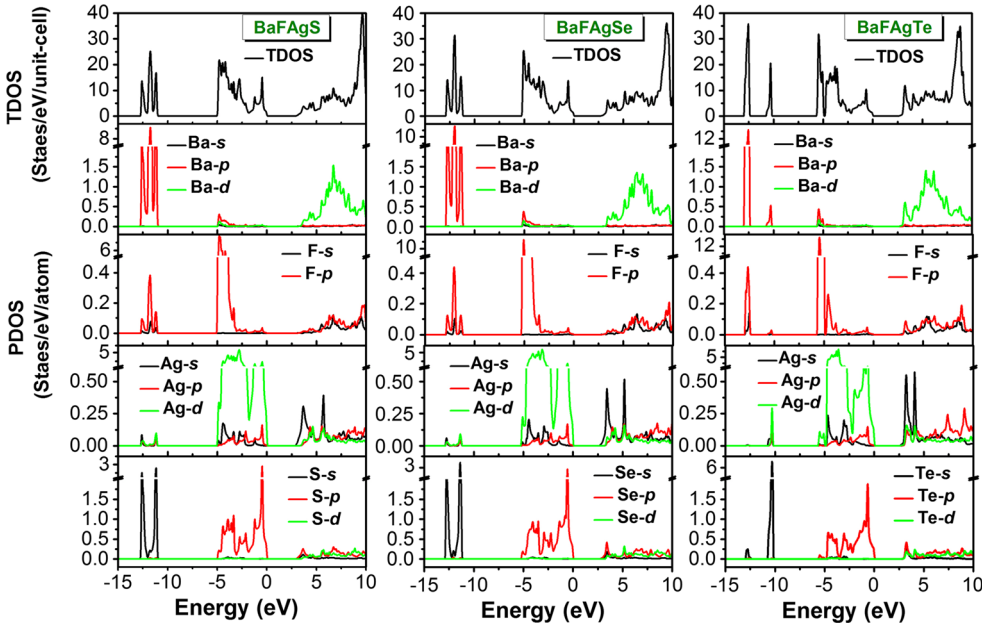

Fig. 6. The total and atomic-resolved *l*-decomposed densities of states (TDOS and PDOS, respectively) for the BaAgSF, BaAgSeF and BaAgTeF systems. The energy zero level corresponds to the Fermi level.

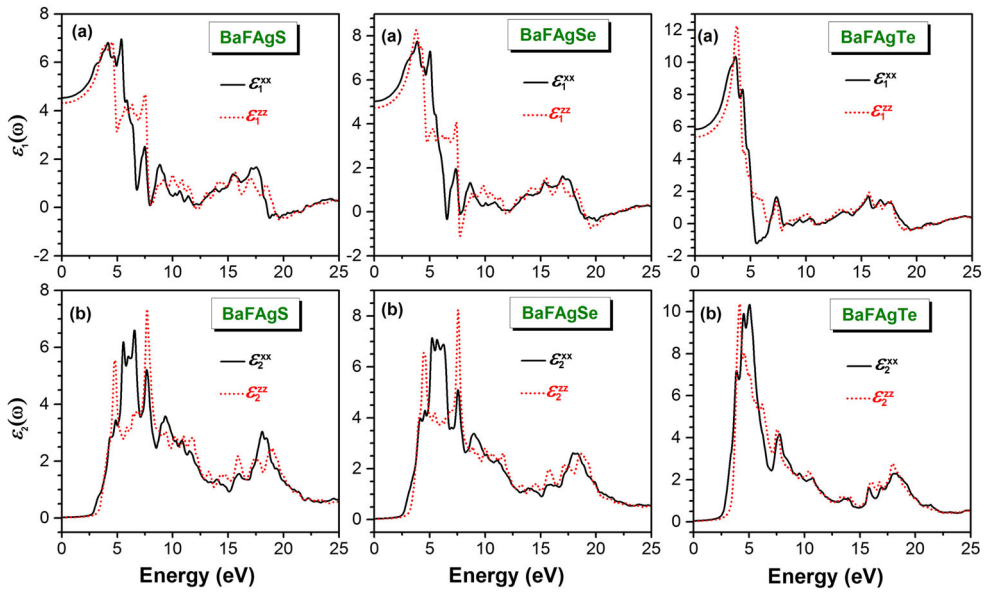

Fig. 7. The frequency-dependent imaginary ($\varepsilon_2(\omega)$ (b)) and real ($\varepsilon_1(\omega)$ (a)) parts of the dielectric function tensor components for the BaAgSF, BaAgSeF and BaAgTeF systems.

compounds are depicted in Fig. 6. Three narrow band valence groups centred at about ∼−54, ∼−26 and ∼−24 eV, which are not shown in Fig. 6 for clarity of the diagrams, are mainly formed from the 4*p*-Ag, 5*s*-Ba and 2*s*-F states, respectively. The lower valence band group (Fig. 6) in the BaAgSF and BaAgSeF DOS spectra exhibits three well-distinguished peaks that are made predominantly of the 5*p*-Ba and n*s*-chalcogen states (n = 3 for S, n = 4 for Se and n = 5 for Te) with a small contribution from the 2*p*-F states. In the BaAgTeF DOS diagram, this valence band group splits into two groups clearly separated by an energy gap because the 5*s*-Te states are located somewhat higher in energy than the 5*p*-Ba ones. The upper valence band group (UVB), which is extended from approximately −5.5 eV to Fermi level E_F, is formed of two main structures. The lower structure of the UVB, ranging from approximately −5.5 eV to −2.0 eV, is formed from the 4*d*-Ag, 2*p*-F and n*p*-

Ch states and the higher one, which is extended approximately from −2.0 eV to E_F, is attributed to the 4*d*-Ag states well mixed with n*p*-*Ch* states (n = 3 for S, n = 4 for Se and n = 5 for Te). The hybridization of the n*p*-*Ch* and 4*d*-Ag states suggests that the *Ch*-Ag bonds inside the blocks [Ag*Ch*] are mainly covalent. On the other hand, from the PDOS diagrams, one can easily observe the weak contribution of the Ba states in the UVB group, whereas a consistent contribution of the fluorine states is localised in the bottom of this valence band group. Consequently, the overlapping of Ba and F states is quite weak, indicating that the Ba-F chemical bonding inside the [BaF] blocks is mainly of ionic character. The bottom of the conduction band is attributed to an admixture of the n*s*-*Ch*, 4*sp*-Ag and 5*sd*-Ba states.

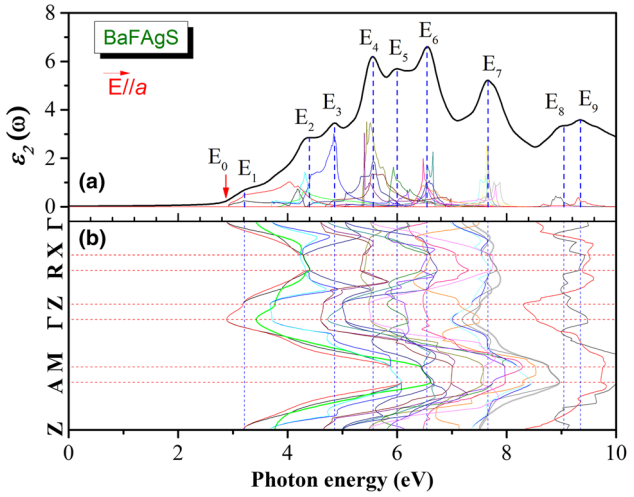

Fig. 8. Decomposition of the imaginary part of the dielectric function $\varepsilon_2^{xx}(\omega)$ into band-to-band contribution (upper panel a) and the transition energy band structure (lower panel b) for BaAgSF. The counting of the bands is down (up) from the top (bottom) of the valence (conduction) band.

Optical Properties

The calculated frequency-dependent dispersive ($\varepsilon_1(\omega)$) and absorptive ($\varepsilon_2(\omega)$) parts of the dielectric function ($\varepsilon(\omega)$) for the BaAgSF, BaAgSeF and BaAgTeF systems are depicted in Fig. 7. Due to the tetragonal symmetry of the title materials, only the diagonal dielectric tensor components, namely $\varepsilon^{xx} = \varepsilon^{yy}$ and ε^{zz}, are non-zero. The dielectric tensor component $\varepsilon^{xx}(\varepsilon^{yy})$ corresponds to the electric fields $\vec{E}$ of the incident radiation parallel to the x-axis (y-axis) (i.e., $\vec{E}//\vec{a}$ ($\vec{E}//\vec{b}$)) and to the z-axis (i.e., $\vec{E}//\vec{c}$). In view of Fig. 7, one can observe the following features: First, there are noticeable differences between the magnitudes, shapes and locations of the main peaks in the $\varepsilon_2^{xx}(\omega)(\vec{E}//\vec{a})$ and $\varepsilon_2^{zz}(\omega)$ $(\vec{E}//\vec{c})$, revealing a strong anisotropy of the dielectric response of the examined systems to the incident radiation. Second, the overall shape of the dielectric

Table VI. Peak positions of the $\varepsilon_2^{xx}(\omega)$ spectrum together with the dominant interband transition contributions to every peak and their location in the Brillouin zone for the BaFAgS compound

Optical structures		Dominant interband transition contributions		
Structure	**Peak position**	**Transition**	**Region**	**Energy (eV)**
E_1	3.21	V2–C1	Z, M–Γ, Z–R, X–Γ	3.21
E_2	4.39	V1–C1	Z, M–Γ, Z–R, X–Γ	3.19
		V1–C2	Z–A, M–Γ	4.30
		V1–C2	Z–A, M–Γ	4.29
E_3	4.86	V2–C2	Z–A, M–Γ	4.85
E_4	5.56	V4–C3	Z–A, M–Γ, X–Γ	5.51
		V4–C2	Z–A, M–Γ	5.57
		V2–C4	Z–A, M–Γ, Z–R	5.51
		V1–C4	Z–A, M–Γ, Z–R	5.53
E_5	6.00	V2–C5	Z–A, M–Γ, Γ–Z, Z–R, X–Γ	5.94
E_6	6.54	V6–C1	Z–A, A–M, M–Γ, Z–R, X–Γ	6.64
		V5–C2	Z–A, A–M, M–Γ, Z–R, X–Γ	6.60
		V4–C5	Z–R, R–X, X–Γ	6.49
		V1–C6	Z–A, M–Γ, Z–R, R–X, X–Γ	6.56
		V1–C8	Z–A, M–Γ, Γ–Z, Z–R, X–Γ	6.47
E_7	7.66	V16–C1	Z–A, M–Γ, Z–R, X–Γ	7.78
		V15–C1	Z–A, M–Γ, Z–R, X–Γ	7.68
		V14–C1	Z–A, M–Γ, Z–R, R–X, X–Γ	7.63
		V13–C1	Z–A, M–Γ, Z–R, R–X	7.62
		V5–C3	Z–A, M–Γ, Z–R, X–Γ	7.79
E_8	9.05	V10–C5	Z–A, M–Γ, Z–R, X–Γ	8.88
E_9	9.35	V1–C16	Z–A, M–Γ, Z–R, X–Γ	9.31

Table VII. Peak positions of the $\varepsilon_2^{zz}(\omega)$ spectrum together with the dominant interband transition contributions to every peak and their location in the Brillouin zone for the BaFAgS compound

Optical structures		Dominant interband transition contributions		
Structure	**Peak position**	**Transition**	**Region**	**Energy (eV)**
E_1	7.69	V2–C1	Z–A, M–Γ, Z–R, X–Γ	4.17
		V3–C2	Z–A, M–Γ, Z–R, X–Γ	4.04
E_2	4.78	V1–C2	Z–A, M–Γ, Z–R, X–Γ	4.90
		V1–C3	Z–A, M–Γ	4.70
		V4–C4	Z–A, M–Γ, Z–R, X–Γ	4.78
E_3	5.86	V1–C5	Z–A, M–Γ	5.94
		V1–C6	Z–A, M–Γ, Γ–Z, Z–R, X–Γ	5.79
		V2–C5	Z–R, X–Γ	5.86
		V4–C5	Z–A, M–Γ, Γ–Z, Z–R, X–Γ	5.90
E_4	6.46	V2–C7	M–Γ, Z–R, X– Γ	6.47
		V3–C6	Z–A, M–Γ, Γ–Z, Z–R, X–Γ	6.43
		V3–C5	Z–A, M–Γ, Z–R, X– Γ	6.42
		V3–C7	Z–A, M–Γ, Γ–Z, Z–R, X–Γ	6.41
		V7–C4	Z–A, Z–R	6.45
E_5	6.87	V6–C2	Z–A, M–Γ	6.87
		V2–C8	Z–A, M–Γ	6.79
		V3–C8	Z–A, M–Γ, Z–R, X–Γ	7.12
		V1–C9	Z–A, M–Γ, Z–R, X–Γ	6.74
		V15–C1	Z–A, M–Γ, Z, Z–R	6.87
E_6	7.69	V14–C1	Z–A, M–Γ, Z–R, X	7.64
		V13–C1	Z–A, M–Γ, Z–R, R–X	7.63
		V5–C4	Z–A, M–Γ, Z–R, R–X	7.73
		V5–C6	Z–A, M–Γ, Z–R, X–Γ	7.82
E_7	8.64	V12–C3	Z–A, M–Γ, Z–R, X–Γ	8.65
E_8	9.35		Z–A	9.29

Table VIII. Peak positions of the $\varepsilon_2^{xx}(\omega)$ spectrum together with the dominant interband transition contributions to every peak and their location in the Brillouin zone for the BaFAgSe

Optical structures		Dominant interband transition contributions		
Structure	**Peak position**	**Transition**	**Region**	**Energy (eV)**
E_1	4.15	V3–C1	Z–A, M–Γ, Z–R, R–X, X–Γ	4.19
		V2–C2	Z–A, M–Γ, Z–R, R–X, X–Γ	4.11
		V1–C1	Z–A, M–Γ, Z, R–X	4.13
E_2	4.59	V3–C2	Z–A, M–Γ, Z–R, X–Γ	4.65
		V2–C2	Z–A, M–Γ, Z–R	4.57
E_3	5.21	V4–C2	Z–A, M–Γ, Z–R	5.20
		V4–C3	Z–A, Γ–Z, Z–R, X–Γ	5.16
		V2–C3	Z–A, M–Γ	5.19
		V1–C4	Z–A, M–Γ, Z–R, X–Γ	5.18
E_4	5.65	V4–C4	Z–A, M–Γ, Z–R, X–Γ	5.60
		V3–C5	Z–A, Z–R, X–Γ	5.71
		V2–C5	Z–A, M–Γ, Γ–Z, Z–R, X–Γ	5.62
		V1–C3	Z–A, M–Γ	5.64
E_5	6.25	V5–C2	Z–A, M–Γ, Z–R, X–Γ	6.31
		V4–C5	Z–R, R–X, X	6.27
		V1–C6	Z–A, M– Γ, Z–R, R–X, X–Γ	6.24
E_6	6.98	V5–C5	Z–A, M–Γ, Γ–Z, Z–R, X–Γ	6.95
		V3–C3	Z–A, M–Γ	6.98
E_7	7.55	V15–C2	R–X, X–Γ	7.59
		V14–C1	Z–A, M–Γ, Z–R, R–X, X–Γ	7.60
		V13–C1	Z–A, M–Γ, Z–R, R–X	7.49
E_8	8.99	V13–C3	Z–A, A–M, M–Γ	9.00
		V1–C15	Z–A, M–Γ, Z–R, X–Γ	9.01

Table IX. Peak positions of the $\varepsilon_2^{zz}(\omega)$ spectrum together with the dominant interband transition contributions to every peak and their location in the Brillouin zone for the BaFAgSe compound

Optical structures		Dominant interband transition contributions		
Structure	**Peak position**	**Transition**	**Region**	**Energy (eV)**
E_1	3.99	V1–C2	Z–A, M–Γ, Z–R, X–Γ	4.00
		V2–C1	Z–A, M–Γ, Z–R, X–Γ	4.03
E_2	4.03	V3–C2	Z–A, M–Γ, Z–R, X–Γ	4.62
		V1–C2	Z–A, M–Γ	4.42
		V2–C3	Z–A, M–Γ, Z–R, X–Γ	4.44
E_3	5.43	V2–C4	Z–A, M–Γ, Z–R	5.41
		V2–C5	Z–A	5.54
		V1–C5	Z–A, Z–R, X–Γ	5.40
		V1–C6	Z–R, X–Γ	5.45
E_4	6.19	V3–C4	Z–A, M–Γ	6.22
		V3–C5	Z–A, M–Γ, Z–R, R, X–Γ	6.22
		V3–C6	Z–A, M–Γ, Z–R, R, X–Γ	6.21
		V3–C7	M–Γ, Z–R	6.19
E_5	6.49	V6–C2	Z–A, M–Γ	6.76
		V3–C8	Z–A, M–Γ, Z–R, X–Γ	6.44
		V2–C8	Z–A, M–Γ, Z–R, X–Γ	6.48
		V1–C9	Z–A, M–Γ, Z–R, X–Γ	6.48
E_6	6.82	V7–C4	Z–A, M–Γ, Z–R, X–Γ	6.78
		V2–C9	Z–A, M– Γ, Z–R, X– Γ	6.76
		V1–C10	Z–A, M–Γ, Z–R, X–Γ	6.84
E_7	7.55	V15–C1	Z–A, M–Γ, Z–R, R–X, X–Γ	7.60
		V14–C1	Z–A, M–Γ, Z–R, R–X, X–Γ	7.58
		V13–C1	Z–A, M–Γ, Z–R, R–X	7.54
		V5–C4	Z–A, Z–R, R–X, X–Γ	7.49
E_8	8.37	V4–C12	Z–A, Z–R, X–Γ	8.39
E_9	8.88	V12–C3	Z–A, M–Γ, Z–R	8.95
		V11–C3	Z–A, M–Γ	8.87
		V11–C5	Z–A, M–Γ, Z–R, R–X, X–Γ	8.95
		V3–C16	Z–A, M–Γ, Z–R, X–Γ	8.89
E_{10}	9.21	V5–C11	Z–A, M–Γ, Z–R, X–Γ	9.23

Table X. Peak positions of the $\varepsilon_2^{xx}(\omega)$ spectrum together with the dominant interband transition contributions to every peak and their location in the Brillouin zone for the BaFAgTe compound

Optical structures		Dominant interband transition contributions		
Structure	**Peak position**	**Transition**	**Region**	**Energy (eV)**
E_1	3.88	V2–C1	Z–A, M–Γ, Z–R, X–Γ	3.81
		V2–C2	Z–A, M–Γ, Z–R, X–Γ	3.89
		V1–C2	Z–A, M–Γ	3.86
		V1–C1	Z–A, M–Γ	3.86
E_2	4.50	V4–C3	Z–R, X–Γ	4.45
		V4–C2	Z–A, M–Γ, Z–R, X–Γ	4.51
		V3–C3	Γ–Z	4.44
		V2–C3	Z–A, M–Γ	4.50
		V1–C4	Z–A, M–Γ, Z–R, X–Γ	4.55
E_3	5.05	V3–C4	Z–A, M–Γ, Z–R, X–Γ	4.99
		V3–C3	Z–A, M–Γ	5.04
		V2–C3	Z–A, M–Γ	5.04
		V2–C5	Z–A, M–Γ, Z–R, X–Γ	5.13
		V1–C7	M–Γ, Z–R, X–Γ	5.13
E_4	7.74	V16–C1	Z–A, M–Γ, Z–R, X–Γ	7.83
		V16–C2	Z–A, M–Γ, Γ–Z, Z–R, X–Γ	7.78
		V15–C1	Z–A, M–Γ, Z–R, X–Γ	7.78
		V15–C2	Z–A, M–Γ, Z–R, X–Γ	7.72

Table XI. Peak positions of the $\varepsilon_2^{zz}(\omega)$ spectrum together with the dominant interband transition contributions to every peak and their location in the Brillouin zone for the BaFAgTe compound

Optical structures		Dominant interband transition contributions		
Structure	**Peak position**	**Transition**	**Region**	**Energy (eV)**
E_1	4.15	V4–C1	M–Γ, Γ–Z, Z–R, X–Γ	4.07
		V2–C2	Z–A, M–Γ	4.13
		V2–C1	Z–A, M–Γ	4.15
		V2–C3	Z–A, M–Γ, Z–R, X–Γ	4.18
		V1–C2	Z–A, M–Γ	4.14
E_2	4.59	V4–C3	Γ–Z, Z–R, X–Γ	4.55
		V3–C3	Z–A, M–Γ	4.60
		V1–C5	Z–R, X–Γ	4.53
		V1–C4	Z–A, M–Γ, Z–R	4.60
		V1–C2	Z–A, M–Γ	4.56
E_3	5.05	V2–C6	Z–A, M–Γ, Γ–Z, Z–R, X–Γ	5.06
		V2–C1	Z–A, M–Γ	5.08
		V1–C5	Z–A, M–Γ, Z–R, X–Γ	5.06
E_4	5.51	V3–C6	Z–A, M– Γ, Γ –Z, Z–R, R–X, X– Γ	5.47
		V3–C3	Z–A, M–Γ	5.50
		V3–C7	Z–A, M–Γ, Z–R, X–Γ	5.49
		V2–C7	Z–A, M–Γ, Z–R, X–Γ	5.51
		V2–C8	Z–A, M–Γ, Γ–Z, Z–R, X–Γ	5.57
E_5	6.16	V3–C3	Z–A, M–Γ	6.19
		V3–C4	Z–A, M–Γ	6.19
		V2–C9	Z–A, M–Γ, Z–R, R–X, X–Γ	6.15
E_6	7.52	V15–C1	Z–A, M–Γ, Z–R, R, X–Γ	7.48
		V14–C2	A–M, M–Γ, Γ–Z, Z–R, X–Γ	7.63
		V14–C1	Z–A, A–M, M–Γ, Z–R, X–Γ	7.47
		V13–C1	Z–A, A–M, M–Γ, Z–R, X–Γ	7.56
		V13–C2	A–M, M–Γ, Γ–Z, Z–R, X–Γ	7.47

Table XII. Calculated static dielectric constant $\varepsilon_1(0)$ and, static refractive index and static optical reflectivity for BaFAgS, BaFAgSe and BaFAgTe as calculated using the TB-mBJ for two different polarizations of the incident radiations, compared with the available data in the scientific literature

System	$\varepsilon_1^{xx}(\mathbf{0})$	$\varepsilon_1^{zz}(\mathbf{0})$	$n^{xx}(\mathbf{0})$	$n^{zz}(\mathbf{0})$	$R^{xx}(\mathbf{0})$	$R^{zz}(\mathbf{0})$
BaFAgS	4.53 5.22[12]	4.33 4.89[12]	2.13	2.08	13.0	12.0
BaFAgSe	5.03	4.74	2.24	2.17	14.6	13.6
BaFAgTe	5.85	5.37	2.42	2.32	17.2	15.8

function spectra of BaAgSF and BaAgSeF are almost similar, whereas that of BaAgTeF is somewhat different from them. This difference can be attributed to the fact that the energy band dispersion of BaAgTeF is somewhat different from those of BaAgSF and BaAgSeF. Third, the intensity of the peaks increases when we move in the following sequence: BaAgSF → BaAgSeF → BaAgTeF. The $\varepsilon_2^{xx}(\omega)$ and $\varepsilon_2^{zz}(\omega)$ spectra start at the same energy (E_0), indicating an isotropic energy gap. However, $\varepsilon_2^{xx}(\omega)$ and $\varepsilon_2^{zz}(\omega)$ grow with different rates. To access the electronic transitions that are responsible for the peaks observed in the $\varepsilon_2(\omega)$ spectra, the $\varepsilon_2(\omega)$ spectrum is decomposed to the individual contribution from each electronic transition from the occupied valence band V_i to the unoccupied conduction band C_j, i.e., determination of the contribution of each allowed electronic transition ($V_i \rightarrow C_j$) to the $\varepsilon_2(\omega)$ spectrum. To determine which electronic states of the bands V_i and C_j are involved in the $V_i \rightarrow C_j$ transition, the electronic transition energies $E_{ij}(k)$ ($E_{ij}(k) = E_{C_j}(k) - E_{V_i}(k)$) are plotted along the high-symmetry directions of the BZ. For sake of brevity, only decomposition of the $\varepsilon_2^{xx}(\omega)$ spectrum of BaAgSF to individual contributions of the electronic transitions ($V_i \rightarrow C_j$) and the corresponding transition energy $E_{ij}(k)$ dispersion are shown in Fig. 8, as representative for the other studied systems. The first threshold energy E_0 of $\varepsilon_2(\omega)$, termed also the fundamental absorption edge,

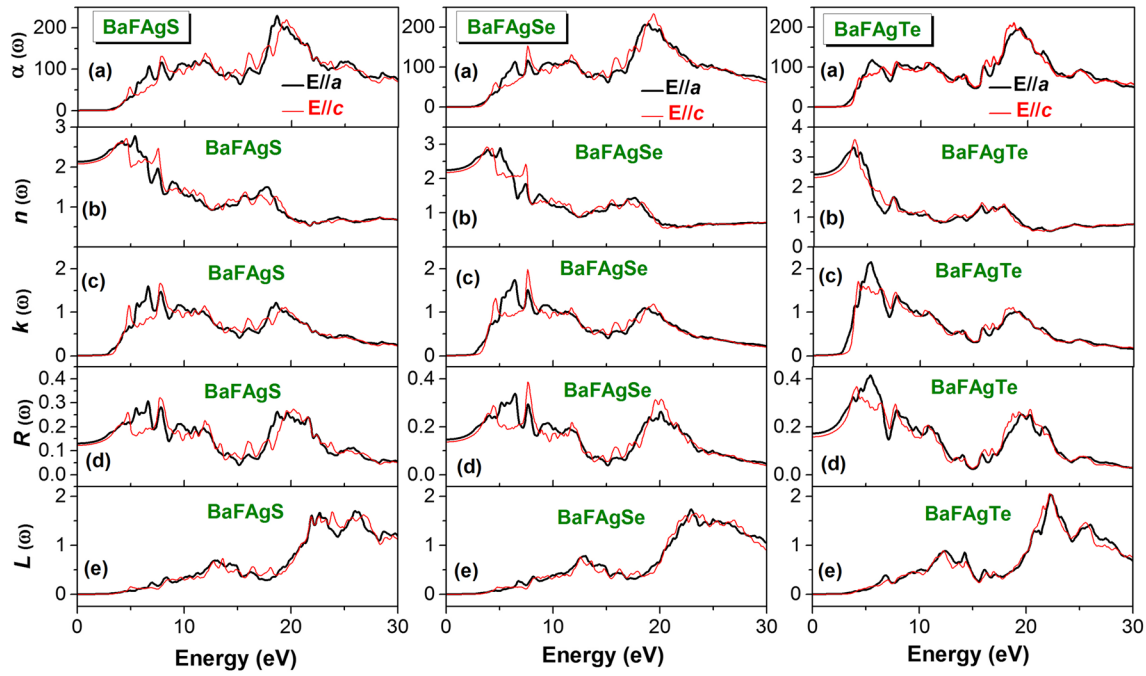

Fig. 9. Frequency-dependent absorption coefficient ($\alpha(\omega)$ (a)), refractive index ($n(\omega)$(b)), extinction coefficient ($k(\omega)$ (c)), optical reflectivity ($R(\omega)$(d)) and energy-loss function ($L(\omega)$(e)) spectra for BaAgSF, BaAgSeF and BaAgTeF systems for two different light polarizations as calculated using the TB-mBJ potential.

is originated from the direct electronic transition between the topmost valence band V_1 and the bottommost conduction band C_1 ($V_1 \rightarrow C_1$). It is to be noted that the bands counting is up (down) from the bottommost (topmost) of the conduction (valence) band. The locations of the major peaks E_i (i = 1, 2…etc.) and the origin of the dominant optical transitions in an energy range up to 10 eV are listed in Tables VI, VII, VIII, IX, X, and XI. The obtained electronic static dielectric constant $\varepsilon^e(0) = \varepsilon_1$ ($\omega \rightarrow 0$), which is a parameter of fundamental importance in many aspects of material properties, is given in Table XII. Our results are in agreement with the available theoretical results for BaAgSF.[12] The $\varepsilon_1(0)$ increases in the following sequence: BaAgSF $\rightarrow$ BaAgSeF $\rightarrow$ BaAgTeF and the ε_1^{xx} ($\omega \rightarrow 0$) component is larger than the $\varepsilon_1^{zz}(\omega \rightarrow 0)$ component. The $\varepsilon_1(0)$ value increases when the energy gap E_g decreases. This is in accordance with the Penn model[55]: $\varepsilon_1(0) \approx 1 + (\hbar\omega_p/E_g)^2$; $\varepsilon_1(0)$ is inversely proportional with E_g, i.e., smaller E_g yields larger $\varepsilon_1(0)$.

Figure 9 presents the frequency-dependent coefficient of absorption $\alpha(\omega)$, index of refraction $n(\omega)$, coefficient of extinction $k(\omega)$, reflectivity $R(\omega)$ and electron energy-loss function $L(\omega)$ for incident radiation polarized both along the a-axis ($\vec{E}//\vec{a}$) and c-axis ($\vec{E}//\vec{c}$) in a wider spectral region up to 30 eV. The optical spectra for $\vec{E}//\vec{a}$ are quite different from those for $\vec{E}//\vec{c}$, implying the optical anisotropy of these systems. The optical absorption coefficient $\alpha(\omega)$ is an important criterion to judge if a material could have an eventual application in the photoelectric field. The examined compounds exhibit a high coefficient of absorption (higher than 10^4 cm^{-1}) in a large energy range extending from the absorption edge E_g (from ~2.6 eV to 2.9 eV) up to 30 eV, suggesting that they could be suitable absorber layers for photovoltaic applications. Obviously, these materials with a band gap higher than 2.6 eV may absorb the blue and violet rays of the visible spectrum. The calculated refractive index spectra for the three examined materials are given in Fig. 9b. The refractive index reaches its maximum in the near ultraviolet (~3.8–5 eV). One can note the refractive index value increases when going from BaAgSF to BaAgSeF to BaAgTeF, which is in accordance with the usual trend of the refractive index, i.e., the refractive index increases when the band gap decreases. The calculated static refractive index ($n(0)$), which is a very important physical quantity for semiconductors, is listed in Table XII. From Fig. 9d, one can observe that the title systems exhibit a weak reflectivity at low energies and the magnitude of the reflectivity increases slightly when going from BaAgSF to BaAgSeF to BaAgTeF. Calculated static reflectivity coefficients ($R(0)$) of the three studied systems are given in Table XII. The energy loss-function $L(\omega)$ spectra are depicted in Fig. 9e.

CONCLUSIONS

Structural, elastic, electronic and optical properties of three LaOAgS-type silver fluoride chalcogenides: BaAgSF, BaAgSeF and BaAgTeF were studied in the present work using first-principles density theory calculations. Successful determination of the equilibrium structural parameters of the BaAg*Ch*F materials using pseudopotential plane-wave density functional theory reveals that an increase of the atomic number of the *Ch* chalcogenide element leads to an increase of the lattice constants and a decrease of the bulk modulus. The a-axis is more resistant to compressional deformations than the c-axis. After that, single-crystal and polycrystalline elastic moduli and related properties were numerically estimated. The obtained results reveal that the considered materials can be classified as soft materials with ductile character and a considerable elastic anisotropy.

DFT-based FP-LAPW method within the GGA08 and TB-mBJ functionals was used to perform the band structure and density of states diagrams. The examined materials are found to be wide direct band gap Γ–Γ semiconductors, from ∼2.6 eV to ∼2.9 eV. An increase of the atomic number Z of the chalcogen element causes a decrease of the band gap value. The bottommost of the conduction band is contributed mainly by np-*Ch*, 4p-Ag and 5d-Ba states. The topmost valence band is almost dispersionless and is contributed by the hybridized np-*Ch* and 4d-Ag states. The inter-atomic chemical bonding inside the [Ag*Ch*] blocks is of covalent character while that inside the [BaF] ones is of ionic character. Based on the accurate band structure obtained using TB-mBJ, the absorptive and dispersive parts of the dielectric function, absorption coefficient, refractive index, extinction coefficient, optical reflectivity and energy-loss function spectra were calculated for the [100] and [001] polarized incident radiation in a wide energy range up to 30 eV. The calculated optical spectra show a noticeable anisotropy. An increase of the atomic number of the *Ch* element leads to an increase of the magnitude of the peaks of the optical spectra. The zero-frequency limit $\varepsilon_1(0)$ increases when the energy band gap value decreases. The origins of the observed structures in the optical spectra are assigned in terms of the calculated energy band structure.

ACKNOWLEDGEMENT

The authors (A. Bouhemadou and S. Bin-Omran) extend their appreciation to the International Scientific Partnership Program ISPP at King Saud University for funding this research work through JSPP# 0025.

REFERENCES

1. D.O. Charkin, P.S. Berdonosov, V.A. Dolgikh, and P. Lightfoot, *J. Alloys Compd.* 292, 118 (1999).
2. D.O. Charkin, A.V. Urmanov, and S.M. Kazakov, *J. Alloys Compd.* 516, 134 (2012).
3. D.O. Charkin, A.V. Urmanov, I.V. Plokhikh, A.D. Korshunov, A.N. Kuznetsov, and S.M. Kazakov, *J. Alloys Compd.* 585, 644 (2014).
4. D.O. Charkin and X.N. Zolotova, *Crystallogr. Rev.* 13, 201 (2007).
5. A. Zakutayev, R. Kykyneshi, G. Schneider, D.H. McIntyre, and J. Tate, *Phys. Rev. B* 81, 155103 (2010).
6. V.K. Gudelli, V. Kanchana, G. Vaitheeswaran, D.J. Singh, A. Svane, N.E. Christensen, and S.D. Mahanti, *Phys. Rev. B* 92, 045206 (2015).
7. R. Pöttgen and D. Johrendt, *Z. Naturforsch. B* 63, 1135 (2008).
8. M. Palazzi and S. Jaulmes, *Acta Cryst. B* 37, 1337 (1981).
9. K. Ueda, H. Hiramatsu, M. Hirano, T. Kamiya, M. Hirano, and H. Hosono, *Thin Solid Films* 496, 8 (2006).
10. H. Yanagi, S. Ohno, T. Kamiya, H. Hiramatsu, M. Hirano, and H. Hosono, *J. Appl. Phys.* 100, 033717 (2006).
11. Y. Kamihara, T. Watanabe, M. Hirano, and H. Hosono, *J. Am. Chem. Soc.* 130, 3296 (2008).
12. V.V. Bannikov, I.R. Shein, and A.L. Ivanovskii, *J. Solid State Chem.* 196, 601 (2012).
13. J.F. Wager, D.A. Keszler, and R.E. Presley, *Transparent Electronics* (Berlin: Springer, 2008).
14. M. Yasukawa, K. Ueda, and H. Hosono, *J. Appl. Phys.* 95, 3594 (2004).
15. H. Hiramatsu, K. Ueda, H. Ohta, T. Kamiya, and M. Hirano, *Appl. Phys. Lett.* 87, 211107 (2005).
16. J.A. Spies, R. Schafer, J.F. Wager, P. Hersh, H.A.S. Platt, D.A. Keszler, G. Schneider, R. Kykyneshi, J. Tate, X. Liu, A.D. Compaan, and W.N. Shafarman, *Sol. Energy Mater. Sol. Cells* 93, 1296 (2009).
17. D.C. Johnston, *Adv. Phys.* 59, 803 (2010).
18. K. Ueda, H. Hiramatsu, H. Ohta, M. Hirano, T. Kamiya, and H. Hosono, *Phys. Rev. B* 69, 55305 (2004).
19. H. Kamioka, H. Hiramatsu, M. Hirano, K. Ueda, T. Kamiya, and H. Hosono, *J. Lumin.* 112, 66 (2005).
20. V.V. Bannikov, I.R. Shein, and A.L. Ivanovskii, *Solid State Commun.* 150, 2069 (2010).
21. V.V. Bannikov, I.R. Shein, and A.L. Ivanovskii, *Solid State Sci.* 14, 89 (2012).
22. J.P. Perdew, S. Burke, and M. Ernzerhof, *Phys. Rev. Lett.* 77, 3865 (1996).
23. C.S. Wang and W.T. Pickett, *Phys. Rev. Lett.* 7, 597 (1983).
24. W.G. Aulbur, L. Jönsson, and J.W. Wilkins, *Solid State Phys.* 54, 1 (1999).
25. S.Zh. Karazhanov, P. Ravindran, H. Fjellvag, and B.G. Svensson, *J. Appl. Phys.* 106, 123701 (2009).
26. O. Boudrifa, A. Bouhemadou, Ş. Uğur, R. Khenata, S. Bin-Omran, and Y. Al-Douri, *Philos. Mag.* 96, 2328 (2016).
27. A. Bouhemadou, D. Allali, S. Bin-Omran, E.M.A. Al Safi, R. Khenata, and Y. Al-Douri, *Mater. Sci. Semicond. Process.* 38, 192 (2015).
28. S.J. Clark, M.D. Segall, C.J. Pickard, P.J. Hasnip, M.J. Probert, K. Refson, and M.C. Payne, *Z. fuer Kristallographie* 220, 567 (2005).
29. J.P. Perdew and A. Zunger, *Phys. Rev. B* 23, 5048 (1981).
30. J.P. Perdew, A. Ruzsinszky, G.I. Csonka, O.A. Vydrov, G.E. Scuseria, L.A. Constantin, X. Zhou, and K. Burke, *Phys. Rev. Lett.* 100, 136406 (2008).
31. D. Vanderbilt, *Phys. Rev. B* 41, 7892 (1990).
32. J.D. Pack and H.J. Monkhorst, *Phys. Rev. B* 16, 1748 (1977).
33. T.H. Fischer and J. Almlof, *J. Phys. Chem.* 96, 9768 (1992).
34. H. Hill, *Phys. Soc. Sect. A Proc.* 65, 349 (1952).
35. A.D. Becke and E.R. Johnson, *J. Chem. Phys.* 124, 221101 (2006).
36. F. Tran, P. Blaha, and K. Schwarz, *J. Phys. Condens. Matter* 19, 196208 (2007).
37. F. Tran and P. Blaha, *Phys. Rev. Lett.* 102, 226401 (2009).
38. D. Koller, F. Tran, and P. Blaha, *Phys. Rev. B* 83, 195134 (2001).
39. P. Blaha, K. Schwarz, G.K.H. Madsen, D. Kvasnicka, and J. Luitz, *An Augmented Plane Wave + Local Orbitals Program for Calculating Crystal Properties* (Wien: University Karlheinz Schwarz, 2013).

40. F. Birch, *Phys. Rev.* 71, 809 (1947).
41. F.D. Murnaghan, *Natl. Acad. Sci. Proc.* 30, 244 (1944).
42. P. Vinet, J.H. Rose, J. Ferrante, and J.R. Smith, *J. Phys. Condens. Matter* 1, 1941 (1989).
43. M. Born and K. Huang, *Dynamical Theory of Crystal Lattices* (Oxford: Clarendon Press, 1965).
44. Z.J. Wu, E.J. Zhao, H.P. Xiang, X.F. Fao, X.J. Liu, and J. Meng, *Phys. Rev. B* 76, 054115 (2007).
45. S.F. Pugh, *Philos. Mag.* 45, 823 (1954).
46. P. Ravindran, L. Fast, P.A. Korzhavyi, B. Johansson, J. Wills, and O. Eriksson, *J. Appl. Phys.* 84, 4891 (1998).
47. P. Lloveras, T. Castán, M. Porta, A. Planes, and A. Saxena, *Phys. Rev. Lett.* 100, 165707 (2008).
48. S.I. Ranganathan and M. Ostoja-Starzewski, *Phys. Rev. Lett.* 101, 055504 (2008).
49. J.F. Nye, *Properties of Crystals* (Oxford: Clarendon Press, 1985).
50. A. Bedjaoui, A. Bouhemadou, and S. Bin-Omran, *High Press. Res.* 36, 198 (2016).
51. O.L. Anderson, *J. Phys. Chem. Solids* 24, 909 (1963).
52. E. Schreiber, O.L. Anderson, and N. Soga, *Elastic Constants and Their Measurements* (New York: McGraw-Hill, 1973).
53. J. Feng, B. Xiao, R. Zhou, W. Pan, and D.R. Clarke, *Acta Mater.* 60, 3380 (2012).
54. H. Yanagi, J. Tate, S. Park, C.H. Park, D.A. Keszler, M. Hirano, and H. Hosono, *J. Appl. Phys.* 100, 083705 (2006).
55. D.R. Penn, *Phys. Rev.* 128, 2093 (1960).

Journal of Alloys and Compounds 759 (2018) 32–43

Contents lists available at ScienceDirect

Journal of Alloys and Compounds

journal homepage: http://www.elsevier.com/locate/jalcom

Electronic and thermoelectric properties of the layered BaFAg*Ch* (*Ch* = S, Se and Te): First-principles study

K. Boudiaf [a], A. Bouhemadou [a, *], Y. Al-Douri [b, c], R. Khenata [d], S. Bin-Omran [e], N. Guechi [f]

[a] Laboratory for Developing New Materials and Their Characterizations, Department of Physics, Faculty of Science, University Ferhat Abbas Setif 1, Setif 19000, Algeria
[b] Nanotechnology and Catalysis Research Center (NANOCAT), University of Malaya, 50603 Kuala Lumpur, Malaysia
[c] Physics Department, Faculty of Science, University of Sidi-Bel-Abbes, 22000, Algeria
[d] Laboratoire de Physique Quantique de La Matière et de Modélisation Mathématique (LPQ3M), Université de Mascara, 29000 Algeria
[e] Department of Physics and Astronomy, College of Science, King Saud University, P.O. Box 2455, Riyadh 11451, Saudi Arabia
[f] Department of Science of Matter, Faculty of Science, University of Medea, Medea 26000, Algeria

ARTICLE INFO

Article history:
Received 20 February 2018
Received in revised form
4 May 2018
Accepted 12 May 2018

Keywords:
LaOAgS-Type layered crystal
First-principles calculations
Boltzmann transport theory
Spin-orbit coupling
Electronic structure
Effective masse
Thermoelectric parameters

ABSTRACT

By using the full potential linearized augmented plane wave (FP-LAPW) method, the electronic properties of the layered BaAg*Ch*F (*Ch* = S, Se, Te) were investigated. Both the standard GGA and the TB-mBJ potential were used to model the exchange-correlation potential. To evaluate the spin-orbit coupling (SOC) effect, both the scalar relativistic and full relativistic calculations were performed. The SOC effect is found to be not negligible in the title compounds. The FP-LAPW band structure and the semi-classical Boltzmann transport theory were used to study the charge-carrier concentration and temperature dependences of the thermoelectric parameters, including Seebeck coefficient, electrical conductivity, thermal conductivity and figure of merit. Our results show that the values of the thermoelectric parameters of the *p*-type compounds are larger than that of the *n*-type ones. The optimal *p*-type doping concentrations and temperatures that yield the maximum values of the figure of merit of the title compounds were calculated. These are important parameters to guide experimental works.

1. Introduction

The history of thermoelectricity backs to 1821, when Seebeck observed that if two dissimilar materials (copper and bismuth) are joined together and the junctions are held at different temperatures, *T* and T + ΔT, a voltage difference, ΔV, proportional to the temperature difference ΔT [1,2], i.e., $\Delta V = -S\Delta T$, is developed. The ratio of the developed voltage to the temperature gradient, $S = -\Delta V/\Delta T$, which is related to an intrinsic property of materials, is called Seebeck coefficient (also known as thermopower). Generally, thermoelectricity, which is the direct conversion of heat into electricity, is the term that indicates the physical phenomena resulting from the motion of charge carriers under the action of temperature gradient [1].

Recently, thermoelectric materials (TE) attract a heightened interest because they would allow the fabrication of both efficient thermoelectric generators that transfer the lost heat energy into a useful electrical energy (Seebeck effect) and efficient refrigerators that utilize electricity for cooling (Peltier effect) [3]. The conversion of waste heat into electrical energy may play an important role in our current challenge to develop alternative energy technologies to reduce our dependence on fossil fuels and reduce greenhouse gas emissions. Efficient thermoelectric devices could be realized if high-efficient TE could be elaborated. The performance of TE can be quantified by the dimensionless figure of merit *ZT* given by Ref. $ZT = \frac{S^2\sigma}{\kappa}T$ [2], where *S*, σ, *T* and κ are the Seebeck coefficient, electrical conductivity, absolute temperature and thermal conductivity that includes both the electronic (κ_e) and lattice (κ_l) contributions, i.e., $\kappa = \kappa_e + \kappa_l$. A high *ZT* requires a combination of high electrical conductivity, high thermopower and low thermal conductivity. Though there is no theoretical upper limit of the *ZT* value, it is challenging to achieve higher values because the three conflicting transport parameters *S*, σand κ[4]. Therefore, a compromise has to be reached between *S*, σand κ to enhance *ZT*.

* Corresponding author.
E-mail addresses: a_bouhemadou@yahoo.fr, abdelmadjid.bouhemadou@gmail.com, abdelmadjid_bouhemadou@univ-setif.dz (A. Bouhemadou).

https://doi.org/10.1016/j.jallcom.2018.05.142
0925-8388/

Efficient TE materials can be obtained via two principal ways. The first one is by increasing the value of $S^2\sigma$ (known as power factor (*PF*)), which define the electrical property of materials, by engineering the electronic structure around the Fermi level [5,6]. The second way is by reducing the lattice thermal conductivity κ_l by introducing phonon scattering centres, nanostructuring and increasing the grain boundaries [7–9].

The layered quaternary LaOAgS-type compounds (also known as "1111" structure), such as oxychalcogenides and fluorochalcogenides, have recently received an increasing amount of interest [10–32] because of their natural superlattice features, such as near two-dimensional electronic structures. They are potential candidates for a wide range of technological applications, such as *p*-type transparent semiconductors [10,24,26,30], thermoelectrics [12–14,18,28], optoelectronic devises [10,31] and photovoltaics [24,32]. The present work focuses on the BaAg*Ch*F (*Ch* = S, Se, Te) compounds.

The quaternary barium silver fluoride chalcogenides BaAg*Ch*F (*Ch* = S, Se) have been synthetized and their structural parameters determined by Charkin and co-workers [16]. They crystallize in the tetragonal LaOAgS-type structure, symmetry group *P*4/*nmm*. They are constituted of an alternating quasi-two-dimensional blocks [BaF] and [Ag*Ch*] stacked along the $\vec{c}$ crystallographic axis in the sequence … [BaF]/[Ag*Ch*]/[BaF]/[Ag*Ch*] …, in another word, they are a natural superlattice structure. A $1 \times 2 \times 1$ supercell of the BaAgSF crystal is shown in Fig. 1 for a better illustration of the layered structure of the considered compounds. The BaAg*Ch*F (*Ch* = S, Se, Te) compounds appear as interesting candidates for thermoelectric applications [12,18] owing to their layered structure. On the theoretical side, Bannikov and co-workers [20] calculated the electronic structures and optical spectra of BaAgSF and BaAgSeF employing the full-potential linearized augmented plane wave (FP-LAPW) method with the generalized gradient approximation (GGA). Boudiaf et al. [29] investigated the elastic properties of BaAgSF, BaAgSeF and BaAgTeF using the pseudopotential plane wave method with the GGA and their electronic and optical properties using the FP-LAPW method with the modified Beck-Johnson potential, which is more accurate than the GGA for the calculation of the energy band structure and optical spectra. Unfortunately, both previous studies [20,29] did not include the spin-orbit coupling effect that is not negligible in the case of the BaAg*Ch*F (*Ch* = S, Se and Te) systems. Therefore, the first objective of the present work is the calculation of the electronic properties, including band structure, charge-carrier effective masses, density of states and density of charge distribution, of the title compounds using the FP-LAPW method with the modified Beck-Johnson potential including the spin-orbit coupling. Additionally, the BaAg*Ch*F crystals have natural superlattice characteristics, which would result in very favourable electronic properties for thermoelectrics [12,14]. Therefore, the second objective is the prediction of the thermoelectric properties of the BaAg*Ch*F compounds as functions of charge-carrier concentration and temperature using the semi-classical Boltzmann theory in combination with the band structure obtained via the FP-LAPW method.

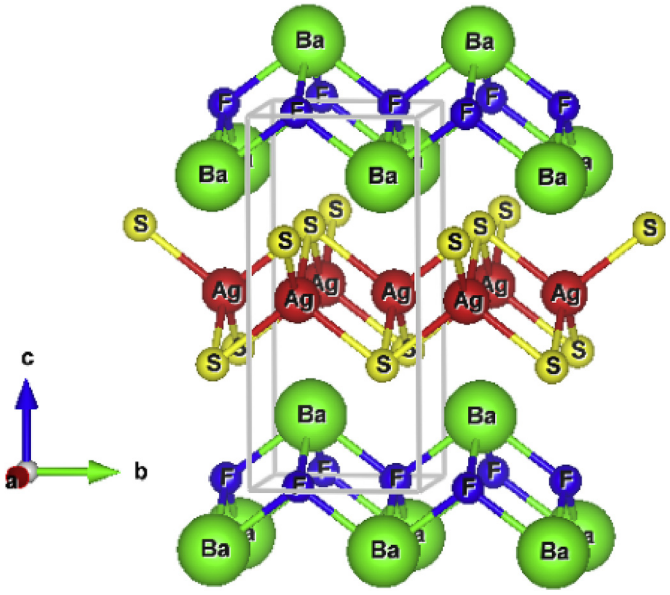

Fig. 1. $1 \times 2 \times 1$ super cell of BaAgSF.

2. Computational methods

Calculation of the optimized structural parameters, including the lattice parameters (*a* and *c*) and atomic position coordinates, and the electronic properties of the BaAg*Ch*F (*Ch* = S, Se and Te) compounds were performed using the full-potential linearized augmented plane wave (FP-LAPW) method [33] based on the density functional theory (DFT) as implemented in the WIEN2k code [34]. For the structural properties, the electronic exchange and correlation effects were treated using the generalized gradient approximation (GGA) as parameterized by Perdew et al. (the so-called GGA-PBEsol or GGA08) [35]. It is well known that the calculated DFT band gaps with the traditional approximations, such as the local density approximation (LDA) or the GGA, are underestimated compared to the measured ones [36–39]. Different schemes have been developed to overcome this issue, such as the hybrid functionals and the GW approach. Unfortunately, these aforementioned schemes are computationally very demanding compared to the LDA and GGA. Fortunately, Tran and Blaha [40–42] have developed a new functional entitled Tran-Blaha modified Beck-Johnson potential (denoted TB-mBJ), which better describes the electronic properties and gives rise to better estimation of the band gap [43]. The TB-mBJ approach is a decent alternative for the GW approach and hybrid functionals; it can achieve a comparable accuracy with a much lower computing time. Therefore, for the electronic band structure, in addition to the GGA08, we have used the TB-mBJ potential to model the electronic exchange and correlation effects. To evaluate the spin-orbit coupling effect on the examined properties of the title compounds, we have calculated them both with and without including the spin–orbit coupling. The calculation with including the spin-orbit coupling, i.e., full relativistic calculations, is denoted SOC and that without including the spin-orbit coupling, i.e., scalar relativistic calculations, is denoted SR. In the FP-LAPW method, the unit cell is divided into non-overlapping spheres centered at the atomic sites, which are labeled muffin-tin spheres (MTS), and the space between the MTS, which is labeled interstitial region (IR). Linear combinations of radial atomic functions and their energy derivatives times spherical harmonics are used to expand the wave functions inside the MTS, whereas a plane wave basis set is used in the IR. The plane wave basis set cut-off K_{max} (the maximum plane wave vector in the *k*-space) was chosen equal to $10/R_{MT}^{min}$ ($R_{MT}^{min} K_{max} = 10$), where R_{MT}^{min} is the smallest muffin-tin sphere radius. The muffin-tin sphere radii were chosen to ensure no charge leakage out of the MTS. The Brillouin zone integration was replaced by a summation over $16 \times 16 \times 7$ Monkhorst-Pack [44] *k*-points. The self-consistent field iterations were repeated until the calculated total energy of the crystal converged to less than 10^{-5} Ry. and the maximum force on

any atom was smaller than 0.5 *mRy*./a.u. (*a.u.*: atomic unit).

The thermoelectric properties, including Seebeck coefficient, electrical conductivity and thermal conductivity, of the considered compounds were calculated from the energy bands using the Boltzmann transport theory with the rigid band approach (RBA) [45,46] and the constant scattering time approximation (CRTA) as implemented in the BoltzTrap program [47]. Based on this approach, the Seebeck coefficient (S) and the electrical conductivity (σ) as functions of absolute temperature T and chemical potential μ can be calculated from the band structure calculation by integrating the transport distribution tensor $\overline{\sigma}_{\alpha\beta}(\varepsilon)$ as follows [47]:

$$\sigma_{\alpha\beta}(T,\mu) = \frac{1}{\Omega}\int \overline{\sigma}_{\alpha\beta}(\varepsilon)\left[-\frac{\partial f_0(T,\varepsilon,\mu)}{\partial E}\right]d\varepsilon, \quad (1)$$

$$S_{\alpha\beta}(T,\mu) = \frac{1}{eT\Omega\sigma_{\alpha\beta}(T,\mu)}\int \overline{\sigma}_{\alpha\beta}(\varepsilon)(\varepsilon-\mu)\left[-\frac{\partial f_0(T,\varepsilon,\mu)}{\partial \varepsilon}\right]d\varepsilon, \quad (2)$$

where α and β are tensor indices, Ω is the volume of the unit cell, f_0 is the Fermi-Dirac distribution function and e is the electron charge. The essential part of σ and S is the transport distribution function tensor $\overline{\sigma}_{\alpha\beta}$(E), which contains the system dependent information, defined as:

$$\overline{\sigma}_{\alpha\beta}(\varepsilon) = \frac{e^2}{N}\sum_{i,k}\tau_{i,k}v_\alpha(i,\mathrm{k})v_\beta(i,\mathrm{k})\frac{\delta(\varepsilon-\varepsilon_{i,k})}{\delta\varepsilon} \quad (3)$$

where N is the number of k-points, i is the band index, $\boldsymbol{k}$ is the wave vector and $v_\alpha(i,\mathrm{k})$ ($\alpha = x, y, z$) is the αth component of the group velocity v(i, k) of charge-carriers, which can be obtained directly from the band structure calculation as:

$$v_\alpha(i,\mathrm{k}) = \frac{1}{\hbar}\frac{\partial \mathrm{E}_{i,\mathrm{k}}}{\partial \mathrm{k}_\alpha} \quad (4)$$

where $\hbar$is the reduced Planck constant.

The wave vector dependent relaxation time ($\tau_{i,k}$) appearing in the expression of $\overline{\sigma}_{\alpha\beta}$(E) is difficult to be determined from first-principles calculations and hence eq. (3) is solved under constant relaxation time approximation (RTA). Because of the high sensibility of the transport properties to the number of k-points, the Brillouin zone sampling was performed with a uniform $50 \times 50 \times 23$ Monkhorst-Pack k-point grid.

3. Results and discussion

3.1. Structural properties

The BaAg*Ch*F (*Ch* = S, Se, Te) compounds crystallize in a layered tetragonal structure of the LaOAgS-type, space group *P*4/*nmm* (n.189) [16–20,25]. This structure may be viewed as alternating blocks of [BaF] and [Ag*Ch*] stacked along the $\vec{c}$ crystallographic axis, as shown in Fig. 1. There are four inequivalent atomic positions in the conventional cell, which are Ba: 2*c* (1/4, 1/4, z_{Ba}), F: 2*a* (3/4, 1/4, 0), Ag: 2b (3/4, 1/4, 1/2) and *Ch*: (1/4, 1/4, z_{Ch}), where z_{Ba} and z_{Ch} are the z-coordinates of the Ba and *Ch* atoms, respectively. At the first step, we calculated the equilibrium structural parameters, including the lattice parameters (a and c) and the atomic position coordinates, using the GGA08 with and without including the spin-orbit coupling effect. The optimized structural parameters of the examined materials along with the available experimental reports are listed in Table 1. The optimized lattice parameters are in excellent agreement with the corresponding measured ones [16]; the relative deviation (d(%)) of the calculated lattice parameter $x_{cal.}$ from the measured one $x_{Expt.}$ ($d(\%) = [(x_{cal.} - x_{Expt.})/x_{Expt.}] \times 100$) does not exceed 1%. The electronic and thermoelectric properties were performed at these optimized structures.

To confirm the chemical and structural stabilities of the studied crystals, we have calculated their cohesive energies ($E_{Coh.}$) and formation enthalpies (ΔH). The cohesive energy is the energy that is required for the crystal to decompose into free atoms. The more negative the formation enthalpy and cohesive energy the more stable the structure. The cohesive energy $E_{Coh.}$ and formation enthalpy ΔH of the studied systems were calculated using the following expressions:

$$\Delta H = \frac{1}{N_{Ba}+N_F+N_{Ag}+N_{Ch}}\left[E_{tot}^{BaFAgCh} - \left(N_{Ba}E_{tot}^{Ba(solid)} + N_F E_{tot}^{F(gaz)} + N_{Ag}E_{tot}^{Ag(solid)} + N_{Ch}E_{tot}^{Ch(solid)}\right)\right]$$

$$E_{Coh.} = \frac{1}{N_{Ba}+N_F+N_{Ag}+N_{Ch}}\left[E_{tot}^{BaFAgCh} - \left(N_{Ba}E_{tot}^{Ba(atom)} + N_F E_{tot}^{F(atom)} + N_{Ag}E_{tot}^{Ag(atom)} + N_{Ch}E_{tot}^{Ch(atom)}\right)\right]$$

where N_{Ba}, N_F, N_{Ag} and N_{Ch} are the numbers of Ba, F, Na and *Ch* atoms, respectively, in the unit-cell of the BaFAg*Ch* compound; $E_{tot}^{BaFAgCh}$ is the total energy of the unit-cell of BaFAg*Ch*; $E_{tot}^{Ba(solid)}$, $E_{tot}^{Ag(solid)}$ and $E_{tot}^{Ch(solid)}$ are the total energies per atom of the solid state of the Ba, Ag and *Ch* pure elements, respectively; $E_{tot}^{F(gaz)}$ is the total energy per atom of the gas state of the pure element F; $E_{tot}^{Ba(atom)}$, $E_{tot}^{F(atom)}$, $E_{tot}^{Ag(atom)}$ and $E_{tot}^{Ch(atom)}$ are the total energies of the Ba, F, Ag and *Ch* isolated atoms, respectively. The obtained values for the cohesive energies and formation enthalpies are listed in Table 1. The calculated cohesive energies and formation enthalpies of the BaAg*Ch*F (*Ch* = S, Se, Te) compounds are negative, confirming their chemical and structural stabilities.

3.2. Electronic properties

The calculated band energy dispersions of the BaAg*Ch*F (*Ch* = S, Se, Te) systems along some selected high-symmetry directions in the Brillouin zone (BZ) using the TB-mBJ potential with and without including the spin-orbit coupling (SOC and SR) are depicted in Fig. 2. One can note that the band profiles of the three examined compounds look quite similar. All three studied compounds are direct wide energy band gap semiconductors; both the conduction band minimum (CBM) and valence band maximum (VBM) are localized at the Γ-point in the BZ. The main difference between the band structures of the examined compounds is the size of their band gaps. The calculated energy band gaps using the GGA08-SR, GGA08-SOC, TB-mBJ-SR and TB-mBJ-SOC of the investigated systems are gathered in Table 2 along with the available theoretical results in the scientific literature. It is worth to note that the previous calculations did not include the spin-orbit coupling. We visualize the calculated energy band gap values using the GGA08-SR, GGA08-SOC, TB-mBJ-SR and TB-mBJ-SOC in Fig. 3 to facilitate the comparison between them. From Figs. 2 and 3, and Table 2, one can make the following conclusions:

(i) The inclusion of the spin-orbit coupling causes the splitting of bands at the valence band maximum. The SOC band splitting at the valence band maximum is 25 meV in BaAgSF, 108 meV in BaAgSeF and 269 meV in BaAgTeF.
(ii) The TB-mBJ-SOC energy band gaps of BaFAgS, BaFAgSe and BaFAgTe are reduced by approximately 0.97%, 2.44% and

Table 1
Calculated lattice parameters ($a = b$ and c, in Å unit), relative deviation from the experimental value $d(\%) = [(x - x_{Expt.})/x_{Expt.}] \times 100$ ($x = a, c$), internal atomic coordinates (Z_{Ba} and Z_{Ch}), formation enthalpies (ΔH, in eV) and cohesion energies ($E_{Coh.}$, in eV) for BaAg*Ch*F (*Ch* = S, Se, Te) compared with the corresponding experimental ones.

	BaFAgS			BaFAgSe			BaFAgTe	
	RS	SOC	Expt [16].	RS	SOC	Expt [16].	RS	SOC
a	4.2035	4.1963	4.2406	4.3177	4.3078	4.3449	4.4987	4.5013
d(%)	−0.87	−1.04		−0.63	−0.85			
c	9.2423	9.2327	9.3029	9.3327	9.3349	9.4018	9.5035	9.4515
d(%)	−0.65	−0.75		−0.73	−0.71			
Z_{Ba}	0.1698	0.1687	0.1665	0.1627	0.1567	0.1598	0.1497	0.1452
Z_{Ch}	0.6745	0.6752	0.6760	0.6803	0.6819	0.6798	0.6849	0.6859
ΔH	−5.9081			−5.2899			−5.2115	
E_{Coh}	−7.7244			−7.5893			−7.4296	

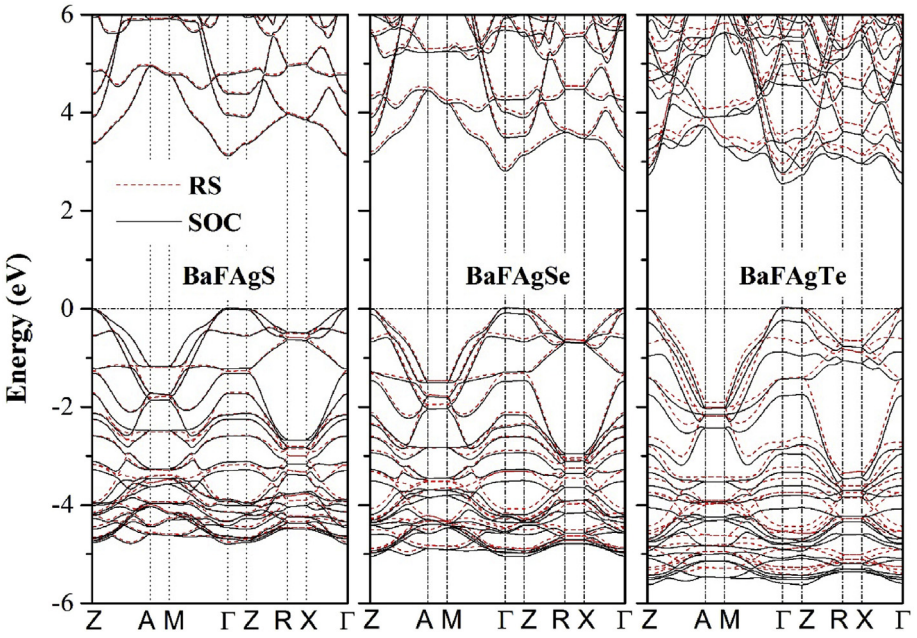

Fig. 2. Calculated energy band structure for the BaAg*Ch*F (*Ch* = S, Se, Te) compounds using the TB-mBJ-SR (Red dashed lines) and the TB-mBJ-SOC (Black solid lines). (For interpretation of the references to colour in this figure legend, the reader is referred to the Web version of this article.)

Table 2
Calculated fundamental energy band gap (E_g, in eV unit) for the BaAg*Ch*F (*Ch* = S, Se, Te) compounds compared with previous calculations.

System	Present cal.				Previous cal.
	GGA08-SR	GGA08-SOC	mBJ-SR	mBJ-SOC	
BaAgSF	1.44	1.43	3.13	3.10	1.387 [21] 2.889 [29]
BaAgSeF	1.25	1.17	2.85	2.78	1.278 [21] 2.663 [29]
BaAgTeF	1.55	1.34	2.71	2.52	2.595 [29]

7.54%, respectively, compared to the corresponding ones obtained using the TB-mBJ-SR.

(iii) The SOC effect increases when going from BaAgSF to BaAgSeF to BaAgTeF. This trend may be attributed to the increase of the atomic number of the chalcogen atoms; $Z^{(S)} = 16$, $Z^{(Se)} = 34$ and $Z^{(Te)} = 52$.

(iv) The substitution of the *Ch* atom in the BaFAg*Ch* series in the sequence S→Se→Teleads to a monotonously narrowing of the TB-mBJ fundamental band gap. It is not the case when using the GGA08.

(v) The TB-mBJ-SOC approach improves the band gap values of BaAgSF, BaAgSeF and BaAgTeF by approximately 54%, 58%

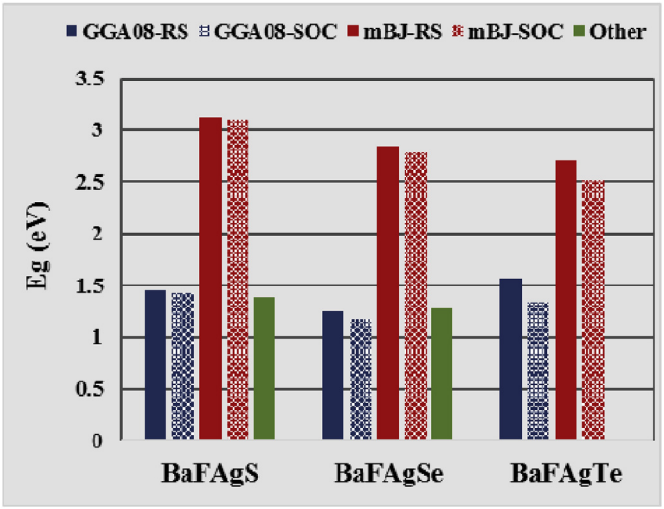

Fig. 3. Comparison between the calculated fundamental band gap (Γ-Γ) values (E_g, in eV) obtained using different approaches: GGA08-SR, GGA08-SOC, mBJ-SP and mBJ-SOC for the BaAg*Ch*F (*Ch* = S, Se, Te) compounds.

Table 3
Calculated hole (m_h^*) and electron (m_e^*) effective masses for the BaAg*Ch*F (*Ch* = S, Se, Te) at the CBM and VBM, respectively, along the $\vec{a}$-axis (Γ-X direction in *k*-space), *ab*-plane (Γ-M direction) and $\vec{c}$-axis (Γ -Z direction). The effective mass values are given in the unit of free electron massm_0.

Carrier type	m_h^*			m_e^*		
Directions	Γ-X	Γ -Z	Γ-M	Γ-X	Γ -Z	Γ-M
BaFAgS	1.00	14.14	0.95	0.57	0.79	0.57
BaFAgSe	0.64	9.31	0.63	0.45	0.61	0.45
BaFAgTe	0.42	7.63	0.41	0.32	1.82	0.32

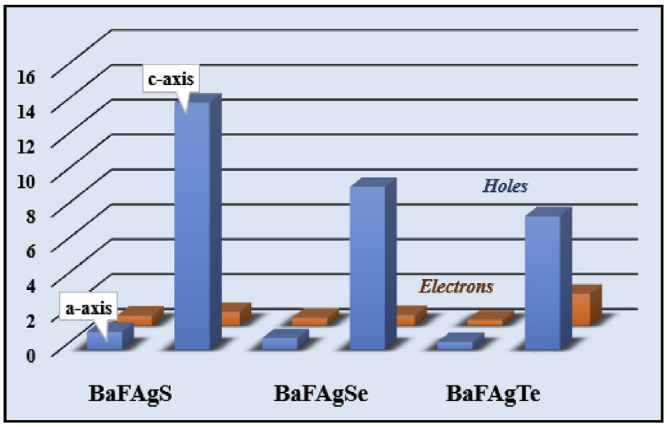

Fig. 4. Comparison between the calculated hole and electron effective mass values at the valence band maximum and conduction band minimum, respectively, along the *a* and *c* crystallographic axes for the BaAg*Ch*F (*Ch* = S, Se, Te) compounds. The values are given in the unit of free electron mass.

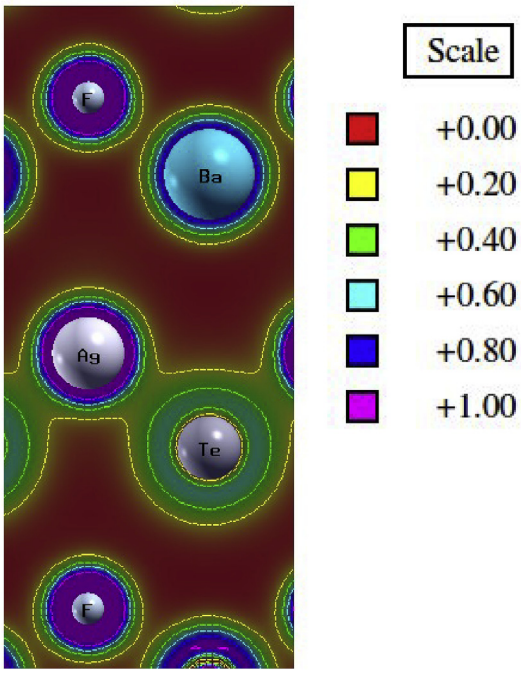

Fig. 6. Contour plot of the electron charge density distribution in the plane (400) for BaAgTeF.

and 47%, respectively, compared to the corresponding ones obtained using the GGA08-SOC. There is no experimental data for the energy band gaps of the BaFAg*Ch* (*Ch* = S, Se, Te) compounds to be compared with our results. However, if we bring in mind that the DFT-GGA band gap is approximately 30 – 50% smaller than the corresponding experimental one [48,49], we can expect that the calculated TB-mBJ band gap values might be in a reasonable agreement with the real ones. The TB-mBJ-SOC band gaps of the BaAg*Ch*F compounds, which range from 2.52 eV to 3.10 eV, are comparable with the measured band gaps for some isostructural compounds: SrCuSF (3.0 eV) [11], SrCuSeF (2.7 eV) [11], SrCuSF (3.2 eV) [10], BaCuSeF (3.0 eV) [10] and BaCuTeF (2.3 eV) [27].

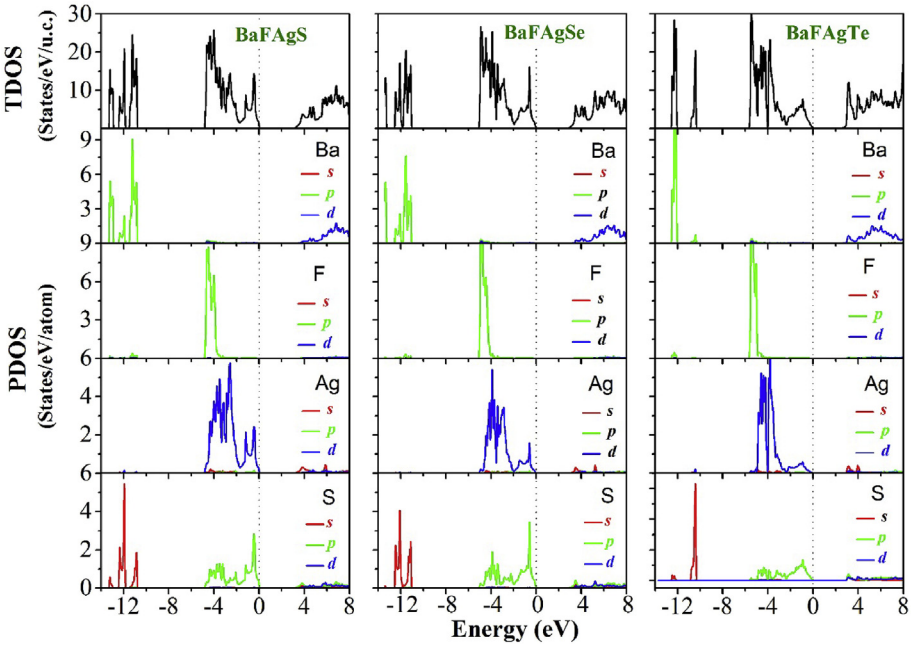

Fig. 5. Calculated projected (PDOS) and total (TDOS) densities of states for the BaAg*Ch*F (*Ch* = S, Se, Te) compounds.

Table 4
Calculated 3D elastic constant (C_β, in GPa unit), 3D deformation potential (E_β, in eV unit) and the minimum lattice thermal conductivity (k_{min}, in $Wm^{-1}K^{-1}$ unit) using Cahill model for the BaAg*Ch*F (*Ch* = S, Se, Te) compounds.

	C_β		E_β				k_{min}
	a-axis	*c*-axis	*a*-axis		*c*-axis		
			hole	Elec.	hole	Elec.	
BaAgSF	110.32	77.78	9.35	11.83	10.98	13.94	0.612
BaAgSeF	103.60	62.92	9.70	12.40	9.88	12.97	0.544
BaAgTeF	94.26	50.53	10.59	13.37	9.78	12.80	0.420

(vi) From Fig. 2, one can observe the presence of quasiflat valence bands along the $\Gamma \rightarrow Z$, $R \rightarrow X$ and $M \rightarrow A$directions in the Brillouin zone, along with highly dispersive valence bands in the other high symmetry directions. This is consistent with the layered structure of the considered compounds.

(vii) The dispersion of the valence bands around the VBM is highly anisotropic; the upper valence bands show a large dispersion around the VBM along the $\Gamma \rightarrow M$ and $\Gamma \rightarrow X$ directions in the reciprocal space (*k*-space) and a pronounced flatness along the $\Gamma \rightarrow Z$ direction. The flatness of the upper valence bands along the $\Gamma \rightarrow Z$ direction in the *k*-space promotes a large hole effective mass along the *c*-axis direction, while their large dispersion along the $\Gamma \rightarrow M$ and $\Gamma \rightarrow X$ directions in the *k*-space reveal a small hole mass along the *a*-axis direction and in the *ab*-plane. The simultaneous presence of large and small hole effective masses is a favourable indicator of thermoelectric performance; small hole effective mass is favourable for good electrical conductivity, while large hole effective mass is favourable for large Seebeck coefficient for *p*-type compounds. This noticeable dependence of the dispersion of the valence bands on the crystallographic directions is an indicative of a highly bonding anisotropy in the layered BaAg*Ch*F. The bonds along the *c*-axis (interlayer bonding) should differ considerably from those in the *ab*-plane (intralayer bonding)

(viii) The conduction bands exhibit a pronounced dispersion along all the considered directions in the BZ, suggesting that the *n*-type compounds should show less thermoelectric performance than the *p*-type ones.

Transport properties in semiconductors are principally controlled by the effective masses of the charge-carriers. Therefore, it becomes necessary to estimate the effective masses of electrons and holes along different crystallographic directions at the band edges of the studied materials. The predicted effective masses of holes (m_h^*) at the valence band top and of electrons (m_e^*) at the conduction band bottom towards three different directions in the *k*-space; $\Gamma \rightarrow Z$, $\Gamma \rightarrow X$ and $\Gamma \rightarrow M$, for the title compounds are listed in Table 3. To facilitate the comparison between the values of m_h^* and m_e^*, the obtained results are visualized in Fig. 4. It is apparent that both m_h^* and m_e^* exhibit noticeable dependences on the crystallographic directions. The values of m_h^* and m_e^* along the *c*-axis ($\Gamma \rightarrow Z$ direction in the *k*-space) are significantly larger than the corresponding ones along the *a*-axis ($\Gamma \rightarrow M$ direction in the *k*-space) and in the *ab*-plane ($\Gamma \rightarrow X$direction in the *k*-space). According to these results, the mobility of charge-carries along the *a*-axis should be significantly larger than that along the *c*-axis, while the Seebeck coefficient will be larger along the *c*-axis. The obtained results reveal also that the hole effective mass is more dependent on the crystallographic direction than the electron one, demonstrating that the anisotropy of the effective mass and its related properties, such as Seebeck coefficient and electrical conductivity, should be more pronounced in the *p*-type compounds than in the *n*-type

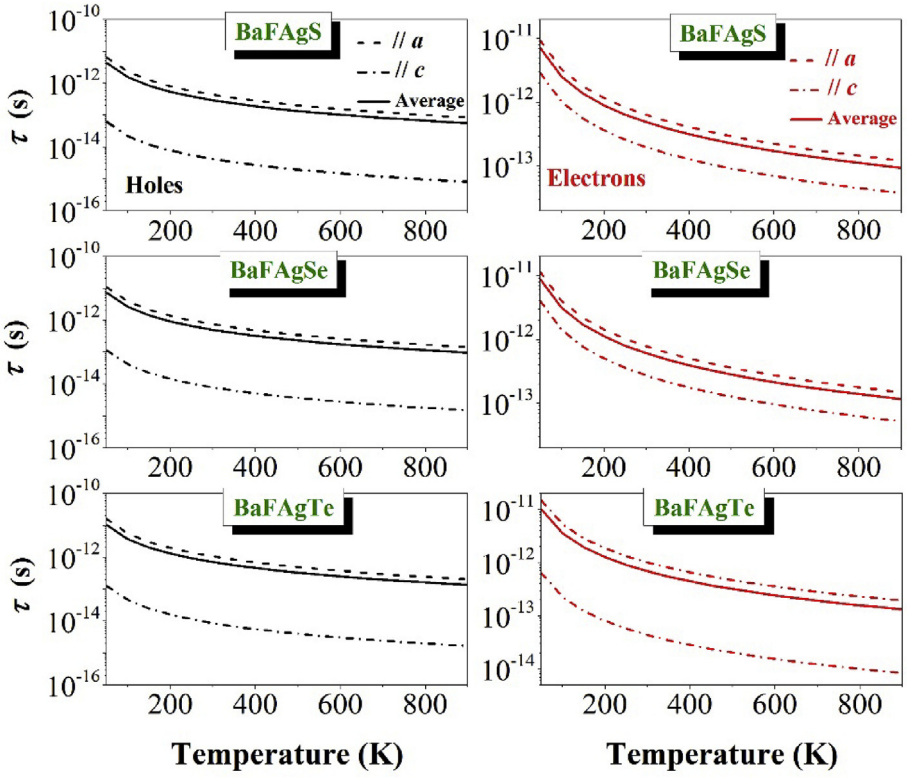

Fig. 7. Temperature dependence of the relaxation time (τ) for the BaAg*Ch*F (*Ch* = S, Se, Te) compounds.

ones. On another side, the hole effective mass is larger than the electron one, suggesting that the mobility of holes should be small than that of electrons in the considered compounds. Therefore, as the electrical conductivity σ is inversely proportional to the charge-carrier masses, one can expect that for the same charge-carrier concentration and temperature, the electrical conductivity σ of the *n*-type system should be larger than that of the *p*-type one. Moreover, as the Seebeck coefficient *S* is proportional to the effective masses of charge-carriers, one can expect that the *S* of the *p*-type system should be larger than that of the *n*-type one. The charge-carrier effective masses decrease when going from BaAgSF to BaAgSeF to BaAgTeF, suggesting that BaAgSF should have the highest Seebeck coefficient and BaAgTeF should have the highest electrical conductivity. There is no available experimental or theoretical data about the charge-carrier masses in the literature to be compared with our results.

The total and atomic-projected *l*-decomposed densities of states (TDOS and PDOS) of the investigated compounds are depicted in Fig. 5. The near-Fermi part of the upper valence band group, which ranges approximately from −2.0 eV to 0 eV, is composed of the hybridized Ag: 4d and *Ch*: n*p* (*Ch* = S (n = 3), Se (n = 4), Te (n = 5)) orbitals, while the lower part, which ranges approximately from −2.0 eV to −5.5 eV, is dominated by the F: 2*p* and Ag: 4d states. The conduction band bottom is also composed of the states related to the blocks [Ag*Ch*]. Therefore, both the VBM and CBM are composed exclusively of the Ag: 4d and *Ch*: n*p* states of the blocks [Ag*Ch*].

For more insight into the chemical bonding of the considered compounds, the charge density distribution map in the (400) plane for BaAgTeF, as representative, is shown in Fig. 6. From this figure, one can note that the intralayer bonding in the [Ag*Ch*] and [BaF] blocks, i.e., Ag-*Ch* and Ba-F bonds, are of mixed ionic and covalent

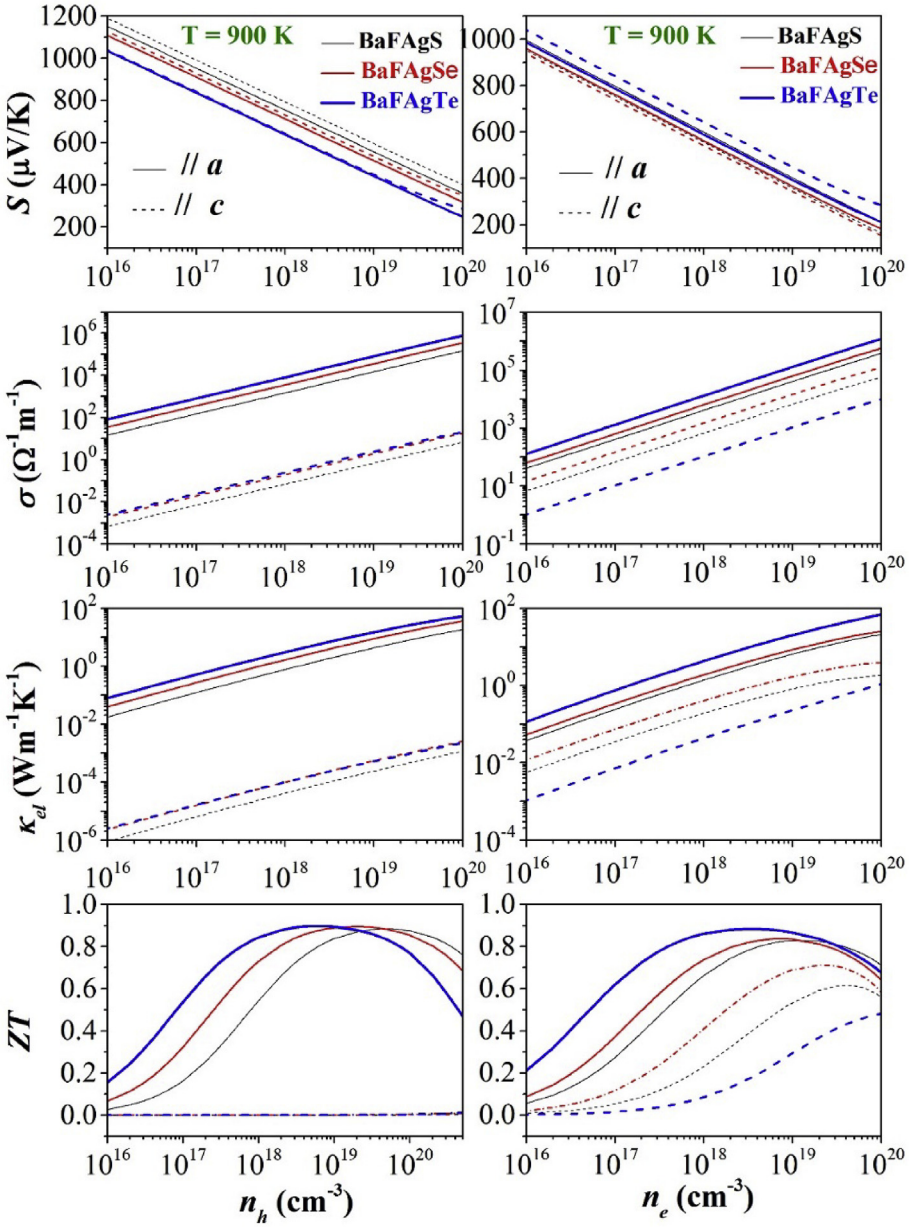

Fig. 8. Charge carrier concentration dependence of the Seebeck coefficient, electrical condctivity, electronic thermal conductivity and figure of merite for T = 900 K for the BaAg*Ch*F (*Ch* = S, Se, Te) compounds.

nature. The Ag-*Ch* bond inside the [Ag*Ch*] layer is predominantly of covalent character, which is due to the strong hybridization between Ag: 4d and *Ch*: n*p*, while the Ba-F bond *in* the layer [BaF] is predominantly ionic. The interlayer bonding between the [AgCh] and [BaF] blocks is ionic. This predominantly covalent character of the chemical bonds along the *a*-axis and their predominantly ionic nature along the *c*-axis lead to the quasi two-dimensional electronic structure.

3.3. Thermoelectric properties

3.3.1. Relaxation time and lattice thermal conductivity

Within the CRTA, the Seebeck coefficient can be calculated without any adjustable parameters; however, the electrical conductivity has to be calculated with respect to the relaxation time τ, therefore it is crucial to determine τ to estimate the electrical conductivity and thermal conductivity. Generally, two ways are proposed to determine the τ value: (i) from the experimental value of the resistivity [49], or (ii) from a theoretical calculation. As there are no experimental data that allow the calculation of the τ values of the considered compounds, a theoretical method was used to estimate τ. An approximation that has a large success for calculating τ is based on the deformation potential theory developed by Bardeen and Shockley [50–52]: $\tau = \frac{2\sqrt{2\pi}\, C_\beta \hbar^4}{3(m^* K_B T)^{\frac{3}{2}} E_\beta^2}$, where C_β is the 3D elastic constant, E_β is the 3D deformation potential and m* is the charge-carrier effective mass. The method to calculate E_β and C_β can be found in Ref. [53]. The necessary parameters to calculate τ are listed in Tables 3 and 4. The variation of τ as function of temperature is depicted in Fig. 7. Practically, temperature dependence of the relaxation time is similar in the three studied compounds;

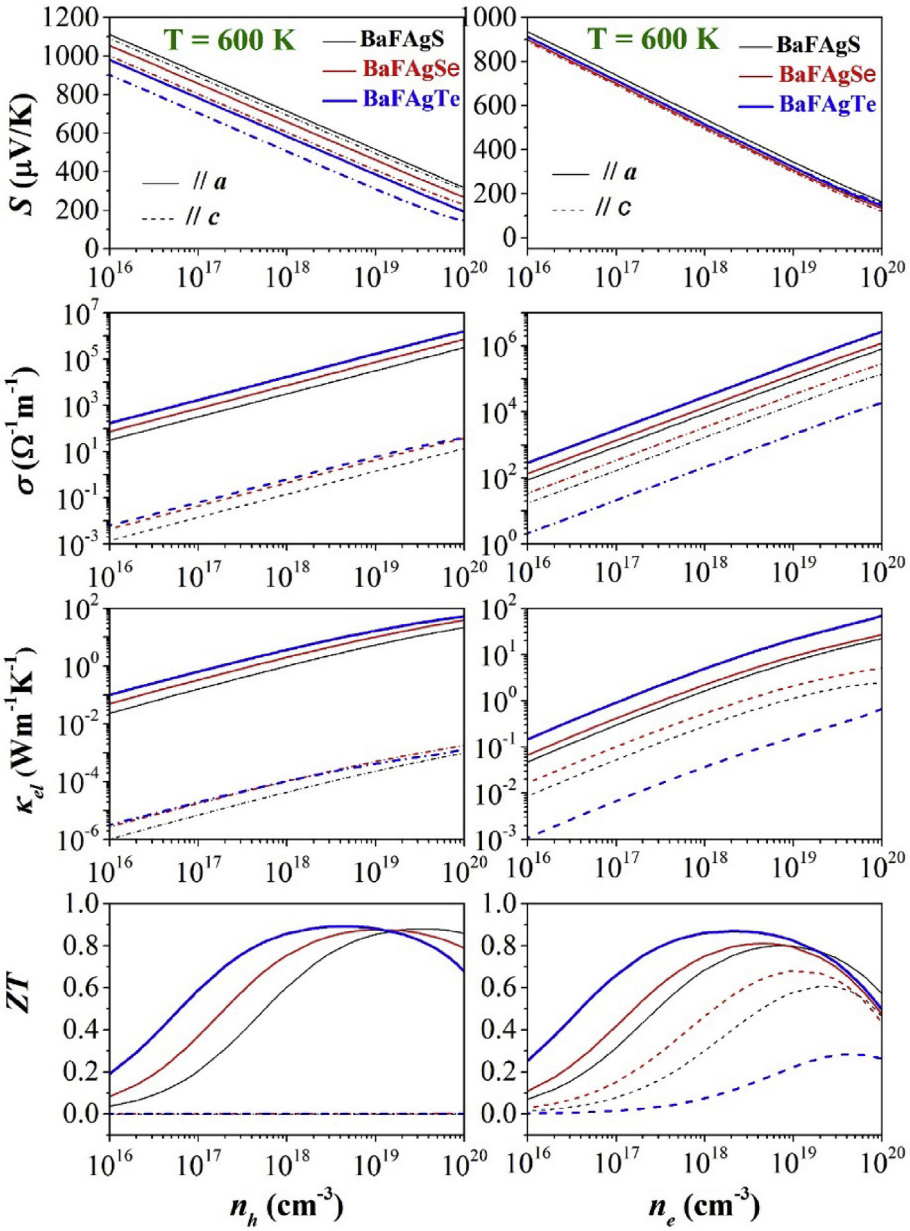

Fig. 9. Charge carrier concentration dependence of the Seebeck coefficient, electrical condctivity, electronic thermal conductivity and figure of merite for T = 600 K for the BaAg*Ch*F (*Ch* = S, Se, Te) compounds.

the relaxation time decreases with increasing temperature. When temperature increases, the thermal speed of electrons increases and consequently collisions between electrons become more considerable, and the vibration amplitude of atoms around their mean positions also increases; all these decrease the relaxation time.

For more accurate calculation of the thermoelectric parameters, it is necessary to calculate the contribution of the lattice vibration into the thermal conductivity. Usually, the best values of the figure of merit of materials occur at mid or high temperature, and at this range of temperature, their lattice thermal conductivities (κ_l) are comparable to their minimum lattice conductivities (κ_{min}). At high temperature, the lattice thermal conductivity deceases to a lower limit κ_{min} with increasing temperature. The minimum lattice thermal conductivity κ_{min} can be calculated using Cahill model [54,55], which gives a good estimation of the minimum lattice thermal conductivity for a large class of materials [54–57]. The calculated values of the minimum lattice thermal conductivity κ_{min} for the considered compounds are listed in Table 4. The calculated κ_{min} of the three studied compounds are smaller than unity, suggesting that these compounds might be good TE candidates.

3.3.2. Thermoelectric properties

Variation of the Seebeck coefficient, electrical conductivity, thermal conductivity and figure of merit as functions of carrier concentration for both *p*-type and *n*-type BaAgSF, BaAgSeF and BaAgTeF in the range $10^{16} - 10^{20} cm^{-3}$ along the [100] (*a*-axis) and [001] (*c*-axis) crystallographic directions for T = 300, 600 and 900 K are plotted in Figs. 8–10. The absolute value (magnitude) of the Seebeck coefficient *S* decreases with increasing carrier concentration and increases with increasing temperature for both the *n*-type and *p*-type compounds. This is a common trend in thermoelectric

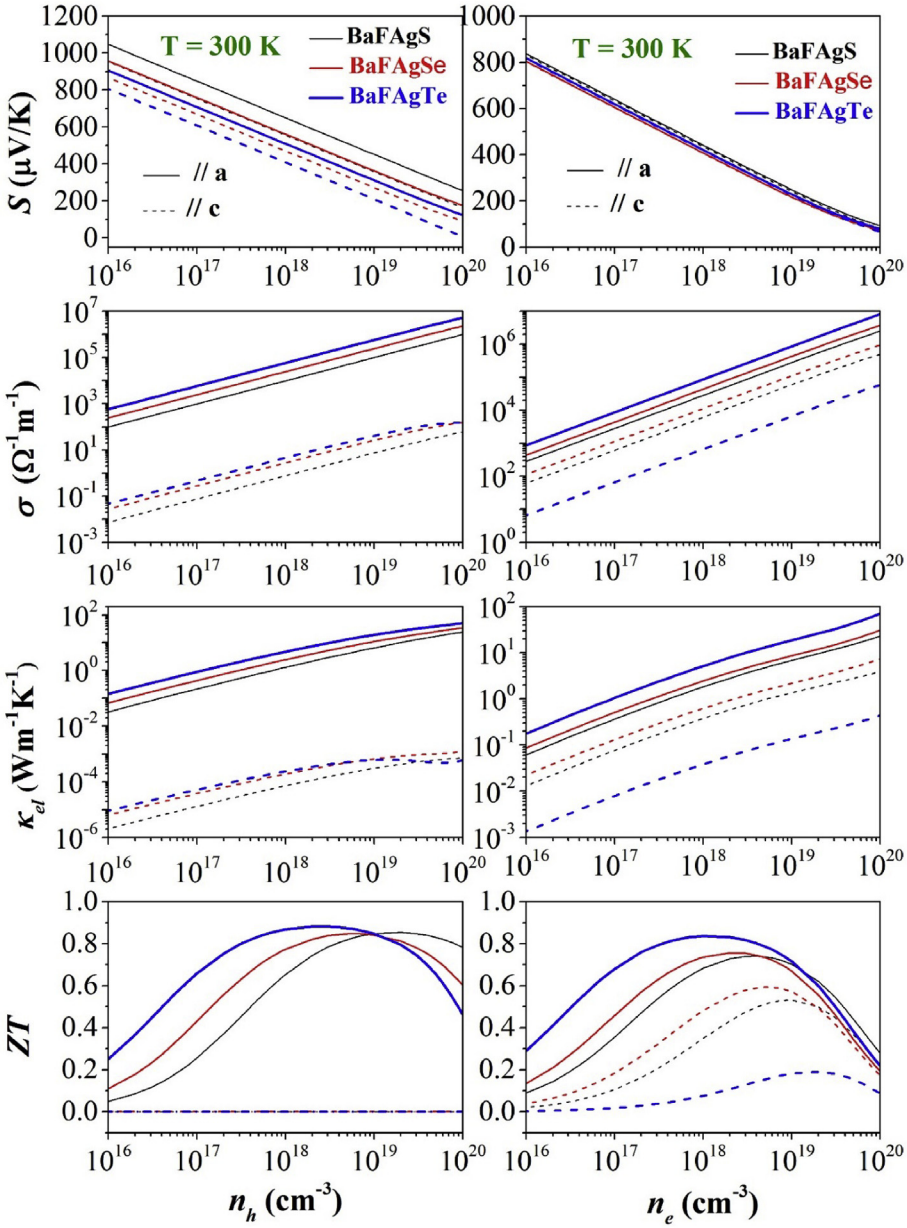

Fig. 10. Charge carrier concentration dependence of the Seebeck coefficient, electrical condctivity, electronic thermal conductivity and figure of merite for T = 300 K for the BaAg*Ch*F (*Ch* = S, Se, Te) compounds.

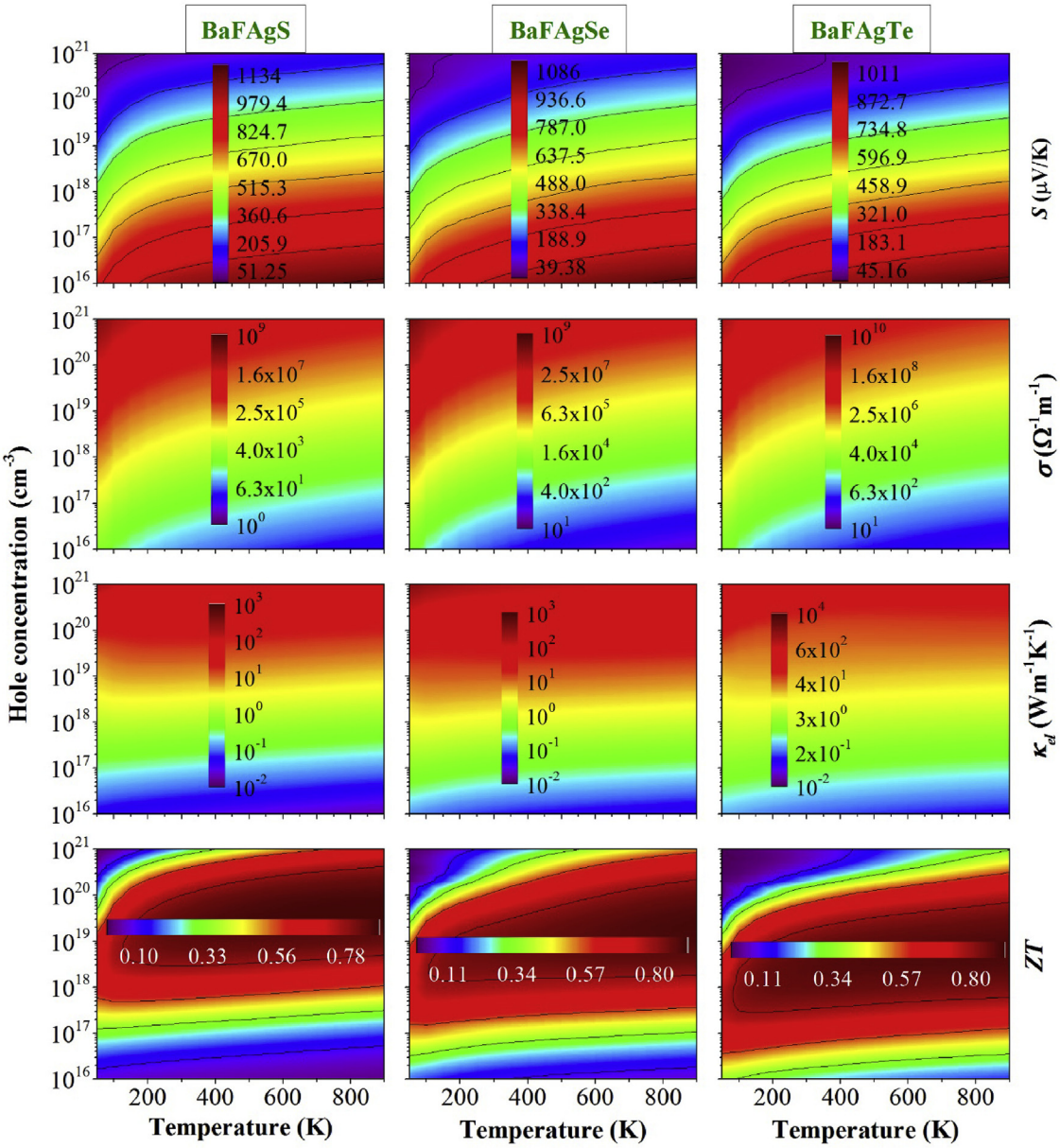

Fig. 11. Maps of the calculated hole concentration and temperature dependences of the Seebeck coefficient (*S*, in μV/K unit), electrical conductivity (σ, in $\Omega^{-1}m^{-1}$ unit), electronic thermal conductivity (κ_{el}, in $Wm^{-1}K^{-1}$ unit) and figure of merit (*ZT*, dimensionless) for the BaAgChF (*Ch* = S, Se, Te) compounds.

materials. The magnitude of *S* for the *p*-type system is higher than that of the *n*-type one throughout the considered concentration range of charge carriers. This result is consistent with the already predicted result from the calculated charge-carrier masses; large effective masses of charge-carriers translates to a high Seebeck coefficient *S*. Thus, one can conclude that the *p*-type BaAgSF, BaAgSeF and BaAgTeF compounds are more favourable for TE performance than the *n*-type ones. Therefore, we focus our study on the *p*-type compounds. The thermopower *S* shows practically the same behavior regarding the variation of carrier concentration and temperature for the three studied compounds. This behavior is attributed to the similarity of their energy band dispersions around the Fermi level. For the same temperature and same charge-carrier concentration, the value of *S* decreases when we move from BaAgSF to BaAgSeF to BaAgTeF. This might be due to the decrease of the charge-carrier effective masses when we move in the same sequence. The Seebeck coefficient has almost an isotropic behavior along the different crystallographic directions.

From Figs. 8–10, one can note that the electrical conductivity, electronic thermal conductivity and figure of merit are considerably anisotropic, which is consistent with the layered structure of the title compounds. The electrical conductivity, thermal conductivity and figure of merit of the *p*-type compounds along the *a*-axis and in the *ab*-plane are considerably larger than the corresponding ones along the *c*-axis. This might be because the lower hole effective mass along the *a*-axis and in the *ab*-plane (the Γ→M and Γ→X directions in the *k*-space) compared to the corresponding one along the *c*-axis (the Γ→Z direction in the *k*-space). The pronounced upper valence band dispersions along the Γ→M and Γ→X directions in the *k*-space, induced by the Ag-*Ch* (*Ch* = S, Se, Te) covalent bonding, result in a relatively low hole effective masses and thus a relatively high hole conductivity along these directions. The anisotropy of the electrical and thermal conductivities in the *n*-type compounds is less pronounced than that in the p-type one. This

might be due to the almost equal values of the electron effective masses along the different crystallographic directions.

It is very important to know the best ranges of the charge carrier concentration and temperature where the TE efficiency is high. High TE efficiency requires a high Seebeck coefficient, high electrical conductivity and low thermal conductivity. Fig. 11 shows the Seebeck coefficient (S), electrical conductivity (σ), electronic thermal conductivity (κ_{el}), and factor of merit (ZT) maps as functions of temperature and carrier concentration along the a-direction for the p-type BaAgSF, BaAgSeF and BaAgTeF. Fig. 11 shows that the Seebeck coefficient increases with increasing temperature and decreases with increasing hole concentration, but at high hole concentration, it saturates at high temperatures. The electrical conductivity decreases with increasing temperature for a fixed hole concentration. The thermal conductivity remains approximately constant with increasing temperature for a fixed hole concentration. However, at a fixed temperature, both the electrical and thermal conductivities increase sharply with increasing hole concentration. The influence of carrier concentration on the figure of merit is much more evident than that of the temperature. The high values of the figure of merit are found for carrier concentration around $10^{19}\,cm^{-3}$ with a large range of temperature from 300 K to 900 K. For BaFAgS, $ZT_{//a} = 0.88$ for $T = 900$ K and hole concentration of $5 \times 10^{19}\,cm^{-3}$, for BaFAgSe, $ZT_{//a} = 0.89$ for $T = 900$ K and hole concentration of $2 \times 10^{19}\,cm^{-3}$ and for BaFAgTe, $ZT_{//a} = 0.90$ for $T = 900$ K and hole concentration of $6 \times 10^{18}\,cm^{-3}$. It is worth to note here that ZT of the considered compounds attains a value slightly higher than the aforementioned ones for temperature higher than 900 K. The thermoelectricity efficiency of the studied compounds can be enhanced if one could reduce the lattice thermal conductivity κ_l by introducing further phonon scattering centres by alloying or doping by chemical elements that reduce the lattice thermal conductivity.

4. Conclusion

In this work, we have investigated the structural, electronic and thermoelectric properties of the barium silver fluoride chalcogenides BaAg*Ch*F (*Ch* = S, Se, Te) using the full potential linearized augmented plane wave approach in the framework of density functional theory. The GGA-PBEsol optimized structural parameters of the title compounds are in excellent agreement with the available experimental data. Analysis of the calculated band structures using the GGA-PBEsol and TB-mBJ both with and without including the spin-orbit coupling reveals that the studied compounds are direct band gap semiconductors. The spin-orbit coupling effect leads to the split of the valence band maximum at Γ-point and to the reduction of the band gap value. This effect increases with increasing atomic number of the chalcogenide atom. The simultaneous presence of flat and dispersive bands at the valence band maximum of the studied compounds is a favourable indicator of their thermoelectric performance. The charge-carrier effective masses exhibit noticeable dependence on the crystallographic directions; their values along the c-axis are significantly larger than the corresponding ones along the a-axis. Calculated density of states and charge density distribution show that the Ag-*Ch* bond inside the [Ag*Ch*] layer is predominantly of covalent character, the Ba-F bond *in* the layer [BaF] is predominantly ionic and the interlayer bonding between the [AgCh] and [BaF] blocks is ionic. Calculated Seebeck coefficient demonstrates that p-type title compounds are more favourite for thermoelectric performance than the n-type ones. The calculated thermoelectric parameters exhibit a strong dependence on the crystallographic directions. The tile compounds show more thermoelectric performance along the a-axis than along the c one. We are not aware of any experimental or theoretical data for the temperature and carrier concentration dependences of the thermoelectrics properties of the considered compounds, so we look forward for the experimentalist to confirm our obtained results.

Acknowledgment

The authors (A. Bouhemadou and S. Bin-Omran) extend their appreciation to the International Scientific Partnership Program ISPP at King Saud University for funding this research work through JSPP# 0025.

References

[1] P.S. Kireev, Semiconductor Physics, Vysshaya Shkola, Moscow, 1975.
[2] T.M. Tritt, M.A. Subramanian, Thermoelectric materials, phenomena, and applications: a bird's eye view, MRS Bulletin 31 (2006) 188–198.
[3] D.A. Polvani, J.F. Meng, N.V. Chandra Shekar, J. Sharp, J.V. Badding, Large improvement in thermoelectric properties in pressure-tuned p-type $Sb_{1.5}Bi_{0.5}Te_3$, Chem. Mater. 13 (2001) 2068–2071.
[4] M.K. Yadav, B. Sanyal, First-principles study of thermoelectric properties of Li-based half-Heusler alloys, J. Alloys Compd. 622 (2015) 388–393.
[5] T. Fang, S. Zheng, T. Zhou, H. Chen, P. Zhang, Validity of rigid-band approximation in the study of thermoelectric properties of p-type FeNbSb-based half-Heusler compounds, J. Electron. Mater. 46 (2017) 3030–3035.
[6] Y. Takagiwa, Y. Pei, G. Pomrehn, G.J. Snyder, Dopants effect on the band structure of PbTe thermoelectric material, Appl. Phys. Lett. 101 (2012), pp. 092102–1-3.
[7] T. Takabatake, K. Suekuni, T. Nakayama, E. Kaneshita, Phonon-glass electron-crystal thermoelectric clathrates: Experiments and theory, Rev. Mod. Phys. 86 (2014) 669–716.
[8] A.J. Minnich, M.S. Dresselhaus, Z.F. Ren, G. Chen, Bulk nanostructured thermoelectric materials: current research and future prospects, Energy Environ. Sci. 2 (2009) 466–479.
[9] O. Delaire, J. Ma, K. Marty, A.F. May, M.A. McGuire, M.H. Du, D.J. Singh, A. Podlesnyak, G. Ehlers, M.D. Lumsden, B.C. Sales, Giant anharmonic phonon scattering in PbTe, Nat. Mater. 10 (2011), pp. 614–1-9.
[10] H. Yanagi, J. Tate, S. Park, C.-H. Park, D.A. Keszler, P-type conductivity in wide-band-gap BaCuQF (Q = S, Se), Appl. Phys. Lett. 82 (2003), pp. 2814–1-3.
[11] H. Yanagi, J. Tate, S. Park, C. Park, D.A. Keszler, M. Hirano, H. Hosono, Valence band structure of BaCuSF and BaCuSeF, J. Appl. Phys. 100 (2006), pp. 083705–1-4.
[12] D. Zou, H. Zheng, J. Li, Predicted thermoelectric properties of natural superlattice structural compounds BaCuChF (*Ch= S, Se and Te*) *by first-principles calculations*, J. Alloys Compd. 686 (2016) 571–576.
[13] A.K.F. Ul Islam, M.A. Helal, M.N.H. Liton, M. Kamruzzaman, H.M.T. Islam, First principles study of electronic structure dependent optical properties of oxy-chalcogenides BiOCuCh (Ch=S, Se, Te), Indian J. Phys. 91 (2017) 403–412.
[14] V.K. Gudelli, V. Kanchana, G. Vaitheeswaran, D.J. Singh, A. Svane, N.E. Christensen, S.D. Mahanti, Electronic structure, transport, and phonons of SrAgChF (Ch=S, Se, Te): Bulk superlattice thermoelectrics, Phys. Rev. B 92 (2015), pp. 045206–1-8.
[15] D.O. Charkin, A.V. Urmanov, I.V. Plokhikh, A.D. Korshunov, A.N. Kuznetsov, S.M. Kazakov, Synthesis and crystal structures of novel LaOAgS-type alkaline earth-zinc, manganese, and cadmium fluoride pnictides, J. Alloys Compd. 585 (2014) 644–649.
[16] D.O. Charkin, A.V. Urmanov, S.M. Kazakov, Preparation and crystal structures of novel LaOAgS-type copper and silver fluoride chalcogenides, J. Alloys Compd. 516 (2012) 134–138.
[17] A.P. Richard, J.A. Russell, A. Zakutayev, L.N. Zakharov, D.A. Keszler, J. Tate, *Synthesis, structure, and optical properties of BiCuOCh* (*Ch=S, Se, and Te*), J. Solid State Chem. 187 (2012) 15–19.
[18] D. Zou, S. Xie, Y. Liu, J. Lin, J. Li, Electronic structures and thermoelectric properties of layered BiCuOCh oxychalcogenides (Ch = S, Se and Te): first-principles calculations, J. Mater. Chem. A 1 (2013) 8888–8896.
[19] G. Liu, H. Sun, J. Zhou, Q. Li, X.G. Wan, Thermal properties of layered oxy-chalcogenides BiCuOCh (Ch = S, Se, and Te): a first-principles calculation, J. Appl. Phys. 119 (2016), pp. 185109–1-7.
[20] V.V. Bannikov, I.R. Shein, A.L. Ivanovskii, Electronic, optical properties and chemical bonding in six novel 1111-like chalcogenide fluorides AMChF (*A=Sr, Ba; M=Cu, Ag; and Ch=S, Se, Te*) *from first principles calculations*, J. Solid State Chem. 196 (2012) 601–606.
[21] V.V. Bannikov, I.R. Shein, A.L. Ivanovskii, Structural, electronic properties and inter-atomic bonding in layered chalcogenide oxides LaMChO (*where M = Cu, Ag, and Ch = S, Se*) *from FLAPW-GGA calculations*, Solid State Sci. 14 (2012) 89–93.
[22] A. Zakutayev, J. Tate, H.A.S. Platt, D.A. Keszler, C. Hein, T. Mayer, A. Klein, W. Jaegermann, Electronic properties of BaCuChF (Ch = S, Se, Te) surfaces and BaCuSeF/ZnPc interfaces, J. Appl. Phys. 107 (2010), pp. 103713–1-8.
[23] V.V. Bannikov, I.R. Shein, A.L. Ivanovskii, Design of novel magnetic materials

based on ZrCuSiAs-like semiconducting pnictide-oxides from first-principles calculations, Solid State Commun. 150 (2010) 2069–2071.
[24] A. Zakutayev, J. Tate, G. Schneider, Defect physics of BaCuChF (Ch = S, Se, Te) p-type transparent conductors, Phys. Rev. B 82 (2010), pp. 195204–1-8.
[25] A. Zakutayev, R. Kykyneshi, G. Schneider, D.H. McIntyre, J. Tate, Electronic structure and excitonic absorption in BaCuChF (Ch = S, Se, and Te), Phys. Rev. B 81 (2010), pp. 155103–1-9.
[26] R. Pöttgen, D. Johrendt, Materials with ZrCuSiAs-type structure, Z. Naturforsch. B Chem. Sci. 63 (2008) 1135–1148.
[27] C.-H. Park, R. Kykyneshi, A. Yokochi, J. Tate, D.A. Keszler, Structure and physical properties of BaCuTeF, J. Solid State Chem. 180 (2007) 1672–1677.
[28] M. Yasukawa, K. Ueda, H. Hosono, Thermoelectric properties of layered oxy-selenides La1-xSr xCuOSe (x=0 to 0.2), J. Appl. Phys. 95 (2004) 3594–3597.
[29] K. Boudiaf, A. Bouhemadou, O. Boudrifa, K. Haddadi, F. Saad Saoud, R. Khenata, Y. Al-Douri, S. Bin-Omran, M.A. Ghebouli, Structural, elastic, electronic and optical properties of LaOAgS-type silver fluoride chalcogenides: first-principles study, J. Electron. Mater. 46 (2017) 4539–4556.
[30] J.F. Wager, D.A. Keszler, R.E. Presley, Transparent Electronics, Springer, Berlin, 2008.
[31] H. Hiramatsu, K. Ueda, H. Ohta, T. Kamiya, M. Hirano, M. Kikuchi, H. Yanagi, T. Kamiya, H. Hosono, Heavy hole doping of epitaxial thin films of a wide gap p-type semiconductor, LaCuOSe, and analysis of the effective mass, Appl. Phys. Lett. 91 (2007), pp. 012104–1-3.
[32] A. Zakutayev, J. Tate, S. Xie, B.J. Gibbons, H.A.S. Platt, D.A. Keszler, A. Barati, A. Klein, W. Jaegermann, Interdiffusion at the BaCuSeF/ZnTe interface, Thin Solid Films (2011) 7369–7373.
[33] L. Nordstrom, D.J. Singh, Plane Waves, Pseudopotentials and the LAPW Method, Springer, Berlin, 2006.
[34] P. Blaha, K. Schwarz, G. Madsen, D. Kvasnicka, J. Luitz, Schwarz, wien2k, An Augmented Plane Wave + Local Orbitals Program for Calculating crystal Properties, Vienna University of Technology, Austria, 2016.
[35] J.P. Perdew, A. Ruzsinszky, G.I. Csonka, O.A. Vydrov, G.E. Scuseria, L.A. Constantin, X. Zhou, K. Burke, Restoring the density-gradient Expansion for exchange in solids and surfaces, Phys. Rev. Lett. 10 (2008), pp. 136406–1-4.
[36] J.P. Perdew, A. Zunger, Self-interaction correction to density-functional approximations for many-electron systems, Phys. Rev. B 23 (1981) 5048–5079.
[37] J.P. Perdew, M. Levy, Physical content of the Exact Kohn-Sham orbital energies: band gaps and derivative discontinuities, Phys. Rev. Lett. 51 (1983) 1884–1887.
[38] L.J. Sham, M. Schlüter, Density-functional theory of the energy gap, Phys. Rev. Lett. 51 (1983) 1888–1891.
[39] P. Mori-Sanchez, A.J. Cohen, W. Yang, Localization and delocalization Errors in density functional theory and implications for band-gap prediction, Phys. Rev. Lett. 100 (2008), pp. 146401–1-4.
[40] A.D. Becke, E.R. Johnson, A simple effective potential for exchange, J. Chem. Phys. 124 (2006) 221101–221104.
[41] F. Tran, P. Blaha, K. Schwarz, Band gap calculations with Becke–Johnson exchange potential, J. Phys. Condens. Matter 19 (2007), pp. 196208–1-8.
[42] F. Tran, P. Blaha, Accurate band gaps of semiconductors and insulators with a semilocal exchange-correlation potential, Phys. Rev. Lett. 102 (2009), pp. 226401–1-4.
[43] D. Koller, F. Tran, P. Blaha, Merits and limits of the modified Becke-Johnson exchange potential, Phys. Rev. B 83 (2011), pp. 195134–1-10.
[44] J.D. Pack, H.J. Monkhorst, Special points for Brillouin-zone integrations, Phys. Rev. B 16 (1977) 1748–1749.
[45] T. Fang, S. Zheng, T. Zhou, H. Chen, P. Zhang, Validity of rigid-band approximation in the study of thermoelectric properties of p-type FeNbSb-based half-Heusler compounds, J. Electron. Mater. 46 (2017) 3030–3035.
[46] M.S. Lee, S.D. Mahanti, Validity of the rigid band approximation in the study of the thermopower of narrow band gap semiconductors, Phys. Rev. B 85 (2012) 1651491–1651498.
[47] G.K.H. Madsen, D.J. Singh, BoltzTraP. A code for calculating band-structure dependent quantities, Comput. Phys. Commun. Phys. Commun 175 (2006) 67–71.
[48] C.S. Wang, W.T. Pickett, Density-functional theory of Excitation spectra of semiconductors: application to Si, Phys. Rev. Lett. 51 (1983) 597–600.
[49] S.Zh Karazhanov, P. Ravindran, H. Fjellvag, B.G. Svensson, Electronic structure and optical properties of $ZnSiO_3$ and Zn_2SiO_4, J. Appl. Phys. 106 (2009), pp. 123701–1-7.
[50] S. Lemal, J. Varignon, D.I. Bilc, P. Ghosez, Thermoelectric properties of layered calcium cobaltite $Ca_3Co_4O_9$ from hybrid functional first-principles calculations, Phys. Rev. B 95 (2017), pp. 075205–1-13.
[51] J. Bardeen, W. Shockley, Deformation potentials and mobilities in non-polar crystals, Phys. Rev. 80 (1950) 72–80.
[52] F.B. Beleznay, F. Bogár, J. Ladik, Charge Carrier mobility in quasi-one-dimensional systems: application to a guanine stack, J. Chem. Phys. 119 (2003) 5690–5695.
[53] J. Xi, M. Long, L. Tang, D. Wang, Z. Shuai, First-principles prediction of charge mobility in carbon and organic nanomaterials, Nanoscale 4 (2012) 4348–4369.
[54] X. Zhang, C. Wang, Y. Wang, Influence of the elements (Pn = As, Sb, Bi) on the transport properties of p-type Zintl compounds Ba_2ZnPn_2, Comput. Mater. Sci. 127 (2017) 8–14.
[55] D.G. Cahill, R.O. Pohl, Heat flow and lattice vibrations in glasses, Solid State Commun. 70 (1989) 927–930.
[56] D.G. Cahill, S.K. Watson, R.O. Pohl, Lower limit to the thermal conductivity of disordered crystals, Phys. Rev. B 46 (1992) 6131–6140.
[57] A. Zevalkink, S.P. Gregory, S. Johnson, J. Swallow, Z.M. Gibbs, G.J. Snyder, Influence of the triel elements (m = Al, Ga, in) on the transport properties of $Ca_5M_2Sb_6$ *zintl compounds*, Chem. Mater. 24 (2012) 2091–2098.